SYNTHESIS, CHARACTERIZATION AND APPLICATIONS OF MAGNETO-RESPONSIVE FUNCTIONAL MATERIALS

EDITED BY: Yancheng Li, Jinbo Wu, Yingdan Liu and Xinglong Gong
PUBLISHED IN: Frontiers in Materials

frontiers Research Topics

ISSN 1664-8714
ISBN 978-2-88971-165-9
DOI 10.3389/978-2-88971-165-9

About Frontiers

Frontiers is more than just an open-access publisher of scholarly articles: it is a pioneering approach to the world of academia, radically improving the way scholarly research is managed. The grand vision of Frontiers is a world where all people have an equal opportunity to seek, share and generate knowledge. Frontiers provides immediate and permanent online open access to all its publications, but this alone is not enough to realize our grand goals.

Frontiers Journal Series

The Frontiers Journal Series is a multi-tier and interdisciplinary set of open-access, online journals, promising a paradigm shift from the current review, selection and dissemination processes in academic publishing. All Frontiers journals are driven by researchers for researchers; therefore, they constitute a service to the scholarly community. At the same time, the Frontiers Journal Series operates on a revolutionary invention, the tiered publishing system, initially addressing specific communities of scholars, and gradually climbing up to broader public understanding, thus serving the interests of the lay society, too.

Dedication to Quality

Each Frontiers article is a landmark of the highest quality, thanks to genuinely collaborative interactions between authors and review editors, who include some of the world's best academicians. Research must be certified by peers before entering a stream of knowledge that may eventually reach the public - and shape society; therefore, Frontiers only applies the most rigorous and unbiased reviews.
Frontiers revolutionizes research publishing by freely delivering the most outstanding research, evaluated with no bias from both the academic and social point of view. By applying the most advanced information technologies, Frontiers is catapulting scholarly publishing into a new generation.

What are Frontiers Research Topics?

Frontiers Research Topics are very popular trademarks of the Frontiers Journals Series: they are collections of at least ten articles, all centered on a particular subject. With their unique mix of varied contributions from Original Research to Review Articles, Frontiers Research Topics unify the most influential researchers, the latest key findings and historical advances in a hot research area! Find out more on how to host your own Frontiers Research Topic or contribute to one as an author by contacting the Frontiers Editorial Office: frontiersin.org/about/contact

SYNTHESIS, CHARACTERIZATION AND APPLICATIONS OF MAGNETO-RESPONSIVE FUNCTIONAL MATERIALS

Topic Editors:
Yancheng Li, University of Technology Sydney, Australia
Jinbo Wu, Shanghai University, China
Yingdan Liu, Yanshan University, China
Xinglong Gong, University of Science and Technology of China, China

Citation: Li, Y., Wu, J., Liu, Y., Gong, X., eds. (2021). Synthesis, Characterization and Applications of Magneto-Responsive Functional Materials. Lausanne: Frontiers Media SA. doi: 10.3389/978-2-88971-165-9

Table of Contents

04 ***Editorial: Synthesis, Characterization, and Applications of Magneto-Responsive Functional Materials***
Yancheng Li, Xinglong Gong, Yingdan Liu and Jinbo Wu

06 **In-situ *Capacitance Sensing for the Settlement of Magnetorheological Fluid: Simulation and Experiments***
Honghui Zhang, Zhiyuan Zou, Na An, Ningsong Xiong and Xu Yang

13 ***A Review on Structural Configurations of Magnetorheological Fluid Based Devices Reported in 2018–2020***
Dezheng Hua, Xinhua Liu, Zengqiang Li, Pawel Fracz, Anna Hnydiuk-Stefan and Zhixiong Li

28 ***Improved Magnetorheological Properties by Using Ionic Liquid as Carrier Liquid of Magnetorheological Fluids***
Yu Tong, Xiaoguang Li, Penghui Zhao, Xufeng Dong, Zhanjun Wu and Min Qi

33 ***Field–Frequency-Dependent Non-linear Rheological Behavior of Magnetorheological Grease Under Large Amplitude Oscillatory Shear***
Huixing Wang, Tianxiao Chang, Yancheng Li, Shaoqi Li, Guang Zhang and Jiong Wang

50 ***Enhanced Magnetorheological Performance of Carbonyl Iron Suspension Added With Barium Ferrite Nanoparticle***
Hyo Seon Jang, Qi Lu and Hyoung Jin Choi

59 ***Magneto-Induced Normal Stress of Magnetorheological Gel Under Quasi-Statically Monotonic and Periodically Cyclic Loading***
Runsong Mao, Xudan Ye, Huixing Wang, Guang Zhang and Jiong Wang

72 ***The Roles of Magnetorheological Fluid in Modern Precision Machining Field: A Review***
He Lu, Dezheng Hua, Baiyi Wang, Chengli Yang, Anna Hnydiuk-Stefan, Grzegorz Królczyk, Xinhua Liu and Zhixiong Li

83 ***Sliding Mode Active Disturbance Rejection Control for Magnetorheological Impact Buffer System***
Bin Wang, Wanjun Wang and Zhaochun Li

99 ***Magneto-Sensitive Rubber in a Vehicle Application Context – Exploring the Potential***
Bochao Wang, Tao Hu, Longjiang Shen, Jun Li, Zhenbang Xu, Leif Kari and Xinglong Gong

114 ***Nonlinear Magneto-Electro-Mechanical Response of Physical Cross-Linked Magneto-Electric Polymer Gel***
Xiwen Fan, Yu Wang, Bochao Wang, Longjiang Shen, Jun Li, Zhenbang Xu, Sheng Wang and Xinglong Gong

frontiers in Materials

EDITORIAL
published: 08 July 2021
doi: 10.3389/fmats.2021.710474

Editorial: Synthesis, Characterization, and Applications of Magneto-Responsive Functional Materials

Yancheng Li[1], Xinglong Gong[2], Yingdan Liu[3] and Jinbo Wu[4]*

[1]School of Civil and Environmental Engineering, University of Technology Sydney, Sydney, NSW, Australia, [2]CAS Key Laboratory of Mechanical Behavior and Design of Materials, Department of Modern Mechanics, CAS Center for Excellence in Complex System Mechanics, University of Science and Technology of China (USTC), Hefei, China, [3]State Key Lab of Metastable Materials Science and Technology, College of Materials Science and Engineering, Yanshan University, Qinhuangdao, China, [4]Materials Genome Institute, Shanghai University, Shanghai, China

Keywords: magneto-responsive, magnetorheological, characterization, application, numerical

Editorial on the Research Topic

Synthesis, Characterization, and Applications of Magneto-Responsive Functional Materials

BACKGROUND

Magneto-responsive functional materials, in particular, magnetorheological (MR) materials (in forms of liquid, elastomer, grease, or others), have gained significant attention from around the world. The materials, with drastic rheological property changes, have been heavily investigated to develop smart devices and applications, ranging from micro-sized sensors to large-scale energy dissipation devices for civil engineering applications. Cross-disciplinary research activities are still booming with aims to: 1) render larger MR effect with better stability and durability; 2) understand and characterize the complex material behavior with existing or new rheology theories; 3) apply innovations to design MR devices or actuators in many forms for respective targeted applications; and, 4) address underlying concerns from end-customers for application-related obstacles. This Research Topic is set to provide a platform for scientists and researchers to exchange the latest developments in the field. The topic includes wide coverage of the focusing theme on technologies and innovations in the aforementioned four areas. We are proud to present 10 peer-reviewed contributions offering insights on synthesis, characterization, and applications of MR materials from leading researchers.

MAJOR HIGHLIGHTS OF THE CONTRIBUTIONS

MR fluids as important MR material that are used to design various intelligent vibration control devices, such as brakes, clutches, dampers, and mounts, as well as medical apparatus. Over the past 2 decades, numerous designs have been proposed and tested based on the four operational modes of the MR fluid. To summarise the latest developments, Hua et al. presented a dedicated review of the structural configurations of MR fluid based devices in 2018–2020. In particular, the section on MR fluid devices for medical application includes several innovative devices, such as robotic bone biopsy, haptic actuator, and tactile device, which are highlights worthy of attention. Conclusive remarks and future perspectives are also offered by the authors. Another topic review on the role of MR fluid in

OPEN ACCESS

Edited and reviewed by:
Weihua Li,
University of Wollongong, Australia

****Correspondence:***
Yancheng Li
yancheng.li@uts.edu.au

Specialty section:
This article was submitted to Smart Materials, a section of the journal Frontiers in Materials

Received: *16 May 2021*
Accepted: *26 May 2021*
Published: *08 July 2021*

Citation:
Li Y, Gong X, Liu Y and Wu J (2021) Editorial: Synthesis, Characterization, and Applications of Magneto-Responsive Functional Materials. Front. Mater. 8:710474. doi: 10.3389/fmats.2021.710474

precision machining is given by Lu et al. The state-of-the-art review on the surface polishing equipment is the first piece in the community to comprehend outstanding research and work in the area.

There has been a continuous effort in upgrading the performance of MR fluid, in terms of larger MR effect, low sedimentation, and high stability. When subjected to a magnetic field, the particles in the carrier form chain or column structures along the field direction, which can only be broken until an external force/stress reaches a certain threshold, namely yield stress. The improvement of MR effect can be achieved through modifications to the magneto particles and carrier fluids. The interface between particles and carrier fluids plays a substantial role in the performance of MR fluid. Tong et al. proposed the use of ionic liquid and silicon oil with the same viscosity as a carrier fluid to prepare MR fluid. They showed that the new MR fluid possesses higher yield stress of up to 90 kPa, around 20 kPa more than a silicon oil based MR fluid. The results of this experiment are explained by the enhanced interactions between the particles, encouraged by the fact that ion fragments in the ionic liquid formed an ion layer on the surface of the particles. Jang et al. adopted another approach to enhance the MR effect, i.e., coating Carbon Iron (CI) particles with hard-magnetic barium ferrite (BF) nanoparticles. The hard-magnetic BF nanoparticles have a hexagonal plate-like structure and high magnetocrystalline anisotropy, high Curie point, relatively high magnetic saturation value and coercive force, and superior chemical stability and corrosion resistance. SEM images reveal that the $BaFe_{12}O_{19}$ particles are attached to the space between the CI particles, which enhanced the MR efficiency, reduced particle aggregation, and thus improved suspension stability.

The gravitational force of the heavy ferrite particle induces settling of the particles due to the mismatch with the low-density carrier fluid. Sedimentation in MR fluid has indeed become a burning issue to resolve facing the application of MR devices, or at least with technology to monitor the sedimentation inside the device. Zhang et al. propose an *in-situ* capacitance sensing approach to capture the settlement of MR fluid within an MR damper cylinder. They designed an open plate capacitor configuration and the system was calibrated using theoretical simulation and experiment. The proposed system can be used for the long-term monitoring of the particle settling of MR fluid in any fabricated MR device.

To overcome the influence of disturbances, either internal or external, on the performance of the MR impact buffer system, B. Wang and Li. proposed a hybrid control strategy with sliding mode active disturbance rejection control based on extended state observer. The proposed control method is validated through numerical simulation and exhibits superiority with fast response, minimal overshooting, and great immunity to nonlinear hysteresis.

Besides MR fluids, other forms of MR materials such as MR elastomer, gel, and grease, have been been the focus of recent research. Similar to the trajectory of MR fluids, research activities on other MR materials are mainly from material scientists and are expected to rapidly shift to engineering. Wang et al. explored the feasibility of MR elastomer (also called Magneto-Sensitive rubber, or MS rubber) to be used in semi-active vehicle suspension. A constitutive model was proposed to accurately replicate the behavior of MS rubber. They then used an H-infinity control strategy for a quarter car model featuring MS rubber semi-active suspension to examine the performances under a bump and a random ground excitation. Future perspectives on this proposal are discussed, with ample insights presented. Gong et al. developed a novel MR polymer gel utilizing carbon nanotubes and CI particles to mix into the polymer gel matrix. An unusual nonlinear magneto-electro-mechanical response, i.e. rate-dependence, was observed together with high performance sensing behavior. Thus, the new material has promising futures in both active control and electromechanical sensing, either separately or combined. Mao et al. investigated the magneto-induced normal stress in MR gel under quasi-statically monotonic and periodically cyclic loading. Detailed experimental testing and observation can all be found in this article with ample insights.

Understanding the rheological properties is the key to unlock the potentials of MR materials for future applications. Usually, storage/loss modules and Lissajous curves from the oscillatory shear tests are used to extrapolate the rheological properties. However, they each possess drawbacks in making the detailed nonlinear behavior more explicit. Wang et al. utilized Fourier transform-Chebyshev analysis to quantitatively interpret the influence and frequency on the non-linear rheology of MR grease. The strain-stiffening/softening and shear thickening/thinning features of the materials can be easily expressed using this method, which offers a new way of examining the complex behavior of MR materials, especially under sophisticated influences of the magnetic field, complex strain, and temperature.

SUMMARY

These Research Topic contributions provide information about the latest developments in magneto-responsive materials in relation to various aspects, such as state-of-the-art review, material development, and characterization, constitutive modelling, numerical methods, and simulation. The editors hope that you find these articles useful and are inspired by them.

AUTHOR CONTRIBUTIONS

YL prepared the draft. XG, YdL, and JW edited the draft.

Conflict of Interest: The authors declare that the research was conducted in the absence of any commercial or financial relationships that could be construed as a potential conflict of interest.

frontiers in Materials

ORIGINAL RESEARCH
published: 25 March 2021
doi: 10.3389/fmats.2021.663925

In-situ Capacitance Sensing for the Settlement of Magnetorheological Fluid: Simulation and Experiments

Honghui Zhang[1,2]*, *Zhiyuan Zou*[1], *Na An*[1], *Ningsong Xiong*[1] and *Xu Yang*[3]

[1] College of Opto-Electronic Engineering, Chongqing University, Chongqing, China, [2] The Key Laboratory for Opto-Electronic Technology and System, Ministry of Education, Chongqing University, Chongqing, China, [3] Chongqing Tiema Industries Group Company Limited, Chongqing, China

In light of the insurmountable sedimentation of magnetorheological (MR) fluid, it is of great significance to ensure the performability of an MR damper by introducing a sensing method for MR fluid settling, and a key indicator to identify the health status of the MR damper is critical. However, the settling monitoring system for MR fluid can nowadays only function in a laboratory with transparent and non-magnetic tubes, which is not qualified for the *in-situ* sensing in a steel-made cylinder. Under the analysis of an open plate capacitor (OPC) configuration, the relationship between the concentration of magnetorheological fluid and the capacitance is investigated by simulation and experiments, and based on OPC, an *in-situ* sensing method for the settlement monitoring of magnetorheological fluid is designed. Long-time settling monitoring is carried out with home-made MR fluids, and the test results show that the sensing method can effectively reflect the status of settled MR fluids, and has the potential to be utilized in the identification of MR fluid compression points, which provides the strategic signal for the probable active or operational re-dispersing of MR fluid.

Keywords: magnetorheological fluid, open plate capacitor, settlement, *in-situ* sensing, dielectric constant

OPEN ACCESS

Edited by:
Yancheng Li,
University of Technology Sydney, Australia

Reviewed by:
Huixing Wang,
Nanjing University of Science and Technology, China
Xufeng Dong,
Dalian University of Technology, China

***Correspondence:**
Honghui Zhang
hhzhang@cqu.edu.cn

Specialty section:
This article was submitted to Smart Materials, a section of the journal Frontiers in Materials

Received: *04 February 2021*
Accepted: *01 March 2021*
Published: *25 March 2021*

Citation:
Zhang H, Zou Z, An N, Xiong N and Yang X (2021) In-situ Capacitance Sensing for the Settlement of Magnetorheological Fluid: Simulation and Experiments. Front. Mater. 8:663925. doi: 10.3389/fmats.2021.663925

INTRODUCTION

Magnetorheological (MR) fluid was first described in 1948 by J. Rabinow, 1 year after Winslow's patent for electrorheological (ER) fluid, but MR fluid prevails with its much higher mechanical performance in relatively low voltages. MR fluid is a suspension of magnetically soft and micron-sized particles in a carrier liquid, typically carbonyl iron (CI) particles and silicon oil, and the rheological properties can be controlled by an applied magnetic field (Rankin et al., 1999). When free of the magnetic field, the particles are dispersed uniformly in the carrier liquid by strong surfactants and the MR fluid generally performs like a quasi-Newtonian fluid (Chen et al., 2015; Aruna et al., 2019).

Under a magnetic field, the particles are aggregated to form chain-like clusters which can undertake strong shear deformation like a Bingham fluid, and the more intense magnetic flux, the higher yield stress exhibited. The phase transition between Newtonian and Bingham behavior is rapid, reversible, and insensitive to temperature over broad temperature ranges, and thus MR fluid can provide simple, quiet, and rapid-response interfaces between electronic controls and mechanical systems, and has been applied to various types of devices such as dampers, clutches, brakes, valves, etc.

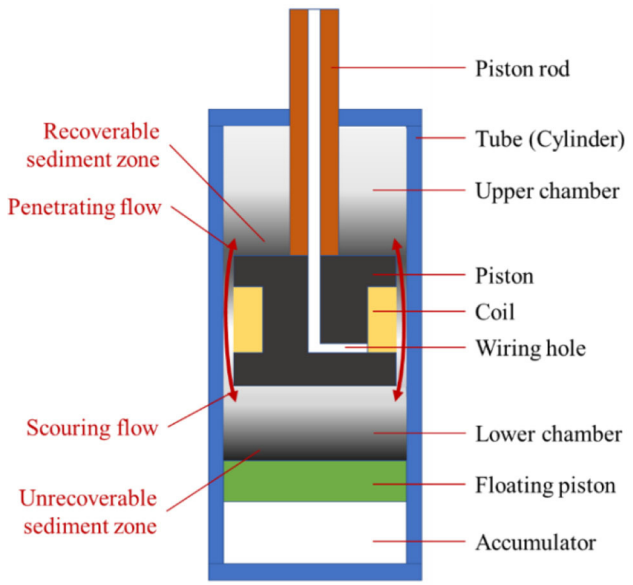

FIGURE 1 | Flow analysis of the MR fluid in a typical MR damper.

Regardless of the ever-developing additives and surfactants, MR fluid tends to be settled because of the density mismatch between the dispersed phase and carrier fluid, which causes the MR damper to stick or degrade, i.e., the performability of the MR damper cannot be ensured if it is standing still for a long time such as the one adopted in earthquake mitigation. The contemporary MR damper, shown in **Figure 1**, mainly works via the principle of flow mode and shear mode with a single tube structure, the accumulator accommodates the volume change, which occurs due to the piston rod getting in and out of the cylinder, which is always located at the bottom end of the cylinder, and a floating piston serves as an isolator between the chambers. According to the flow analysis, the particles aggregated onto the upper end of the piston can be regarded as the recoverable sediment zone when formed after long-time standing of the MR damper, and re-dispersed by penetrating flow induced by the piston reciprocation. But the MR fluid only acts as a scouring flow for the unrecoverable sediment zone over the floating piston because the MR fluid flow stops there, and the MR damper degrades because the particles cannot be brought into the main stream of the MR fluid, which inevitably lowers the actual concentration of MR fluid. Consequently, a system should be established to characterize the health of the MR damper, determining the aggregation state of the MR fluid in the unrecoverable sediment zone is a potential way.

The most commonly used method for MR fluid sedimentation monitoring is visual observation, Gorodkin et al. (2000), Chen and Chen (2003), and Ngatu and Wereley (2007) tracked the mudline in MR fluid settling using a fixed inductor. Xie et al. (2015) investigated the sedimentation comparison between silicone oil and HVLP-based MR fluid, and the sedimentation characterization based on a vertical axis inductance monitoring system (VAIMS) was carried out (Choi et al., 2016) by vertically translating an inductor sensor along the MR fluid column which is enclosed in a transparent tube, and recording the inductance value in a specified time interval until the MR fluid settled to a stable condition in the column. Wen et al. (2019) optimized the VAIMS with a LARS sensor to better locate MR fluid layering while it settled. Cheng et al. (2016) established a complicated system to monitor MR fluid settling via the thermal conductivity change with the concentration, in which the thermal conductivity was monitored at a fixed location but the system was severely dependent on the thermal environment.

Most of the monitoring methods proposed for MR fluid sedimentation were carried out in the laboratory, and the MR fluid was enclosed by a non-magnetic tube, which is favorable for MR fluid preparation and optimization, but it is futile when we hope to investigate the MR fluid which services an actual device such as a damper or clutch. Vezys et al. (2018) developed a method for sedimentation sensing in a MR brake via resistivity measuring, in which the MR fluid sedimentation is characterized with the magnetic field strength and the time of standing still, but failed to correlate the resistivity with the concentration of MR fluid. Gillet et al. (2020) proposed a novel method to track the degradation of an MR clutch by correlating the clearness percentage of MR fluid with the established durability metric of "life dissipated energy" (LDE), where the clearness of MR fluid is sensed by an optical red green blue sensor.

It is obvious that the sedimentation monitoring of MR fluid is of great significance for ongoing applications, but it is difficult to relate the real concentration of the MR fluid with device performance such as dampers, brakes, and clutches, because of the opaqueness and immeasurable inductance in a real steel-made cylinder. Numerical simulations should play an important role for the promotion of effective sedimentation monitoring. There are other factors inducing the degradation of MR devices, but MR fluid sedimentation constructs the greatest challenge for the performability of an MR damper, so an *in-situ* capacitance sensing method is proposed in this paper to better illustrate the MR fluid concentration in the settling process via simulation and experiments.

THEORETICAL BASES

As we know, a parallel plates capacitor is comprised of two face-to-face placed plates and the facing area of the plates is proportional to the capacitance. But when used as a sensing element, the gap distance or the dielectric coefficient of the medium between the plates often interact with the sensed quantities to regulate the capacitance. The dielectric coefficient of the MR fluid will be regulated with the concentration change in the sedimentation of the MR fluid, but the particles will be prevented from getting into the capacitor gap because of the obstruction of plates or the small distance between the plates, no matter if the parallel capacitor is placed horizontally or

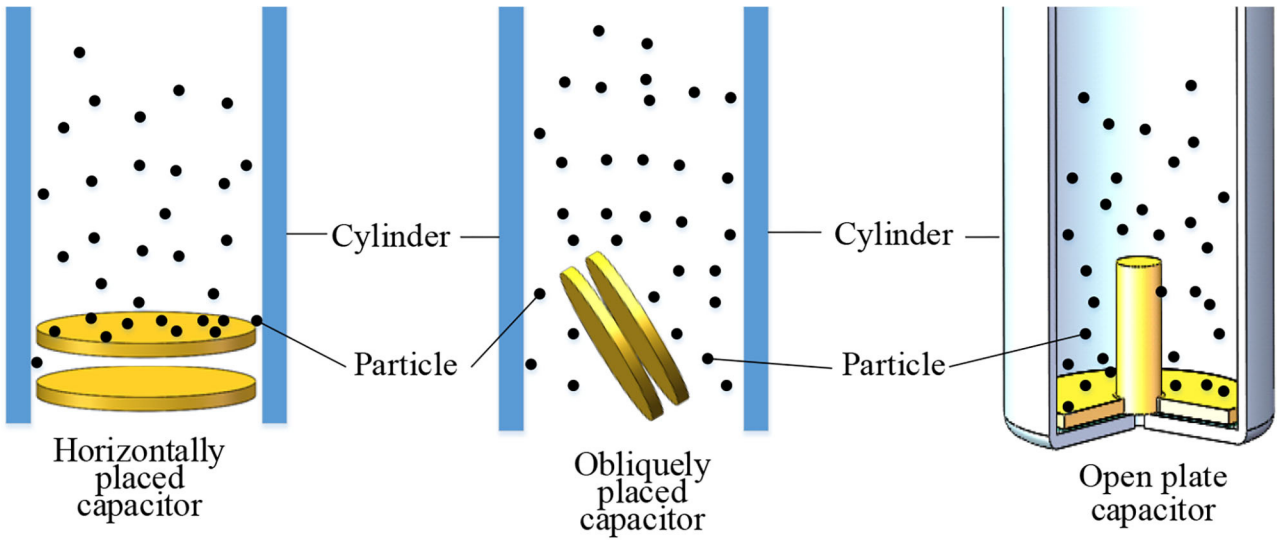

FIGURE 2 | Capacitor configuration for settlement sensing of MR fluid.

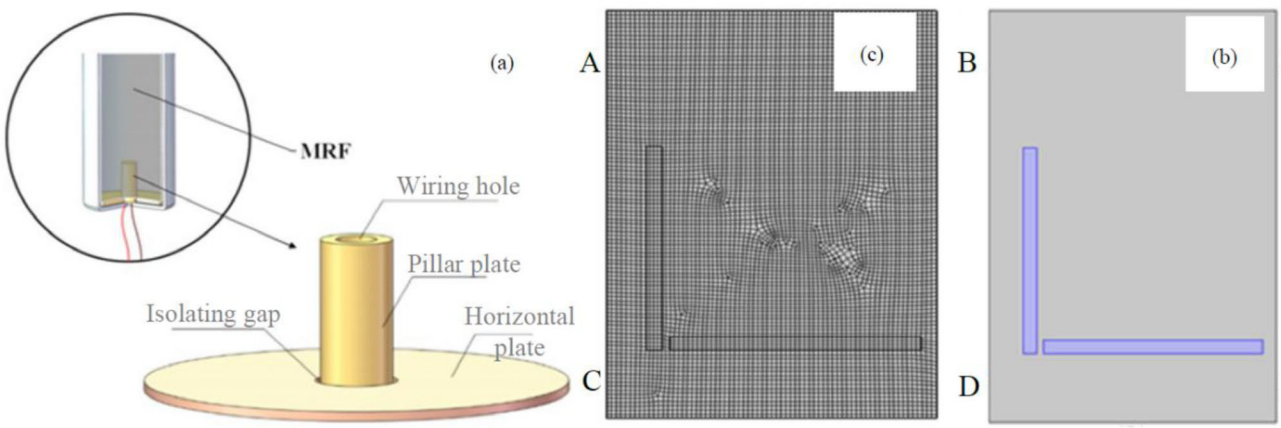

FIGURE 3 | The electromagnetic model of an open plate capacitor; **(a)** sensor configuration; **(b)** electromagnetic model; **(c)** mesh grid of the finite element model.

obliquely as shown in **Figure 2**. An open plate capacitor (OPC), with a bottom-placed horizontal plate and a pillar plate in the center, is proposed in this paper to designate the settling of MR fluid, in which the settled particles will be gathered onto the horizontal plate and effectively change the concentration of the MR fluid enclosed.

As show in **Figure 3a**, the sensing element is *in-situ* because the capacitor is bottom-placed in the steel-made cylinder, and the operation of the MR damper is not affected while the settling monitoring of the MR fluid is continuously operating. A wiring hole is in the center of the pillar plate and an isolating gap is between the two insulated plates to avoid circuit shorting. The horizontal plate is 41 mm in diameter, a little smaller than the steel cylinder which is 42 mm in diameter, and the pillar plate is 8 mm in diameter and of 15 mm in height. To explore the relationship between the concentration of the MR fluid and the capacitance of the open plate capacitor, a COMSOL finite element model is established and shown in **Figure 3b**. In the simulation, a two-dimensional axial symmetric model is employed for the open plate capacitor because of the physical essentials. The boundary conditions are listed as following: the pillar plate is set to be a potential terminal with a 1 V surface voltage, and the horizontal plate is set to be a grounding terminal.

In **Figure 3c**, the open plate capacitor is assumed to be placed in a uniformly distributed MR fluid, and the physical boundaries of AB, BD, and CD are set to be zero electric charge, and AC is the symmetrical axis. The dielectric coefficient of plates is set to be a two-phase augmented composite relative to the MR fluid, and the

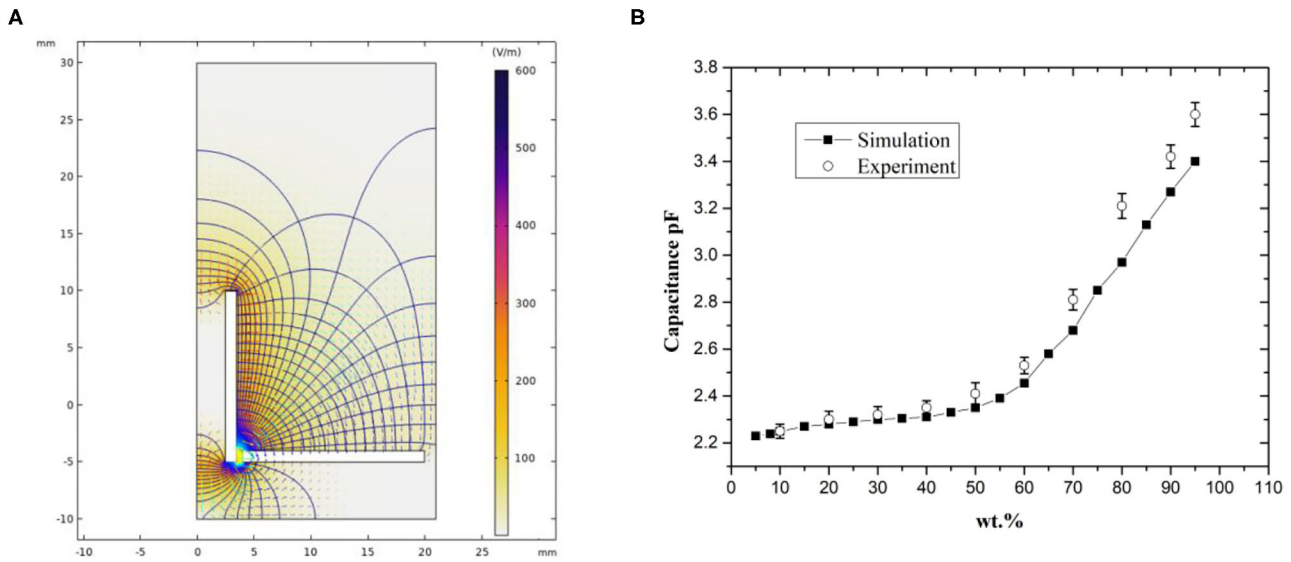

FIGURE 4 | The electromagnetic simulation of the open plate capacitor; **(A)** electric field distribution at 20wt.%; **(B)** the results between the capacitance and the MR fluid concentration.

equivalent relative dielectric coefficient ε satisfies the following Maxwell–Garnett model (Garnett, 1904):

$$\varepsilon = \varepsilon_m + 3\frac{\varphi\varepsilon_p}{(1-\varphi)\,\rho_p/\rho_l + \varphi}\frac{\varepsilon_m - \varepsilon_p}{\varepsilon_m + 2\varepsilon_p - \varphi\left(\varepsilon_m - \varepsilon_p\right)} \quad (1)$$

Where φ is the fraction of carbonyl iron (CI) particles of MR fluid in weight, and ε_p is the relative dielectric coefficient of the CI particles and is set to 60. ε_m is the relative dielectric coefficient of the solute and is set to 2, and ρ_p, ρ_l are the densities of the dispersed particle and dispersing medium, 7,900 and 1,000 kg/m^3, respectively, in this simulation. The discretized finite element model is substituted into the ES solution of COMSOL software and the results are shown in **Figure 4**.

From **Figure 4A**, the electric field in the MR fluid is mainly concentrated at the adjacent zone of the pillar and horizontal plates when the open plate capacitor is applied with 1 V in the pillar plate, and the nearer to the pillar plate, the stronger the electric field. The maximum is 1,217 V/m, the equipotential surface is distributed bowl-like between the two plates. From **Figure 4B**, with the heightening of the MR fluid concentration, the capacitance of the open plate capacitor is increased from 2.23 to 2.71 pF, following an accelerating trend with the MR fluid concentration. Additionally, the results show that there is a deterministic relationship between the MR fluid concentration and the capacitance, and this makes it possible to measure the settled MR fluid concentration by sensing the capacitance output of the open plate capacitor. With LCR equipment in precision of 0.01 pF, the simulated results are also experimentally validated in **Figure 4B** using the home-made MR fluid with simply mixed CI particles in silicone oil with specific concentrations (the details are in section Experiment). The simulation coincides well with the experiment, but the simulation is a little smaller in value because of the error from the Maxwell–Garnett model in high particle concentration. And the result shows that the capacitance-based sensing method will be more sensitive in high MR fluid concentrations, and once the particles settle to a relatively high concentration, the sensing will be more accurate.

EXPERIMENT

MR Fluid Preparation

To speed up the experiment, the home-made MR fluid is prepared to accelerate particle settling, the CI particles with $d_{50} = 5\,\mu$m and the silicone oil with a viscosity of 100 cps are used. The metering in the MR fluid preparation is relatively easy because the concentration is determined by weight ratio. The weight ratio of CI particles and silicone oil is 4:1 when taking an 80% MR fluid concentration as an example, ∼200 ml of silicone oil is weighed by a balance in 0.1 g precision and poured into a transparent beaker and the CI particles (four times the weight of the oil) are mixed into the silicone oil, and then the blend is adequately stirred and mixed by a muddler before measurement, the uniformity of the MR fluid is determined by visual information and manual interaction. The range of MR fluid concentration in weight ratio can be effectively broadened to nearly 100%, and in this paper, MR fluid samples of 10–90% with a 10% interval, and an additional 95% concentration in weight ratio are prepared to validate the simulation results, but only MR fluids, initially in relatively low concentrations of 20, 30, and 40%, are used to track particle settling for exploring the settling process from low to high concentrations. The prepared MR samples are designated as the weight ratio with a prefix of MRF, such as MRF20, MRF30, and MRF40.

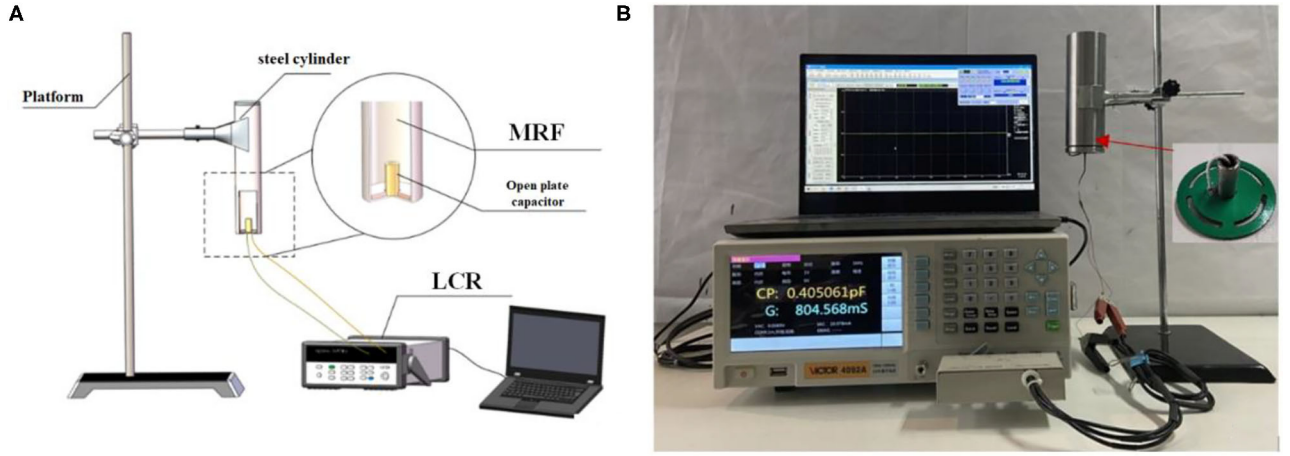

FIGURE 5 | The test setup for MR fluid settlement monitoring and capacitance calibration. **(A)** Scheme diagram. **(B)** Experiment setup.

Test Setup

The test setup is shown in **Figure 5A** and the steel cylinder is held on a stand with the open plate capacitor placed at the bottom, LCR equipment is used to measure the capacitance, and a laptop is included. The steel cylinder is 120 mm in height and the upper end is not covered to allow us to pour and remove the MR fluid. The leading wire is fed through the wiring hole of the pillar plate and the end cover of the cylinder, and then the wiring hole is sealed with epoxy resin. VICTOR brand LCR equipment is used and in a precision of 0.01 pF, the frequency of the capacitance reading is set to 100 kHz.

The Calibration Test

All seven prepared samples are adopted to calibrate the simulation result of the relationship between the MR fluid concentration and the capacitance of the open plate capacitor. Pouring 100 ml of the prepared sample into the cylinder from the upper opening of the cylinder and ensuring the pillar plate is totally immersed in the MR fluid, the capacitance outputs are recorded simultaneously for samples in each concentration, respectively, and the output values are averaged by five-time measurements for each sample. The cylinder functions as an electromagnetic shield and the wall is connected to the grounding terminal of the LCR equipment to avoid electromagnet interference. Because of the long process of MR fluid sedimentation monitoring, the test setup is put into a thermostatic chamber and kept at 20°C.

Sedimentation Monitoring

Based on the *in-situ* monitoring test setup, sedimentation monitoring of MR fluids is carried out with different concentrations, only MRF20, MRF30, and MRF40 are used in the monitoring to speed up the process and the capacitance can be observed from an initial low concentration to the settled high concentration, and all the testing MR fluids used are 100 ml in volume. Because the mudline formation is not easily observed in the steel-made cylinder, the corresponding testing sample of MR fluids are also put in transparent tubes with the same volume as a contrast, the emergence and following descent of the mudline are recorded with a time interval of 10 min until they remain unchanged. The capacitance acquisition is started when the testing MR fluids are poured into the steel-made cylinders and the transparent tubes simultaneously, and the acquired capacitance is transferred into the concentration of the MR fluid according to the calibration test shown in **Figure 5B**.

RESULTS AND DISCUSSION

The results of settlement monitoring are shown in **Figure 6**. As shown in **Figure 6A**, the mudline height descends and the MRF20 concentration increases at the bottom of the cylinder with increasing time because of the sedimentation. The mudline descends from initially 180 mm to 121 mm and the concentration rises from 20.0 to 64.5 wt.%, respectively, after 100 min of settling. The mudline heights are 55 and 23 mm, respectively, at the second and the third hundredth minute, and eventually end at 8 mm, but the concentrations are 90.1 and 95.1 wt.% in the same time scale, and then finally approach 100%. As a contrast (as shown in **Figures 6B,C**), at the time scale of the 1st, 2nd, and 3rd hundredth minute, the mudline heights and concentrations for MRF30 are 144 mm, 64.5 wt.%, 109 mm, 80.6 wt.%, and 70 mm, 86.9 wt.%, and the counterparts for MRF40 are 162 mm, 44.5 wt.%, 137 mm, 51.5 wt.%, and 110 mm, 59.7 wt.%.

For each observation, the descent of the mudline height gets slower with the increment of the measured concentration, this can be seen when the concentration of the MR fluid is low, the distance between particles is enough to prevent the interaction between particles, and the Stokes law is satisfied correspondingly. However, when the concentration of MR fluid gets higher, the distance between particles reduces and even results in contact

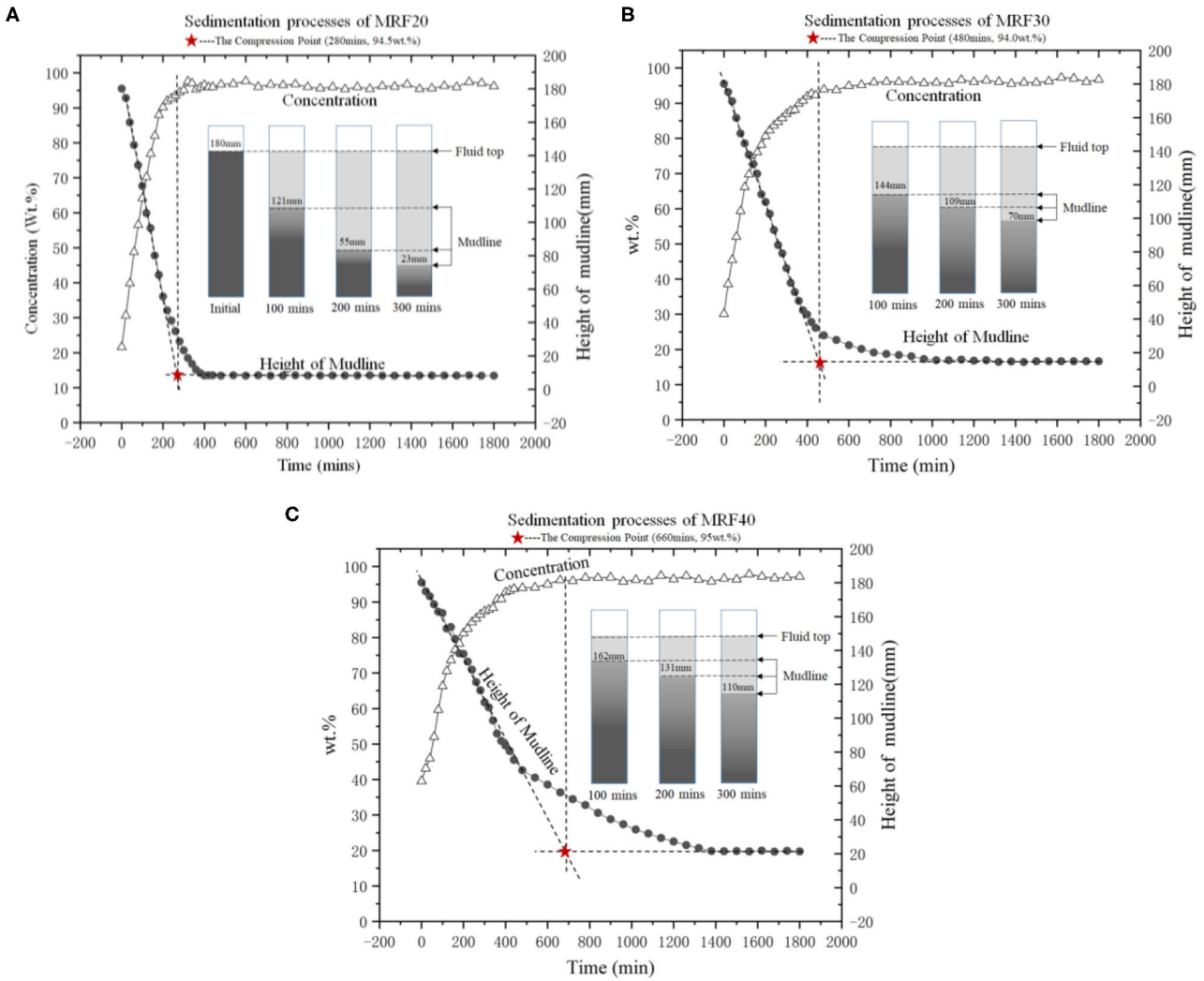

FIGURE 6 | Sedimentation processes of MRF: **(A)** MRF20; **(B)** MRF30; **(C)** MRF40.

between them, the conflict and squeeze between particles will delay the settling of the particles.

Besides, the comparison between the settlement of different MR fluid samples shows that the higher the initial concentration of the MR fluid, the slower the sedimentation will be. The time lengths needed for the fully settled status of MRF20, MRF30, and MRF40 are about 400, 950, and 1,400 min, respectively. Additionally, initial sedimentation presents a relatively steady settling rate with a constant slope, and the lower the concentration of MR fluid, the bigger the slope. According to Kynch's theory of sedimentation (Kynch, 1952), the process can be divided into a constant settling region, transition region, and consolidation region, and there is a compression point in the transition region, which can be determined theoretically by the tangent method. For the settling curve of MRF20, MRF30, and MRF40, the compression points are determined as in **Figure 6**, and the corresponding time scales are about 280, 480, and 660 min, respectively.

In addition, as a critical sedimentation point identifies the point at which the pulp-supernatant interface goes from zone settling into compression, the compression point will be the starting point of the sediment consolidation, and can be seen as a key indicator of the health status of the MR damper. It is obvious that the time of compression points appearance diverges with the concentration of MR fluid, however, the relatively constant concentration of MR fluid is measured at the cylinder bottom and it is about 94.5% in weight ratio. Accordingly, a re-dispersing mechanism should be introduced to actively or operationally disperse the settled MR fluid to avoid the failure of the device, *in-situ* capacitance sensing will play an important role as the triggering signal to start the re-dispersing mechanism. For commercial MR fluid, the appearance of the compression point can be expected much later, but the measured capacitance

of the open plate capacitor, thus the concentration of MR fluid, will be expected.

CONCLUSION

For the settling characteristics of MR fluid in a steel-made cylinder of a real MR damper, an open plate capacitor configuration based on *in-situ* sensing is proposed in this paper and LCR equipment is used as the acquisition of the capacitance, which is regulated by the settled MR fluid. The relationship between the capacitance value and the concentration of MR fluid in weight ratio is calibrated by simulation and experiments, and long-time settlement monitoring is carried out to pursue an effective indicator to reflect the status of settled MR fluid and act as a representation of the performability of a promising MR damper. The following conclusions can be drawn in the sedimentation of MR fluid:

The capacitance of open plate capacitor is positively correlated with the concentration of MR fluid, the higher the concentration, the higher the capacitance and the faster the increment of the capacitance. However, the higher the concentration of MR fluid, the slower the settling will be.

In the experiments, although the occurrence of Kynch's theory-based compression point diverges temporally, the corresponding concentration almost stays constant at about 94.5 wt.%, and the characterization of the open plate capacitor is qualified to be the triggering signal to start an active or operational re-dispersing mechanism for an MR damper, which confronts a risk of failure under MR fluid sedimentation.

DATA AVAILABILITY STATEMENT

The raw data supporting the conclusions of this article will be made available by the authors, without undue reservation.

AUTHOR CONTRIBUTIONS

HZ is the corresponding author for this submission, and he started and supervised the entire research. ZZ finished all the experiments for this paper. NA and NX jointly completed the simulation job, and finally, XY contributed on the test-up and the experimental schemes. All authors are contributing on the manuscript and the research.

FUNDING

This research is supported by the Natural Science Foundation of China (No. 62073050).

REFERENCES

Aruna, M. N., Rahman, M. R., Joladarashi, S., and Kumar, H. (2019). Influence of additives on the synthesis of carbonyl iron suspension on rheological and sedimentation properties of magnetorheological (MR) fluids. *Mater. Res. Express* 6, 086105. doi: 10.1088/2053-1591/ab1e03

Chen, F., Tian, Z. Z., and Wu, X. F. (2015). Novel process to prepare high-performance magnetorheological fluid based on surfactants compounding. *Mater. Manuf. Process* 30, 210–215. doi: 10.1080/10426914.2014.892967

Chen, L. S., and Chen, D. Y. (2003). Permalloy inductor based instrument that measures the sedimentation constant of magnetorheological fluids. *Rev. Sci. Instrum.* 74, 3566–3568. doi: 10.1063/1.1581356

Cheng, H. B., Zhang, X. P., Liu, G. Z., Ma, W. T., and Wereley, N. M. (2016). Measuring the sedimentation rate in a magnetorheological fluid column via thermal conductivity monitoring. *Smart Mater Struct* 25, 055007. doi: 10.1088/0964-1726/25/5/055007

Choi, Y. T., Xie, L., and Wereley, N. M. (2016). Testing and analysis of magnetorheological fluid sedimentation in a column using a vertical axis inductance monitoring system. *Smart Mater. Struct.* 25, 04LT01. doi: 10.1088/0964-1726/25/4/04LT01

Garnett, J. C. M. (1904). Colours in metal glasses and in metallic films. *Philos. Trans. R. Soc. A Math. Phys. Eng. Sci.* 203, 385–420. doi: 10.1098/rsta.1904.0024

Gillet, B., Landry-Blais, A., Lamy, M., Pilon, R., and Plante, J. S. (2020). An optical red green blue sensor for monitoring the degradation of magnetorheological fluids in flow-recirculating high-torque clutch actuators. *J. Intel. Mater. Syst. Struct.* doi: 10.1177/1045389X20932220

Gorodkin, S. R., Kordonski, W. I., Medvedeva, E. V., Novikova, Z. A., Shorey, A. B., and Jacobs, S. D. (2000). A method and device for measurement of a sedimentation constant of magnetorheological fluids. *Rev. Sci. Instrum.* 71, 2476–2480. doi: 10.1063/1.1150638

Kynch, G. J. (1952). A theory of sedimentation. *Trans. Faraday Soc.* 48, 166–176. doi: 10.1039/tf9524800166

Ngatu, G. T., and Wereley, N. M. (2007). Viscometric and sedimentation characterization of bidisperse magnetorheological fluids. *IEEE Trans. Magn.* 43, 2474–2476. doi: 10.1109/TMAG.2007.893867

Rankin, P. J., Horvath, A. T., and Klingenberg, D. J. (1999). Magnetorheology in viscoplastic media. *Rheol. Acta* 38, 471–477 doi: 10.1007/s003970050198

Vezys, J., Mazeika, D., Kandrotaite-Janutiene, R., Dragasius, E., Kilikevicius, A., and Korobko, E. V. (2018). Sedimentation influence on magnetorheological brake torque. *Moment Strength Mater.* 50, 357–367. doi: 10.1007/s11223-018-9979-4

Wen, M. F., Chambers, J., Sherman, S. G., and Wereley, N. M. (2019). Monitoring sedimentation of magnetorheological fluids using a vertical axis monitoring system with a low aspect ratio sensor coil. *Smart Mater. Struct.* 28, 025039. doi: 10.1088/1361-665X/aaf757

Xie, L., Choi, Y. T., Liao, C. R., and Wereley, N. M. (2015). Characterization of stratification for an opaque highly stable magnetorheological fluid using vertical axis inductance monitoring system. *J. Appl. Phys.* 117, 17C754. doi: 10.1063/1.4918629

Conflict of Interest: XY was employed by the Chongqing Tiema Industries Group Company Limited.

The remaining authors declare that the research was conducted in the absence of any commercial or financial relationships that could be construed as a potential conflict of interest.

frontiers in Materials

REVIEW
published: 25 March 2021
doi: 10.3389/fmats.2021.640102

A Review on Structural Configurations of Magnetorheological Fluid Based Devices Reported in 2018–2020

Dezheng Hua[1], Xinhua Liu[1,2], Zengqiang Li[2], Pawel Fracz[3], Anna Hnydiuk-Stefan[4] and Zhixiong Li[5]**

[1]School of Mechatronic Engineering, China University of Mining and Technology, Xuzhou, China, [2]Technology and Innovation Research Center of Jiang Yan EDZ, Taizhou, China, [3]Department of Manufacturing Engineering and Automation Products, Opole University of Technology, Opole, Poland, [4]Department of Power Engineering Management, Opole University of Technology, Opole, Poland, [5]Yonsei Frontier Lab, Yonsei University, Seoul, Republic of Korea

Magnetorheological fluid (MRF) is a kind of smart materials with rheological behavior change by means of external magnetic field application, which has been widely adopted in many complex systems of different technical fields. In this work, the state-of-the-art MRF based devices are reviewed according to structural configurations reported from 2018 to 2020. Based on the rheological characteristic, the MRF has a variety of operational modes, such as flow mode, shear mode, squeeze mode and pinch mode, and has unique advantages in some special practical applications. With reference to these operational modes, improved engineering mechanical devices with MRF are summarized, including brakes, clutches, dampers, and mounts proposed over these 3 years. Furthermore, some new medical devices using the MRF are also investigated, such as surgical assistive devices and artificial limbs. In particular, some outstanding advances on the structural innovations and application superiority of these devices are introduced in detail. Finally, an overview of the significant issues that occur in the MRF based devices is reported, and the developing trends for the devices using the MRF are discussed.

Keywords: magnetorheological fluid, magnetorheological fluid-based devices, structural configuration, magnetorheological fluid brakes, magnetorheological fluid clutch, magnetorheological fluid damper, magnetorheological medical devices

OPEN ACCESS

Edited by:
Yancheng Li,
University of Technology Sydney, Australia

Reviewed by:
Phu Xuan Do,
Vietnamese-German University, Vietnam
Xufeng Dong,
Dalian University of Technology, China
Dingxin Leng,
Ocean University of China, China

****Correspondence:***
Xinhua Liu
liuxinhua@cumt.edu.cn
Zhixiong Li
zhixiong.li@yonsei.ac.kr

Specialty section:
This article was submitted to Smart Materials, a section of the journal Frontiers in Materials

Received: *10 December 2020*
Accepted: *19 January 2021*
Published: *25 March 2021*

Citation:
Hua D, Liu X, Li Z, Fracz P, Hnydiuk-Stefan A and Li Z (2021) A Review on Structural Configurations of Magnetorheological Fluid Based Devices Reported in 2018–2020. Front. Mater. 8:640102. doi: 10.3389/fmats.2021.640102

INTRODUCTION

Magnetorheological fluid (MRF), as a kind of smart materials, has been widely studied by scholars due to its controllable rheological properties in a few milliseconds (Jackson et al., 2018; Fu et al., 2020; Zheng et al., 2020). In the technical fields of vibration isolation (Rossi et al., 2018; Phu and Choi, 2019), energy absorption (Ahamed et al., 2016; Yoon J.-Y. et al., 2020), and actuation control (Hong et al., 2019; Zhang L. et al., 2019) et al., MRF has a unique advantage as the main part of the manipulation or regulation mechanism. Therefore, MRF based devices have great potential in structural optimization and innovative development and show outstanding performance in engineering (Hu et al., 2019; Yuan et al., 2019; Zhou et al., 2020) and medical fields (El Wahed, 2020).

MRF based devices are mainly based on four operational modes of MRF, including flow mode, shear mode, squeeze mode and pinch mode, which show different performance in various practical application requirements (Elsaady et al., 2020a). Using the above four operational modes, widely studied engineering mechanical devices mainly involve brake, clutch, damper, and mount etc. (Ahamed et al., 2018). Because the MRF can generate a reliable and stable magnetorheological

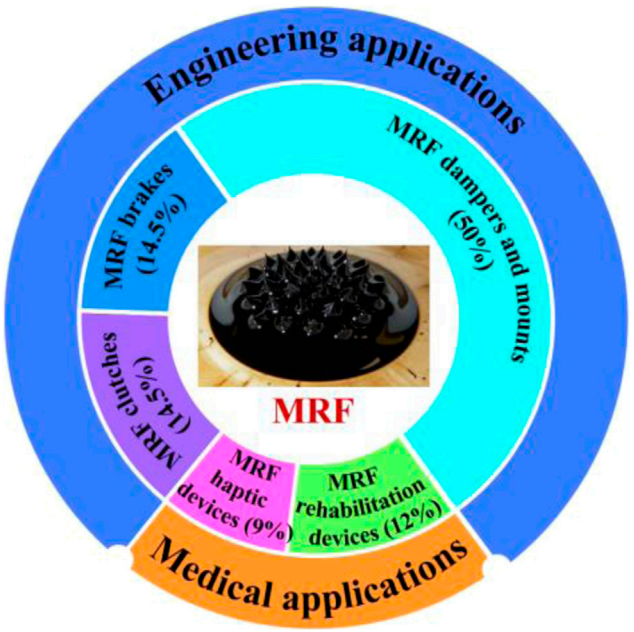

FIGURE 1 | Classification of MRF based devices with proportions according to the referred literatures.

phenomenon with fast response and strong controllability in the magnetic field environment (Juan et al., 2011), MRF based devices generally have a low failure rate and high regulating ability. However, with the change of the production environment and the improvement of application requirements, these MRF based devices have gradually exposed some defects, such as weak magnetic field (Lee et al., 2018), unstable MRF because of overheated electromagnetic coils (Wang et al., 2019b), settlement of MRF in the idle state (Bastola et al., 2019), leakage of MRF (Tu et al., 2019), and an overall large and bulky devices volume (Li J. H. et al., 2018). Therefore, in view of the various problems in practical applications, many scholars have proposed different improvements and optimization methods based on traditional structures, which has greatly enhanced the performance of the MRF based devices.

Furthermore, different from the above application types, the MRF has been further developed, and has in recent years become an important part of the haptic feedback system (Song et al., 2018b) and artificial limbs (Pandit et al., 2018) in the medical field. In the haptic feedback system based on the MRF, using the controlled rheological characteristics, a resistance environment similar to the real sense of touch is generated and transmitted to the operator, which is widely applied to the teleoperated catheter operating system (Song et al., 2018a) or intelligent haptic interface devices (Topcu et al., 2018). Moreover, in some medical auxiliary and customized devices, such as prostheses (Jing et al., 2018; Zhou and Liu, 2020), rehabilitation protection devices (Zhou et al., 2020), and skeletons (Veronneau et al., 2018), the MRF has been widely studied for advantages of adjustable stiffness and easy structure integration. Based on these specific applications, novel product structures and design methods are proposed using the MRF, which fully reflects the irreplaceable role of the smart material in many advanced technologies.

Having thus described some basic concepts and providing a broad categorization, some typical MRF based devices are investigated in engineering and medical applications from 2018 to 2020. In this work, 104 academic articles from these 3 years are used as a reference, reporting on the novel structure configurations, design purposes, and advantages of MRF based devices. Based on the above classification introduction, the proportions of different development directions are shown in **Figure 1**. Furthermore, some drawbacks of the MRF filled devices are also summarized. After a discussion, conclusions, and outline, prospects for the development of MRF based devices are presented.

MAGNETORHEOLOGICAL FLUID BRAKES IN ENGINEERING APPLICATIONS

A brake is a device with the function of making moving parts (or moving machinery) slow down, stop or maintain the stopped state, which is widely used in lifting transportation equipment, mining equipment, construction engineering equipment, and marine ship equipment. Increasing brake torque, eliminating hysteresis time, optimizing device volume and weight, and reducing energy consumption are the main directions of developing new MRF brakes (Bazargan-Lari, 2019; Zhu et al., 2019). Some MRF brakes reported from 2018 to 2020 are summarized in **Table 1**.

In 2018, a radial multi-pole-and-layer MRF brake with higher torque and torque density was proposed, shown in **Figure 2A** (Wu et al., 2018). In this design, two superposition magnetic fields are generated by inner and outer coils with 12 magnetic poles, and four media layers of MRF are located in these coils. The braking characteristics of the device are significantly improved, but the added coils increase the overall weight and energy consumption. Furthermore, an MRF brake was designed with a multi-drum architecture, shown in **Figure 2B** (Qin et al., 2018). The device is compact and light-weight, generating four gaps of MRF, which increases the shear area but also requires higher manufacturing accuracy. In order to enhance the braking torque, except the above structural changes, a configuration of an MRF brake with three coils on each side of the brake housing was designed, shown in **Figure 2C** (Nguyen et al., 2019). The device provides better braking performance than a traditional single side-coil MRF brake. However, the device is also unable to avoid the defects of being heavy, having high energy consumption, and temperature interference. Different from the above design solution, an MRF brake was proposed to avoid meaningless loss, where permanent magnets were used to attract MRF into a neighboring gap, shown in **Figure 3A** (Shamieh and Sedaghati, 2018). Through eliminating contact of the MRF and rotor, power loss due to the zero-field viscous torque is decreased. On the other hand, in the braking state of the device, the effective shear area of MRF is small and the braking torque is limited. Moreover, an elastomeric baffle device with MRF was proposed and applied for the electronic joystick machine shown in **Figure 3B** (Elliott and

TABLE 1 | Novel MRF brakes in 2018–2020.

No.	References	Type	Improved method
1	Zhu and Geng (2018)	Brake with shear and differential pressure mode	Simulating Wankel engine configuration to realize intelligent brake quickly
2	Wu et al. (2018)	Multi-pole-and-layer type brake with shear mode	Using two layers structure with six pairs of coils to improve magnetic field strength
3	Qin et al. (2018)	Multi-drum type brake with shear mode	Adding the number of layers in the drum to increase the working area of MRF.
4	Nguyen et al. (2019)	Multi-coil type brake with shear mode	Adopting three coils on each side of the brake housing to improve magnetic field strength
5	Shamieh and Sedaghati (2018)	Permanent magnets and coil type brake with shear mode	Using permanent magnets to absorb MRF to reduce the energy loss caused by zero field viscosity
6	Elliott and Buckner (2018)	Piston type brake with shear mode	Combining MRF and baffle with simple structure to control the electronic joystick
7	Zhu et al. (2019)	Disc-and-drum type brake with shear mode	Optimizing structure size and verifying phenomenon of shear thinning in high speed
8	Dai et al. (2019)	Rotary micro brake with shear mode	Combining with turbine generator with compact structure
9	Qin et al. (2019)	Multi drum type brake with shear mode	Designing a hollowed casing structure to fill with actuator
10	Wang et al. (2019a)	Disc type brake with squeeze and shear mode	Using squeeze-shear mode and water-cooling way simultaneously to improve the brake performance
11	Wang and Bi (2020)	Disc type brake with squeeze and shear mode	Adopting an automatic squeeze and shear mode to improve the torque output
12	Zhang D. et al. (2020)	Disc type brake with shear mode	Coupling multiple brakes to conduct the torsional forward of snake-like robot

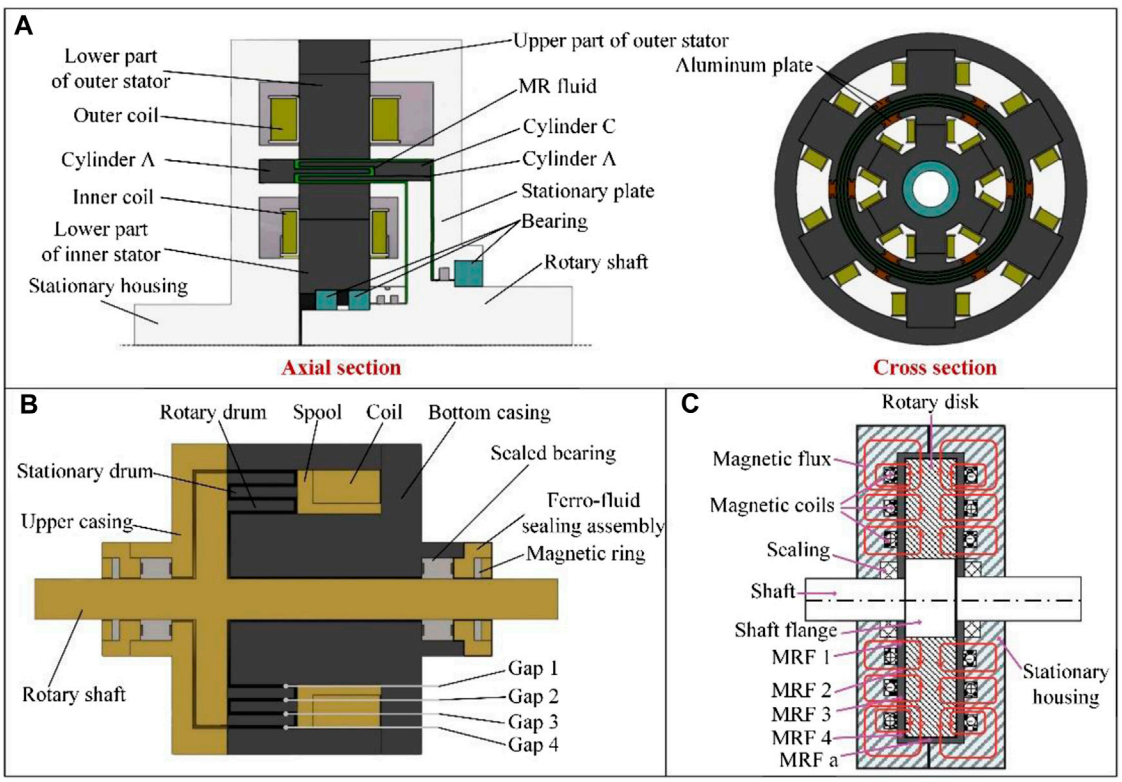

FIGURE 2 | (A) Multi-pole-and-layer MRF brake (Wu et al., 2018). **(B)** Multi-drum MRF brake (Qin et al., 2018). **(C)** Multiple side-coil MRF brake (Nguyen et al., 2019).

Buckner, 2018). The device provides controllable resistance to axial motion of the center shaft and has the advantages of reducing cost and complexity.

In 2019, a micro-brake was proposed to regulate a miniature turbine generator based on MR fluid and MR grease, respectively, shown in **Figure 4A** (Huang et al., 2018; Dai et al., 2019). In the simple device, an electromagnetic coil fills internal space, and low permeability materials are used to maximize the magnetic field density. The brake can improve enough resistance when the turbine generator is working at high wind speeds. Similar to a compact structure, a novel hollowed multi-drum MRF brake was proposed to deal with the magnetic hysteresis, shown in **Figure 4B** (Qin et al., 2019). The device has a multi-drum mode, and a hollowed casing filled with actuator provides the

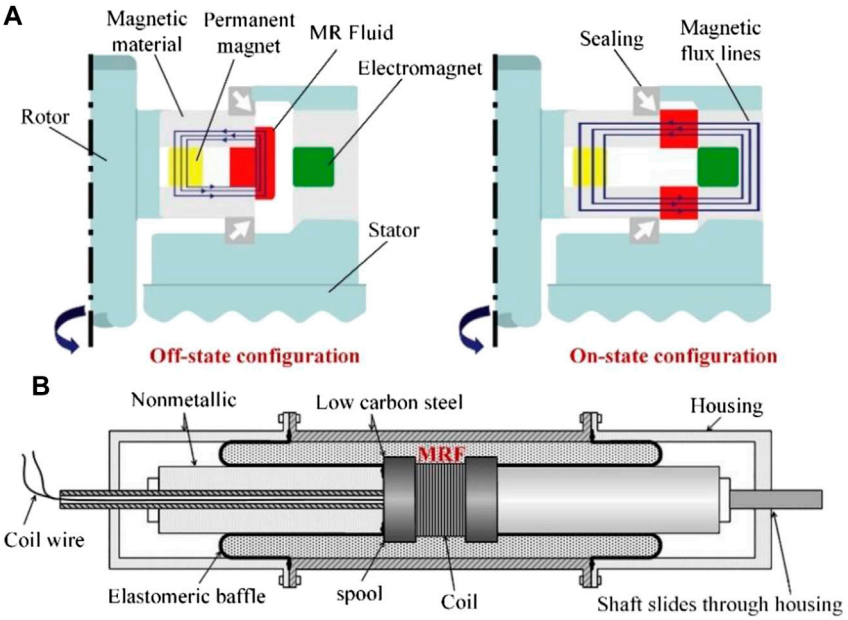

FIGURE 3 | (A) MRF brake without zero-field viscous torque (Shamieh and Sedaghati, 2018). **(B)** Elastomeric baffle MRF device (Elliott and Buckner, 2018).

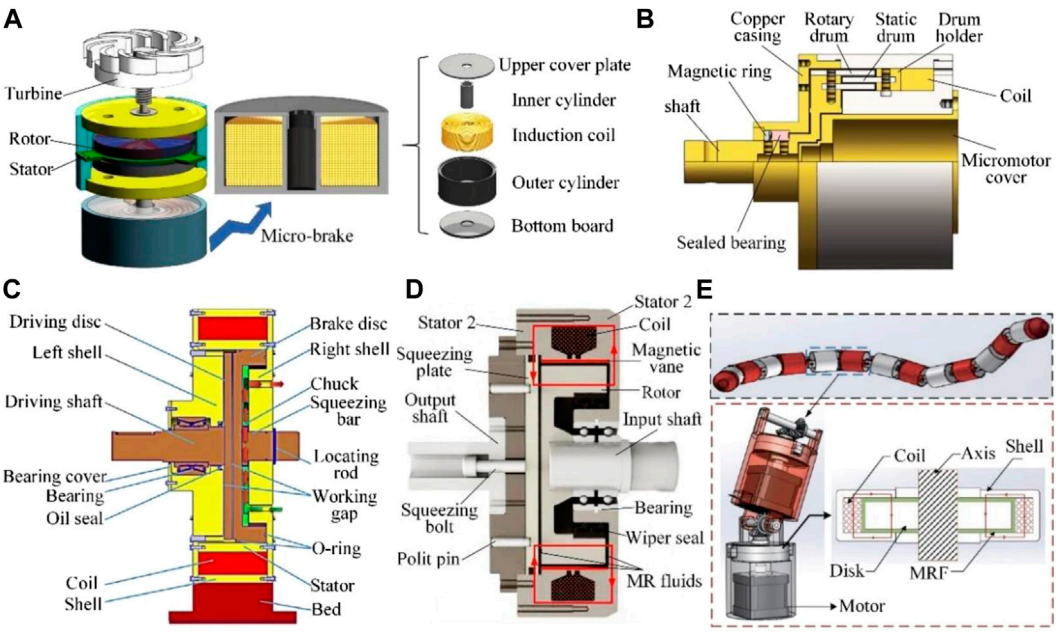

FIGURE 4 | (A) Rotary micro-brake (Dai et al., 2019). **(B)** Multi-drum MRF brake (Qin et al., 2019). **(C)** High-torque squeezing MRF brake (Wang et al., 2019a). **(D)** MRF brake with squeeze-shear mode (Wang and Bi, 2020). **(E)** Snake like robot with MRF actuators (Zhang D. et al., 2020).

important reference of the composite structure. But these compact structures tend to increase the MRF temperature and cause the braking torque to decrease. Then, a squeezing brake was presented to reduce the effect of temperature on MRF, shown in **Figure 4C** (Wang et al., 2019a). In this device, several flumes are designed to dissipate the heat of MRF and brake disc, the water-cooling method effectively improves the working time and maintains high brake torque. However, the flumes increase the size of the brake and require the addition of water circulation equipment. Furthermore, in 2020, an MRF brake under squeeze-shear mode was designed, in which a squeezing bolt was presented to produce compressive force for transmission

TABLE 2 | Novel MRF clutches in 2018–2020.

No.	References	Type	Improved method
1	Fernandez et al. (2018)	Drum type clutch with shear mode	Using a steel cylinder moved in and out the clutch device to adjust magnetic field of permanent magnet.
2	Wang W. D. et al. (2019)	Disc type clutch with shear mode	Providing a human-robot interaction MRF clutch and optimizing structure sizes
3	Wu et al. (2019)	Multi hollow disc type clutch with shear mode	Designing a complex transmission disc with a plurality of magnetic conductive columns and flumes for cooling liquid
4	Kikuchi et al. (2020)	Multi disc type clutch with shear mode	Presenting a multi-clutch coupling scheme
5	Olszak et al. (2019)	Valve type clutch with flow mode	Simulating the structure of electric pump and replacing oil fluid with MRF to realize the power transmission control
6	Yang and Chen (2019)	Drum type clutch with shear mode	Proposing a wedge-shaped clearance between the inner and outer cylinders for uniform distribution of magnetic field
7	Wang X. et al. (2019)	Conical type clutch with shear and squeeze mode	Adopting shape memory alloy to provide squeeze mode and improving torque output performance
8	Xiong et al. (2019)	Disc type clutch with shear and squeeze mode	Adopting electrothermal shape memory alloy to provide squeeze mode and improving transmission performance
9	Binyet and Chang (2020)	Disc type clutch with shear mode	Changing the position of permanent magnets to control the working mode of MRF and reducing energy consumption
10	Pilon et al. (2020)	Disc type clutch with shear mode	Designing a 3D screw flight made of MRF and improving the durability of device

performance, and a magnetic vane was set to ensure that a magnetic flux crosses both sides of the rotor, shown in **Figure 4D** (Wang and Bi, 2020). Utilizing the combined mode, the MRF device generated higher torque compared to those without compression. Moreover, an MRF brake with adaptive stiffness control was applied to a snake-like robot shown in **Figure 4E** (Zhang D. et al., 2020). Although this device has only the most basic brake structure, a number of MRF brakes are assembled head to tail, that is, the brake can also be regarded as an actuator. By flexibly controlling the output torque of each joint MRF brake, the twisting motion of the snake-like robot can be realized. Since the motion of each joint is different, the actuators with MRF need to be controlled, separately.

MAGNETORHEOLOGICAL FLUID CLUTCHES IN ENGINEERING APPLICATIONS

A clutch is a commonly used mechanism in transmission or actuation equipment and can separate or engage motion components at any time (Tian et al., 2018; Wang W. D. et al., 2019). As a special power switch, a high-quality clutch has some basic requirements such as a smooth joint, rapid and complete separation, a small sized exterior profile, good wear resistance, adequate heat dissipation capacity, is easy to operate, and is labor saving. Aiming to realize the above working performance, new clutches based on MRF have been extensively studied and have unique advantages in many engineering applications. Some MRF clutches from 2018 to 2020 are summarized in **Table 2**.

In 2018, an MRF clutch was presented using permanent magnets, which is covered by a steel cylinder (Fernandez et al., 2018). The steel cylinder is adjusted to move the clutch device in and out and alters the intensity of the magnetic field around MRF to vary transmitted torque. This method can quickly control the magnetic field without changing the position of permanent magnets. In 2019, an MRF transmission device was proposed for high-power applications, shown in **Figure 5A** (Wu et al., 2019). It can be seen from the schematic configuration that a multi-hollow transmission disc was designed, and each single disc has a plurality of magnetic conductive columns and flumes for cooling liquid. The structure design with maximum output torque of 1880 N m and slip power of 70 kW has great working performance. Because of the large working area of the cooling liquid and MRF, the sealing requirements and production costs for this device are high. Based on the coupled operation mode, a multi-disc MRF clutch was presented, two of which are fixed on the casing and shaft, shown in **Figure 5B** (Kikuchi et al., 2020). Utilizing the clutch, a new actuator with flexible torque control can be assembled for the haptic device. Moreover, a hydrodynamic MRF clutch shown in **Figure 5C** was proposed, where the centrifugal forces in the pump actuate MRF to flow through the channel placed in the magnetic valve and the cross over turbine (Olszak et al., 2019). Thus, the turbine torque is controlled by regulating excited voltage of the electromagnetic coil. On the other hand, there are higher restrictions on particle size and precipitation characteristics of MRF in this device. In addition, to address the problem of an uneven magnetic field, a wedge clearance was designed in a drum type MRF transmission device (Yang and Chen, 2019). The outer cylinder is connected with the driving shaft, and the inner cylinder with an inclined surface is connected with the driven shaft. MRF fills the wedge-shaped clearance between the inner and outer cylinders. The results show that when the wedge angle is about 1.074°, the magnetic induction intensity in the working gap has the most uniform distribution, which is conducive to a stable and accurate torque output.

In order to maintain a stable working performance and to improve transmission torque, a hybrid model combined with MRF and shape memory alloy was proposed by Wang X. et al. (2019) and Xiong et al. (2019) shown in **Figure 6A**. When the temperature reaches a critical phase transition value, the electrothermal shape memory spring outputs pressure and pushes the friction disc to squeeze the active disc. The MRF

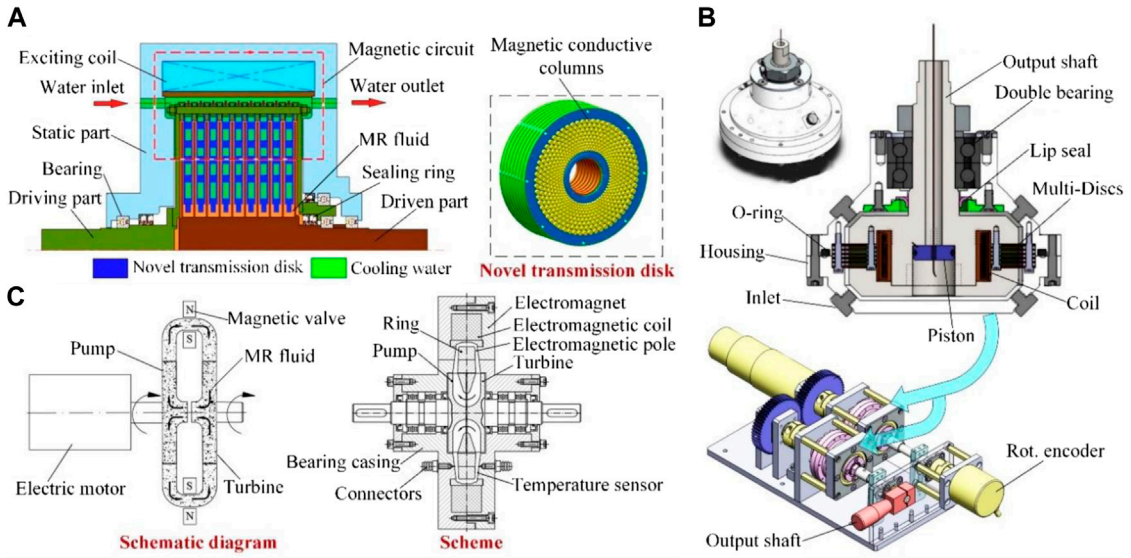

FIGURE 5 | (A) High-power MRF clutch (Wu et al., 2019). **(B)** Multi-layered disc MRF clutch and twin-driven MRF actuator (Kikuchi et al., 2020). **(C)** Hydrodynamic clutch with MRF (Olszak et al., 2019).

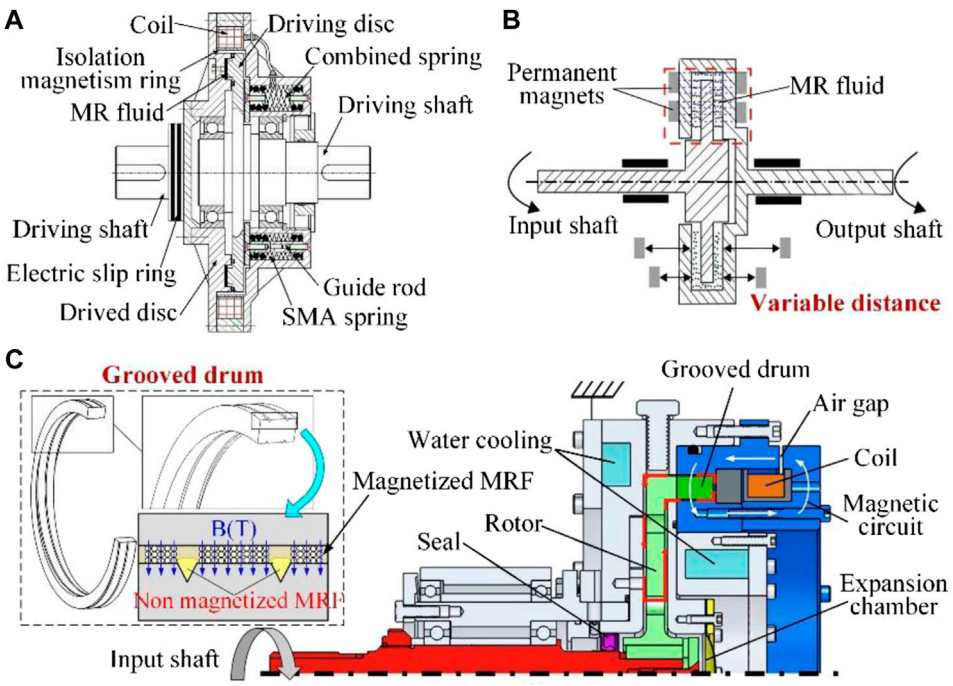

FIGURE 6 | (A) MRF and shape memory alloy combined clutch (Xiong et al., 2019). **(B)** MRF clutch-brake with permanent magnets (Binyet and Chang, 2020). **(C)** MRF clutch with grooved drum (Pilon et al., 2020).

device adds the squeezing working mode with a compact structure, but the operating time of this mode is limited by temperature. In 2020, with the aim to reduce chattering, an MRF clutch-brake was proposed, as shown in **Figure 6B** (Binyet and Chang, 2020). In this device, permanent magnets are placed in a casing that can axially slide, which allows a good shielding from the magnetic flux in the off mode. Permanent magnets are conducted to mechanically excite the device, offering simplicity and a reliable operation. However, the magnetic field gradient on the surface of permanent magnets is large and the

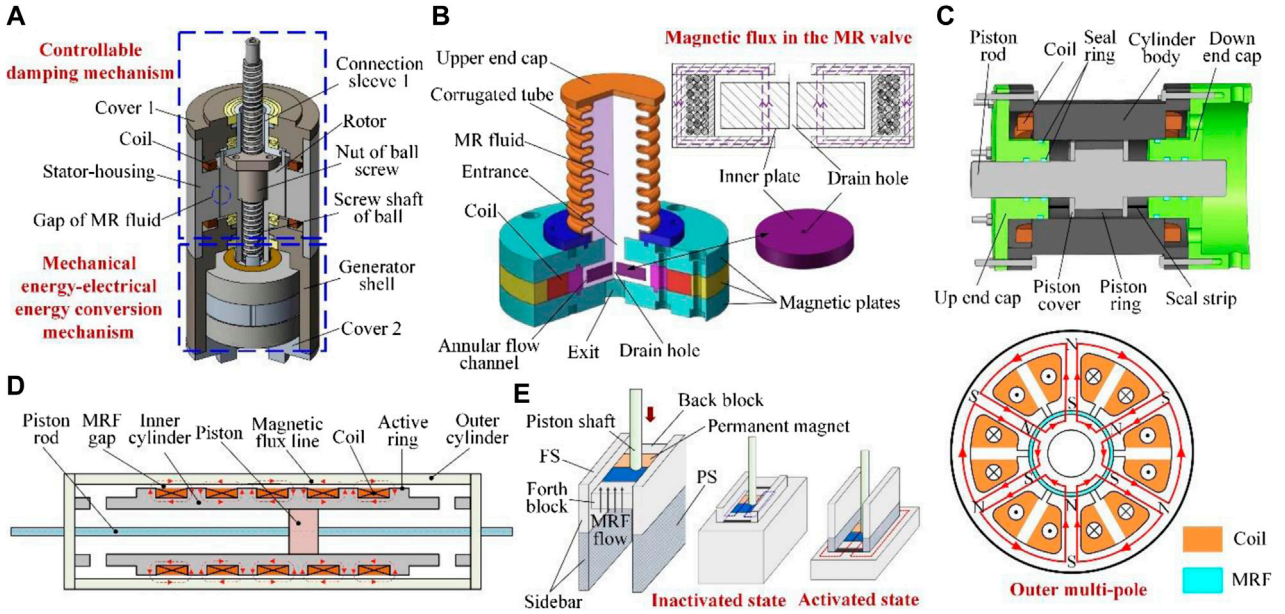

FIGURE 7 | (A) Power-generated MRF absorber (Bai et al., 2018). **(B)** MRF absorber with center drain hole (Li Z. Q. et al., 2018). **(C)** Outer multi-pole MRF damper (Liu et al., 2018). **(D)** Internal bypass MRF absorber (Bai et al., 2018). **(E)** MRF damper with permanent magnet (Lee et al., 2018).

magnetization of MRF is not uniform. In addition, MRF after magnetization and the permanent magnets are magnetically attractive, thus a large force is required to separate them. To improve durability, a magnetic screw pump was studied to promote fluid mixing within an MRF clutch, shown in **Figure 6C** (Pilon et al., 2020). Instead of having solid flights, the screw flights are made of 3D structures of MRF formed by the concentration of the magnetic field lines around helical grooves. From durability test results, the specific structure can increase durability by up to 42% when compared to a standard MRF based clutch.

MAGNETORHEOLOGICAL FLUID DAMPERS AND MOUNTS IN ENGINEERING APPLICATIONS

As a new type of mechanical device, MRF dampers and mounts have the ability to provide variable damping (Xu et al., 2018b), mitigate adverse vibration (Dong et al., 2018), and recycle kinetic energy (Wang et al., 2018), and play a key role in many fields (Ha et al., 2018; Lv et al., 2020). For different engineering applications, the development of high-performance MRF dampers and mounts has always been a research hotspot, such as adjusting local structure size, optimizing internal magnetic field, and updating configuration design.

In 2018, based on the concept of functional integration, an MRF device was proposed with controllable damping, energy recovery, and velocity self-sensing, shown in **Figure 7A** (Bai et al., 2018). In this device, a damping mechanism with MRF generates torque, which is then translated to a linear damping force *via* a ball screw. Cooperating with a permanent magnet rotor and generator stator, the ball screw converts the mechanical energy to an electrical energy for storage or directly to power electromagnetic coils. To reduce harmfulness from an overshoot to a buffered object, an MRF energy absorber, as a controllable damper, was presented and is shown in **Figure 7B** (Li Z. Q. et al., 2018). In the device, a structure configuration of a central drain hole is designed on the inner plate to share the drop pressure of MRF and cannot be affected by the magnetic field. However, the design forms a straight flow channel of MRF, which limits the increase of the damping force. To have a better vibration isolation effect, an MRF damper was designed by utilizing multiple electromagnetic poles integrated in the cylinder, shown in **Figure 7C** (Liu et al., 2018). In the MRF damper, the magnetic flux density in the annular flow channel is effectively increased compared with that of the traditional channel, and the multi-pole structure could minimize the dimension of the piston to improve the active area for a great dynamic range of the damping force. Although the device reduces the volume of the piston and MRF, it increases the size and number of coils, and does not decrease the overall weight. Furthermore, an internal bypass MRF shock absorber was proposed for vibration control of high-speed, and is shown in **Figure 7D** (Bai et al., 2019). The MRF device consists mainly of the inner and outer coaxially arranged cylinders and one piston. Five electromagnetic coils wound on the outer wall of the inner cylinder increase work length of the fluid gap, and the decoupling windings from the piston effectively improve the stroke of the damper. As the inner cylinder is constrained mainly by the MRF and piston, when the center of inner cylinder is shifted from the axis of the device, the movement of the piston rod may be affected, and the outer cylinder can be damaged. Moreover, to optimize the response time of the damper, an MRF damper with a

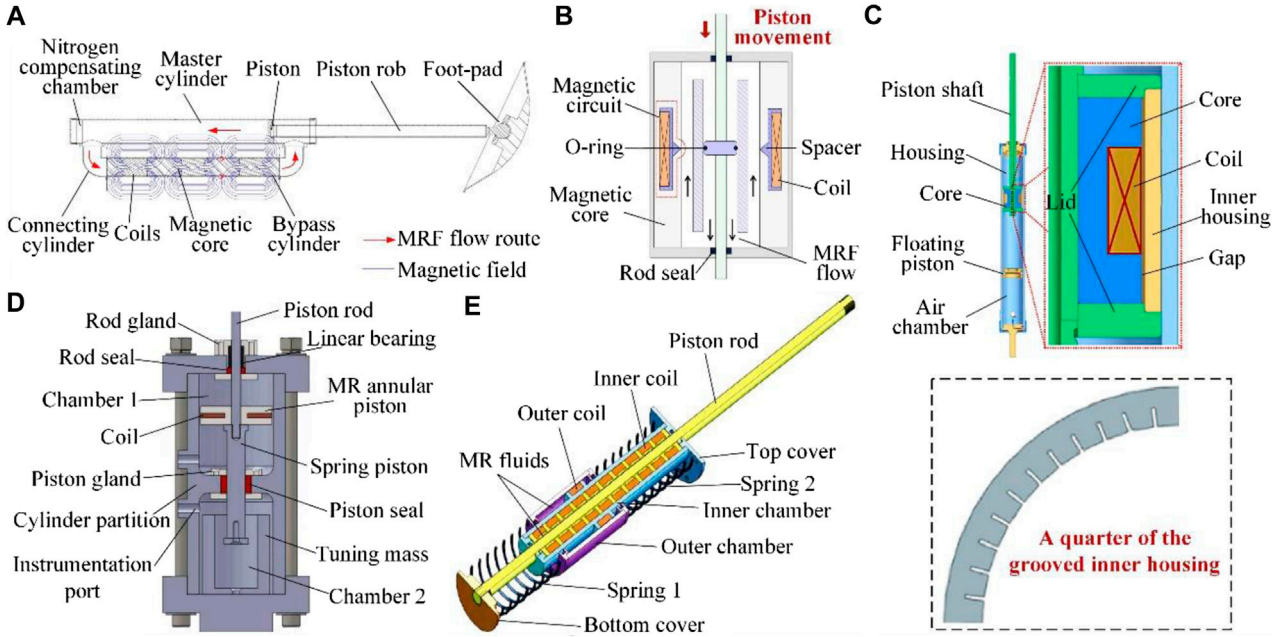

FIGURE 8 | (A) MRF damper with combination structure (Wang C. et al., 2019). **(B)** MRF damper with pinch mode (Lee et al., 2019). **(C)** MRF damper with fast response (Yoon et al., 2019). **(D)** Bi-directional liquid spring MRF damper (Maus and Gordaninejad, 2019). **(E)** MRF damper with two chamber damping units (Deng H. X. et al., 2019).

permanent magnet was proposed, and is shown in **Figure 7E** (Lee and Choi, 2019). Using ferromagnetic and paramagnetic sidebars shaped by a rectangular column, the step input of the damping force is achieved by the structure design of the magnetization area.

In 2019, an MRF damper, shown in **Figure 8A**, was proposed for the lunar lander, which can absorb the impact energy from complex landing surfaces (Wang C. et al., 2019). In the device, a combined structure of master and bypass cylinders is designed, where the master cylinder is connected with the piston rod to receive the external impact; the bypass cylinder with coils adjusts the flow viscosity of MRF to change damping. Thus, the MRF in the damper has a definite flow circuit, and damping control is reliable. Furthermore, an MRF damper with a pinch mode was proposed, where a triangle-shaped nonmagnetic spacer is designed to separate the magnetic core and to generate undulating magnetic field lines, shown in **Figure 8B** (Lee et al., 2019). Utilizing the magnetic field circuit, a pinch mode is formed in the annular MRF damper, and the pinch effect is verified in experiments. To realize a fast response, an MRF damper was designed and is shown in **Figure 8C** (Yoon et al., 2019; Yoon D. S. et al., 2020). A soft magnetic composite is selected as the core material and the inner surface of the housing is machined with grooves. Through these improvements, the eddy current effect on response time is reduced in the MRF device. In addition, a bi-directional liquid spring damper with MRF was presented and is shown in **Figure 8D** (Maus and Gordaninejad, 2019). The device with a two-chamber design has equal or dissimilar spring rates in compression and rebound, and the spring rate can also be pre-set independently in both compression and rebound. Because of the two-chamber structure, the sealing area of MRF needs to be increased relatively. Based on the combined operation mode, MRF dampers with an inner and outer chamber damping units were presented (Deng H. X. et al., 2019; Huang et al., 2019). The inner chamber damping unit is connected to a vibrating object, while the outer is connected to a spring, and is shown in **Figure 8E**. Specifically, the inner unit is set as the piston rod of the outer unit, and outer coil is wound around the outer wall of the inner unit. The combined operation mode effectively expands the control range of the damping force and the stroke range of the piston rod. However, as the damping force is regulated jointly by the spring and MRF, the accurate output of the device is more complicated.

In 2020, aiming to reduce the sedimentation of MRF, a damper shown in **Figure 9A** was designed (Huang et al., 2020). In this device, a permanent magnet is embedded in the piston to drive particles back and forth, and a conductive strip is disposed to monitor particle chains of MRF for a sedimentation amount. On the other hand, the permanent magnet also enhances the resistance of the piston during normal movement and increases the energy consumption. To realize a huge range change of the damping force, an MRF damper with a squeeze and valve mode was presented, and is shown in **Figure 9B** (Ruan et al., 2020). In this device, the piston has an internal channel that divides MRF into three parts. With the movement of the piston, MRF has squeeze and valve working modes at the same time. Furthermore, a bypass MRF damper was proposed with a serpentine flux valve type, and is shown in **Figure 9C** (Idris et al., 2020). The valve of MRF is connected to a cylinder in the

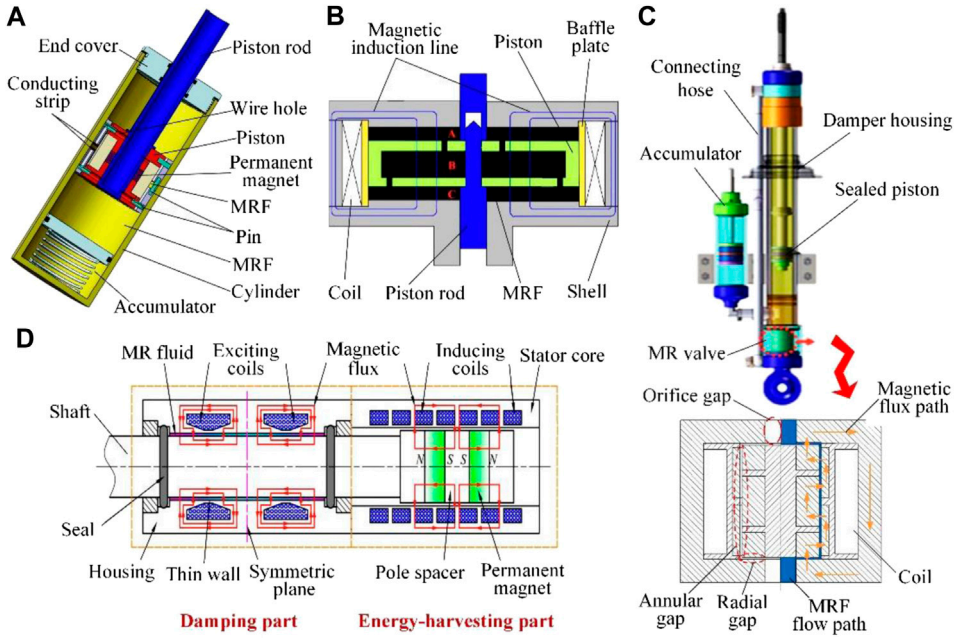

FIGURE 9 | (A) MRF damper with self-monitoring (Huang et al., 2020). **(B)** MRF damper with squeeze-valve mode (Ruan et al., 2020). **(C)** MRF damper with serpentine flux valve (Idris et al., 2020). **(D)** MRF damper with self-powered (Bui et al., 2020).

same center axis but is not attached to the piston. So, the device has a larger dynamic range and is less bulky than conventional structures. Moreover, to reuse vibration energy and to simplify the structure, a self-powered MRF damper was proposed for washing machines (Bui et al., 2020). The device integrates an energy-harvesting technology, where induced power from induction coils is directly transmitted to excitation coils of the damper to generate a corresponding damping force, as shown in **Figure 9D**.

In addition, some other MRF dampers, mounts, and absorbers with a vibration reduction effect have been studied and optimized in key positions to effectively improve the working performance. These MRF devices are also summarized for corresponding improved methods, as shown in **Table 3**.

MAGNETORHEOLOGICAL FLUID BASED DEVICES IN MEDICAL APPLICATIONS

With the development of remote surgery and robot-assisted equipment, the MRF plays an increasingly important role in the medical field. The MRF is mainly applied in two aspects—tactile feedback devices and medical wearable rehabilitation devices. The research results obtained between 2018 and 2020, are briefly summarized in **Table 4**.

Using MRF to simulate the feedback of different environments and to provide operators with real tactile experience are currently hot research topics. In 2018, for surgical robotic applications, a force generator module with MRF was developed to provide force-feedback information (Shokrollahi et al., 2020). The device, shown in **Figure 10A**, is capable of rapidly re-producing forces generated in tele-robotic bone biopsy procedures and provides a wide range of force measurements. However, it is difficult to simulate all the stress ranges only using MRF in the areas where the hardness changes greatly between bone and soft tissue. In 2019, an MRF spherical actuator with haptic feedback was proposed to the applications of joysticks (Chen D. P. et al., 2019). The actuator, shown in **Figure 10B**, has a special stator that replaces the traditional single coil with eight separate coils and magnetic circuits, which can achieve control of forces in different interaction directions. Furthermore, an endovascular catheterization system shown in **Figure 10C** was proposed, which consists of a master device and a slave device (Yin et al., 2018; Guo et al., 2019). In the slave device, the catheter moves in the blood vessel and sends real resistance obtained by the sensor to the master device. The master device uses MRF to simulate the resistance, thus giving the remote physician a realistic sense and improving the safety of surgery. This master device provides an approximate damping environment, but in a particular direction, the variation of damping is not very differentiated. Similarly, to realize a certain stiffness and damping properties of human tissue, a controllable tactile device was designed, where MRF was immersed into porous polyurethane foam and sealed by adhesive tape (Park et al., 2020). The device, shown in **Figure 10D**, can capture several different repulsive forces of human organs generated at an operating site in minimally invasive surgery and can improve the real tactile sensing of the remote doctor.

Moreover, MRF also has many new applications in medical rehabilitation equipment. In 2018, a prosthetic knee with a novel MRF brake was proposed, assisting humans to realize normal gait movement (Mousavi and Sayyaadi, 2018). The MRF brake,

TABLE 3 | Other MRF dampers, mounts and absorbers in 2018–2020.

No	References	Type	Improved method
1	Xin et al. (2018)	Piston type damper with shear-flow mode	Presenting a double-ended damping structure to reduce the random vibration of pipeline
2	Chen C. et al. (2018)	Piston type damper with flow mode	Converting wasted mechanical energy into useful electrical energy to power damper itself
3	Urkucu and Keles (2018)	Mount with flow mode	Comparing two decoupled plates with slots and holes in MR mount
4	Deng et al. (2018)	Non-piston type damper with shear mode	Replacing piston with a suspension rod and realizing unlimited work stroke
5	Xu et al. (2018a)	Piston type damper with flow mode	Utilizing two dis-springs to re-left itself
6	Cheng et al. (2018)	Piston type damper with flow mode	Using meandering magnetic circuit to improve damping performance
7	Sassi et al. (2018)	Piston type damper with flow mode	Placing excitation current and magnetic field outside the damper
8	Yang et al. (2019)	Piston type damper with flow mode	Adding an aluminum slider to reduce the unbalance of damper rod and avoid magnetic leakage
9	Ning et al. (2019)	Rotor type damper with shear mode	Proposing a variable admittance concept
10	Oh and Choi (2019)	Piston type damper with flow mode	Comparing two different dampers, with and without orifice holes in the piston
11	Chen B. et al. (2019)	Two-dimensional plate type damper with shear mode	Optimizing structure design parameters
12	Zhang J. L. et al. (2019)	Disc type damper with shear mode	Utilizing the coil with trapezoidal cross section to improve magnetic field distribution
13	Christie et al. (2019a)	Disc type damper with shear mode	Optimizing structure design parameters
14	Ouyang et al. (2019)	Piston type damper with flow mode	Adopting multi-stage parallel coil structure to realize various magnetic field variations
15	Desai et al. (2019)	Piston type damper with flow mode	Optimizing magnetic field of twin-tube structure
16	Han et al. (2019)	Piston type damper with flow mode	Investigating different pole length and different number of magnetic cores
17	Qiang et al. (2019)	Disc type damper with shear mode	Using ultrasonic field to reduce the angular momentum losses of device without magnetic field
18	Deng L. et al. (2019)	Combined dampers with shear mode	Assembling drum-type damper and disc-type damper
19	Kim et al. (2020)	Piston type damper with shear mode	Utilizing ferromagnetic and paramagnetic materials to adjust damping coefficient
20	Kang et al. (2020)	Piston type damper with flow mode	Optimizing structure design parameters
21	Zhong et al. (2020)	Integrated shock absorber with flow and shear mode	Combining inerter, damper and spiral spring to realize adjustable inertance and damping characteristics
22	Wei et al. (2020)	Blade valve type damper with flow mode	Combining blade and two MR valves with parallel plate damping channel in compact structure
23	Zareie et al. (2019), Zareie and Zabihollah (2020), Zareie et al. (2020)	SMA MRF type damper with flow mode	Proposing a structural control element for high performance of control system
24	Zhang X. J. et al. (2020)	Piston type damper with squeeze mode	Integrating the characteristics of pumping hydraulic damper and MR valve with squeeze mode
25	Elsaady et al. (2020b)	Piston type damper with flow mode	Optimizing magnetic field distribution
26	Zhao et al. (2020)	Piston type damper with flow mode	Integrating four axial fan-shaped magnetic poles on magnetic core to enhance output performance

TABLE 4 | Main applications of MRF in the medical field in 2018–2020.

No	References	Application
1	Shokrollahi et al. (2020)	Robotic bone biopsy device with haptic feedback
2	Chen D. P. et al. (2019)	Multi-direction spherical actuator for haptic applications
3	Guo et al. (2019)	Endovascular catheterization system with haptic force feedback
4	Park et al. (2020)	Simulated human tissues with controllable tactile forces
5	Mousavi and Sayyaadi (2018)	MRF brake with drum of arc form surface for prosthetic knee
6	Wahed and Balkhoyor (2018)	Prosthetic joints with MRF damper of ball-and-socket structure
7	Chen Z. P. et al. (2018), Chen et al. (2019a, 2019b)	Microneedle arrays for minimally invasive surgery, transdermal drug delivery and smart wearable equipment
8	Oba et al. (2019)	Semi-active ankle-foot orthosis with MRF link mechanism
9	Christie et al. (2019b)	Prosthetic leg with MRF damper of T-shaped drum
10	Zahedi et al. (2020)	Soft exoskeleton with MRF damper to suppress pathological tremor

shown in **Figure 11A**, has a T-shaped drum with an arc form surface boundary, which can meet the requirements for flexible variation of the braking torque. To enhance the rehabilitation of the human shoulder and upper limb, a multi-freedom MRF based damper with a ball-and-socket structure was proposed (Wahed and Balkhoyor, 2018; Wahed and Wang, 2019). The new damper shown in **Figure 11B** can effectively simulate the motion of human joints and provides a rehabilitation training environment. Further, the device can refine the design of damping forces in different directions to realize the control of damping variation in

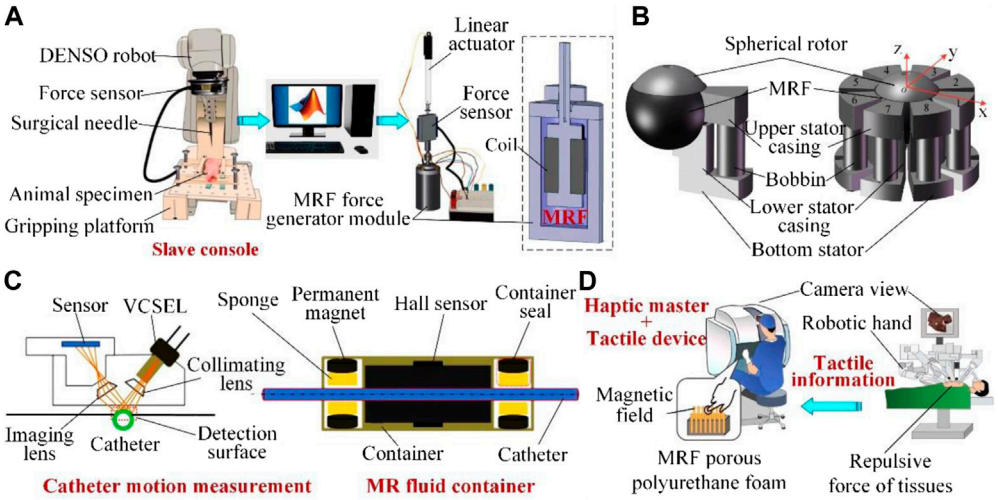

FIGURE 10 | (A) MRF haptic device for robotic bone biopsy (Shokrollahi et al., 2020). **(B)** Multi-direction MRF actuator for haptic applications (Chen D. P. et al., 2019). **(C)** Endovascular catheterization system with haptic feedback (Guo et al., 2019). **(D)** Tactile device to simulate human tissues forces (Park et al., 2020).

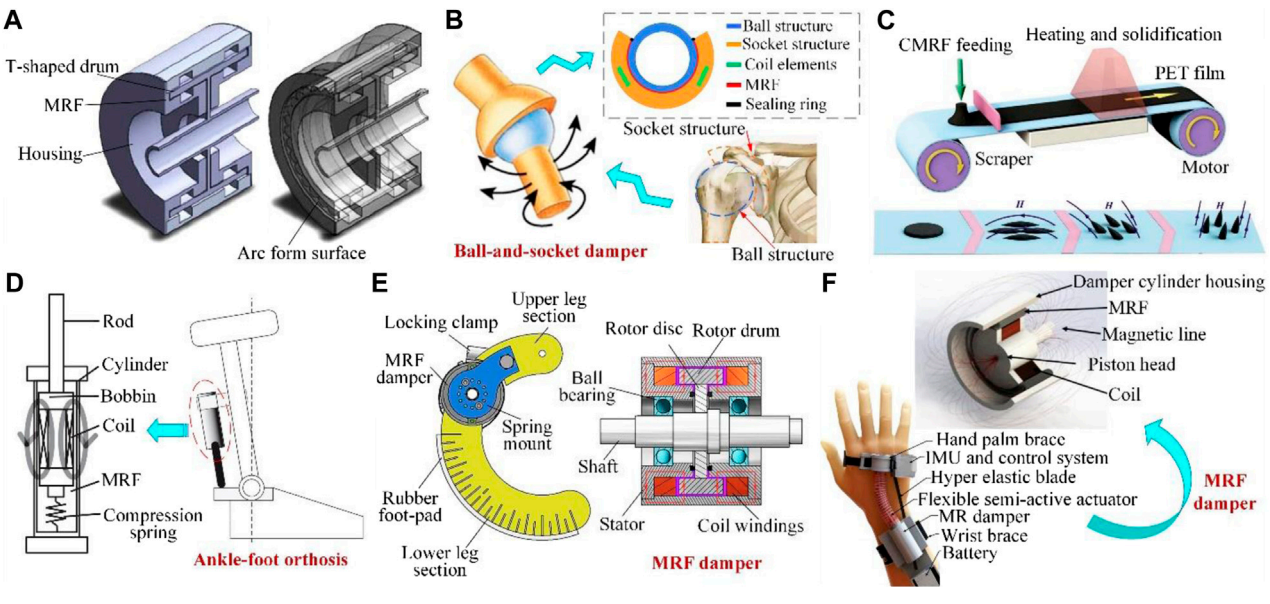

FIGURE 11 | (A) MRF damper with drum of an arc surface boundary (Mousavi and Sayyaadi, 2018). **(B)** Smart ball-socket actuator for upper limb rehabilitation (Wahed and Balkhoyor, 2018). **(C)** Magnetization-induced self-assembling process of microneedle array (Chen Z. P. et al., 2018; Chen et al. 2019a; Chen et al., 2019b). **(D)** MRF damper for ankle-foot orthosis (Oba et al., 2019). **(E)** MRF based variable stiffness leg (Christie et al., 2019b). **(F)** MRF soft exoskeleton (Zahedi et al., 2020).

multi-directions. Furthermore, using a drawing lithography approach, some MRF microneedles were fabricated for minimally invasive surgery, transdermal drug delivery, and smart wearable equipment (Chen Z. P. et al., 2018; Chen et al. 2019a; Chen et al., 2019b). In a gradient magnetic field, the MRF is magnetized and generates fusiform patterns, which results in different forms of microneedle arrays after heating and solidifying, as shown in **Figure 10C**. The MRF microneedles are cheaper and simpler to produce than traditional precision machining. With the aim to prevent paralysis and gait abnormalities affecting human ankle joints, a semi-active ankle-foot orthosis with an MRF link mechanism was designed (Oba et al., 2019). The MRF device, combined with a compression spring, can mitigate foot slap and toe drag during different phases of movement, as shown in **Figure 11D**. Similarly, for movement recovery, an MRF variable stiffness leg was designed to improve energy efficiency and gait stability (Christie et al., 2019b). The device, shown in **Figure 11E**, is housed in the lower leg section, whose output shaft is linked to the upper leg section. When the coil current is zero, the leg has a soft

single spring stiffness, while huge damping torque is achieved under a large input current. Therefore, the device has a relatively wide range of damping variation. Moreover, based on the assistive technologies, a novel soft exoskeleton with MRF damper was proposed to suppress pathological tremor (Zahedi et al., 2020). The MRF damper connected with a flexible elliptic spring can assist in suppressing tremor of the wrist joint in 3 ° of freedom with varying intensity, as shown in **Figure 11F**. This device prevents wrist tremor with a less constrained area on the hand surface, which thus reduces the suppression effect of a small amplitude tremor.

CONCLUSION AND PROSPECTIVE

According to different structure configurations, MRF based devices reported from 2018 to 2020 are investigated in this work, including MRF brakes, MRF clutches, MRF dampers and mounts for engineering applications, and other new devices for medical applications. In terms of the literature presented above, improvement methods are mainly concentrated in the following ways: Use of multiple coils or magnetic poles to enhance magnetic field strength; Improving the combination of braking structure and active structure to increase the effective contact area of MRF; Replacing the coil with a permanent magnet, or adjusting the size and position of the permanent magnet to improve working performance; Optimizing the magnetic circuit to improve the utilization ratio of the magnetic field; Changing the position of the magnetic field in the working process to avoid settling of MRF or reducing the zero field viscosity. There have been many successful applications that have come from these improvements, but some problems still need to be addressed. By adding coils and magnetic poles, the volume and weight of devices can be larger, which is not easy to disassemble and cost may also be increased. Furthermore, when the working area of MRF is enlarged, the wear is relatively enhanced and the working temperature is also increased, so the rheological property is decreased. By adopting a bypass or extension structure, the output range of devices is extended, but the response time and maximum output force needs to be balanced. In addition, when the MRF is applied in haptic devices, it is still limited to simulating the feedback forces that are in different directions at the same time or one direction with large variation gradient.

In light of the practical application requirements, some development directions are proposed for MRF based devices. The combination of working modes in a limited volume may play a greater role, such as shear-squeeze mode, flow-squeeze mode, etc. The cooperation of magnetic materials and coils can be further developed to increase strength, flexibility, and utilization of the magnetic field, and can reduce power consumption. In order to improve the service life of devices and the accuracy of fault diagnoses, some structure can be designed to measure the working temperature and wear condition of MRF. With the increasing torque output, the energy loss caused by zero field viscosity should be seriously considered, where an ultrasonic wave can be used to reduce zero field viscosity or can cut off the contact between MRF and the rotor to avoid unnecessary energy consumption. Aiming to improve the accuracy of haptic feedback in complex structures, MRF can be combined with other rheological materials or magnetic actuated elastic materials to design a multilayer configuration.

The application potential of MRF in different fields will be further explored. For example, according to the variable damping and stiffness characteristics of MRF, intelligent wearable devices can be used in medical treatment to prevent joint vibration; in virtual reality devices, the motion damping is changed for the wearer to increase the experience of a real environment; in the remote control of medical or other fields, real-time tactile feedback is simulated for operators to improve the sense of reality. Although these directions present many challenging problems, the need for practical applications will certainly drive current research of MRF based devices forward.

AUTHOR CONTRIBUTIONS

DH: Methodology, software, data curation, writing-original draft preparation. XL: Conceptualization, methodology, analysis. ZL: Resources, visualization, investigation. PF: Analysis, writing-reviewing and editing. AH-S: Resources, funding acquisition, writing-reviewing and editing. ZL: Conceptualization, writing-reviewing and editing, funding acquisition.

FUNDING

This work was supported in part by the Future Scientists Program of China University of Mining and Technology (2020WLKXJ025), the Postgraduate Research and Practice Innovation Program of Jiangsu Province (KYCX20_1986) and Priority Academic Program Development of Jiangsu Higher Education Institutions (PAPD).

REFERENCES

Ahamed, R., Choi, S.-B., and Ferdaus, M. M. (2018). A state of art on magneto-rheological materials and their potential applications. *J. Intell. Mater. Syst. Struct.* 29 (10), 2051–2095. doi:10.1177/1045389X18754350

Ahamed, R., Ferdaus, M. M., and Li, Y. (2016). Advancement in energy harvesting magneto-rheological fluid damper: a review. *Korea Aust. Rheol. J.* 28 (4), 355–379. doi:10.1007/s13367-016-0035-2

Bai, X.-X., Zhong, W.-M., Zou, Q., Zhu, A.-D., and Sun, J. (2018). Principle, design and validation of a power-generated magnetorheological energy absorber with velocity self-sensing capability. *Smart Mater. Struct.* 27 (7), 1–43. doi:10.1088/1361-665X/aac7ef

Bai, X. X., Shen, S., Wereley, N. M., and Wang, D. H. (2019). Controllability of magnetorheological shock absorber: I. Insights, modeling and simulation. *Smart Mater. Struct.* 28 (1), 1–44. doi:10.1088/1361-665X/aaf072

Bastola, A. K., Ang, E., Paudel, M., and Li, L. (2019). Soft hybrid magnetorheological elastomer: gap bridging between MR fluid and MR

elastomer. *Colloids Surf. A Physicochem. Eng. Asp.* 583, 1–35. doi:10.1016/j.colsurfa.2019.123975

Bazargan-Lari, Y. (2019). Design and shape optimization of MR brakes using Nelder-Mead optimization algorithm. *Mech. Ind.* 20 (6), 1–9. doi:10.1051/meca/2019017

Binyet, E. M., and Chang, J.-Y. (2020). Magnetohydrodynamics modelling of a permanent magnets activated MRF clutch-brake. *Microsyst. Technol.* 26 (11), 3451–3457. doi:10.1007/s00542-020-04910-w

Bui, Q.-D., Nguyen, Q. H., Nguyen, T. T., and Mai, D.-D. (2020). Development of a magnetorheological damper with self-powered ability for washing machines. *Appl. Sci.* 10 (12), 1–22. doi:10.3390/app10124099

Chen, B., Huang, D., Li, C., and Chen, C. (2019). Design and modeling for 2D plate type MR damper. *Front. Mater.* 6, 1–28. doi:10.3389/fmats.2019.00028

Chen, C., Chan, Y. S., Zou, L., and Liao, W.-H. (2018). Self-powered magnetorheological dampers for motorcycle suspensions. *Proc. Inst. Mech. Eng. D J. Automob. Eng.* 232 (7), 921–935. doi:10.1177/0954407017723761

Chen, D. P., Song, A. G., Tian, L., Ouyang, Q. Q., and Xiong, P. W. (2019). Development of a multidirectional controlled small-scale spherical MR actuator for haptic applications. *IEEE/ASME Trans. Mechatron.* 24 (4), 1597–1607. doi:10.1109/TMECH.2019.2916099

Chen, Z. P., Ren, L., Li, J. Y., Yao, L. B., and Chen, Y. (2018). Rapid fabrication of microneedles using magnetorheological drawing lithography. *Acta Biomater.* 65, 283–291. doi:10.1016/j.actbio.2017.10.030

Chen, Z. P., Ye, R., Lee, W., Ji, D. W., Zhang, Y. X., and Yang, Y. L. (2019a). Magnetization-induced self-assembling of bendable microneedle arrays for triboelectric nanogenerators. *Adv. Electron. Mater.* 5 (5), 1–9. doi:10.1002/aelm.201800785

Chen, Z. P., Ye, R., Yang, J. B., Lin, Y. Y., Lee, W. H., and Li, J. W. (2019b). Rapidly fabricated microneedle arrays using magnetorheological drawing lithography for transdermal drug delivery. *ACS Biomater. Sci. Eng.* 5 (10), 5506–5513. doi:10.1021/acsbiomaterials.9b00919

Cheng, M., Chen, Z. B., and Xing, J. W. (2018). Design, analysis, and experimental evaluation of a magnetorheological damper with meandering magnetic circuit. *IEEE Trans. Magn.* 54 (5), 1–10. doi:10.1109/TMAG.2018.2797090

Christie, M. D., Sun, S., Deng, L., Ning, D. H., Du, H., Zhang, S. W., et al. (2019a). A variable resonance magnetorheological-fluid-based pendulum tuned mass damper for seismic vibration suppression. *Mech. Syst. Signal Process.* 116, 530–544. doi:10.1016/j.ymssp.2018.07.007

Christie, M. D., Sun, S., Ning, D. H., Du, H., Zhang, S. W., and Li, W. H. (2019b). A highly stiffness-adjustable robot leg for enhancing locomotive performance. *Mech. Syst. Signal Process.* 126, 458–468. doi:10.1016/j.ymssp.2019.02.043

Dai, J., Chang, H., Zhao, R., Huang, J., and Li, K. Q. (2019). Investigation of the relationship among the microstructure, rheological properties of MR grease and the speed reduction performance of a rotary micro-brake. *Mech. Syst. Signal Process.* 116, 741–750. doi:10.1016/j.ymssp.2018.07.004

Deng, H. X., Deng, J. L., Yue, R., and Han, G. H. (2019). Design and verification of a seat suspension with variable stiffness and damping. *Smart Mater. Struct.* 28 (6), 1–11. doi:10.1088/1361-665X/ab18d4

Deng, H. X., Han, G. H., Zhang, J., and Wang, M. X. (2018). Development of a non-piston MR suspension rod for variable mass systems. *Smart Mater. Struct.* 27 (6), 1–10. doi:10.1088/1361-665X/aabc2b

Deng, L., Sun, S. S., Christie, M. D., and Yang, J. (2019). Experimental testing and modelling of a rotary variable stiffness and damping shock absorber using magnetorheological technology. *J. Intell. Mater. Syst. Struct.* 30 (10), 1453–1465. doi:10.1177/1045389X19835955

Desai, R. M., Jamadar, M. E. H., Kumar, H., Joladarashi, S., and Sekaran, S. C. R. (2019). Design and experimental characterization of a twin-tube MR damper for a passenger van. *J. Braz. Soc. Mech. Sci. Eng.* 41 (8), 1–12. doi:10.1007/s40430-019-1833-5

Dong, X. M., Liu, W. Q., An, G. P., Zhou, Y. Q., and Yu, J. Q. (2018). A novel rotary magnetorheological flexible joint with variable stiffness and damping. *Smart Mater. Struct.* 27 (10), 1–25. doi:10.1088/1361-665X/aae00e

El Wahed, A. K. (2020). A novel hydraulic actuation system utilizing magnetorheological fluids for single-port laparoscopic surgery applications. *Materials* 13 (6), 1–13. doi:10.3390/ma13061380

Elliott, C. M., and Buckner, G. D. (2018). Design optimization of a novel elastomeric baffle magnetorheological fluid device. *J. Intell. Mater. Syst. Struct.* 29 (19), 3774–3791. doi:10.1177/1045389X18799211

Elsaady, W., Oyadiji, S. O., and Nasser, A. (2020a). A review on multi-physics numerical modelling in different applications of magnetorheological fluids. *J. Intell. Mater. Syst. Struct.* 31 (16), 1855–1897. doi:10.1177/1045389X20935632

Elsaady, W., Oyadiji, S. O., and Nasser, A. (2020b). Magnetic circuit analysis and fluid flow modeling of an MR damper with enhanced magnetic characteristics. *IEEE Trans. Magn.* 56 (9), 1–20. doi:10.1109/TMAG.2020.3011669

Fernandez, M. A., Chang, J.-Y., and Huang, C.-Y. (2018). Development of a passive magnetorheological fluid clutch with field-blocking mechanism. *IEEE Trans. Magn.* 54 (11), 1–5. doi:10.1109/TMAG.2018.2834389

Fu, Y., Yao, J. J., Zhao, H. H., Zhao, G., Wan, Z. S., and Guo, R. Z. (2020). A muscle-like magnetorheological actuator based on bidisperse magnetic particles enhanced flexible alginate-gelatin sponges. *Smart Mater. Struct.* 29 (1), 1–13. doi:10.1088/1361-665X/ab515f

Guo, S. X., Song, Y., Yin, X. C., Zhang, L. S., Tamiya, T., and Hirata, H. (2019). A novel robot-assisted endovascular catheterization system with haptic force feedback. *IEEE Trans. Robot.* 35 (3), 685–696. doi:10.1109/TRO.2019.2896763

Ha, Q., Royel, S., and Balaguer, C. (2018). Low-energy structures embedded with smart dampers. *Energy Build.* 177, 375–384. doi:10.1016/j.enbuild.2018.08.016

Han, C., Kim, B.-G., Kang, B.-H., and Choi, S.-B. (2019). Effects of magnetic core parameters on landing stability and efficiency of magnetorheological damper-based landing gear system. *J. Intell. Mater. Syst. Struct.* 31 (2), 198–208. doi:10.1177/1045389X19862639

Hong, S.-W., Yoon, J.-Y., Kim, S.-H., Lee, S.-K., Kim, Y.-R., Park, Y.-J., et al. (2019). 3D-Printed soft structure of polyurethane and magnetorheological fluid: a proof-of-concept investigation of its stiffness tunability. *Micromachines* 10 (10), 1–9. doi:10.3390/mi10100655

Hu, G., Zhang, J., Zhong, F., and Yu, L. (2019). Performance evaluation of an improved radial magnetorheological valve and its application in the valve controlled cylinder system. *Smart Mater. Struct.* 28 (4), 1–18. doi:10.1088/1361-665X/ab0b4f

Huang, H., Chen, C., Zhang, Z. C., Zheng, J. N., Li, Y. Z., and Chen, S. M. (2020). Design and experiment of a new structure of MR damper for improving and self-monitoring the sedimentation stability of MR fluid. *Smart Mater. Struct.* 29 (7), 1–22. doi:10.1088/1361-665X/ab8839

Huang, H., Sun, S. S., Chen, S. M., and Li, W. H. (2019). Numerical and experimental studies on a new variable stiffness and damping magnetorheological fluid damper. *J. Intell. Mater. Syst. Struct.* 30 (11), 1639–1652. doi:10.1177/1045389X19844003

Huang, J., Dai, J., Zhao, R., Chang, H., and Xie, S. (2018). Investigation on current excitation of magnetorheological-fluid-based microbrake for microturbine generator. *AIAA J.* 56 (10), 4039–4048. doi:10.2514/1.J056948

Idris, M. H., Imaduddin, F., Mazlan, S. A., and Choi, S. B. (2020). A concentric design of a bypass magnetorheological fluid damper with a serpentine flux valve. *Actuators* 9 (1), 1–21. doi:10.3390/act9010016

Jackson, J. A., Messner, M. C., and Dudukovic, N. A. (2018). Field responsive mechanical metamaterials. *Sci. Adv.* 4 (12), 1–9. doi:10.1126/sciadv.aau6419

Jing, Z. J., Sun, S. S., and Ouyang, Y. M. (2018). Design and modeling analysis of a changeable stiffness robotic leg working with magnetorheological technology. *J. Intell. Mater. Syst. Struct.* 29 (19), 3725–3736. doi:10.1177/1045389X18798958

Juan, D. V., Daniel, J. K., and Roque, H. A. (2011). Magnetorheological fluids a review. *Soft Matter* 7, 3701–3710. doi:10.1088/1361-665X/ab515f

Kang, B.-H., Yoon, J.-Y., Kim, G.-W., and Choi, S.-B. (2020). Landing efficiency control of a six-degree-of-freedom aircraft model with magnetorheological dampers: part 1-modeling. *J. Intell. Mater. Syst. Struct.*, 1045389X2094257. doi:10.1177/1045389X20942578

Kikuchi, T., Abe, I., Nagata, T., Yamaguchi, A., and Takano, T. (2020). Twin-driven actuator with multi-layered disc magnetorheological fluid clutches for haptics. *J. Intell. Mater. Syst. Struct.*, 1045389X2094395. doi:10.1177/1045389X20943958

Kim, B. G., Yoon, D. S., Kim, G. W., Choi, S. B., and Tan, A. S. (2020). Design of a novel magnetorheological damper adaptable to low and high stroke velocity of vehicle suspension system. *Appl. Sci.* 10 (16), 1–17. doi:10.3390/app10165586

Lee, T.-H., Kang, B.-H., and Choi, S.-B. (2019). A quasi-static model for the pinch mode analysis of a magnetorheological fluid flow with an experimental validation. *Mech. Syst. Signal Process.* 134, 1–16. doi:10.1088/1361-665X/ab515f10.1016/j.ymssp.2019.106308

Lee, T. H., and Choi, S. B. (2019). On the response time of a new permanent magnet based magnetorheological damper experimental investigation. *Smart Mater. Struct.* 28 (1), 1–31. doi:10.1088/1361-665X/aaf0dc

Lee, T. H., Han, C., and Choi, S. B. (2018). Design and damping force characterization of a new magnetorheological damper activated by permanent magnet flux dispersion. *Smart Mater. Struct.* 27 (1), 1–13. doi:10.1088/1361-665X/aa9ad6

Li, J. H., Liu, Z. H., and Liu, Z. (2018). Electromechanical characteristics and numerical simulation of a new smaller magnetorheological fluid damper. *Mech. Res. Commun.* 92, 81–86. doi:10.1016/j.mechrescom.2018.07.010

Li, Z. Q., Liao, C. R., Fu, B. Y., Jian, X. C., and Shou, M. J. (2018). Study of radial flow mode magnetorheological energy absorber with center drain hole. *Smart Mater. Struct.* 27 (10), 1–16. doi:10.1088/1361-665X/aad932

Liu, S. G., Feng, L. F., Zhao, D., and Huang, H. (2018). The development of an outer multi-pole magneto-rheological damper with high dynamic range of damping force. *Smart Mater. Struct.* 27 (11), 1–27. doi:10.1088/1361-665X/aae004

Lv, H., Zhang, S., Sun, Q., Chen, R., and Zhang, W. J. (2020). The dynamic models, control strategies and applications for magnetorheological damping systems: a systematic review. *J. Vib. Eng. Technol.* 9, 131–147. doi:10.1007/s42417-020-00215-4

Maus, N., and Gordaninejad, F. (2019). A Bi-directional, liquid-spring-magnetorheological-fluid-damper system. *Front. Mater.* 6, 1–11. doi:10.3389/fmats.2019.00006

Mousavi, S. H., and Sayyaadi, H. (2018). Optimization and testing of a new prototype hybrid MR brake with arc form surface as a prosthetic knee. *IEEE/ASME Trans. Mechatron.* 23 (3), 1204–1214. doi:10.1109/TMECH.2018.2820065

Nguyen, N. D., Thang, L. D., Hiep, L. D., and Nguyen, Q. H. (2019). Development of a new magnetorheological fluid–based brake with multiple coils placed on the side housings. *J. Intell. Mater. Syst. Struct.* 30 (5), 734–748. doi:10.1177/1045389X18818385

Ning, D. H., Sun, S. S., Yu, J. Q., and Zheng, M. Y. (2019). A rotary variable admittance device and its application in vehicle seat suspension vibration control. *J. Franklin Inst.* 356 (14), 7873–7895. doi:10.1016/j.jfranklin.2019.04.015

Oba, T., Kadone, H., Hassan, M., and Suzuki, K. (2019). Robotic ankle-foot orthosis with a variable viscosity link using MR fluid. *IEEE/ASME Trans. Mechatron.* 24 (2), 495–504. doi:10.1109/TMECH.2019.2894406

Oh, J.-S., and Choi, S.-B. (2019). Ride quality control of a full vehicle suspension system featuring magnetorheological dampers with multiple orifice holes. *Front. Mater.* 6, 1–10. doi:10.3389/fmats.2019.00008

Olszak, A., Osowski, K., Kesy, Z., and Kesy, A. (2019). Investigation of hydrodynamic clutch with a magnetorheological fluid. *J. Intell. Mater. Syst. Struct.* 30 (1), 155–168. doi:10.1177/1045389X18803463

Ouyang, Q., Hu, H., Qian, C., Zhang, G., Wang, J., and Zheng, J. (2019). Investigation of the influence of magnetic field distribution on the magnetorheological absorber with individually controllable coils. *IEEE Trans. Magn.* 55 (8), 1–13. doi:10.1109/TMAG.2019.2907515

Pandit, S., Godiyal, A. K., and Vimal, A. K. (2018). An affordable insole-sensor-based trans-femoral prosthesis for normal gait. *Sensors* 18 (3), 1–18. doi:10.3390/s18030706

Park, Y.-J., Yoon, J.-Y., Kang, B.-H., Kim, G.-W., and Choi, S.-B. (2020). A tactile device generating repulsive forces of various human tissues fabricated from magnetic-responsive fluid in porous polyurethane. *Materials* 13 (5), 1–14. doi:10.3390/ma13051062

Phu, D. X., and Choi, S.-B. (2019). Magnetorheological fluid based devices reported in 2013-2018: mini-review and comment on structural configurations. *Front. Mater.* 6, 19. doi:10.3389/fmats.2019.00019

Pilon, R., Landry-Blais, A., and Gillet, B. (2020). A magnetic screw pump for magnetorheological clutch durability enhancement. *J. Intell. Mater. Syst. Struct.* 31 (7), 945–955. doi:10.1177/1045389X20906474

Qiang, L. S., Wang, J. S., Chen, C., and Wang, F. F. (2019). Design and analysis of magnetorheological fluid dampers based on ultrasonic effects. *China Mech. Eng.* 30 (14), 1658–1672. doi:10.3969/j.issn.1004-132X.2019.014.004

Qin, H. H., Song, A. G., and Mo, Y. T. (2019). A hybrid actuator with hollowed multi-drum magnetorheological brake and direct-current micromotor for hysteresis compensation. *J. Intell. Mater. Syst. Struct.* 30 (7), 1031–1042. doi:10.1177/1045389X19828473

Qin, H., Song, A., Zeng, X., and Hu, S. (2018). Design and evaluation of a small-scale multi-drum magnetorheological brake. *J. Intell. Mater. Syst. Struct.* 29 (12), 2607–2618. doi:10.1177/1045389X18770878

Rossi, A., Orsini, F., Scorza, A., Botta, F., Belfiore, N., and Sciuto, S. (2018). A review on parametric dynamic models of magnetorheological dampers and their characterization methods. *Actuators* 7 (2), 1–21. doi:10.3390/act7020016

Ruan, X. H., Xuan, S. H., Zhao, J., Bian, H. T., and Gong, X. L. (2020). Mechanical performance of a novel magnetorheological fluid damper based on squeeze-valve bi-mode of MRF. *Smart Mater. Struct.* 29 (5), 1–42. doi:10.1088/1361-665X/ab7e34

Sassi, S., Sassi, A., Cherif, K., and Tarlochan, F. (2018). Magnetorheological damper with external excitation for more efficient control of vehicles' dynamics. *J. Intell. Mater. Syst. Struct.* 29 (14), 2919–2932. doi:10.1177/1045389X18781038

Shamieh, H., and Sedaghati, R. (2018). Development, optimization, and control of a novel magnetorheological brake with no zero-field viscous torque for automotive applications. *J. Intell. Mater. Syst. Struct.* 29 (16), 3199–3213. doi:10.1177/1045389X18758186

Shokrollahi, E., Goldenberg, A. A., Drake, J. M., Eastwood, K. W., and Kang, M. (2020). Application of a nonlinear Hammerstein-Wiener estimator in the development and control of a magnetorheological fluid haptic device for robotic bone biopsy. *Actuators* 7 (4), 1–22. doi:10.3390/act7040083

Song, Y., Guo, S. X., and Yin, X. C. (2018a). Design and performance evaluation of a haptic interface based on MR fluids for endovascular tele-surgery. *Microsyst. Technol.* 24 (2), 909–918. doi:10.1007/s00542-017-3404-y

Song, Y., Guo, S. X., and Yin, X. C. (2018b). Performance evaluation of a robot-assisted catheter operating system with haptic feedback. *Biomed. Microdevices* 20 (2), 50. doi:10.1007/s10544-018-0294-4

Tian, S. L., Chen, X. A., He, Y., Chen, T. C., and Li, P. M. (2018). A dynamic loading system for high-speed motorized spindle with magnetorheological fluid. *J. Intell. Mater. Syst. Struct.* 29 (13), 2754–2765. doi:10.1177/1045389X18778369

Topcu, O., Tascioglu, Y., and Konukseven, E. I. (2018). Modeling and experimental evaluation of a rotary peristaltic magnetorheological fluid device with low off-state torque for haptic interfaces. *J. Braz. Soc. Mech. Sci.* 40 (1), 1–9. doi:10.1007/s40430-017-0930-6

Tu, J. W., Li, Z., and Zhang, J. R. (2019). Development, test, and mechanical model of the leak-proof magnetorheological damper. *Front. Mater.* 6, 1–13. doi:10.3389/fmats.2019.00118

Urkucu, T., and Keles, O. (2018). Magneto-rheological engine mount design and experimental characterization. *J. Mech. Sci. Technol.* 32 (11), 5171–5178. doi:10.1007/s12206-018-1015-y

Veronneau, C., Bigue, J. P. L., Lussier-Desbiens, A., and Plante, J. S. (2018). A high-bandwidth back-drivable hydrostatic power distribution system for exoskeletons based on magnetorheological clutches. *IEEE. Robot. Autom. Lett.* 3 (3), 2592–2599. doi:10.1109/LRA.2018.2812910

Wahed, A. K. E., and Balkhoyor, L. B. (2018). The performance of a smart ball-and-socket actuator applied to upper limb rehabilitation. *J. Intell. Mater. Syst. Struct.* 29 (13), 2811–2822. doi:10.1177/1045389X18780349

Wahed, A. K. E., and Wang, H. C. (2019). Performance evaluation of a magnetorheological fluid damper using numerical and theoretical methods with experimental validation. *Front. Mater.* 6, 1–9. doi:10.3389/fmats.2019.00027

Wang, C., Nie, H., Chen, J., and Lee, H. P. (2019). The design and dynamic analysis of a lunar lander with semi-active control. *Acta Astronaut.* 157, 145–156. doi:10.1016/j.actaastro.2018.12.037

Wang, H. Y., and Bi, C. (2020). Study of a magnetorheological brake under compression-shear mode. *Smart Mater. Struct.* 29 (1), 1–17. doi:10.1088/1361-665X/ab5162

Wang, N. N., Liu, X. H., and Grzegora, K. (2019a). Effect of temperature on the transmission characteristics of high-torque magnetorheological brakes. *Smart Mater. Struct.* 28 (1), 1–20. doi:10.1088/1361-665X/ab134c

Wang, N. N., Liu, X. H., and Zhang, X. H. (2019b). Squeeze-strengthening effect of silicone oil-based magnetorheological fluid with nanometer Fe3O4 addition in high-torque magnetorheological brakes. *J. Nanosci. Nanotechnol.* 19 (5), 2633–2639. doi:10.1166/jnn.2019.15895

Wang, W. D., Sun, T. S., and Yuan, X. Q. (2019). Design and analysis of variable flexible actuator for human-robot interaction. *J. Northwest. Polytechn. Univ.* 37 (2), 242–248. doi:10.1051/jnwpu/20193720242

Wang, X., Huang, J., and Xie, Y. (2019). Research on conical magnetorheological and shape memory alloy composite transmission performance. *J. Mech. Transm.* 43 (8), 36–40. doi:10.16578/j.issn.1004.2539.2019.08.007

Wang, Z. H., Chen, Z. Q., Gao, H., and Wang, H. (2018). Development of a self-powered magnetorheological damper system for cable vibration control. *Appl. Sci.* 8 (1), 118. doi:10.3390/app8010118

Wei, M., Rui, X., Zhu, W., Yang, F., Gu, L., and Zhu, H. (2020). Design, modelling and testing of a novel high-torque magnetorheological damper. *Smart Mater. Struct.* 29 (2), 1–13. doi:10.1088/1361-665X/ab6436

Wu, J., Li, H., Jiang, X., and Yao, J. (2018). Design, simulation and testing of a novel radial multi-pole multi-layer magnetorheological brake. *Smart Mater. Struct.* 27 (2), 1–12. doi:10.1088/1361-665X/aaa58a

Wu, X. F., Huang, C. H., Tian, Z. Z., and Ji, J. J. (2019). Development of a novel magnetorheological fluids transmission device for high-power applications. *Smart Mater. Struct.* 28 (5), 1–13. doi:10.1088/1361-665X/ab0eaf

Xin, D. K., Nie, S. L., Ji, H., and Yin, F. L. (2018). Characteristics, optimal design, and performance analyses of MRF damper. *Shock Vib.* 2018, 6454932. doi:10.1155/2018/6454932

Xiong, Y., Huang, J., and Shu, R. Z. (2019). *Combined transmission performance of magnetorheological and electrothermal shape memory alloy*. China Mechanical Engineering. Available at: http://kns.cnki.net/kcms/detail/42.1294.TH.20201013.1440.009.html.

Xu, L.-H., Xie, X.-S., and Li, Z.-X. (2018a). A self-centering brace with superior energy dissipation capability: development and experimental study. *Smart Mater. Struct.* 27 (9), 1–23. doi:10.1088/1361-665X/aad5b0

Xu, L.-H., Xie, X.-S., and Li, Z.-X. (2018b). Development and experimental study of a self-centering variable damping energy dissipation brace. *Eng. Struct.* 160, 270–280. doi:10.1016/j.engstruct.2018.01.051

Yang, B., Sun, S., Deng, L., Jin, T., Li, W., and Li, H. (2019). Vibration control of a tunnel boring machine using adaptive magnetorheological damper. *Smart Mater. Struct.* 28 (11), 1–14. doi:10.1088/1361-665X/ab41a4

Yang, J., and Chen, S. (2019). Design of a drum type wedge clearance magnetorheological transmission device. *Mach. Tool Hydraul.* 47 (15), 105–110. doi:10.3969/j.issn.1001-3881.2019.15.022

Yin, X., Guo, S., and Song, Y. (2018). Magnetorheological fluids actuated haptic-based teleoperated catheter operating system. *Micromachines* 9 (9), 1–20. doi:10.3390/mi9090465

Yoon, D.-S., Park, Y.-J., and Choi, S.-B. (2019). An eddy current effect on the response time of a magnetorheological damper: analysis and experimental validation. *Mech. Syst. Signal Process.* 127, 136–158. doi:10.1016/j.ymssp.2019.02.058

Yoon, D. S., Kim, G. W., and Choi, S. B. (2020). Response time of magnetorheological dampers to current inputs in a semi-active suspension system modeling, control and sensitivity analysis. *Mech. Syst. Signal Process.* 146, 1–21. doi:10.1016/j.ymssp.2020.106999

Yoon, J.-Y., Hong, S.-W., Park, Y.-J., Kim, S.-H., Kim, G.-W., and Choi, S.-B. (2020). Tunable Young's moduli of soft composites fabricated from magnetorheological materials containing microsized iron particles. *Materials* 13 (15), 1–16. doi:10.3390/ma13153378

Yuan, X. J., Tian, T. Y., and Ling, H. T. (2019). A review on structural development of magnetorheological fluid damper. *Shock Vib.* 2019, 1–34. doi:10.1155/2019/1498962

Zahedi, A., Zhang, B., Yi, A., and Zhang, D. (2020). A soft exoskeleton for tremor suppression equipped with flexible semiactive actuator. *Soft Robot.* 1–16. doi:10.1089/soro.2019.0194

Zareie, S., Alam, M. S., Seethaler, R. J., and Zabihollah, A. (2019). Effect of shape memory alloy-magnetorheological fluid-based structural control system on the marine structure using nonlinear time-history analysis. *Appl. Ocean Res.* 91, 1–9. doi:10.1016/j.apor.2019.05.021

Zareie, S., Alam, M. S., Seethaler, R. J., and Zabihollah, A. (2020). Stability control of a novel frame integrated with an SMA-MRF control system for marine structural applications based on the frequency analysis. *Appl. Ocean Res.* 97, 1–9. doi:10.1016/j.apor.2020.102091

Zareie, S., and Zabihollah, A. (2020). A semi-active SMA-MRF structural stability element for seismic control in marine structures. *Appl. Ocean Res.* 100, 1–9. doi:10.1016/j.apor.2020.102161

Zhang, D., Yuan, H., and Cao, Z. C. (2020). Environmental adaptive control of a snake-like robot with variable stiffness actuators. *IEEE/CAA J. Autom. Sinica* 7 (3), 745–751. doi:10.1109/JAS.2020.1003144

Zhang, J. L., Lu, S. B., and Yu, Y. W. (2019). Design optimization and experiment of a disc-type MR device considering the centrifugal effect and plug flow region. *Smart Mater. Struct.* 28 (8), 1–14. doi:10.1088/1361-665X/ab2b4c

Zhang, L., Wang, W., Shi, Y., Chu, Y., and Ming, X. (2019). A new variable stiffness actuator and its control method. *Ind. Robot Int. J Robot. Res. Appl.* 46, 553–560. doi:10.1108/IR-05-2018-0107

Zhang, X. J., Yang, Y., Sun, S. L., He, G. J., and Li, Z. H. (2020). Methodology on a novel magnetorheological valve controlled damper synthesis design. *Smart Mater. Struct.* 29 (4), 1–11. doi:10.1088/1361-665X/ab72e9

Zhao, D., Zhao, J. B., Zhao, Z. H., Liu, Y., Liu, S. G., and Wang, S. H. (2020). Design and experimental study of the porous foam metal magnetorheological fluid damper based on built-in multi-pole magnetic core. *J. Intell. Mater. Syst. Struct.* 31 (5), 687–703. doi:10.1177/1045389X19898249

Zheng, J., Chen, S., Wu, R., and Chen, C. (2020). The induced field of magnetized wall on the static normal force of magnetorheological fluids. *J. Magn. Magn. Mater.* 504, 1–8. doi:10.1016/j.jmmm.2020.166652

Zhong, W.-M., Zhu, A.-D., Bai, X.-X. F., Wereley, N. M., and Zhang, N. (2020). Integrated shock absorber with both tunable inertance and damping. *Front. Mater.* 7, 1–14. doi:10.3389/fmats.2020.00204

Zhou, H., Zhao, W., Zhang, H., Wang, Y., Wu, X., and Sun, Z. (2020). Magnetorheological seal: a review. *J. Appl. Electromagn. Mech.* 62 (2), 763–786. doi:10.3233/JAE-190082

Zhou, Y., and Liu, L. (2020). "A multifunctional ankle foot orthosis utilizing a magnetorheological actuator," in 2nd international conference on advanced nanomaterials and nanodevices, Shanghai, China, October 23–25, 2019 (IOP Conference Series-Materials Science and Engineering). doi:10.1088/1757-899X/813/1/012001

Zhu, S. X., and Geng, F. (2018). The structure design of a new magnetorhelogical brake. *Hydraul. Pneum. Seals* 9, 83–88. doi:10.1088/1361-665X/ab515f

Zhu, S. X., Zhang, H., and Yan, R. (2019). Research on design and performance of new magnetorheological braking device. *Mach. Tool Hydraul.* 47 (19), 46–51. doi:10.3969/j.issn.1001-3881.2019.19.010

Conflict of Interest: The authors declare that the research was conducted in the absence of any commercial or financial relationships that could be construed as a potential conflict of interest.

frontiers in Materials

ORIGINAL RESEARCH
published: 29 March 2021
doi: 10.3389/fmats.2021.659998

Improved Magnetorheological Properties by Using Ionic Liquid as Carrier Liquid of Magnetorheological Fluids

Yu Tong[1], Xiaoguang Li[1], Penghui Zhao[1], Xufeng Dong[1], Zhanjun Wu[2] and Min Qi[1]**

[1] School of Materials Science and Engineering, Dalian University of Technology, Dalian, China, [2] School of Aeronautics and Astronautics, Dalian University of Technology, Dalian, China

OPEN ACCESS

Edited by:
Yancheng Li,
University of Technology Sydney, Australia

Reviewed by:
Wanli Song,
Northeastern University, China
Wenling Zhang,
Nanjing University of Science and Technology, China

***Correspondence:**
Xufeng Dong
dongxf@dlut.edu.cn
Min Qi
minqi@dlut.edu.cn

Specialty section:
This article was submitted to Smart Materials, a section of the journal Frontiers in Materials

Received: *28 January 2021*
Accepted: *25 February 2021*
Published: *29 March 2021*

Citation:
Tong Y, Li X, Zhao P, Dong X, Wu Z and Qi M (2021) Improved Magnetorheological Properties by Using Ionic Liquid as Carrier Liquid of Magnetorheological Fluids. Front. Mater. 8:659998. doi: 10.3389/fmats.2021.659998

The interface between the particles and the carrier fluids has an important influence on the performance of magnetorheological fluid (MRF). In this study, ionic liquids and silicone oils with the same viscosity and different surface tensions were used as carrier fluids to prepare two different carbonyl iron powder (CIP) magnetorheological fluids. The rheological properties of the two magnetorheological fluids were evaluated by the MCR301 rotating rheometer. The experimental results indicate that ionic liquid-based MRF showed higher shear yield strength and more significant MR effect than silicone oil-based ones in higher magnetic field strength. A possible explanation was proposed and proved through experimental data analysis.

Keywords: magnetorheological fluids, ionic liquid, interface, MR effect, shear stress

INTRODUCTION

Magnetorheological fluid (MRF) is an intelligent suspension that responds to a magnetic field (de Vicente et al., 2011; Xu et al., 2011; Ahamed et al., 2018). Its special feature is that under an external magnetic field, the originally flowing liquid can be transformed into a solid-like state, and when the magnetic field is removed, the original flow state can be restored (Carlson and Jolly, 2000). Such characteristics make MRF have broad application prospects in various fields such as smart dampers, magnetic control clutches, and drug delivery (Olabi and Grunwald, 2007; Harris, 2011; Oh et al., 2013; Han et al., 2014; Najmaei, 2014; Phu and Choi, 2019). MRF is mainly composed of soft magnetic particles and non-magnetic carrier fluid. The most mature one is the combination of silicone oil and BASF's carbonyl iron powder (CIP) (Carlson et al., 1996). Improving the shear yield strength of MRF is an important research direction for its application. Although many studies in recent years have shown that special particle morphology can improve the overall performance of MRF (Tong et al., 2017; Xia et al., 2017; Wang et al., 2019; Han et al., 2020), due to the cheap price and high saturation magnetization, CIP is still the mainstay in actual use.

The MR effect is mainly attributed to the field-induced magnetization of the dispersing particles. When a magnetic field is applied, the magnetized particles attract one anther along the field direction and form chains or even columns (Jolly et al., 1996; Morillas and de Vicente, 2019).

As a result, the suspension cannot flow until the applying shear stress reaches a critical value, which is defined as the yield stress. Increasing the shear yield strength of MRF from the carrier fluid has also been studied (Bossis et al., 2002; de Vicente et al., 2011; Ashtiani et al., 2015). Although the performance of MRF can be improved by using some special carrier fluids, the mechanism is still not very clear and cannot guide the development of new MRF with excellent performance.

Through previous research, it is found that the interface between the magnetic particle and the carrier liquid is an important factor affecting its performance. The performance of MRF can be improved by improving the two-phase interface. The traditional method of using surfactants to change the interface will complicate the composition of the rheological fluid, and cannot distinguish its influencing factors and effects well. Although ionic liquids have been used as carrier fluids for MRF (Guerrero-Sanchez et al., 2007; Gómez-Ramírez et al., 2011; Jönkkäri et al., 2014; Bombard et al., 2015), few people have noticed that although its viscosity is similar to that of silicone oil, its surface tension is higher than that of silicone oil. This will bring different interface effects. In this article, we will use ionic liquid as the carrier fluid of MRF to test the performance of ionic liquid-based MRF, and analyze the influence of interfacial on MRF performance by comparing with silicone oil-based MRF.

EXPERIMENTAL

Preparation of MR Fluid

MR fluids were prepared through a typical preparation process (Tong et al., 2017). Silicone oil (bought from Beijing Hangping silicon and chemical Co., Ltd., 0.5 Pa·s) and 1-octyl-3-methylimidazole tetrafluoroborate (ionic liquid, bought from Linzhou Keneng Material Technology Co., Ltd., 0.44 Pa·s) were used as the carrier liquid. The value of surface tension of silicone oil is 15.9–21 mN/m and that of ionic liquid is 25–45 mN/m. Commercial CN carbonyl iron powder (BASF) was selected as the dispersed phase. They were named as SO-MRF and IL-MRF for short in the following text. The concentration of the two MR fluids were 20% in volume function. All reagents were of analytical grade and used without further purification.

Evaluation of MR Fluids

The magnetorheological properties of MR fluids were measured by a Physica MCR301 rheometer (Anton Paar, Austria) equipped with a magnetorheological module (MRD180). The rheometer can apply different magnetic fields on the parallel plate system (PP20) by changing the direct current. The test gap was 1 mm. The shear yield strength and viscosity of MRF were tested in steady-state shear mode. Tested the curve of shear stress increasing linearly with shear rate from 10 to 100 s^{-1} under different magnetic fields. The response curve of MRF with magnetic field changes at a shear rate of 1 s^{-1} was tested. The variation curves of MRF modulus with shear strain amplitude (0.01–100%) and applied magnetic field (0–436 $kA \cdot m^{-1}$) were tested through the oscillating shear mode. All the tests were taken at 25°C.

RESULTS AND DISCUSSION

The shear yield strength of MRF is an important criterion for evaluating its performance. For MRF, the high shear yield strength reflects its higher MR effect, which is very beneficial for the application of MRF. **Figure 1** is the curve of the shear yield strength of two MRFs as a function of the magnetic field strength (obtained by fitting the results in **Supplementary Figure S1** with Bingham model). The shear yield strength of the two MRFs in the figure increased with the increase of the test magnetic field strength, showing a typical MR effect. It can be clearly seen from the figure that IL-MRF has a higher shear yield strength, which shows that it has a higher MR effect. It is particularly worth noting that under higher magnetic field strength, the difference in shear yield strength of the two MRFs is further enlarged. Because the same CIP was used as the dispersed phase, the only difference in

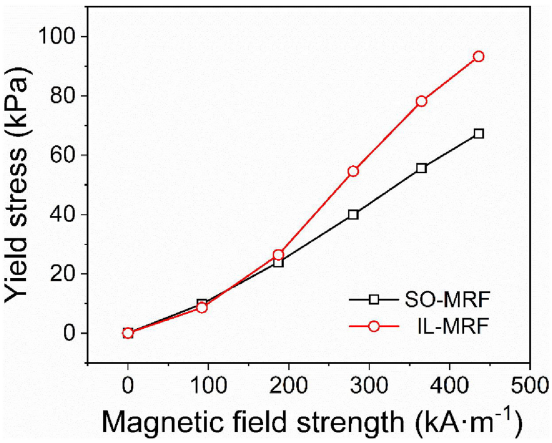

FIGURE 1 | Dependence of yield stress of SO-MRF and IL-MRF on magnetic field.

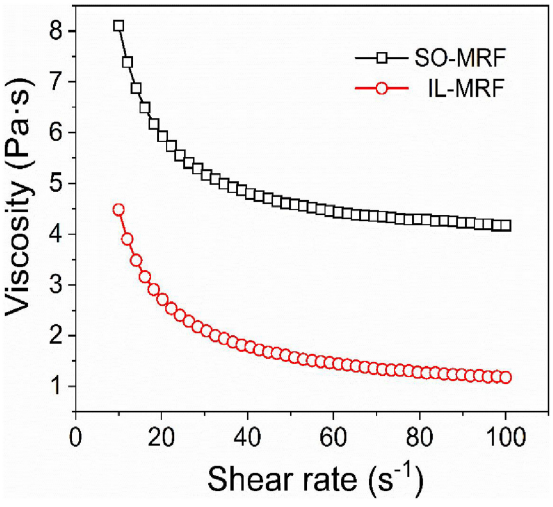

FIGURE 2 | Dependence of viscosity of SO-MRF and IL-MRF on shear rate at zero field.

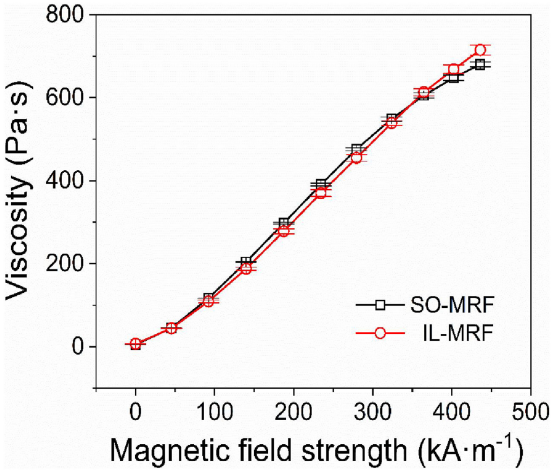

FIGURE 3 | Dependence of viscosity of two MRFs on magnetic field at shear rate of 100 s^{-1}.

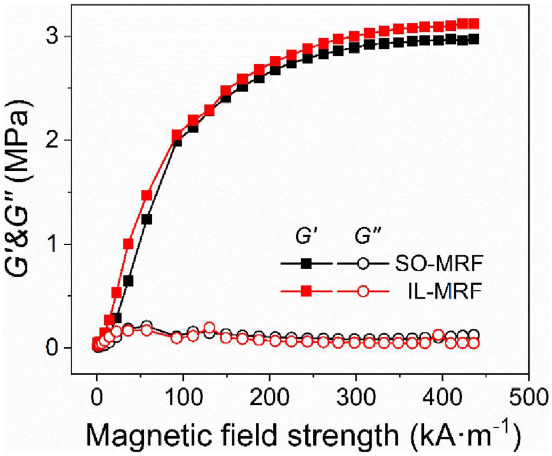

FIGURE 5 | Dependence of the storage modulus G' and loss modulus G'' of SO-MRF and IL-MRF on magnetic field at 0.01% stain amplitude and 10 rad·s^{-1} angular frequency.

MRF was the carrier liquid. Then the performance improvement of IL-MRF has an important relationship with the ionic liquid. The reasons for the improved performance will be analyzed by studying the viscosity of the two MRFs.

Figure 2 is the dependence of viscosity of SO-MRF and IL-MRF on shear rate at zero field. The viscosity of the two magnetorheological fluids decreased as the shear rate increased, showing a typical shear thinning effect. In the zero field, it can be seen that the viscosity of SO-MRF is higher than that of IL-MRF. This is because the viscosity of silicone oil is higher than that of ionic liquid (**Supplementary Figure S2**). **Supplementary Figure S3** shows the viscosity of this two MRFs under different magnetic field strength. Considering that their values are relatively close, the relationship between the viscosity and the magnetic field strength at a shear rate of 100 s^{-1} (When the shear rate is greater than 100 s^{-1}, the viscosity is relatively stable) was tested, as shown in **Figure 3**. In **Figure 3**, the viscosity of the two MRFs increased with the increase of the magnetic field strength, showing a typical MR effect. In a lower magnetic field, since the viscosity of silicone oil is higher than that of ionic liquid, the viscosity of SO-MRF is slightly higher than that of IL-MRF. However, as the magnetic field strength increased, the viscosity increase rate of IL-MRF is higher than that of SO-MRF. Under a higher magnetic field, the viscosity of IL-MRF is higher than that of SO-MRF. This interesting phenomenon is inseparable from the higher surface tension of ionic liquids (Wasserscheid and Keim, 2000). Unlike the larger molecules of silicone oil, there are small ion fragments in ionic liquids, and its larger surface tension is related to this special ion fragment. We believe that these ion fragments are small relative to the particle size of CIP, so they are easily adsorbed on the surface of CIP to form an ion layer, like showing in **Figure 4**. This ion layer approaches each other when the particles are approached by the magnetic field. The van der Waals force between them will enhance the interaction

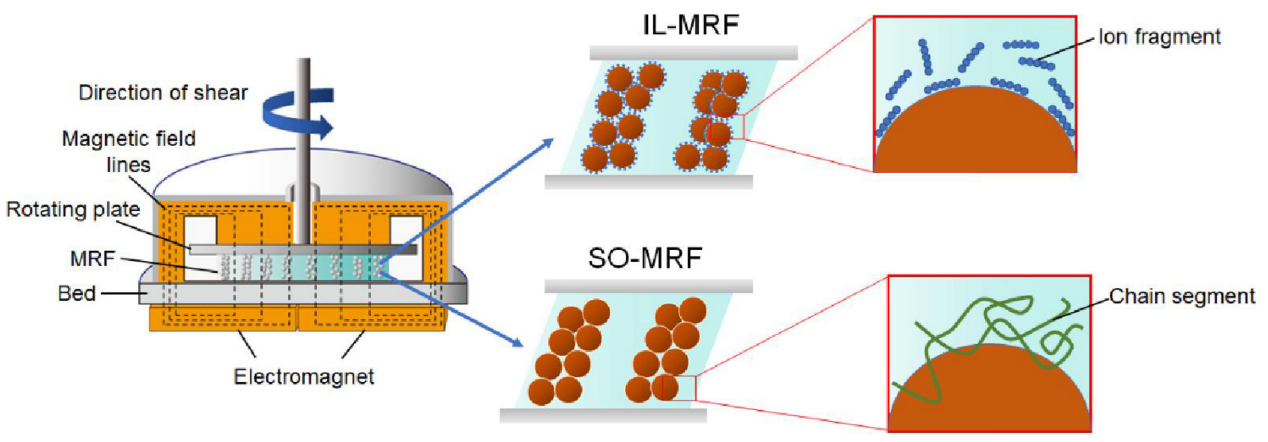

FIGURE 4 | Imaginary schematic diagram of the interface of SO-MRF and IL-MRF.

between the particles, thus forming a more stable structure, which ultimately makes IL-MRF have a higher shear yield strength and higher viscosity. This enhancement effect is amplified as the distance between particles decreases. However, it is difficult to directly observe this layer of ion fragments. Therefore, we indirectly prove our guess by analyzing the structural stability of the two MRFs.

The modulus of MRF can reflect the stability of its structure. From **Supplementary Figure S4**, we determined the linear viscoelastic region of the two MRFs, and selected the strain amplitude of 0.01% and the angular frequency of 10 rad·s^{-1} as the test conditions to test the dependence of the modulus of SO-MRF and IL-MRF on different magnetic fields. The results in **Figure 5** show that the storage modulus G' of IL-MRF is higher than that of SO-MRF, and its loss modulus G'' is lower than that of SO-MRF, which indicates that the structure formed by CIP in IL-MRF is more stable. As other conditions are the same, this proves our previous guess that the special properties of ionic liquids enhance the interaction between particles to improve the performance of MRF. Of course, to prove this conjecture, more experiments, such as computational simulations, are needed.

CONCLUSION

In this research, an ionic liquid-based magnetorheological fluid was produced and its performance was analyzed through testing. Experimental results showed that the shear yield strength of IL-MRF was significantly improved in higher magnetic field strength. The ion fragments in the ionic liquid would form an ion layer on the surface of the particles to improve the interaction between the particles and enhance the MR effect of IL-MRF under a magnetic field. This enhancement effect is confirmed by the MRF modulus results. The experimental results can explain our hypothesis, but more precise analysis and calculations will be reflected in our future work.

DATA AVAILABILITY STATEMENT

All datasets generated for this study are included in the article/**Supplementary Material**, further inquiries can be directed to the corresponding author/s.

AUTHOR CONTRIBUTIONS

YT: methodology and writing—original draft preparation. XL: preparation and test. PZ: mechanism. XD: supervision, conceptualization, and writing—reviewing and editing. ZW: visualization. MQ: validation. All authors contributed to the article and approved the submitted version.

FUNDING

This research was financial funded by the National Key R&D Program of China under the Grant No. 2018YFC0705603.

SUPPLEMENTARY MATERIAL

The Supplementary Material for this article can be found online at: https://www.frontiersin.org/articles/10.3389/fmats.2021.659998/full#supplementary-material

REFERENCES

Ahamed, R., Choi, S., and Ferdaus, M. M. (2018). A state of art on magneto-rheological materials and their potential applications. *J. Intell. Mater. Syst. Struct.* 29, 2051–2095. doi: 10.1177/1045389X18754350

Ashtiani, M., Hashemabadi, S. H., and Ghaffari, A. (2015). A review on the magnetorheological fluid preparation and stabilization. *J. Magn. Magn. Mater.* 374, 716–730. doi: 10.1016/j.jmmm.2014.09.020

Bombard, A. J. F., Gonçalves, F. R., and de Vicente, J. (2015). Magnetorheology of carbonyl iron dispersions in 1-Alkyl-3-methylimidazolium ionic liquids. *Ind. Eng. Chem. Res.* 54, 9956–9963. doi: 10.1021/acs.iecr.5b02824

Bossis, G., Volkova, O., Lacis, S., and Meunier, A. (2002). "Magnetorheology: fluids, structures and rheology," in *Ferrofluids: Magnetically Controllable Fluids and Their Applications*, ed. S. Odenbach (Berlin: Springer Berlin Heidelberg), 202–230. doi: 10.1007/3-540-45646-5_11

Carlson, J. D., Catanzarite, D. M., and St Clair, K. A. (1996). Commercial magneto-rheological fluid devices. *Int. J. Mod. Phys. B* 10, 2857–2865. doi: 10.1142/S0217979296001306

Carlson, J. D., and Jolly, M. R. (2000). MR fluid, foam and elastomer devices. *Mechatronics* 10, 555–569. doi: 10.1016/S0957-4158(99)00064-1

de Vicente, J., Klingenberg, D. J., and Hidalgo-Alvarez, R. (2011). Magnetorheological fluids: a review. *Soft Matter* 7, 3701–3710. doi: 10.1039/C0SM01221A

Gómez-Ramírez, A., López-López, M. T., González-Caballero, F., and Durán, J. D. G. (2011). Stability of magnetorheological fluids in ionic liquids. *Smart Mater. Struct.* 20:045001. doi: 10.1088/0964-1726/20/4/045001

Guerrero-Sanchez, C., Lara-Ceniceros, T., Jimenez-Regalado, E., Raşa, M., and Schubert, U. S. (2007). Magnetorheological fluids based on ionic liquids. *Adv. Mater.* 19, 1740–1747. doi: 10.1002/adma.200700302

Han, W. J., An, J. S., and Choi, H. J. (2020). Enhanced magnetorheological characteristics of hollow magnetite nanoparticle-carbonyl iron microsphere suspension. *Smart Mater. Struct.* 29:055022. doi: 10.1088/1361-665x/ab7f43

Han, Y., Oh, J., Kim, J., and Choi, S. (2014). Design and experimental evaluation of a tactile display featuring magnetorheological fluids. *Smart Mater. Struct.* 23:077001. doi: 10.1088/0964-1726/23/7/077001

Harris, D. C. (2011). "History of magnetorheological finishing," in *Proceedings of the SPIE* (Bellingham, WA: SPIE) 8016, 1–22.

Jolly, M. R., Carlson, J. D., and Muñoz, B. C. (1996). A model of the behaviour of magnetorheological materials. *Smart Mater. Struct.* 5, 607–614. doi: 10.1088/0964-1726/5/5/009

Jönkkäri, I., Isakov, M., and Syrjälä, S. (2014). Sedimentation stability and rheological properties of ionic liquid–based bidisperse magnetorheological fluids. *J. Intell. Mater. Syst. Struct.* 26, 2256–2265. doi: 10.1177/1045389X14551436

Morillas, J. R., and de Vicente, J. (2019). Yielding behavior of model magnetorheological fluids. *Soft Matter* 15, 3330–3342. doi: 10.1039/C9SM00275H

Najmaei, N. (2014). *Design of a Haptic Interface for Medical Applications Using Magneto-Rheological Fluid Based Actuators*. London, UK: The University of Western Ontario.

Oh, J. S., Kim, J. K., Lee, S. R., Choi, S. B., and Song, B. K. (2013). Design of tactile device for medical application using magnetorheological

fluid. *J. Phys. Conf. Ser.* 412:012047. doi: 10.1088/1742-6596/412/1/012047

Olabi, A. G., and Grunwald, A. (2007). Design and application of magneto-rheological fluid. *Mater. Des.* 28, 2658–2664. doi: 10.1016/j.matdes.2006.10.009

Phu, D. X., and Choi, S. (2019). Magnetorheological fluid based devices reported in 2013–2018: mini-review and comment on structural configurations. *Front. Mater.* 6:19. doi: 10.3389/fmats.2019.00019

Tong, Y., Dong, X., and Qi, M. (2017). High performance magnetorheological fluids with flower-like cobalt particles. *Smart Mater. Struct.* 26:025023. doi: 10.1088/1361-665X/aa57cc

Wang, G., Zhao, D., Li, N., Zeng, Y., Han, S., Ma, Y., et al. (2019). Facile synthesis of hierarchically structured flower-like Fe3O4 microspheres for high-performance magnetorheological fluids. *J. Ind. Eng. Chem.* 79, 217–225. doi: 10.1016/j.jiec.2019.06.040

Wasserscheid, P., and Keim, W. (2000). Ionic liquids—new "solutions" for transition metal catalysis. *Angew. Chem. Int. Ed.* 39, 3772–3789. doi: 10.1002/1521-3773(20001103)39:21<3772::AID-ANIE3772<3.0.CO;2-5

Xia, Z., Wu, X., Peng, G., Wang, L., Li, W., and Wen, W. (2017). A novel nickel nanowire based magnetorheological material. *Smart Mater. Struct.* 26:054006. doi: 10.1088/1361-665x/aa5bd0

Xu, Y., Gong, X., Xuan, S., Zhang, W., and Fan, Y. (2011). A high-performance magnetorheological material: preparation, characterization and magnetic-mechanic coupling properties. *Soft Matter* 7:5246. doi: 10.1039/c1sm05301a

Conflict of Interest: The authors declare that the research was conducted in the absence of any commercial or financial relationships that could be construed as a potential conflict of interest.

frontiers in Materials

ORIGINAL RESEARCH
published: 13 April 2021
doi: 10.3389/fmats.2021.642049

Field–Frequency-Dependent Non-linear Rheological Behavior of Magnetorheological Grease Under Large Amplitude Oscillatory Shear

Huixing Wang[1,2], Tianxiao Chang[1], Yancheng Li[2], Shaoqi Li[2], Guang Zhang[1] and Jiong Wang[1]**

[1] School of Mechanical Engineering, Nanjing University of Science and Technology, Nanjing, China, [2] School of Civil and Environmental Engineering, University of Technology Sydney, Sydney, NSW, Australia

OPEN ACCESS

Edited by:
Brahim Aissa,
MPB Technologies & Communications, Canada

Reviewed by:
U. Ubaidillah,
Sebelas Maret University, Indonesia
Tongfei Tian,
University of the Sunshine Coast, Australia

***Correspondence:**
Yancheng Li
yancheng.li@uts.edu.au
Jiong Wang
wjiongz@njust.edu.cn

Specialty section:
This article was submitted to Smart Materials, a section of the journal Frontiers in Materials

Received: 15 December 2020
Accepted: 17 March 2021
Published: 13 April 2021

Citation:
Wang H, Chang T, Li Y, Li S, Zhang G and Wang J (2021) Field–Frequency-Dependent Non-linear Rheological Behavior of Magnetorheological Grease Under Large Amplitude Oscillatory Shear. Front. Mater. 8:642049. doi: 10.3389/fmats.2021.642049

This article investigates the influence of frequency on the field-dependent non-linear rheology of magnetorheological (MR) grease under large amplitude oscillatory shear (LAOS). First, the LAOS tests with different driving frequencies were conducted on MR grease at four magnetic fields, and the storage and loss moduli under the frequency of 0.1, 0.5, 1, and 5 Hz were compared to obtain an overall understanding of the frequency-dependent viscoelastic behavior of MR grease. Based on this, the three-dimensional (3D) Lissajous curves and decomposed stress curves under two typical frequencies were depicted to provide the non-linear elastic and viscous behavior. Finally, the elastic and viscous measures containing higher harmonics from Fourier transform (FT)-Chebyshev analysis were used to quantitatively interpret the influence of the frequency on the non-linear rheology of MR grease, namely, strain stiffening (softening) and shear thickening (thinning), under LAOS with different magnetic fields. It was found that, under the application of the magnetic field, the onset of the non-linear behavior of MR grease was frequency-dependent. However, when the shear strain amplitude increased in the post-yield region, the non-linear rheology of MRG-70 was not affected by the oscillatory frequency.

Keywords: MR grease, non-linear rheology, frequency, large amplitude oscillatory shear, field

INTRODUCTION

Magnetorheological (MR) grease is a kind of magneto-induced smart material that is normally prepared by dispersing magnetic particles in grease matrix. With the utilization of viscoelastic continuous phases, i.e., grease matrix, MR grease can effectively avoid the sedimentation problem of magnetic particles, which often occurred in conventional MR fluid. So far, MR grease has been used in the application of many MR devices, namely MR damper (Shiraishi et al., 2011; Sakurai and Morishita, 2017), MR clutch (Kavlicoglu et al., 2015), MR brake (Sukhwani and Hirani, 2008), and MR engine mount (Sarkar et al., 2015). By comparing conventional MR devices using MR

fluid, the MR grease device can maintain good settlement stability for a long period of time. In addition, considering the lubricating properties of the grease matrix, it can reduce the wear and tear of the moving parts of the devices and increase life, which eventually will reduce the maintenance cost in the long run. In the operation of MR devices, the internal MR grease usually works in the shear mode, which mainly includes steady shear and oscillatory shear (Zhang et al., 2019, 2020; Li et al., 2020). Therefore, it is necessary to conduct investigations on the rheological properties of MR grease under steady shear and oscillatory shear, which can provide insight and understanding for the design and application of MR grease devices.

To date, the rheology of MR grease under steady shear and oscillatory shear was studied by a number of researchers. For steady shear, researchers mainly focused on the dependence of rheological parameters, namely viscosity, yield stress, the magnetic field, shear rate, and temperature. Sahin et al. (2007) studied the yield stress and viscosity of MR grease under steady shear and compared them with the results obtained using conventional silicon-based MR fluid. They found that the yield stress of MR grease is higher than that of the traditional MR fluid, which is at the expense of increased off-state viscosity of MR grease (Sahin et al., 2007). Park et al. investigated the flow curve responses of MR grease with different external magnetic fields under steady shear. They indicated that MR grease presents the properties of Bingham fluid under the application of the magnetic field (Park et al., 2011). Mohamad et al. (2018) examined the field-dependent rheology of MR grease with platelike particles. They found that the platelike carbonyl iron (CI)-based MR grease can provide higher yield stress than spherical particle-based MR grease at a low magnetic field with a low weight fraction of particles (Mohamad et al., 2018). Wang et al. (2019a,b,c) investigated the temperature-dependent rheology of MR grease under steady shear. They demonstrated that the influence of temperature on the rheological properties of MR grease decreased with the magnetic field (Wang et al., 2019a,b,c). For oscillatory shear, the main focus is the influence of the magnetic field, oscillatory shear strain, and frequency on the dynamic parameters, such as storage/loss modulus and loss factor. Rankin et al. (1999) tested the storage modulus of MR grease under a series of the strain sweep tests. They found that the storage modulus of MR grease under the small strain amplitude is time-dependent (Rankin et al., 1999). Park et al. (2011) studied the influence of oscillatory frequency on storage and loss moduli under different magnetic fields. They found that the storage and loss moduli are all independent of frequency at a fixed magnetic field (Park et al., 2011). Mohamad et al. (2016) tested the relationship between dynamic parameters and oscillatory shear strain under different magnetic fields. They concluded that the linear viscoelastic (LVE) range (storage modulus independent of shear strain) of MR grease is smaller compared with the MR gel, and the relative MR effect of MR grease is larger than that of the MR fluid (Mohamad et al., 2016). In addition, Mohamad et al. (2019a,b) also investigated the field-dependent viscoelastic and transient response of MR grease with different particle shapes. They found that the shape of the CI particles (CIPs) has a significant effect on the field-dependent behaviors of MR grease, e.g., the bidisperse MR grease with platelike CI particles exhibits an increase in the initial apparent viscosity and the stiffness property compared with MR grease with spherical particles only (Mohamad et al., 2019a,b).

Although a lot of research was conducted on the rheological properties of MR grease under steady shear and oscillatory shear, the rheological study of MR grease under oscillatory shear, especially large amplitude oscillatory shear (LAOS), is yet to be fully explored. The reason is that the storage and loss moduli, which are normally acquired from rheometer and used to characterize the rheology of MR grease under oscillatory shear, may not be sufficient to characterize the rheology of MR grease under LAOS. As shown in a previous research, under LAOS, the shear strain amplitude that was applied on MR grease enters into the non-linear range (Hyun et al., 2011). The response stress wave deviates from the sine wave and contains higher harmonics. The output moduli from the commercial rheometer, namely storage modulus (G') and loss modulus (G''), are the first harmonic moduli of the Fourier transform of the response data (Wilhelm, 2002). This method that ignores the contribution of higher modulus but only considers the first harmonic modulus will inevitably result in the loss of rich information when characterizing the rheology of MR grease under LAOS.

Recently, we introduced a non-linear characterization method, namely Fourier transform (FT)-Chebyshev analysis (Wilhelm, 2002; Cho et al., 2005), which could detect the higher harmonics triggered by LAOS. Compared with commonly used approaches, namely elastic Lissajous curves, storage/loss modulus, and FT analysis, we found that the FT-Chebyshev analysis could provide more insight on non-linear viscoelastic (NLVE) behavior of MR materials under LAOS. Subsequently, we also utilized the FT-Chebyshev analysis to quantitatively analyze the non-linearity of MR grease under different strain amplitudes at a fixed frequency (Wang et al., 2020). In addition to the oscillatory strain amplitude, frequency is an important factor that affects the non-linear rheological properties of MR grease. Exploring the influence of the frequency on the non-linear behavior of MR grease is the basis for the development of efficient control algorithms in practical MR grease device applications. Thus, in this article, we investigate the field-dependent non-linearity of MR grease under LAOS at different driving frequencies. First, MR grease with a 70% weight percentage of CIPs (MRG-70) is prepared, and the LAOS test with different driving frequencies is conducted on MR grease at four different magnetic fields. Then, the storage and loss moduli at different frequencies are compared. Later, the influence of the frequency on the non-linear rheology is qualitatively analyzed by the three-dimensional (3D) Lissajous curves and the stress decomposed method. Finally, the elastic and viscous measures containing higher harmonics from the FT-Chebyshev analysis under different frequencies are calculated to further characterize the field-dependent non-linear rheology under LAOS at different driving frequencies.

MATERIALS AND METHODS

Preparation of MR Grease

For this research, MR grease is composed of lithium-based commercial grease and CIPs. The lithium-based commercial grease (Gadus S2 V220, Shell Ltd., Zhuhai, China) has an NLGI grade of 0, which presents the appearance of brown mustard. The CIPs are obtained from BASF Ltd. (Ludwigshafen, Germany) and have an average diameter of 6 μm. We prepared MRG-70 in this study. The preparation processes are as follows: first, 140 g of CIPs and 60 g of commercial grease were weighed and put into two different vials. Then, the commercial grease was stirred at 500 rpm for 10 min at the temperature of 80℃. Finally, the prepared CIPs were dispersed into the commercial grease with a mechanical stirrer at 800 rpm until the grease and the CIPs form a stable and homogeneous product.

Experiment Methods

Fibrous Structure Observation

Magnetorheological (MR) grease has almost no sedimentation problem because of the fibrous structure of the grease matrix. The microstructures of the grease matrix and MRG-70 were observed with a scanning electron microscopy (SEM) (FEI, Quanta 250 FEG). As indicated in a previous study, lubricating greases are highly structured colloidal dispersions consisting of a thickener dispersed in the base oil (Wang et al., 2019a). Due to the influence of the base oil, it is difficult to see the fibrous structures of the untreated MR grease through SEM. Delgado et al. reported the solvent infiltration method to extract the base (Delgado et al., 2006). However, we found this method to be effective only for the grease with a higher NLGI grade. In this article, we used ultrasonic centrifugation to extract the base oil, which mainly consists of three parts: (1) adding a small amount of sample into the hexane and stirring it with a glass rod for 30 s; (2) using ultrasonic dispersion for 5 min; and (3) centrifuging for 2 min at 10,000 rpm and discarding the centrifugal fluid. Repeating the above steps three times can provide the sample without the base oil.

Rheological Test

The rheological tests of MR grease under LAOS were all carried out using the MCR 302 rheometer (Anton Paar instrument, Graz, Austria) in parallel-plate geometry with a diameter of 20 mm. In the experiment, 0.4 ml of MRG-70 was injected into the gap between the upper parallel plate and the base. The gap was kept constant at 1 mm throughout the test. The temperature was always controlled at 25°C. In each LAOS test, a series of sinusoidal strain waves with different strain amplitudes and frequencies were performed at a fixed magnetic field. The strain amplitude varies from 0.01 to 100%, and the frequency is set as 0.1 and 1.0 Hz, respectively. Two different magnetic fields, i.e., 0 and 391 kA/m, were selected for this study. To obtain a homogeneous reproducible test, the sample was pre-sheared under 1/s for 1 min and stalled for 30 s before formal testing. LAOS experiments are tested for at least 30 cycles to ensure the response stress at a steady state.

Rheological Analysis of LAOS Data

To obtain the elastic and viscous measures, the LAOS data analysis processes are performed as follows: first, the real-time response stress was analyzed by the FT-Chebyshev analysis, and then, the n-th order elastic and viscous moduli, i.e., G' n and G'' n, were calculated (Wilhelm, 2002). Second, according to the analysis of the results provided by Ewoldt et al. (2008), the elastic and viscous Chebyshev coefficients, i.e., e_n and v_n, can be calculated as follows:

$$\begin{aligned} e_n &= \sum_{\substack{n=1 \\ n\ odd}} G_n^{'}(-1)^{(n-1)/2} \\ v_n &= \sum_{\substack{n=1 \\ n\ odd}} G_n^{''}/\omega \end{aligned} \tag{1}$$

where $n = 1, 3, 5\ldots$ and ω is the angular frequency of LAOS.

Then, the newly defined elastic and viscous measures can be represented as:

$$S = \frac{4e_3 - 4e_5 + 8e_7 + \cdots}{e_1 + e_3 + e_5 + e_7 + \cdots} \tag{2}$$

$$T = \frac{4v_3 - 4v_5 + 8v_7 + \cdots}{v_1 + v_3 + v_5 + v_7 + \cdots} \tag{3}$$

where S is the strain-stiffening ratio and T is the shear-thickening ratio.

RESULTS AND DISCUSSION

Microstructure of MRG-70 and CIPs

Figure 1 shows the microstructures of the fresh MR grease product, i.e., MRG-70, and its matrix, i.e., commercial grease. **Figure 1a** shows the microstructure of the lithium-based grease matrix **Figure 1b** shows the microstructure of MRG-70, and the white point in the figure is the CIPs and the dark background is the grease matrix. From **Figures 1a,b**, it is difficult to observe the fibrous structure due to the influence of the base oil in grease. **Figures 1c,d** show the microstructures of the grease and MRG-70 with the extracted base oil, respectively. From **Figure 1c**, the obvious 3D fibrous structures can be observed. Due to the function of that entangled fibrous structures, the CIPs in MR grease are trapped when the external magnetic field is not applied, which can effectively avoid the sedimentation problem of conventional MR fluid. In **Figure 1d**, the red arrow represents the CIP, and the green arrow represents the entangled fibrous structures. The CIP entangled by the fibrous structures can be observed.

Oscillatory Strain Sweep Under Different Frequencies and Magnetic Fields

The oscillatory strain sweep is widely utilized to detect the viscoelastic rheological behavior of MR materials. Based on

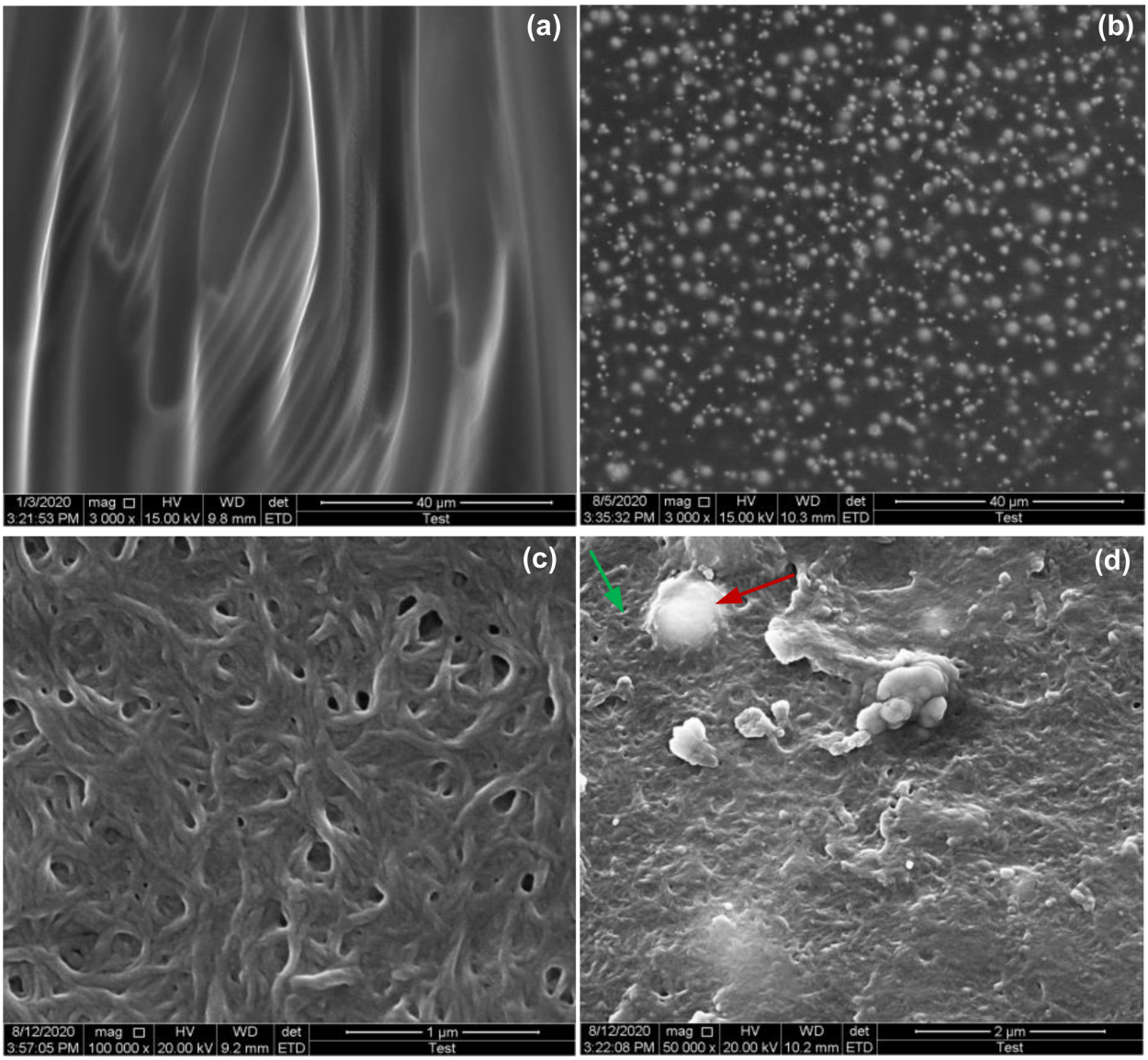

FIGURE 1 | SEM images of **(a)** grease matrix and **(b)** MRG-70 without magnetic field. **(c)** and **(d)** microstructures of the grease and MRG-70 with the extracted base oil, respectively. The red arrow shows the CIP, and the green arrow shows the entangled fibrous structures.

whether the storage and loss moduli response depends on the input strain amplitude, the oscillatory strain sweep can be divided into LVE and NLVE ranges (Upadhyay et al., 2013; Agirre-Olabide et al., 2014). In the NLVE range, the stress response normally contains higher harmonics than the input frequency. The LVE moduli, i.e., G' and G'', are actually the real and imaginary coefficients of the first harmonics (Wilhelm et al., 2000). **Figure 2** shows the field-dependent storage and loss moduli which vary with shear strain amplitude under different frequencies, i.e., 0.1, 0.5, 1, and 5 Hz. **Figures 2A,B** show that, irrespective of the frequency, the LVE range without the magnetic field is wider than that with the magnetic field, e.g., the critical strain amplitude between LVE and NLVE is around 0.2% without the magnetic field. When the magnetic field is applied, the critical strain amplitude decreases to about 0.08%. This is because the stronger CIP chain and cluster structures are formed in the direction of the magnetic field. In addition, in the NLVE range, for MRG-70 with the magnetic field at the fixed frequency of 0.1 Hz (see **Figure 2A**), both storage and loss moduli monotonically decrease with the strain amplitude, indicating the intercycle shear thinning behavior. When the oscillatory frequency is higher than 0.1 Hz, i.e., 0.5, 1, and 5 Hz (see **Figures 2B–D**), the storage modulus of MRG-70 with the magnetic field still exhibits a monotonic decrease, while the loss modulus presents a typical overshoot at the onset of the non-linear, and this phenomenon is more pronounced at the higher magnetic field, e.g., 391 kA/m. The reason for the above feature may relate to the shear rate-dependent viscoelastic relaxation and thixotropy of the CIPs chain structures induced by the external magnetic field (Ghosh et al., 2019). Through the earlier analysis,

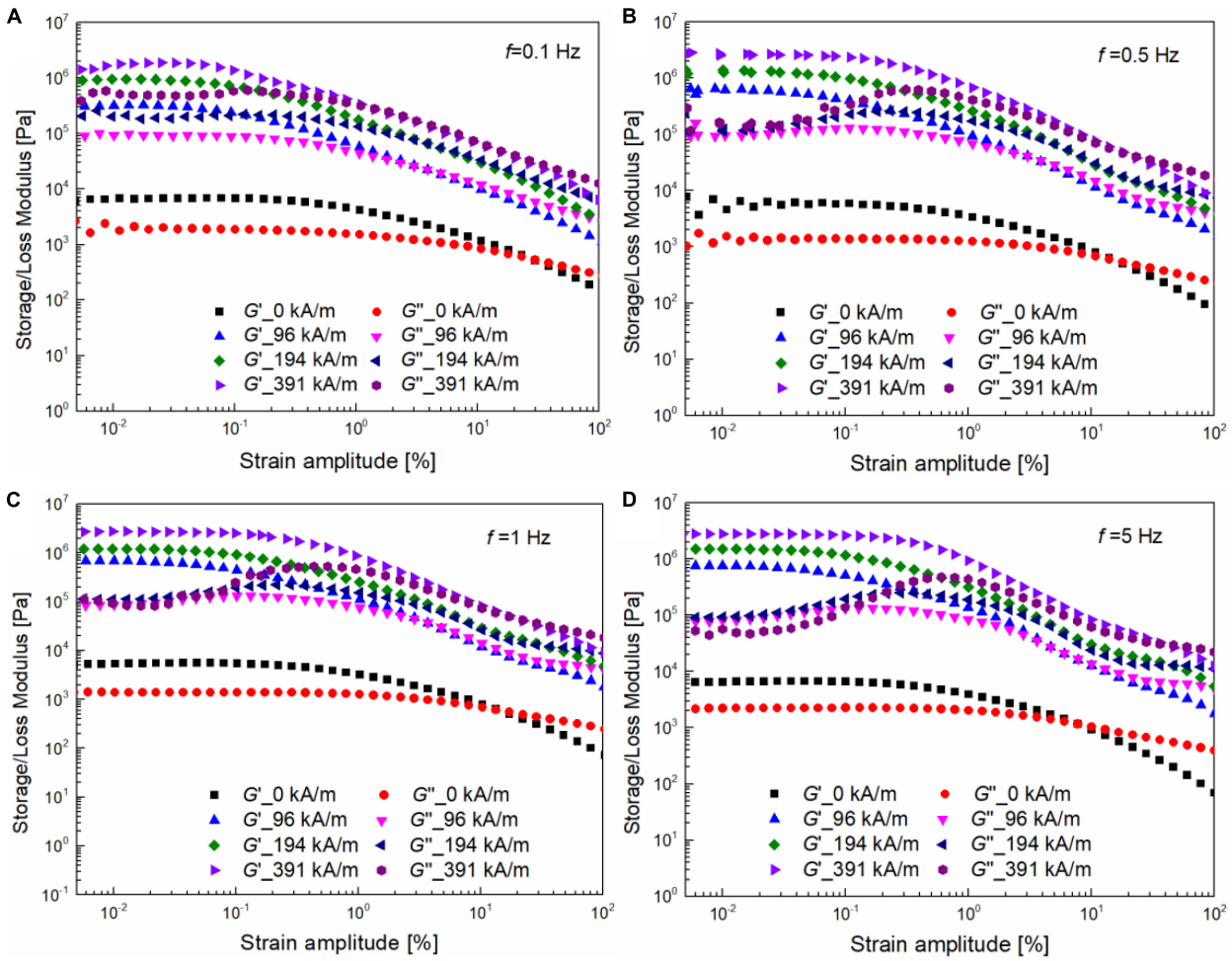

FIGURE 2 | Oscillatory strain sweeps were conducted under different magnetic fields, i.e., 0, 96, 194, and 391 kA/m, at the fixed frequencies of **(A)** 0.1, **(B)** 0.5, **(C)** 1, and **(D)** 5 Hz.

it can be seen that, when the frequency rises from 0.1to 5 Hz, MRG-70 mainly exhibits two viscoelastic characteristics, namely strain thinning in which *G*' and *G*" decrease in the NLVE range at 0.1 Hz and weak strain overshoot in which *G*' decreases but *G*" increases, followed by a decrease in the NLVE range at the frequencies of 0.5, 1, and 5 Hz. Thus, the following part of the paper will focus on the behavior of MR grease at 0.1 and 1 Hz to characterize the above frequency-dependent viscoelasticity under LAOS with different magnetic fields. In summary, the viscoelastic behavior of MRG-70 under the oscillatory shear can be divided into three parts: the LVE part, the onset of the NLVE part, and the post NLVE part. In the LVE part, the storage modulus was maintained constantly due to the elastic deformation of the CIPs structures. As the shear strain amplitude approached the yield point, i.e., the onset of the NLVE part, the CIPs chain or cluster structures start to rupture, resulting in the overshot behavior of loss modulus which is closely related to the frequency and the magnetic field. With the further increase in the strain amplitude, loss modulus exceeds the storage modulus, indicating that MRG-70 entered into the viscous flow that prevents viscous dominant. At this time, the destruction of CIPs chain structures caused by shear and rearrangement of CIPs induced the magnetic field to reach an equilibrium state.

Field-Dependent Elastic and Viscous Lissajous Curves

It is well known that the storage/loss modulus obtained from the oscillatory strain sweep demonstrates the average viscoelastic properties over different oscillation cycles, i.e., intercycle rheology. However, it is difficult to characterize the viscoelastic properties within an oscillation cycle, especially when the shear strain enters the non-linear regime, i.e., intracycle non-linear rheology (Hyun et al., 2011). To characterize the intracycle non-linear properties of MRG-70 under the LAOS test, the dependence of the response stress on time, shear strain, and shear rate within one cycle for two different strain amplitudes at a fixed frequency of 1 Hz is depicted in **Figure 3**. **Figures 3A–D** show the stress response and the FT-Chebyhev analysis of MRG-70 under the oscillatory shear with the strain amplitude in the linear regime, i.e., 0.1%. In this study, the response stress of MRG-70 remained in a standard sinusoidal waveform (**Figure 3A**). The elastic Lissajous curve shown in

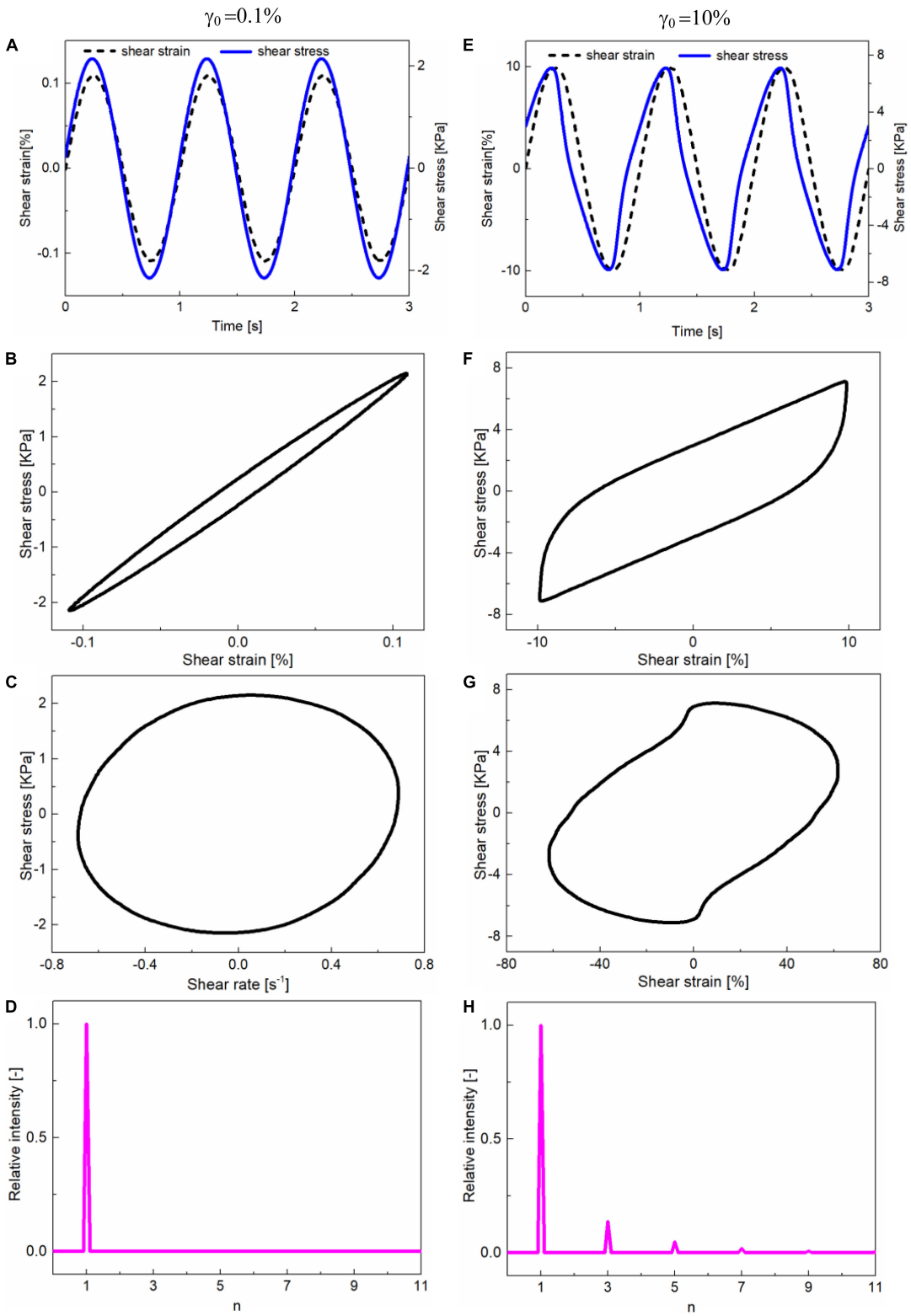

FIGURE 3 | (A,E) represent the dependence of input strain and response stress on time. **(B,F)** show the Lissajous curves of the shear stress that varies with the shear strain (elastic Lissajous curves). **(C,G)** show the Lissajous curves of the shear stress that varies with the shear rate (viscous Lissajous curves). **(D,H)** show the results from FT-Chebyshev analysis. The data used in **(A–D)** were obtained from the LAOS test with γ = 0.1% and f = 1 Hz. The data used in **(E–H)** were obtained from the LAOS test with γ = 10% and f = 1 Hz. All these tests were conducted on the magnetic field of 391 kA/m.

Figure 3B presented an elliptical shape where the tangent slope at zero strain is equal to the storage modulus, i.e., G', and the area of the curve is proportional to the loss modulus, i.e., G''. The above linear response can also be confirmed by the results of FT-Chebyshev analysis where the relative intensity from higher harmonics ($n \geq 3$) is equal to 0 (**Figure 3D**). However, when the shear strain amplitude increased into the non-linear regime, e.g., 10%, as shown in **Figures 3E–H**, the time–history curve of the response stress shown in **Figure 3E** deviated from the sinusoidal waveform. In the present study, the elastic and viscous Lissajous curves were all distorted, indicating the intracycle non-linearities of strain stiffening and shear thinning, respectively. In this case, the contribution from higher-order harmonics was detected by the FT-Chebyshev analysis (**Figure 3H**). By comparing the stress response of MRG-70 under different shear strain amplitudes, i.e., 0.1 and 10%, it can be concluded that the non-linearity of MRG-70 was strongly dependent on the strain amplitude. In the following section, the strain dependence of the non-linearity for MRG-70 under different frequencies is discussed.

In the 3D Lissajous curve at a fixed shear strain amplitude, the maximum instantaneous shear strain corresponds to the minimum instantaneous shear rate, e.g., when $\gamma\ (\boldsymbol{t}) = \gamma_0$, the shear rate is equal to 0. Similarly, when $\gamma\ (t) = 0$, the instantaneous shear rate reaches the maximum, i.e., $\pm\ \gamma_0\omega$. As the shear strain amplitude varies, the intracycle stress at the maximum instantaneous shear strain (shear rate), which is shown in the shear strain (shear rate) domain, i.e., elastic and viscous Lissajous curves, changes, and its location, can be used to characterize the elastic and viscous contribution (Goudoulas and Germann, 2019a,b). **Figure 4** depicts the comparison of the 3D Lissajous curves under different shear strain amplitudes, i.e., 0.01, 1, 10, and 100% at a fixed frequency of 1 Hz. At sufficient small strain amplitude shown in **Figure 4A**, i.e., 0.01%, the area of the elastic Lissajous (curve the green line in **Figure 4A**) tends to be very small, and MRG-70 has the maximum intracycle stress at γ_0. On the other hand, the intracycle stress at the maximum shear rate, i.e., $\pm\ \gamma_0\omega$, in the approaches of the corresponding viscous Lissajous (curves the blue line in **Figure 3A**) was 0. This demonstrates that, at sufficient small strain amplitude, the viscous contribution is 0, and MRG-70 only presents elasticity during the oscillatory shear. With the further increase in shear strain amplitude, i.e., 1 and 10% (**Figures 4B,C**), the area of the elastic Lissajous curves rapidly increases and the intracycle stress at the maximum shear rate increases between 0 and maximum stress, indicating the emergence of the viscous contribution. Thus, MRG-70 at the medium shear strain amplitude showed the viscoelastic behavior composed of elastic deformation and viscous dissipation. When the shear strain amplitude increased to a large value, i.e., 100%, the elastic Lissajous curves showed a shape of quadrilateral that represents the typical flow-induced structure of MRG-70 under oscillatory shear with 100% strain (Goudoulas and Germann, 2019a). Besides, the intracycle stress at the maximum shear rate in the approaches of the corresponding viscous Lissajous curves increased to the maximum value, indicating that the non-linearity of MRG-70 at 100% comes mainly from the viscous flow. In summary, the contribution of the viscous part to the non-linearity of MRG-70 was highly strain amplitude-dependent.

To provide a further qualitative analysis on the effect of frequency and the magnetic field on the non-linear rheology of MRG-70 under LAOS, the field-dependent elastic and viscous Lissajous curves under LAOS with two typical driving frequencies are shown in **Figures 5–8**. The left and right columns in **Figures 5–8** represent the elastic and viscous Lissajous curves, respectively, in which the red dash lines represent the corresponding decomposed shear stress, i.e., the intracycle elastic and viscous stress. From **Figure 5**, without the magnetic field, the Lissajous curves under the oscillatory frequency of 0.1 Hz maintained linear behavior up to 4% shear strain. This is further validated by the decomposed elastic and viscous stress that linearly increased with instantaneous intracycle shear strain and rate, respectively. However, as the oscillatory frequency increases to 1 Hz, the critical shear strain from linearity to non-linearity was decreased, i.e., around 1%, which demonstrated that the onset of the non-linear behavior was frequency-dependent. On the other hand, when the shear strain amplitude increased into the non-linear regime, the non-linearities seem to be less affected by the frequency, i.e., at frequencies of 0.1 and 1 Hz, and the non-linearities of MRG-70 show the combination of strain stiffening of elastic stress and shear thinning for energy dissipation, which is confirmed by the upturn of the decomposed elastic stress and the downturn of the decomposed viscous stress. In addition, as the shear strain amplitude increased to a large value, e.g., 100%, the contribution of the elastic stress to the non-linearity was kept constant over a wide range of the oscillatory shear. For example, from the elastic Lissajous curves at 100% shear strain amplitude shown in **Figure 5**, the decomposed elastic stress linearly changed with the instantaneous intracycle shear strain between − 90 and 90%. When the instantaneous intracycle shear strain approached the maximum value, i.e., 100%, the decomposed elastic stress presented a sharp increase. However, the similar behavior was not appeared in the decomposed viscous stress, in which the slope of that curve slowly changed over the whole oscillatory shear.

Figures 6, **7** show the frequency-dependent elastic and viscous Lissajous curves under the small and medium magnetic fields, i.e., 96 and 194 kA/m, respectively. Different from MRG-70 without the magnetic field, when the magnetic field, i.e., 96 or 194 kA/m, is applied, the elastic Lissajous curves of MRG-70 deviated from the elliptical shape at the strain amplitude of 1% due to the arrangement of the CIPs along the direction of the magnetic field, indicating that the LVE range was magnetic field-dependent. Moreover, in the NLVE range, the elastic and viscous Lissajous curves were observed to be less affected by the frequency when the shear strain amplitude increased from 1 to 10%. With the further increase in the strain amplitude, the shape of the elastic and Lissajous curves exhibited a strong frequency dependency. For example, at the shear strain amplitude of 60% under 0.1 Hz, as shown in **Figures 6**, **7**, the elastic Lissajous curves presented a plateau after the shear strain changed the direction. However, a typical overshoot behavior was observed under the frequency of 1 Hz. Such behavior was further strengthened as the shear strain amplitude increased to 100%. The reason for the above characteristics can be attributed to

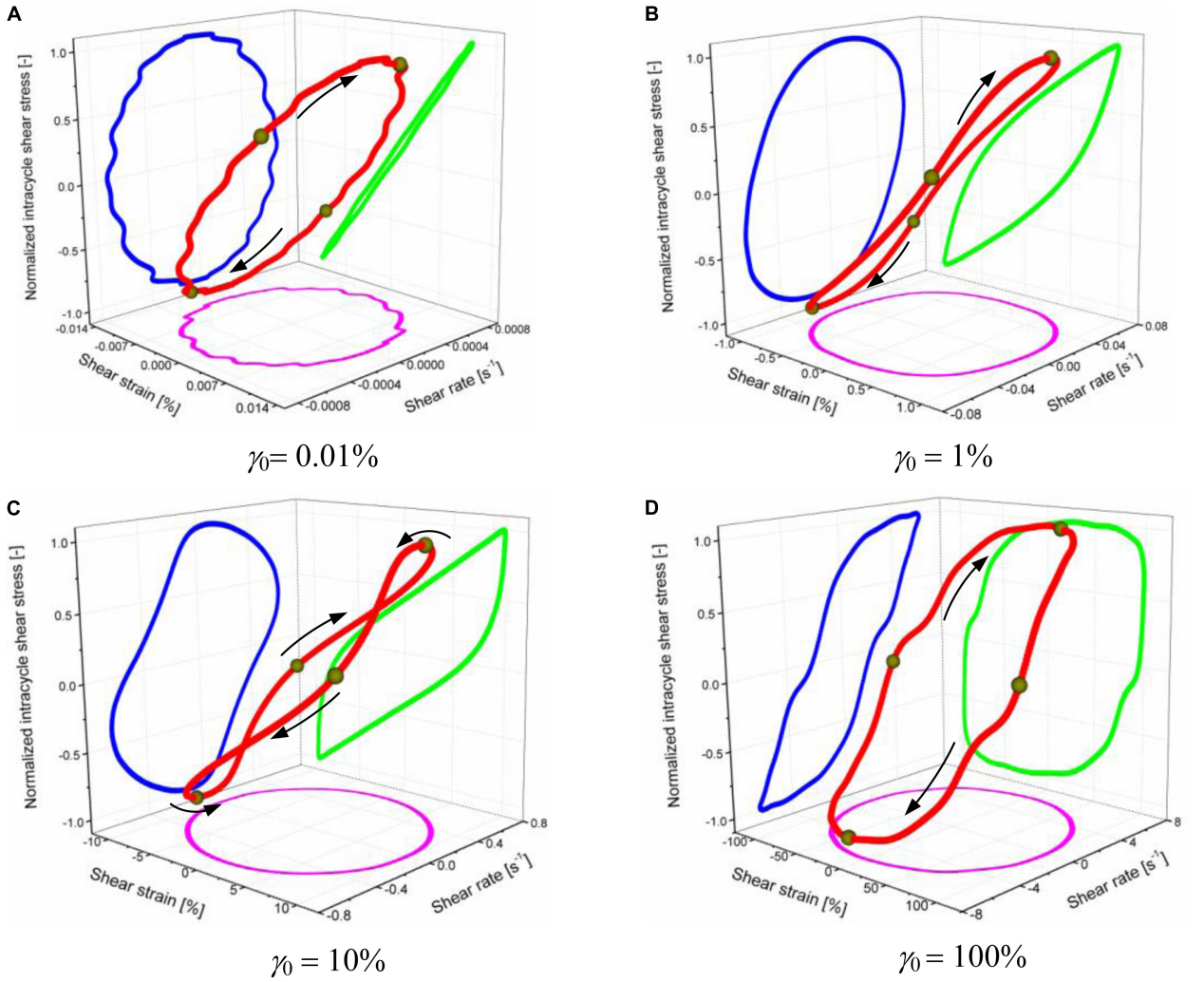

FIGURE 4 | Three-dimensional normalized intracycle stress response of MRG-70 under different shear strain amplitudes, i.e., **(A)** 0.01%, **(B)** 1%, **(C)** 10%, and **(D)** 100%. The frequency *f* was always kept at 1 Hz. The external magnetic field was set as 391 kA/m.

the frequency-dependent relaxation of the CIPs chain or cluster structures. On the other hand, from the decomposed elastic and viscous stress, as shown in **Figures 5–7**, at two frequencies, i.e., 0.1 and 1 Hz, the elastic non-linearity of MRG-70 under the magnetic fields of 0, 96, and 194 kA/m always showed strain stiffening. However, the viscous non-linearity contains two types, namely shear thickening and then shear thinning, as the magnetic field increases from 96 to 194 kA/m. This is different from MRG-70 that only exhibits viscous non-linearity of shear thickening under zero magnetic field.

Figure 8 depicts the elastic and viscous Lissajous curves under the application of the large magnetic field, i.e., 391 kA/m. In **Figure 8**, the LVE response, represented by the elliptical shape of the Lissajous curves, can be observed at sufficient small shear strain amplitude, i.e., 0.1%. When the shear strain increased from 0.1 to 100%, it was observed that the non-linear behavior of MRG-70 under the magnetic field of 391 kA/m was almost independent of the oscillatory frequency, and the typical overshoot behavior was disappeared, which is different from that under the small and medium magnetic fields, i.e., 96 and 194 kA/m, as shown in **Figures 6**, **7**. In the NLVE range, the non-linearity of MRG-70 with the magnetic field of 391 kA/m, shown in the elastic domain, was similar to that under the magnetic field of 194 kA/m, i.e., strain stiffening, and the viscous non-linearity of MRG-70 first presented an obvious shear thickening, followed by shear thinning. By comparing **Figures 5–8**, as the magnetic field increased from 0 to 391 kA/m, the decomposed elastic stress curve under 0.1% strain amplitude approaches coincided with the elastic Lissajous curves, and the slope of the corresponding decomposed viscous stress curve tended to be zero, and this feature was less affected by the frequency. Therefore, we can conclude that MRG-70 at the large magnetic field, i.e., 391 kA/m, under sufficient small strain amplitude almost exhibits purely elastic materials, which is attributed to the fact that the stronger chain or cluster structures are formed. Moreover, in the NLVE range with a large strain

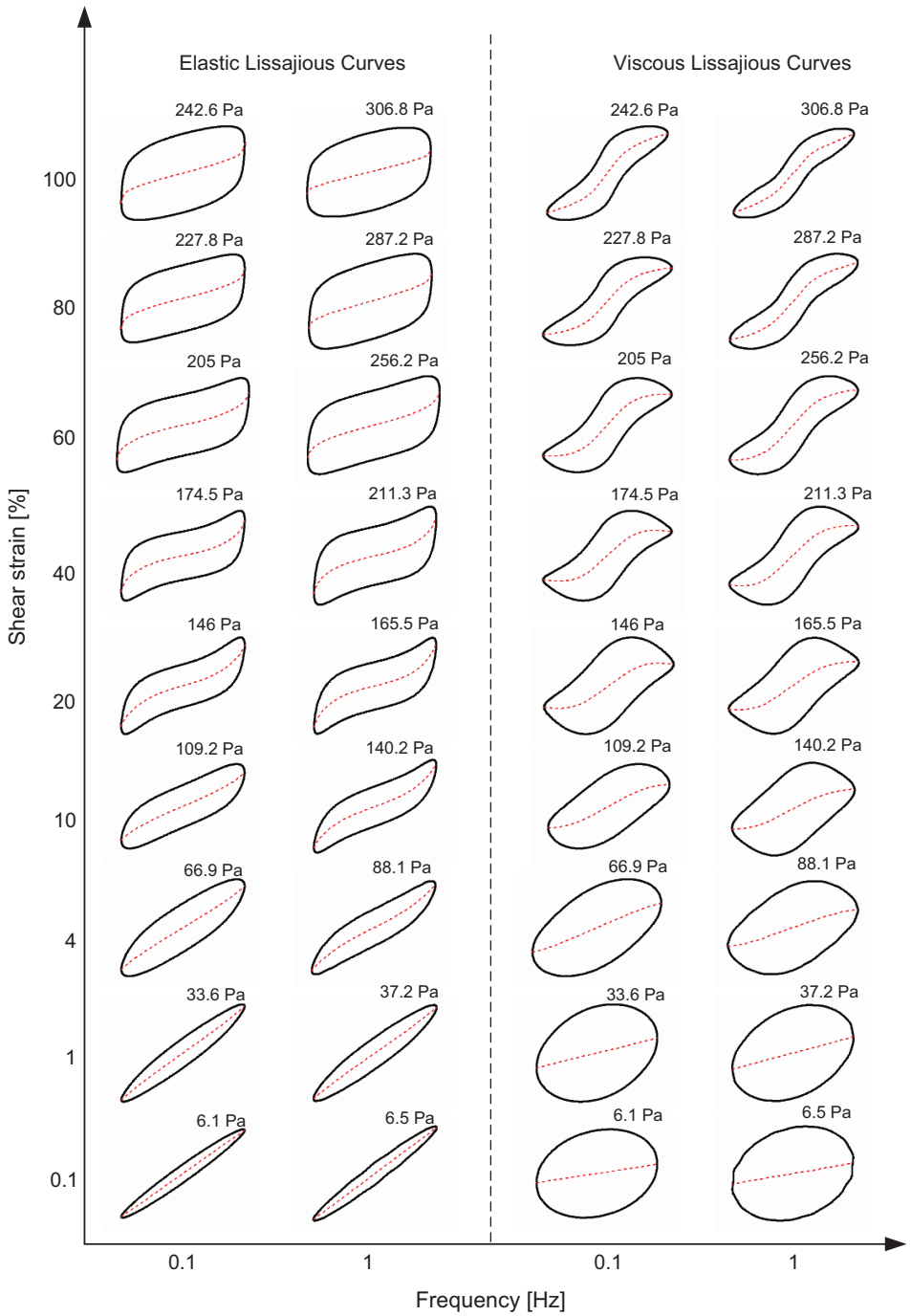

FIGURE 5 | Elastic and viscous Lissajous curves of MRG-70 generated from the strain-controlled oscillatory shear under the magnetic field of 0 kA/m. Each curve is positioned according to the imposed value of shear strain and frequency. The red dash line represents the corresponding decomposed elastic and viscous stress, respectively. The value above each curve is the maximum shear stress τ_{max}.

amplitude, as the increase of the magnetic field, the elastic curves of MRG-70 gradually formed a quadrilateral shape, indicating that the apparent flow-induced structure was dominated by viscosity. This was also validated by the decomposed elastic and viscous stress. Another interesting phenomenon that can be found from **Figures 6–8** is that, as the magnetic field increases, the decomposed elastic stress at the higher shear strain amplitude was zero during the instantaneous intracycle shear strain. For example, under the magnetic field of 391 kA/m at 100% strain amplitude, the decomposed elastic stress of MRG-70 would be zero during the instantaneous intracycle shear strain between − 45 and 45%. This implies that the contribution of

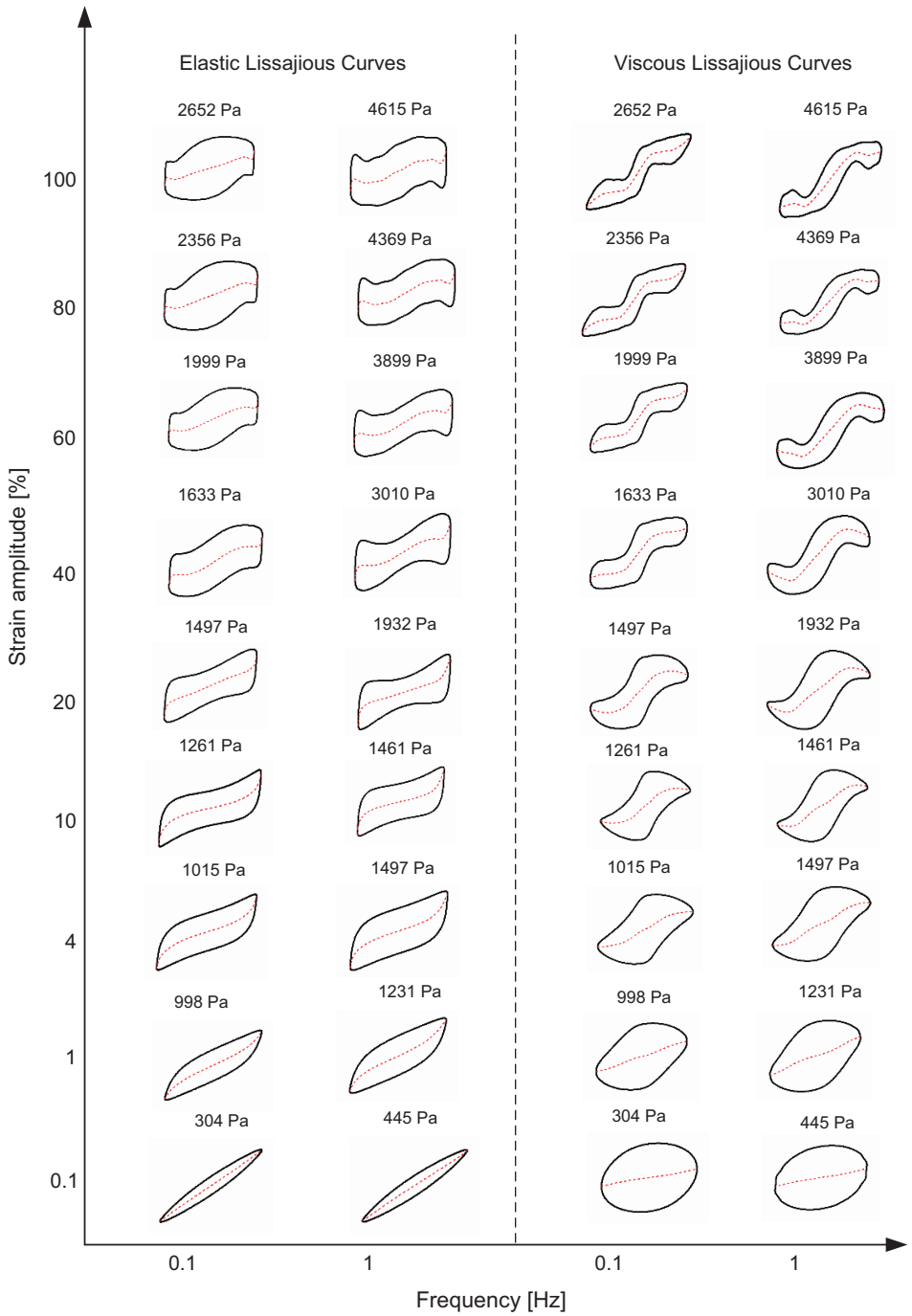

FIGURE 6 | Elastic and viscous Lissajous curves of MRG-70 generated from the strain-controlled oscillatory shear under the magnetic field of 96 kA/m. Each curve is positioned according to the imposed value of shear strain and frequency. The red dash line represents the corresponding decomposed elastic and viscous stress. The value above each curve is the maximum shear stress τ_{max}.

the intracycle elastic stress to the non-linearity within that range is almost zero. In summary, by comparing **Figures 5–8**, it can be concluded that the external magnetic field has a large impact on the non-linearity rheology of MRG-70, especially the viscous contribution to the non-linearity at large shear strain amplitude, and the effect of the oscillatory frequency on the non-linearity was also magnetic field-dependent. For instance, due to the formation of the stronger CIPs chain or cluster structures under the large magnetic field, i.e., 391 kA/m, MRG-70 exhibited purely elastic material behavior at sufficient small strain, e.g., 0.1%, but fluidlike structure was dominated by viscous dissipation at large shear strain, e.g., 100%.

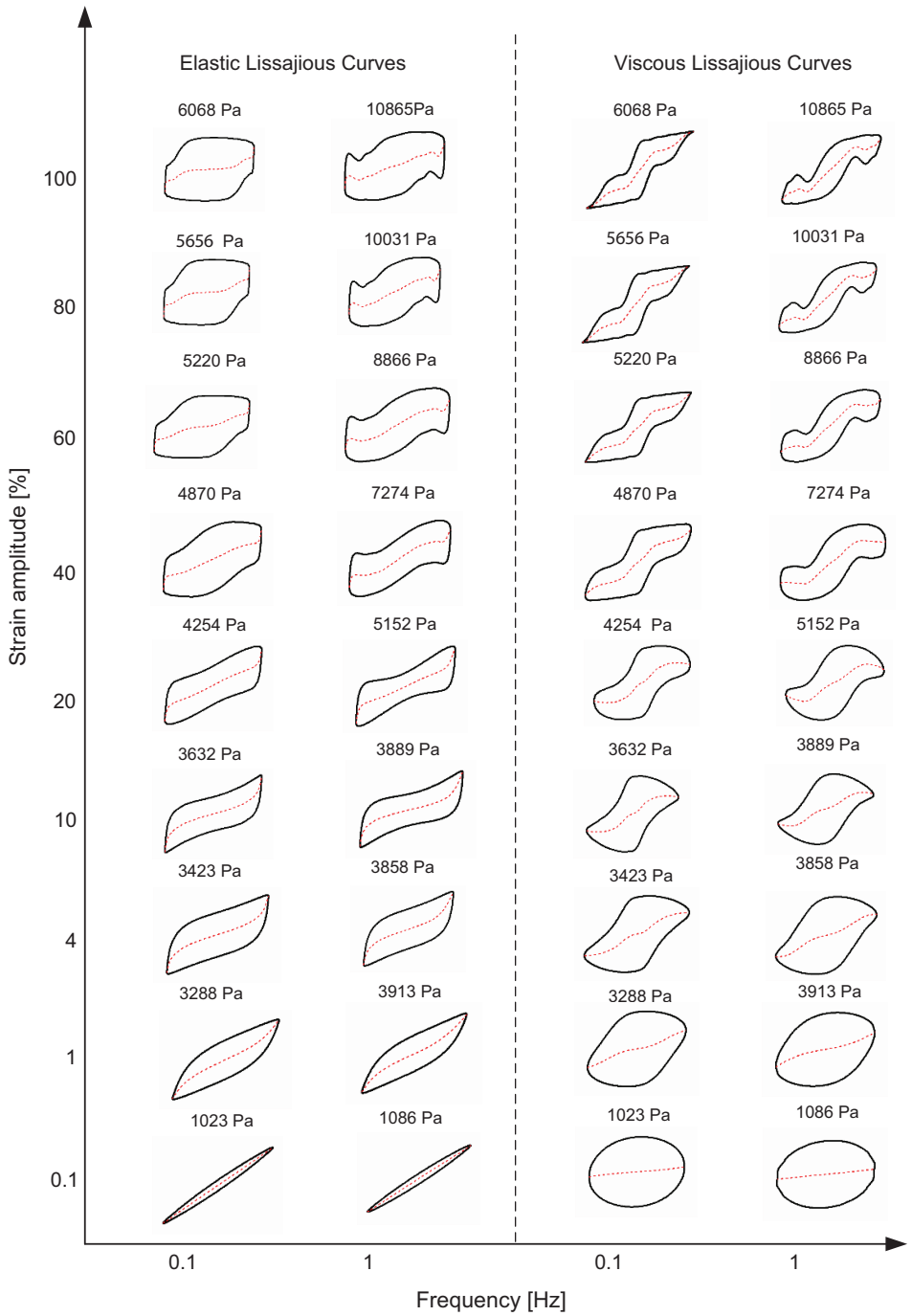

FIGURE 7 | Elastic and viscous Lissajous curves of MRG-70 generated from the strain-controlled oscillatory shear under the magnetic field of 194 kA/m. Each curve is positioned according to the imposed value of shear strain and frequency. The red dash line represents the corresponding decomposed elastic and viscous stress. The value above each curve is the maximum shear stress τ_{max}.

Elastic and Viscous Measures of MRG-70

The elastic and viscous measures, i.e., Chebyshev coefficients ratios, strain-stiffening, and shear-thickening ratios, corresponding to **Figures 5–8**, were used to quantitatively analyze the field-dependent non-linearities of MRG-70 at two different frequencies. In this study, we used the different orders of elastic (viscous) Chebyshev coefficients, i.e., e_1 (v_1), e_3 (v_3), e_5 (v_5), etc., to calculate the strain-stiffening (shear-thickening) ratios since they can better reconstruct the decomposed elastic (viscous) stress. **Figure 9** shows the elastic measures, i.e., third-order elastic Chebyshev coefficient, e_3/e_1, and strain-stiffening ratio, S, as a function of the shear strain amplitude under

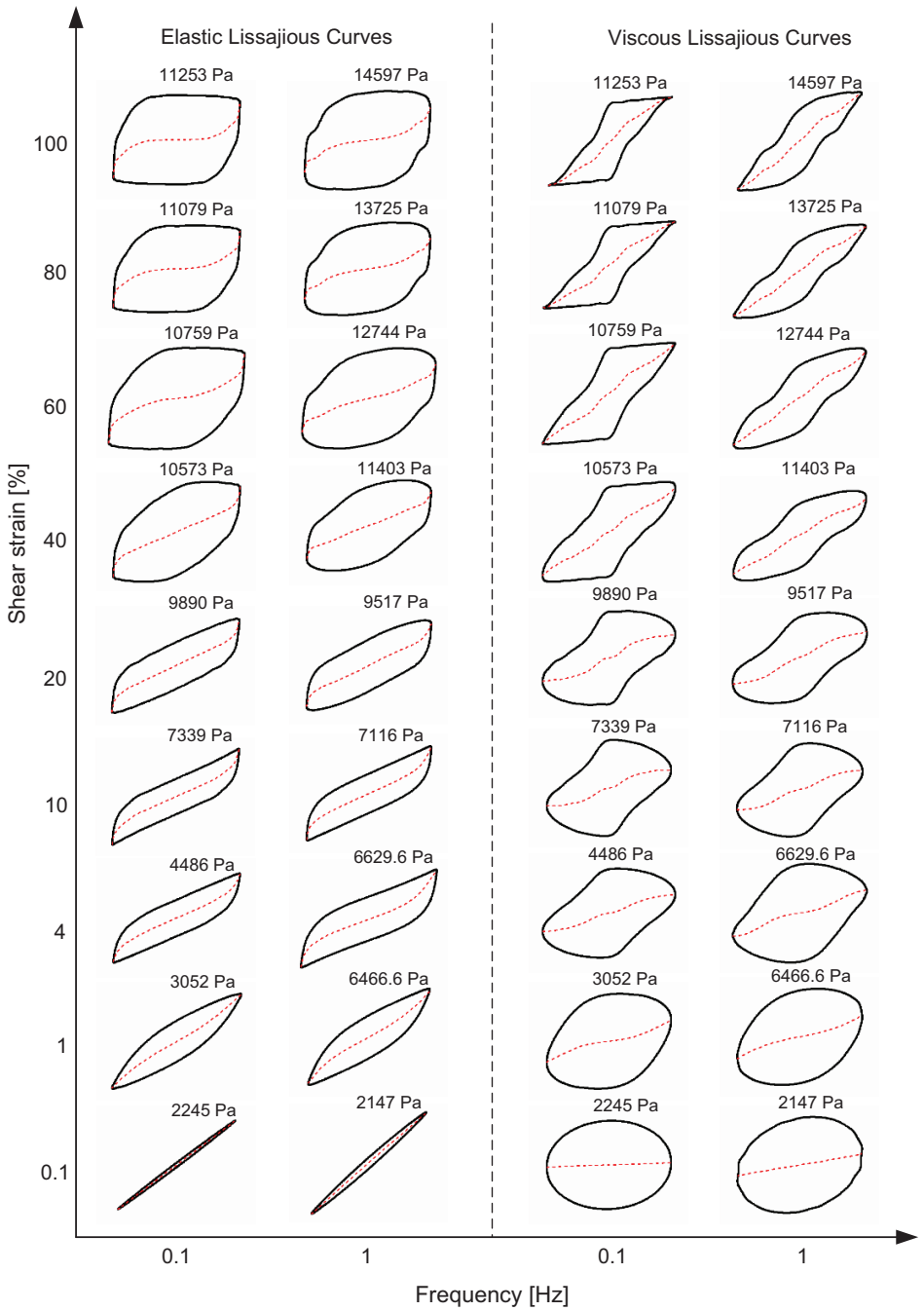

FIGURE 8 | Elastic and viscous Lissajous curves of MRG-70 generated from the strain-controlled oscillatory shear under the magnetic field of 391 kA/m. Each curve is positioned according to the imposed value of shear strain and frequency. The red dash line represents the corresponding decomposed elastic and viscous stress. The value above each curve is the maximum shear stress τ_{max}.

different oscillatory frequencies, i.e., 0.1 and 1 Hz, and magnetic fields, i.e., 0, 96, 194, and 391 kA/m. As mentioned in the "Introduction" section, S and e_3/e_1 have the same sign and can be used to interpolate the intracycle non-linearities of elastic, i.e., S and $e_3/e_1 > 0$ represent strain stiffening and S and $e_3/e_1 < 0$ represent strain softening (Ewoldt et al., 2008). From **Figure 9**, S and e_3/e_1 all tended to zero at low shear strain amplitude, i.e., 0.4, 0.06, 0.1, and 0.4% for 0, 96, 194, and 391 kA/m, indicating the LVE response. The critical shear strain obtained in this study was little different from that shown in **Figures 5–7**. The reason is that, for detecting the transition from linearity to non-linearity, higher-order Chebyshev coefficient were more accurate than the elastic and viscous Lissajous curves (Renou et al., 2010). After entering into the non-linear range, S and e_3/e_1 had the same

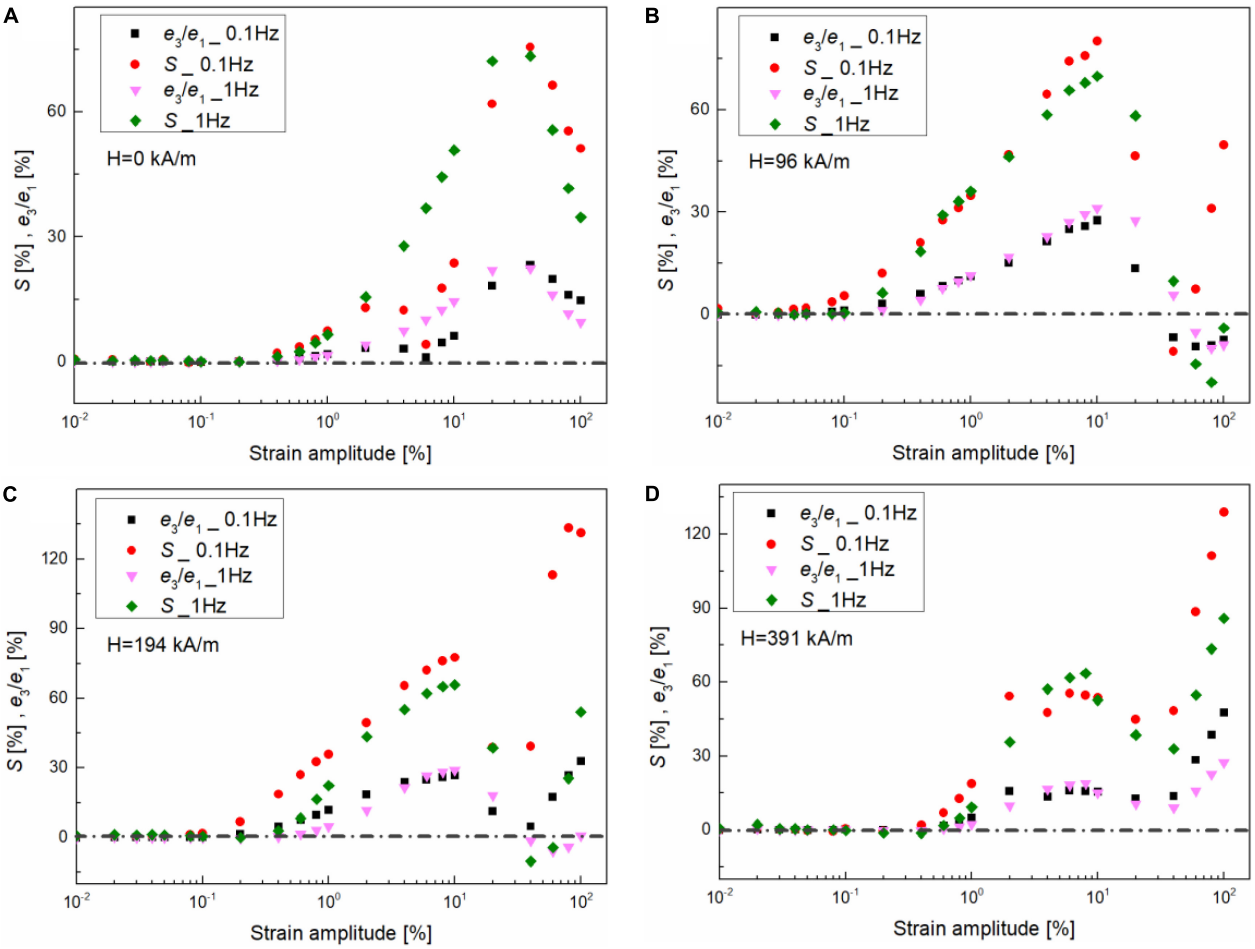

FIGURE 9 | Strain dependence of third-order elastic Chebyshev coefficient, i.e., e_3/e_1, and strain-stiffening ratio, S, for MRG-70 under different oscillatory frequencies, i.e., 0.1 and 1 Hz. The LAOS test was conducted on four different magnetic fields, such as **(A)** 0, **(B)** 96, **(C)** 194, and **(D)** 391 kA/m. The dashed lines indicate the value of zero.

trend and are positive at two different oscillatory frequencies under the magnetic fields of 0 and 391 kA/m, indicating the intracycle strain-stiffening behavior. However, under the small and medium magnetic fields, i.e., 96 and 194 kA/m, S or e_3/e_1 changes to be negative and shows the frequency dependency, suggesting the strain-softening behavior which is different from the results shown in **Figures 6**, **7**. The reason is that the decomposed elastic stress curves are interfered by the yield behavior. Moreover, from **Figures 9A–D**, the dependence of the elastic non-linearity on shear strain amplitude was less affected by the oscillatory frequency but had a close relationship with the external magnetic field. For example, S and e_3/e_1 almost exhibited the same trend with the strain amplitude at two different frequencies. However, under large shear strain amplitude (>40%), S and e_3/e_1 decreased with the shear strain at 0 kA/m but increased with the shear strain amplitude when the magnetic field was applied. This shows that the non-linear elastic contribution at large shear strain amplitude (>40%) was enhanced when the magnetic field was applied. The possible reason is that MRG-70 undergoes the interaction between the breaking and reorganization of the CIPs chain structures under the combination of oscillatory shear and magnetic field.

Figure 10 shows the shear strain amplitude-dependent viscous measures, i.e., third-order viscous Chebyshev coefficient, v_3/v_1, and shear-thickening ratio, T, at two different oscillatory frequencies, i.e., 0.1 and 1 Hz, and magnetic fields, i.e., 0, 96, 194, and 391 kA/m. Similarly, T and v_3/v_1 can be used to interpolate the intracycle non-linearities of viscous, i.e., T and $v_3/v_1 > 0$ representing shear thickening, and T and $v_3/v_1 < 0$ representing shear thinning (Ewoldt et al., 2008). From **Figures 10A–D**, T and v_3/v_1 fluctuate and suffer from more residual noise than the elastic measures within the linear regime at a large magnetic field, i.e., 0–0.07% for 391 kA/m. The reason is that the viscous contribution to the total stress response at this stage was too small, which is also verified in **Figure 8**. Moreover, when the magnetic field is not applied, an identical intracycle non-linear behavior, i.e., shear thinning, was observed throughout the non-linear regime, as indicated by the negative of T and v_3/v_1 (**Figure 10A**). However, when the magnetic field is applied (**Figures 10B–D**), MRG-70 exhibits two

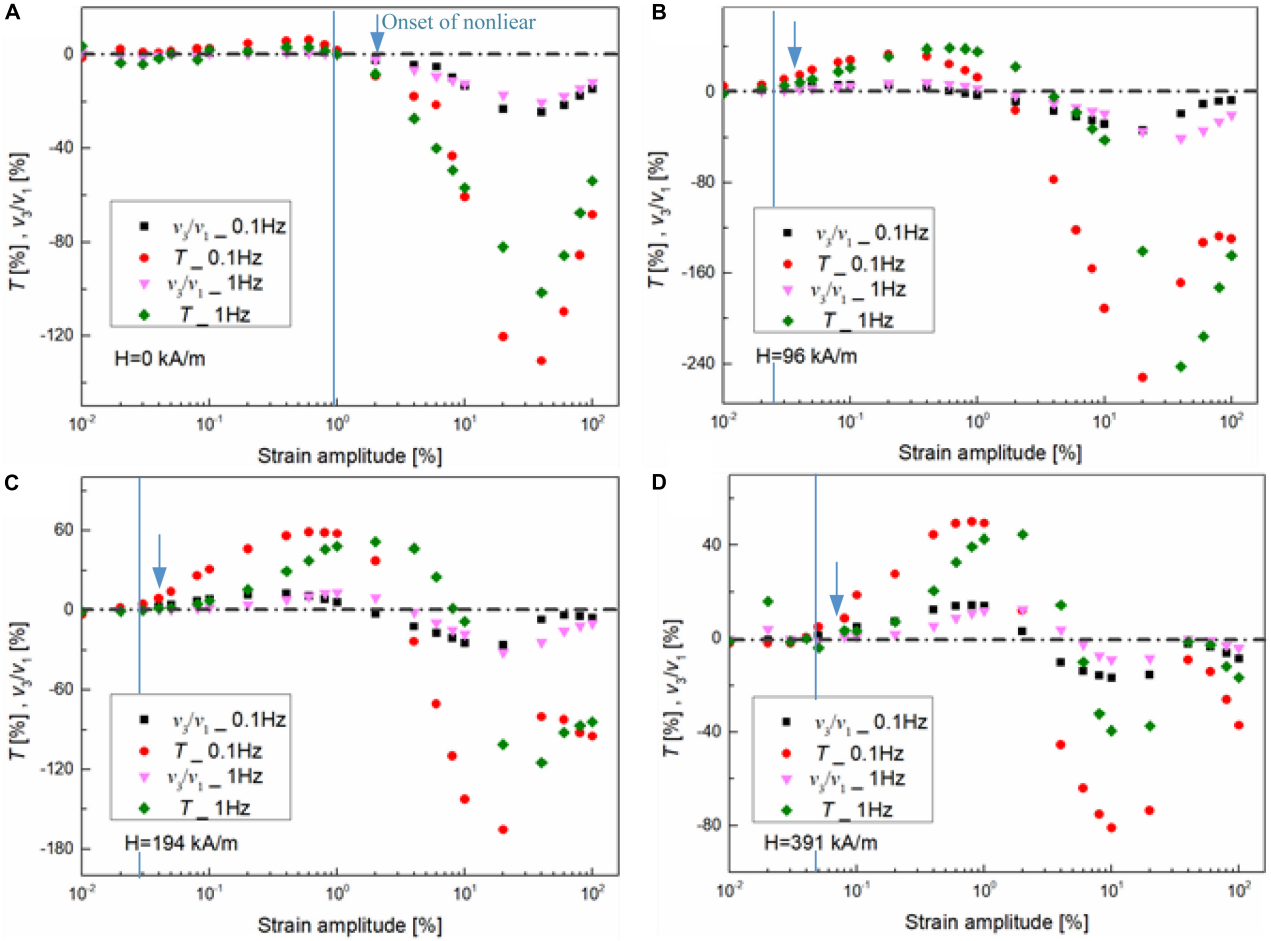

FIGURE 10 | Strain dependence of viscous Chebyshev coefficients ratios, i.e., v_3/v_1, and shear-thickening ratio, T, for MRG-70 under different oscillatory frequency, i.e., 0.1 and 1 Hz. The LAOS test was conducted on four different magnetic fields, such as **(A)** 0, **(B)** 96, **(C)** 194, and **(D)** 391 kA/m. The dashed lines indicate the value of zero. The blue solid line is the boundary between linear and non-linear viscoelastic regimes. The blue arrow indicates the appearance of non-linearity.

different viscous non-linear behaviors in the non-linear regime from 0.1 to 100%, i.e., shear thickening first, followed by shear thinning, which complies with the qualitative analysis shown in **Figures 6**, **7**. Moreover, the critical strain amplitude between shear thickening and shear thinning is frequency- and magnetic field-dependent. For instance, the critical strain amplitude under 0.1 Hz was always smaller than that of under 1 Hz for different magnetic fields, e.g., 15% for 0.1 Hz and 40% for 1 Hz under the magnetic field of 96 kA/m. Comparing **Figure 10** with **Figure 9**, we can conclude that the intracycle non-linearity of viscous seems to be more sensitive to the magnetic field in comparison with the non-linearity of elasticity.

To characterize the frequency-dependent composition of the non-linearity for MRG-70 under different oscillatory strain amplitudes and magnetic fields, the comparison between S and T as a function of strain amplitude is shown in **Figure 11**. It can be seen that, in the LVE range, the elastic and viscous contributions are equal to 0. Along with the increasing shear strain amplitude, the NLVE appeared. From **Figure 11A**, the appearance of the non-linearity without the magnetic field seems to be slightly affected by the magnetic field. However, under the application of the magnetic field shown in **Figures 10B–D**, the onset of the non-linearity is frequency-dependent, i.e., the appearance of the NLVE under 0.1 Hz is always fast than that of under 1 Hz. On the other hand, in the NVLE range, the non-linearity of MRG-70 under the magnetic field of 0 kA/m was portrayed as the combination of strain stiffening ($S > 0$) and shear thinning ($T < 0$) through the non-linear range. However, when the magnetic field is applied, MRG-70 shows a substantial variation with the non-linear strain amplitude. For example, at the magnetic field of 391 kA/m, as shown in **Figure 11D**, MRG-70 only showed shear thickening ($T > 0$) at the onset of the non-linearity, i.e., 0.04 to 0.4%. Then, in the shear range from 0.4 to 2%, the non-linearity consisted of strain stiffening ($S > 0$) and shear thickening ($T > 0$). Above 2% strain, the non-linearity showed the combination of strain stiffening ($S > 0$) and shear thinning ($T < 0$). Interestingly, the similar behavior was also observed for MRG-70 at the oscillatory frequency of 1 Hz (**Figures 11B–D**). Combining the study on the strain dependence storage and loss modulus shown in **Figure 2**, we found that, in

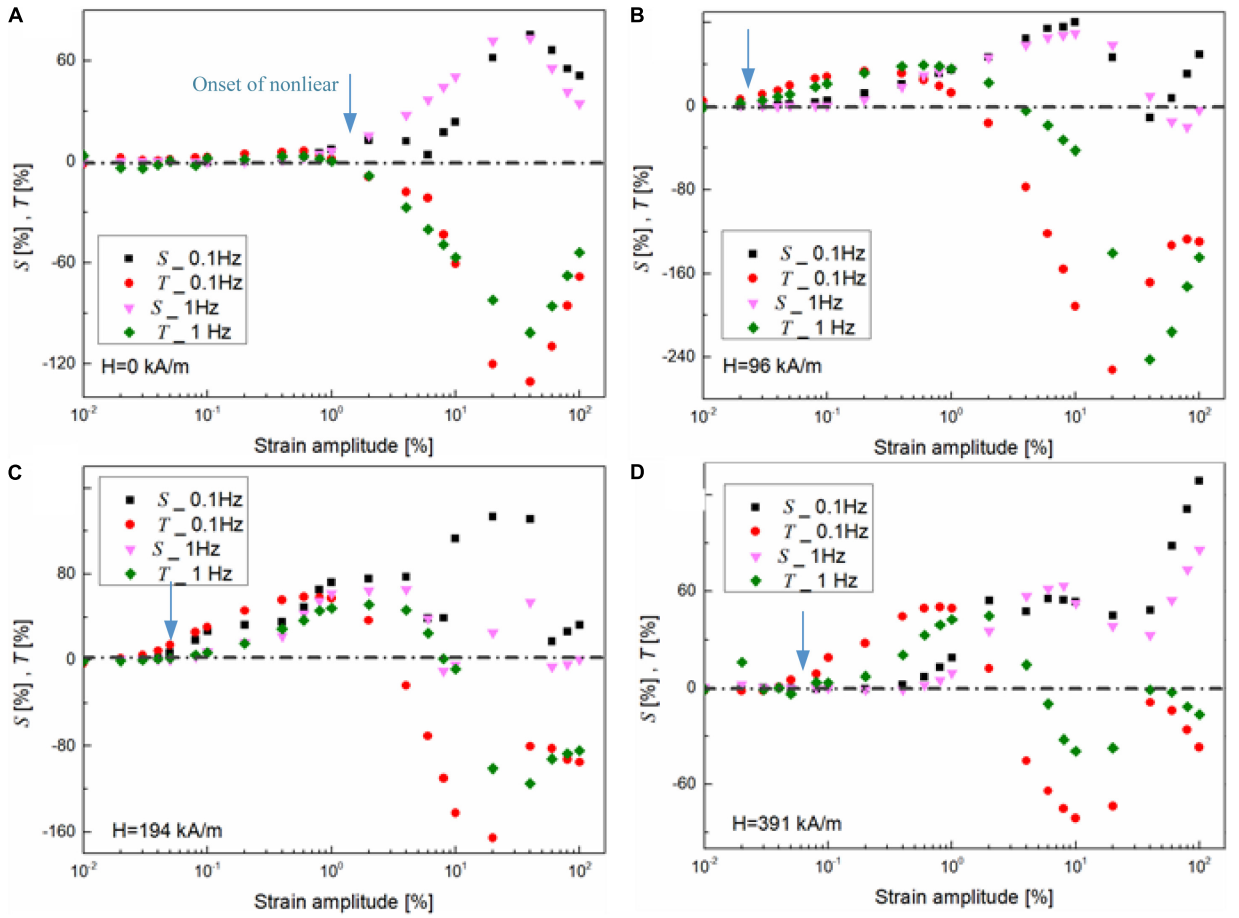

FIGURE 11 | Strain dependence of strain-stiffening ratio and shear-thickening ratio, i.e., *S* and *T*, for MRG-70 under different oscillatory frequencies, i.e., 0.1 and 1 Hz. The LAOS test was conducted on four different magnetic fields, such as **(A)** 0, **(B)** 96, **(C)** 194, and **(D)** 391 kA/m. The dashed lines indicate the value of zero. The blue arrow indicates the appearance of non-linearity.

the shear strain range of $S > 0$ and $T < 0$, e.g., about 4–100% under 96 kA/m, 8–100% under 194 kA/m, and 5–100% under 391 kA/m, the corresponding storage and loss moduli always decreased with the shear strain. This phenomenon indicates that, in the post-yield range, the non-linearity of MRG-70 with the magnetic field exhibited the strain stiffening for the elastic stress and predominant shear thinning of the energy dissipation. Finally, the above analysis points out that the non-linear rheology of MRG-70 had little relationship with the oscillatory frequency but was highly affected by the shear strain amplitude and external magnetic field, which is composed of different elastic and viscous intracycle physical mechanisms.

CONCLUSION

We studied the field-dependent non-linear rheology of MRG-70 under LAOS at different driving frequencies. First, the storage and loss moduli under the frequencies of 0.1, 0.5, 1, and 5 Hz were compared, and the results showed that, when the frequency rose from 0.1 to 5 Hz, MRG-70 mainly exhibits two viscoelastic characteristics, i.e., strain thinning in which *G*' and *G*" decrease in the NLVE range at 0.1 Hz, weak strain overshoot in which *G*' decreases but *G*" increases, followed by a decrease in the NLVE range at frequencies of 0.5, 1, and 5 Hz. Moreover, the viscoelastic behavior of MRG-70 under oscillatory shear can be divided into three parts: linear region, the onset of the non-linear region, and the post-yield region. Second, the 3D Lissajous curves and the decomposed elastic and viscous stress curves were presented and utilized to qualitatively analyze the field-dependent non-linear rheology of MRG-70 at two typical frequencies. It was found that, irrespective of the frequency, MRG-70 always has elasticity during the oscillatory shear at the sufficient small strain amplitude. When the strain amplitude increased to a large value, the elastic Lissajous curves presented with the shape of quadrilateral, and the maximum stress in viscous Lissajous curves was located at the maximum shear strain of $\pm \gamma_0\omega$, indicating that the non-linearity of MRG-70 at 100% mainly comes from viscous flow, and the above behavior has highly dependent on the external magnetic field. Finally, the elastic and viscous measures, i.e., Chebyshev coefficient ratios (e_3/e_1 and v_3/v_1), strain-stiffening ratio (S), and shear-thickening ratio (T),

were used to conduct the quantitative analysis to characterize the non-linear rheology of MRG-70. It was demonstrated that the onset of the non-linear behavior of MR grease was frequency-dependent when the magnetic field was applied. However, in the post-yield region, the field-dependent non-linear rheology of MRG-70 had little relationship with the oscillatory frequency but was highly affected by the shear strain amplitude.

DATA AVAILABILITY STATEMENT

The original contributions presented in the study are included in the article/supplementary material, further inquiries can be directed to the corresponding author/s.

AUTHOR CONTRIBUTIONS

HW: formal analysis, investigation, methodology, writing—original draft. GZ, TC, and SL: resources. YL and JW: supervision. JW: writing—review and editing. All authors contributed to the article and approved the submitted version.

FUNDING

This work has been supported by the National Natural Science Foundation of China (NSFC) grant funded by the Chinese government (Nos. 51675280, 51705467, and 51805209). It has also been supported by the Postgraduate Scientific Innovation Research Foundation of Jiangsu Province (No. KYCX18_0391).

ACKNOWLEDGMENTS

We would like to thank the financial support obtained from China Scholarship Council (CSC) in the exchange program at the University of Technology Sydney, Australia.

REFERENCES

Agirre-Olabide, I., Berasategui, J., Elejabarrieta, M. J., and Bou-Ali, M. M. (2014). Characterization of the linear viscoelastic region of magnetorheological elastomers. *J. Intellig. Mater. Syst. Struct.* 25, 2074–2081. doi: 10.1177/1045389x13517310

Cho, K. S., Hyun, K., Ahn, K. H., and Lee, S. J. (2005). A geometrical interpretation of large amplitude oscillatory shear response. *J. Rheol.* 49, 747–758. doi: 10.1122/1.1895801

Delgado, M., Valencia, C., Sánchez, M., Franco, J., and Gallegos, C. (2006). Influence of soap concentration and oil viscosity on the rheology and microstructure of lubricating greases. *Indust. Eng. Chem. Res.* 45, 1902–1910. doi: 10.1021/ie050826f

Ewoldt, R. H., Hosoi, A., and McKinley, G. H. (2008). New measures for characterizing nonlinear viscoelasticity in large amplitude oscillatory shear. *J. Rheol.* 52, 1427–1458. doi: 10.1122/1.2970095

Ghosh, A., Chaudhary, G., Kang, J. G., Braun, P. V., Ewoldt, R. H., and Schweizer, K. S. (2019). Linear and nonlinear rheology and structural relaxation in dense glassy and jammed soft repulsive pNIPAM microgel suspensions. *Soft Matter.* 15, 1038–1052. doi: 10.1039/c8sm02014k

Goudoulas, T. B., and Germann, N. (2019a). Nonlinear rheological behavior of gelatin gels: in situ gels and individual gel layers filled with hard particles. *J. Coll. Interf. Sci.* 556, 1–11. doi: 10.1016/j.jcis.2019.08.025

Goudoulas, T. B., and Germann, N. (2019b). Nonlinear rheological behavior of gelatin gels: in situ gels and individual layers. *J. Coll. Interf. Sci.* 553, 746–757. doi: 10.1016/j.jcis.2019.06.060

Hyun, K., Wilhelm, M., Klein, C. O., Cho, K. S., Nam, J. G., Ahn, K. H., et al. (2011). A review of nonlinear oscillatory shear tests: analysis and application of large amplitude oscillatory shear (LAOS). *Prog. Poly. Sci.* 36, 1697–1753. doi: 10.1016/j.progpolymsci.2011.02.002

Kavlicoglu, B. M., Gordaninejad, F., and Wang, X. (2015). Study of a magnetorheological grease clutch. *Smart Mater. Struct.* 22:125030. doi: 10.1088/0964-1726/22/12/125030

Li, S., Tian, T., Wang, H., Li, Y., Li, J., Zhou, Y., et al. (2020). Development of a four-parameter phenomenological model for the nonlinear viscoelastic behaviour of magnetorheological gels. *Mater. Design* 194:108935. doi: 10.1016/j.matdes.2020.108935

Mohamad, N., Mazlan, S. A., Choi, S.-B., Aziz, A., Aishah, S., and Sugimoto, M. (2019a). The effect of particle shapes on the field-dependent rheological properties of magnetorheological greases. *Intern. J. Mol. Sci.* 20:1525. doi: 10.3390/ijms20071525

Mohamad, N., Mazlan, S. A., Ubaidillah, Choi, S.-B., Imaduddin, F., and Abdul Aziz, S. A. (2019b). The field-dependent viscoelastic and transient responses of plate-like carbonyl iron particle based magnetorheological greases. *J. Intellig. Mater. Syst. Struct.* 30, 788–797. doi: 10.1177/1045389x19828504

Mohamad, N., Mazlan, S. A., Ubaidillah, S.-B., Choi, M., and Nordin, F. M. (2016). The field-dependent rheological properties of magnetorheological grease based on carbonyl-iron-particles. *Smart Mater. Struct.* 25:095043. doi: 10.1088/0964-1726/25/9/095043

Mohamad, N., Ubaidillah, S., Imaduddin, F., Choi, S.-B., and Yazid, I. (2018). A comparative work on the magnetic field-dependent properties of plate-like and spherical iron particle-based magnetorheological grease. *PLoS One* 13:e0191795. doi: 10.1371/journal.pone.0191795

Park, B. O., Park, B. J., Hato, M. J., and Choi, H. J. (2011). Soft magnetic carbonyl iron microsphere dispersed in grease and its rheological characteristics under magnetic field. *Colloid Polym. Sci.* 289, 381–386. doi: 10.1007/s00396-010-2363-y

Rankin, P. J., Horvath, A. T., and Klingenberg, D. J. (1999). Magnetorheology in viscoplastic media. *Rheol. Acta* 38, 471–477. doi: 10.1007/s003970050198

Renou, F., Stellbrink, J., and Petekidis, G. (2010). Yielding processes in a colloidal glass of soft star-like micelles under large amplitude oscillatory shear (LAOS). *J. Rheol.* 54, 1219–1242. doi: 10.1122/1.3483610

Sahin, H., Gordaninejad, F., Wang, X., and Fuchs, A. (2007). "Rheological behavior of magneto-rheological grease (MRG)," in *Proceedings of the Active & Passive Smart Structures & Integrated Systems*, San Diego, CA.

Sakurai, T., and Morishita, S. (2017). Seismic response reduction of a three-story building by an MR grease damper. *Front. Mechan. Eng.* 12, 224–233. doi: 10.1007/s11465-017-0413-6

Sarkar, C., Hirani, H., and Sasane, A. (2015). Magnetorheological smart automotive engine mount. *Intern. J. Curr. Eng. Technol.* 5, 419–428.

Shiraishi, T., Miida, Y., Sugiyama, S., and Morishita, S. (2011). Typical characteristics of magnetorheological grease and its application to a controllable damper. *Mechan. Eng. J.* 77, 2193–2200. doi: 10.1299/kikaic.77.2193

Sukhwani, V. K., and Hirani, H. (2008). A comparative study of magnetorheological-fluid-brake and magnetorheological-grease-brake. *Tribology* 3, 31–35. doi: 10.2474/trol.3.31

Upadhyay, R., Laherisheth, Z., and Shah, K. (2013). Rheological properties of soft magnetic flake shaped iron particle based magnetorheological fluid in dynamic mode. *Smart Mater. Struct.* 23:015002. doi: 10.1088/0964-1726/23/1/015002

Wang, H., Chang, T., Li, Y., Li, S., Zhang, G., Wang, J., et al. (2020). Characterization of nonlinear viscoelasticity of magnetorheological grease under large oscillatory shear by using Fourier transform-Chebyshev analysis. *J. Intellig. Mater. Syst. Struct.* 32, 614–631.

Wang, H., Li, Y., Zhang, G., and Wang, J. (2019a). Effect of temperature on rheological properties of lithium-based magnetorheological grease. *Smart Mater. Struct.* 28:e035002-13.

Wang, H., Zhang, G., and Wang, J. (2019b). Normal force of lithium-based magnetorheological grease under quasi-static shear with large deformation. *RSC Adv.* 9, 27167–27175. doi: 10.1039/c9ra04987h

Wang, H., Zhang, G., and Wang, J. (2019c). Quasi-static rheological properties of lithium-based magnetorheological grease under large deformation. *Materials* 12:2431. doi: 10.3390/ma12152431

Wilhelm, M. (2002). Fourier-transform rheology. *Macromolecul. Mater. Eng.* 287, 83–105.

Wilhelm, M., Reinheimer, P., Ortseifer, M., Neidhöfer, T., and Spiess, H.-W. (2000). The crossover between linear and non-linear mechanical behaviour in polymer solutions as detected by Fourier-transform rheology. *Rheol. Acta* 39, 241–246. doi: 10.1007/s003970000084

Zhang, G., Li, Y., Wang, H., and Wang, J. (2019). Rheological properties of polyurethane-based magnetorheological gels. *Front. Mater.* 6:56. doi: 10.3389/fmats.2019.00056

Zhang, G., Li, Y., Yu, Y., Wang, H., and Wang, J. (2020). Modeling the nonlinear rheological behavior of magnetorheological gel using a computationally efficient model. *Smart Mater. Struct.* 29: aba809.

Conflict of Interest: The authors declare that the research was conducted in the absence of any commercial or financial relationships that could be construed as a potential conflict of interest.

frontiers in Materials

ORIGINAL RESEARCH
published: 20 April 2021
doi: 10.3389/fmats.2021.667685

Enhanced Magnetorheological Performance of Carbonyl Iron Suspension Added With Barium Ferrite Nanoparticle

Hyo Seon Jang[1], *Qi Lu*[1,2] *and Hyoung Jin Choi*[1,2]*

[1] *Department of Polymer Science and Engineering, Inha University, Incheon, South Korea,* [2] *Program of Environmental and Polymer Engineering, Inha University, Incheon, South Korea*

Hard-magnetic barium ferrite (BF) nanoparticles with a hexagonal plate-like structure were used as an additive to a carbonyl iron (CI) microparticle-based magnetorheological (MR) fluid. The morphology of the pristine CI and CI/BF mixture particles was examined by scanning electron microscopy. The saturation magnetization and coercivity values of each particle were measured in the powder state by vibrating sample magnetometry. The MR characteristics of the CI/BF MR fluid measured using a rotation rheometer under a range of magnetic field strengths were compared with those of the CI-based MR fluid. The flow behavior of both MR fluids was fitted using a Herschel–Bulkley model, and their stress relaxation phenomenon was examined using the Schwarzl equation. The MR fluid with the BF additive showed higher dynamic and elastic yield stresses than the MR fluid without the BF additive as the magnetic field strength increased. Furthermore, the BF nanoparticles embedded in the space between the CI microparticles improved the dispersion stability and the MR performance of the MR fluid.

Keywords: carbonyl iron, barium ferrite, magnetorheological, additive, sedimentation

OPEN ACCESS

Edited by:
Jinbo Wu,
Shanghai University, China

Reviewed by:
Yancheng Li,
University of Technology Sydney, Australia
Xuan Shouhu,
University of Science and Technology of China, China

***Correspondence:**
Hyoung Jin Choi
hjchoi@inha.ac.kr

Specialty section:
This article was submitted to Smart Materials, a section of the journal Frontiers in Materials

Received: *14 February 2021*
Accepted: *19 March 2021*
Published: *20 April 2021*

Citation:
Jang HS, Lu Q and Choi HJ (2021) Enhanced Magnetorheological Performance of Carbonyl Iron Suspension Added With Barium Ferrite Nanoparticle. Front. Mater. 8:667685. doi: 10.3389/fmats.2021.667685

INTRODUCTION

Magnetorheological (MR) fluids consisting of soft-magnetic particles suspended in a medium liquid, including silicone oil and mineral oil, are field-responsive functional materials that can be finely controlled from the liquid-like state to a solid-like phase under an applied magnetic field strength (H) (Svåsand et al., 2009; Sedlačík et al., 2010; Susan-Resiga et al., 2010; Qiao et al., 2012; Ashtiani et al., 2015). Without H, the particles in an MR fluid are dispersed randomly in the MR suspension, following a Newtonian fluid-like behavior at their low-particle volume concentrations. Under an applied H, the field-induced magnetic polarization interactions of the magnetic particles result in the formation of a chain-like form in the parallel direction of the applied H within several tens of milliseconds (Vasiliev et al., 2016). During this rapid and reversible phase transition, the chain structures in the MR fluid undergo breaking and reformation processes, resulting in changes in their viscoelastic characteristics, including shear stress, shear viscosity, and dynamic moduli under an applied magnetic field (Li et al., 2000, 2004; Ahamed et al., 2016). This technology has been introduced to industrial sections, such as damping devices, engine mounts, and MR polishing machines (Choi et al., 2003; Yang et al., 2010; Mao et al., 2014).

Soft-magnetic particles are widely adopted as the dispersed part of the MR fluids, owing to their negligible magnetic hysteresis and supreme magnetization value of saturation (Kordonskii et al., 1999). Among their family, carbonyl iron (CI) microparticles have attracted considerable attention as disperse particles owing to their large magnetic permeability, low coercivity, spherical shape, and appropriate micron size (Bombard et al., 2005). Despite these advantages, the high density of CI microparticles can lead to problems, such as sedimentation and abrasion, which are of concern with long-term industrial applications.

Several techniques have been introduced to overcome these problems, including coating the surface of magnetic microspheres with polymeric or inorganic materials and adding various additives, such as organic clay and inorganic nanoparticles (Vicente et al., 2003; Fang and Choi, 2008; López-López et al., 2008; Aruna et al., 2019). On the other hand, the process of applying a polymeric coating of CI microparticles to decrease the difference in density between the CI microspheres and the non-magnetic fluid is too difficult and complex for industrial application. This is because the coating process is strongly influenced by various factors, such as the reaction temperature, time, and the molar ratio between monomer and initiator. Therefore, the addition of additives to CI-based MR suspensions is rather simple and reliable (Jang et al., 2005; Liu et al., 2015; Han et al., 2019; Aruna et al., 2020; Maurya and Sarkar, 2020).

Various additives, such as organic clays, carbon nanotubes, celluloses, and inorganic particles, have been introduced in MR fluid systems to enhance the sedimentation stability of magnetic particles composed predominantly of MR fluids (Machovsky et al., 2014; Bae et al., 2017; Bossis et al., 2019; Gopinath et al., 2021). On the other hand, non-magnetic additives tend to reduce the MR effect, even though they can solve the sedimentation problem. Thus, the addition of magnetic materials as an additive is an efficient method to increase the sedimentation stability and MR effect of suspensions (Hajalilou et al., 2016; Zhang et al., 2020). Ngatu and Wereley (2007) added iron nanowires of diameter ranging from 5 to 250 nm to the MR fluid to improve the MR effect and the dispersion stability. Han et al. (2020) used hollow-Fe_3O_4 particles fabricated using a solvothermal process as an additive to reduce the sedimentation problem and enhance MR properties of CI-based MR fluid. Recently, Jang et al. (2015) and Kim et al. (2017) added hard-magnetic particles, such as γ-Fe_2O_3 and CrO_2, respectively, to CI-based MR fluids and reported improvement in both the MR behavior and suspension stability.

Barium ferrite ($BaFe_{12}O_{19}$) (BF) with a non-circular plate-like structure and the perpendicular magnetic moment has attracted considerable interest as a high-performance permanent magnet because of its high magnetocrystalline anisotropy, high Curie point, relatively high magnetic saturation (*Ms*) value and coercive force, and superior chemical stability and corrosion resistance (Choi et al., 2000; Wei et al., 2020). Furthermore, non-circular hexagonal plate-like particles have a slower sedimentation rate than spherical or rod-like particles, such as γ-Fe_2O_3 and CrO_2. These hard magnetic particles that have a special shape could increase the Ms value of the CI particles, which is related directly to improving the MR efficiency of MR suspensions. In addition, hard magnetic particles are better able to adhere to the surface of CI particles as an additive, thus increasing the strength of the chain and the tendency to reform broken chain structures during operation. Therefore, BF particles were newly introduced as an additive, and their sedimentation stability was expected to be superior to previously reported additives.

This study examined the sedimentation stability and MR performance of MR suspensions by adding nano-sized BF particles as an additive between micron-sized CI particles. CI-based MR fluids were fabricated using silicone oil, and the BF additive was added to examine the effect of the additive. Their MR behaviors were measured using a rotation rheometer, and the sedimentation stability was recorded using a Turbiscan (MA2000, Formulaction, Toulouse, France).

EXPERIMENTAL

Materials

The CI [Badische Anilin-und-Soda-Fabrik (BASF), standard CM grade, particle density: 7.90 g/cc, diameter: about 4 μm, Germany] microspheres with their *Ms* of 209.5 emu/g and silicone oil (Shin-Etsu Chemical Co., Ltd., KF-96, viscosity: 100 cSt, Japan) were used as a dispersed and a continuous part of the MR fluids, respectively. The hard-magnetic BF (density: 5.28 g/cm^3, Toda Co., Tokyo, Japan) particle was introduced as an additive material. The physical properties of the BF are well-reported with its diameter of 0.13 μm and the aspect ratio of 0.1, corresponding to its thickness of 0.013 μm (Kwon et al., 1997; Choi et al., 2000).

Sample Preparation

Barium ferrite nanoparticles, used as an additive, were prepared by sonication for 1 h and dried. Three different MR fluids were prepared. The CI microparticle-based MR fluid without the additive was made by suspending 50 wt% of CI microspheres in silicone oil (50 wt%). To examine the additive effect, a 0.5 wt% concentration of BF particles with *Ms* of 63.8 emu/g was mixed in silicone oil (49.5 wt%), and CI microparticles (50 wt%) were then added. Furthermore, the pure BF nanoparticle-based MR fluid (50 wt%) was also prepared for comparison. The MR fluid with the additive is called a CI/BF-based MR fluid. A vortex (IKA, Korea. Ltd., GENIUS3) and sonicator (HWASHIN CO., Ltd., Powersonic 410) were used to disperse the magnetic particles uniformly during sample preparation.

Characterization

The surface morphologies of the CI, BF, and CI/BF systems were observed using a high-resolution scanning electron microscopy (HR-SEM, SU-8010, Hitachi, Tokyo, Japan). The dispersion stability of the MR fluids was investigated using a Turbiscan (MA2000, Formulaction, Toulouse, France), and the static magnetic characteristics of the magnetic particles were examined by making them in a powder form through a vibrating sample magnetometer (VSM) (7307, Lakeshore, LA, USA). The particle densities were measured using a gas pycnometer (AccuPyc

1330, Micromeritics, Norcross, GA, USA). Their MR properties were examined using a rotation rheometer (MCR 302, Anton-Paar, Graz, Austria) attached to a device for applying the magnetic field.

RESULTS AND DISCUSSION

Figures 1a–c present SEM images of pristine CI, BF, and their mixtures, respectively. **Figure 1a** shows the pristine CI with a spherical shape and a smooth surface. The mean diameter of the pure CI particle was ∼3 μm. As shown in **Figure 1b**, $BaFe_{12}O_{19}$ had a hexagonal plate-like structure with a mean size of 700 nm. **Figure 1c** exhibited a mixture of pure CI particles and a small amount of $BaFe_{12}O_{19}$ particles. Hexagonal plate-like $BaFe_{12}O_{19}$ particles were attached to the space between pure CI particles. Their hard-magnetic properties, nano size, and unique structure were expected to enhance the MR efficiency and suspension stability by occupying the space between the CI microspheres.

The static magnetic characteristics of the pristine CI, BF, and CI/ BF mixture particles were measured in the powder form *via* VSM, with an applied H from −15 to 15 kOe at room temperature. **Figure 2** shows the magnetic moment as a function of H, in which the measured M_s and coercivity (H_c) of the BF particles were 63.8 emu/g and 1.74 kOe, respectively (Ko et al., 2009). When the 0.5 wt.% of BF particles were added to pure CI, the M_s value of the CI/BF mixture particles appeared to be slightly increased. Overall, BF particles, which exhibit hard-magnetic properties with magnetic hysteresis, could improve the MR performance in the magnetic response of a CI microparticle-based MR fluid, as shown in **Figure 2** (Moon et al., 2016).

Two types of MR fluids were used to measure the MR property. One contained 50 wt.% pure CI microparticles dispersed in 100 cS of silicone oil, and the other contained 0.5 wt.% $BaFe_{12}O_{19}$ particles added at the same ratio as the CI microparticles in the same silicone oil. The measurements were taken using a parallel-plate rotation rheometer under a controlled shear rate mode. For each test, a certain amount of MR suspensions was dropped in the gap of the parallel-plate geometry device and the base plate.

The flow tests were carried out at shear rates in the range of 0.1 to 200 s^{-1} under an applied H of 0 to 343 kA/m. **Figure 3** shows the shear stress τ (a, c) and shear viscosity (b, d) data as a function of the shear rate ($\dot{\gamma}$) under various H for all of the three MR fluids, in which the closed and open symbols refer to an MR fluid without and with BF additive, respectively. According to **Figures 3A,C**, τ of the three MR suspensions increased linearly with increasing shear rate without an applied H, indicating that three MR fluids exhibited Newtonian fluid-like characteristics. On the other hand, the non-Newtonian fluid property of non-linearity between τ and $\dot{\gamma}$, when exposed to external H, was prominent in the three MR samples. This is because the chain-like structure of the magnetized particles was built up by strong magnetic dipole–dipole (D–D) interactions (Zhang and Widom, 1995). In particular, at each H, a CI-based MR fluid containing the BF additive showed higher τ values than those without BF nanoparticles over the entire shear rate range. By applying H,

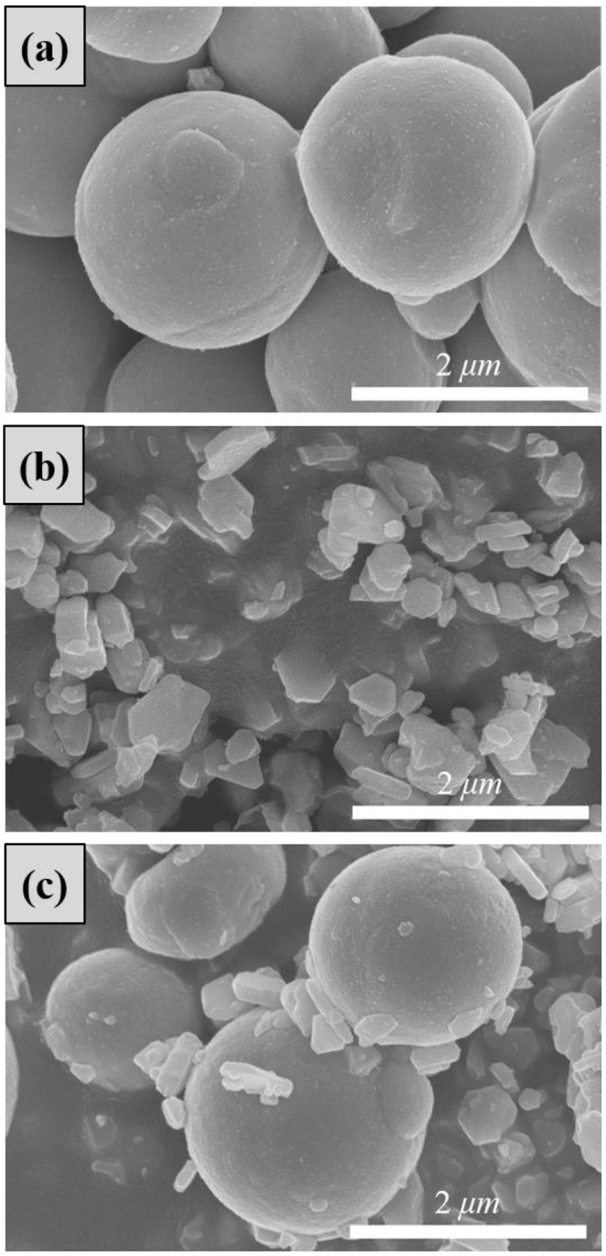

FIGURE 1 | Scanning electron microscopy images of **(a)** pure carbonyl iron (CI) microparticles, **(b)** $BaFe_{12}O_{19}$ nanoparticles, and **(c)** CI/ $BaFe_{12}O_{19}$ mixture.

hexagonal plate-like structured BF particles, which were relatively smaller than CI microparticles, filled the space between the CI microparticles. These structural characteristics promoted the response to the magnetic field, forming stronger chain structures and improving the MR performance. The 0.5 wt% additive concentration was used because too much additive in the MR fluid resulted in a significant increase in shear viscosity without increasing the MR performance (Iglesias et al., 2012; Moon et al., 2016). In addition, the pure BF-based MR fluid has relatively less

shear stress and shear viscosity, which can also be predicted and explained with its low *Ms* value and hard-magnetic property.

On the other hand, the flow behaviors of the two MR suspensions were fitted using the Herschel–Bulkley model to analyze typical steady-shear behavior. This model was expressed as follows:

$$\tau = \tau_y + K\dot{\gamma}^n, \quad \tau \geq \tau_y \tag{1}$$

where τ_y is the yield stress, depending on the applied *H*, shape, and particle concentration, and $\dot{\gamma}$ is the shear rate (Choi et al., 2001; Jang et al., 2015). Both K and n are denoted as the consistency index and power-law exponent, respectively. The τ curves of pristine CI and CI/BF-based MR suspensions were fitted very well to the Herschel–Bulkley Equation (1) at each magnetic field strength. **Figure 3A** presents two MR fluids as a solid line and dotted line (Cvek et al., 2016). **Table 1** lists the optimal parameters obtained from Equation (1), showing the Herschel–Bulkley model.

Similarly, the shear viscosity graphs for both MR fluids showed the same behavior over the shear rates at various *H*, as presented in **Figure 3B**. The viscosities of both MR fluids increased with increasing *H* and exhibited shear-thinning behavior; hence, the viscosity decreased with increasing shear rate. Note that the increase in shear viscosity had an important influence on the MR characteristics (Hong et al., 2013). As *H* increased, the magnetization of the CI microspheres also

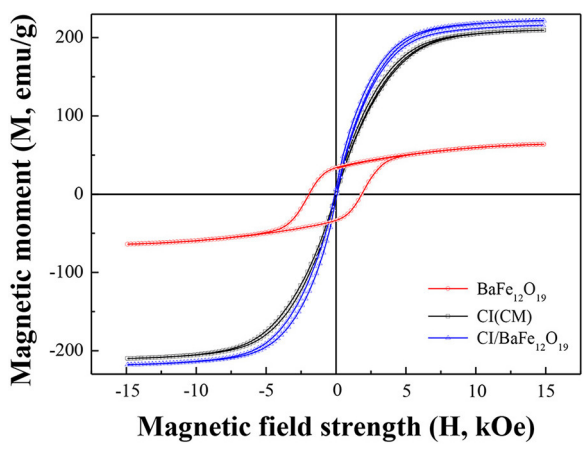

FIGURE 2 | Vibrating sample magnetometer data of pure carbonyl iron (CI) (CM grade), $BaFe_{12}O_{19}$, and CI/$BaFe_{12}O_{19}$ 0.5 wt% mixture.

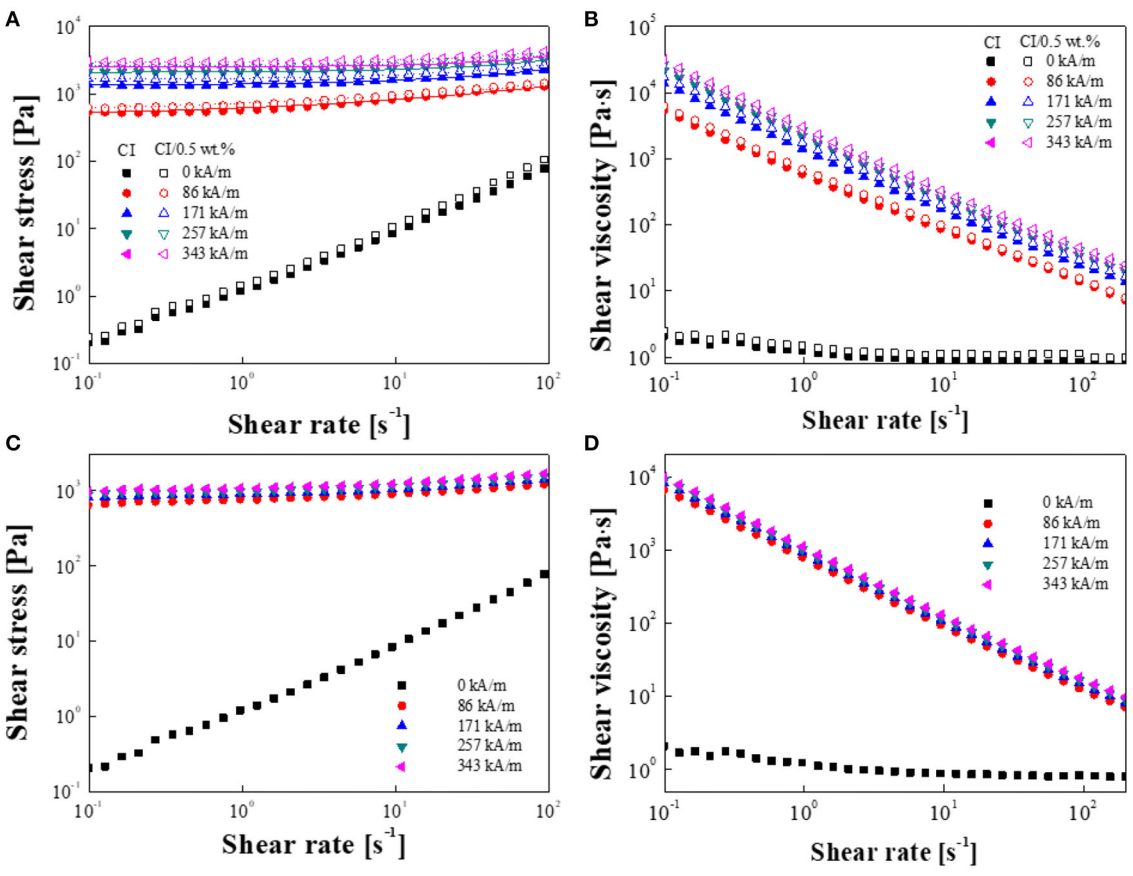

FIGURE 3 | (A) Shear stress and **(B)** shear viscosity of CI/ BaFe12O19 mixture-based MR fluid (open symbol) and pure carbonyl iron (CI)-based magnetorheological (MR) fluid (closed symbol), shear stress **(C)**, and shear viscosity **(D)** of pure barium ferrite (BF)-based MR fluid as a function of shear rate under various magnetic field strengths.

TABLE 1 | The optimal parameters in Herschel–Bulkley (HB) model equation obtained from shear stress data.

MR fluid	Parameters	Magnetic field strength (kA/m)			
		86	171	257	343
CI	τ_{dy}	463	1,333	2,100	2,506
	K	158.8	72.6	43.1	29.3
	n	0.362	0.569	0.703	0.795
CI/$BaFe_{12}O_{19}$ (0.5 wt%)	τ_{dy}	556	1,646	2,581	2,994
	K	172.2	65.1	46.9	43.7
	n	0.354	0.611	0.717	0.737

increased consistently, interfering with the free movement of the particles due to chain formation, thereby increasing the shear viscosity of the MR suspension. While the magnetic D–D interactions between the magnetic microspheres are parallel to the applied stimuli direction, the flow is perpendicular to the stimuli direction. Therefore, the shear viscosity is represented as apparent shear-thinning behavior, resulting from the shear-deformation of the chain structure over the entire $\dot{\gamma}$ range (Hong et al., 2013; Wang et al., 2019).

Without *H*, the CI/BF-based MR suspension showed slightly larger shear viscosity than the MR suspension without the BF nanoparticles because of the reduced hydrodynamic volume by the added BF particle concentration. Under an applied *H*, the shear viscosity of the MR suspension containing the BF additive was higher than that without BF nanoparticles. This suggests that the strength of the chain structure was increased by the added hard magnetic nanoparticles, and the shear stress was increased.

Figure 4 shows the relationship between the τ_y and *H* for both CI microparticles and CI/BF-based MR suspensions. Dynamic τ_y, which is one of the important rheological parameters, was acquired by extrapolating the τ at zero $\dot{\gamma}$ limit for each *H*. In general, the τ_y is expressed by the power-law of *H*, as given in Equation (2):

$$\tau_y \propto H^{\alpha} \tag{2}$$

The magnetic-field-dependent τ_y can be divided into two parts depending on the applied *H* (Ginder et al., 1996). At a low *H*, τ_y is proportional to H^2, following the polarization model due to the attraction force between the magnetized particles (Bossis et al., 1997, 2019). When the magnetic field strength increases to an intermediate value, τ_y will change to $H^{3/2}$, which is similar to the conduction model (Choi et al., 2001). This can be considered an increase in localized magnetization saturation that can decrease the MR performance. At the intermediate value, where local saturation becomes dominant, the equation for the τ_y is given as follows:

$$\tau_y = \sqrt{6}\phi\mu_0 {M_s}^{1/2} H^{3/2} \tag{3}$$

where φ is the magnetic particle volume fraction and μ_0 is the free space permeability (Genç and Phulé, 2002). When a sufficient *H* was applied, all of the particles reached full saturation and became an independent relationship with *H*.

$$\tau_y{}^{\text{sat}} = 0.086\phi\mu_0 {M_s}^2 \tag{4}$$

To analyze the flow effect for MR fluids more accurately and to determine the relationship between τ_y and *H*, the universal yield stress equation was proposed in the presence of a critical *H* (H_c) as follows (Fang et al., 2009):

$$\tau_y(H) = \alpha H^2 \left(\frac{\tanh\sqrt{H/H_c}}{\sqrt{H/H_c}}\right) \tag{5}$$

where α is dependent on the susceptibility of the MR fluid, φ, and particle shape (Ginder et al., 1996; Bossis et al., 2019). H_c is a boundary value dividing the τ_y behavior of the MR suspensions, in which τ_y represents two limiting values with respect to *H* as follows (Chae et al., 2015):

$$\begin{aligned} \tau_y &= \alpha H^2 (H \ll H_c) \\ \tau_y &= \alpha\sqrt{H_c}\, H^{3/2} (H \gg H_c) \end{aligned} \tag{6}$$

Figure 4 shows the relationship between τ_y and *H* for both MR suspensions. The H_c values of both the CI- and CI/BF-based MR fluids were 171 kA m^{-1}. A universal yield stress function was obtained using the following: H_c and $\tau_y(H_c) = 0.762\alpha H_c^2$,

$$\hat{\tau} = 1.313\hat{H}^{3/2}\tanh\sqrt{\hat{H}} \tag{7}$$

The results were fitted onto a single line using this generalized universal yield stress function, as demonstrated in **Figure 5**.

The dynamic oscillation measurements of the MR samples include both the strain amplitude and frequency sweep tests to examine the viscoelastic characteristics of both MR suspensions with and without BF nanoparticles under different *H* up to 343 kA/m. **Figure 6** presents data from the strain amplitude sweep measurements in the strain value from 10^{-2} to 10^{2} at a fixed angular frequency (ω). This test was carried out to select the linear viscoelastic region (γ_{LVE}) before performing the frequency sweep test. Overall, the storage modulus (G′) of the CI/BF MR fluid was slightly larger than that of the MR fluid without an additive in the entire strain range, suggesting that the fluid rigidity was enhanced by the BF additive (Wei et al., 2010). In particular, the G′ of both MR suspensions showed a steady plateau region up to 3×10^{-2} %, which was called the LVE region.

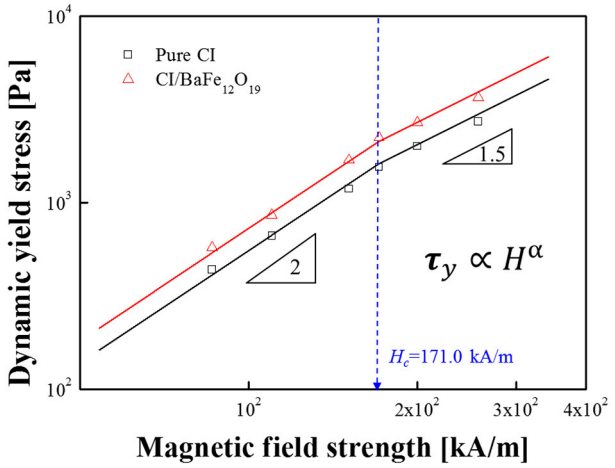

FIGURE 4 | Dynamic yield stress as a function of magnetic field strength for both pure carbonyl iron (CI)-(square symbol) and CI/$BaFe_{12}O_{19}$ mixture-based magnetorheological (MR) fluids (triangle symbol).

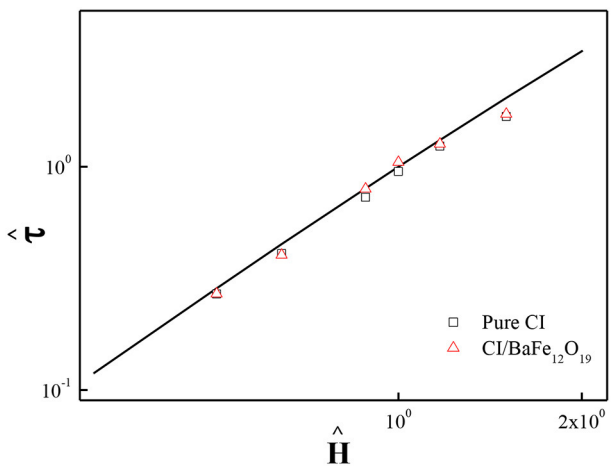

FIGURE 5 | Universal plot of $\hat{\tau}$ *vs*. $\hat{H}$ for pure carbonyl iron (CI; square symbol) and CI/$BaFe_{12}O_{19}$ mixture-based magnetorheological (MR) fluids (triangle symbol). The solid line is obtained using Equation (7).

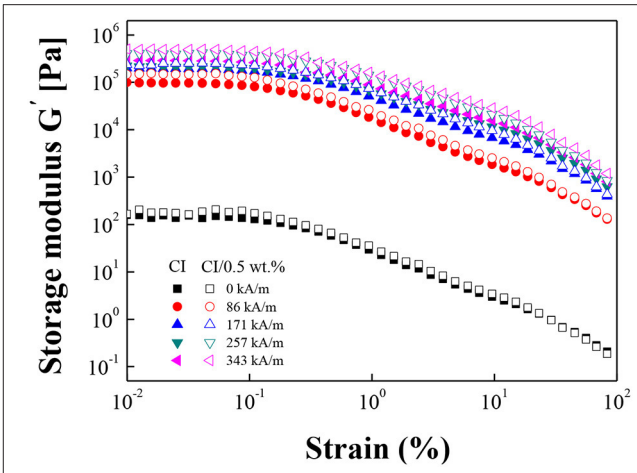

FIGURE 6 | Strain amplitude sweep test for pure carbonyl iron (CI; closed symbol) and CI/$BaFe_{12}O_{19}$ mixture–(open symbol) based magnetorheological (MR) fluids under various magnetic field strengths.

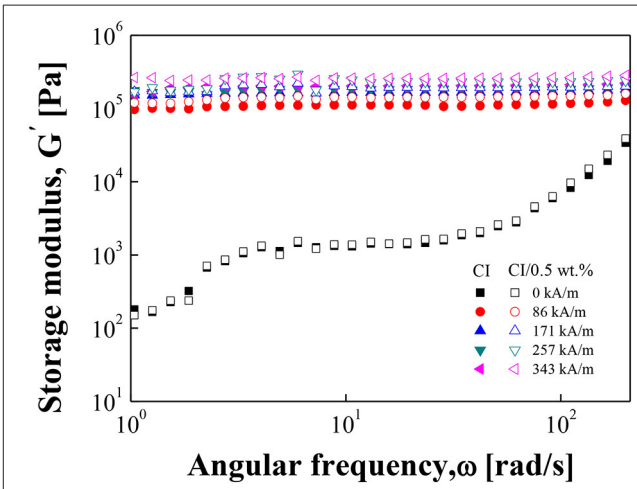

FIGURE 7 | Angular frequency sweep test for pure carbonyl iron (CI; closed symbol) and CI/$BaFe_{12}O_{19}$ mixture–(open symbol) based MR fluids at constant strain (0.03%).

When the strain exceeded a certain level, the storage modulus decreased sharply with increasing strain. This behavior is called the Payne effect, and it was attributed to an irreversible change in the microstructure of the material because of a sufficiently large strain (Gong et al., 2012).

The frequency sweep test was taken with a given strain of 3 $\times$ 10^{-2}%, as determined by the previous amplitude sweep test. **Figure 7** presents G′ as a function of ω at a constant strain for two MR fluids. When H was not applied, the G′ of both MR fluids was not large enough, and fluid-like characteristics were observed. When the H was applied, the G' of both MR fluids showed a stable region over the entire ω, and the value increased gradually with increasing H. This suggests that the two MR fluids transitioned from a fluid-like state to a solid-like state under the influence of H, and a stronger chain structure was formed as H increased. Furthermore, when comparing the two MR fluids over the entire frequency range, the G′ of the MR fluid containing the additive was larger than that of the fluid without an additive.

As shown in **Figure 8**, the solid-like behaviors of the two MR fluids can be interpreted more closely by the Schwarzl equation for deriving their stress relaxation modulus, $G(t)$, which was calculated using the G′ and loss (G″) modulus values obtained in the frequency sweep experiment shown in **Figure 7**. The Schwarzl equation is expressed as Equation 8 below (Chae et al., 2015):

$$G(t) \approx G'(\omega) - 0.566G''(\omega/2) + 0.203G''(\omega) \qquad (8)$$

The $G(t)$ of both MR suspensions showed steady plateau behaviors under an applied magnetic field, unlike G(t) in the absence of a magnetic field over time. In other words, the relaxation feature did not appear as a function of time (**Figure 8**). Thus, the stable solid-like behavior of both MR fluids was

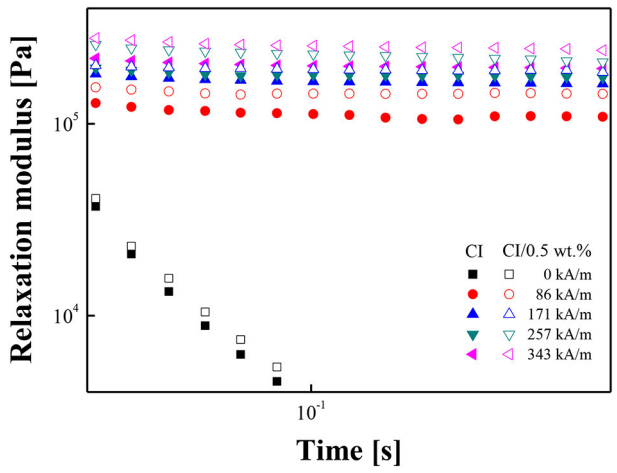

FIGURE 8 | Relaxation modulus of the pure carbonyl iron (CI; closed symbol) and CI/$BaFe_{12}O_{19}$ (open symbol) -based MR fluids as a function of time.

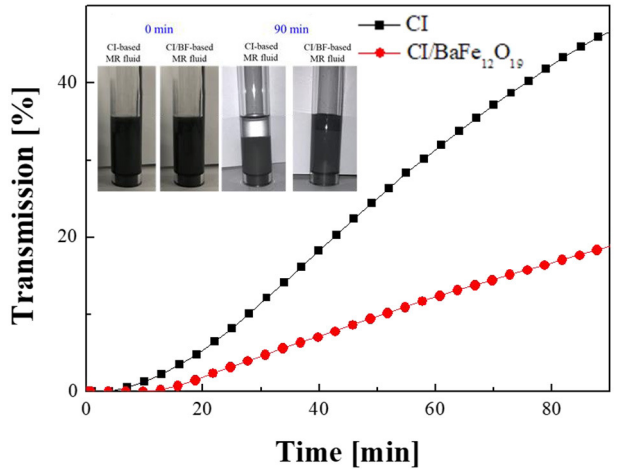

FIGURE 9 | Sedimentation stability curve verse time for pure carbonyl iron (CI; square symbol) and CI/$BaFe_{12}O_{19}$ mixture-based MR fluids (circle symbol).

studied as a function of time because of the strongly increased interactions between the CI particles under an external *H*.

As shown in **Figure 9**, the sedimentation stability of both MR fluids was investigated using Turbiscan in cylindrical glass cells, each containing a 40-mm MR fluid. The measurements were carried out by illuminating a light source from the bottom to the top at regular intervals (Buron et al., 2004). From the measurements, the transmission was plotted as a function of time (Upadhyay et al., 2013). Initially, the transmission of both MR fluids was close to zero. The absence of transmitted light indicates that the scattered light was not transmitted through the uniformly suspended particles in the MR fluid. After a few minutes, the transmission of a pristine CI-based MR fluid increased faster than that of a fluid containing the $BaFe_{12}O_{19}$ additive for the same time. This is because pure CI-based MR fluid particles aggregated more easily than the CI/$BaFe_{12}O_{19}$-based MR fluid particles and precipitated quickly to the bottom of the cell over time, showing slightly higher transmission. On the other hand, the CI/$BaFe_{12}O_{19}$-based MR fluid exhibited a low transmission due to the additive, showing a stable and improved dispersion state. This was attributed to the reduced particle density from the $BaFe_{12}O_{19}$ nanoparticles attached between the CI particles. The distance between the centers of the two magnetic particles determined the interaction between the particles, and for the two magnetic plates, this distance is the thickness of the particles. However, this value is significantly less than that of two spherical or elongated particles (Lisjak and Mertelj, 2018). As a result, the D–D interactions between two plate-like particles are strong, resulting in better stability of the MR suspension. Therefore, the addition of $BaFe_{12}O_{19}$ magnetic particles improved the sedimentation stability compared with the pristine CI-based MR suspension.

CONCLUSIONS

This study examined the effects of a hard-magnetic BF additive on a CI-based MR fluid. SEM and TEM revealed the morphology of the BF nanoparticles adsorbed in empty spaces between CI microspheres. The magnetic characteristics of the BF nanoparticles were confirmed using VSM. Two types of MR fluids with and without the $BaFe_{12}O_{19}$ additive in CI-based MR fluids were prepared to compare the rheological behavior and sedimentation stability under various *H*. The flow behavior of both MR fluids followed a typical Herschel–Bulkley model when an external *H* was applied, and a CI-based MR fluid with the $BaFe_{12}O_{19}$ additive exhibited improved MR characteristics, such as the yield stress, shear viscosity, and dynamic modulus with increasing *H*. Furthermore, the sedimentation stability of the CI-based MR fluid with the $BaFe_{12}O_{19}$ additive was improved remarkably by the reduced particle density due to the effect of the additive in the space between CI microspheres. Based on these results, synergistic effects were demonstrated to improve the MR properties and sedimentation stability of the ferromagnetic $BaFe_{12}O_{19}$ additive for a pure CI-based MR fluid.

DATA AVAILABILITY STATEMENT

The raw data supporting the conclusions of this article will be made available by the authors, without undue reservation.

AUTHOR CONTRIBUTIONS

HJC and HSJ designed the experiments. HSJ conducted the measurements. HSJ and QL analyzed the experimental data. HJC acquired the funding. All authors contributed to the article and approved the submitted version.

FUNDING

This work was supported by the National Research Foundation of Korea (2021R1A4A2001403).

REFERENCES

Ahamed, R., Ferdaus, M. M., and Li, Y. (2016). Advancement in energy harvesting magneto-rheological fluid damper: a review. *Korea Aust. Rheol. J.* 28, 355–379. doi: 10.1007/s13367-016-0035-2

Aruna, M. N., Rahman, M. R., Joladarashi, S., and Kumar, H. (2019). Influence of additives on the synthesis of carbonyl iron suspension on rheological and sedimentation properties of magnetorheological (MR) fluids. *Mater. Res. Express* 6:086105. doi: 10.1088/2053-1591/ab1e03

Aruna, M. N., Rahman, M. R., Joladarashi, S., and Kumar, H. (2020). Investigation of sedimentation, rheological, and damping force characteristics of carbonyl iron magnetorheological fluid with/without additives. *J. Braz. Soc. Mech. Sci. Eng.* 42:228. doi: 10.1007/s40430-020-02322-5

Ashtiani, M., Hashemabadi, S. H., and Ghaffari, A. (2015). A review on the magnetorheological fluid preparation and stabilization. *J. Magn. Magn. Mater.* 374, 716–730. doi: 10.1016/j.jmmm.2014.09.020

Bae, D. H., Choi, H. J., Choi, K., Nam, J. D., Islam, M. S., and Kao, N. (2017). Microcrystalline cellulose added carbonyl iron suspension and its magnetorheology. *Colloids Surf. A* 514, 161–167. doi: 10.1016/j.colsurfa.2016.11.052

Bombard, A. J. F., Alcântara, M. R., Knobel, M., and Volpe, P. L. O. (2005). Experimental study of mr suspensions of carbonyl iron powders with different particle sizes. *Int. J. Mod. Phys. B* 19, 1332–1338. doi: 10.1142/S0217979205030268

Bossis, G., Lemaire, E., Volkova, O., and Clercx, H. (1997). Yield stress in magnetorheological and electrorheological fluids: a comparison between microscopic and macroscopic structural models. *J. Rheol.* 41, 687–704. doi: 10.1122/1.550838

Bossis, G., Volkova, O., Grasselli, Y., and Ciffreo, A. (2019). The role of volume fraction and additives on the rheology of suspensions of micron sized iron particles. *Front. Mater.* 6:4. doi: 10.3389/fmats.2019.00004

Buron, H., Mengual, O., Meunier, G., Cayr,é, I., and Snabre, P. (2004). Optical characterization of concentrated dispersions: applications to laboratory analyses and on-line process monitoring and control. *Polym. Int.* 53, 1205–1209. doi: 10.1002/pi.1231

Chae, H. S., Piao, S. H., Maity, A., and Choi, H. J. (2015). Additive role of attapulgite nanoclay on carbonyl iron-based magnetorheological suspension. *Colloid Polym. Sci.* 293, 89–95. doi: 10.1007/s00396-014-3389-3

Choi, H. J., Cho, M. S., Kim, J. W., Kim, C. A., and Jhon, M. S. (2001). A yield stress scaling function for electrorheological fluids. *Appl. Phys. Lett.* 78, 3806–3808. doi: 10.1063/1.1379058

Choi, H. J., Kwon, T. M., and Jhon, M. S. (2000). Effects of shear rate and particle concentration on rheological properties of magnetic particle suspensions. *J. Mater. Sci.* 35, 889–894. doi: 10.1023/A:1004742223080

Choi, S. B., Song, H., Lee, H., Lim, S., Kim, J., and Choi, H. J. (2003). Vibration control of a passenger vehicle featuring magnetorheological engine mounts. *Int. J. Veh. Des.* 33, 2–16. doi: 10.1504/IJVD.2003.003567

Cvek, M., Mrlik, M., and Pavlinek, V. (2016). A rheological evaluation of steady shear magnetorheological flow behavior using three-parameter viscoplastic models. *J. Rheol.* 60, 687–694. doi: 10.1122/1.4954249

Fang, F. F., and Choi, H. J. (2008). Noncovalent self-assembly of carbon nanotube wrapped carbonyl iron particles and their magnetorheology. *J. Appl. Phys.* 103:07A301. doi: 10.1063/1.2829019

Fang, F. F., Choi, H. J., and Jhon, M. S. (2009). Magnetorheology of soft magnetic carbonyl iron suspension with single-walled carbon nanotube additive and its yield stress scaling function. *Colloids Surf. A* 351, 46–51. doi: 10.1016/j.colsurfa.2009.09.032

Genç, S., and Phulé, P. P. (2002). Rheological properties of magnetorheological fluids. *Smart Mater. Struct.* 11, 140–146. doi: 10.1088/0964-1726/11/1/316

Ginder, J. M., Davis, L. C., and Elie, L. D. (1996). Rheology of magnetorheological fluids: models and measurements. *Int. J. Mod. Phys. B* 10, 3293–3303. doi: 10.1142/S0217979296001744

Gong, X., Xu, Y., Xuan, S., Guo, C., Zong, L., and Jiang, W. (2012). The investigation on the nonlinearity of plasticine-like magnetorheological material under oscillatory shear rheometry. *J. Rheol.* 56, 1375–1391. doi: 10.1122/1.4739263

Gopinath, B., Sathishkumar, G. K., Karthik, P., Martin Charles, M., Ashok, K. G., Ibrahim, M., et al. (2021). A systematic study of the impact of additives on structural and mechanical properties of Magnetorheological fluids. *Mater. Today Proc.* 37, 1721–1728. doi: 10.1016/j.matpr.2020.07.246

Hajalilou, A., Mazlan, S. A., and Shila, S. T. (2016). Magnetic carbonyl iron suspension with Ni-Zn ferrite additive and its magnetorheological properties. *Mater. Lett.* 181, 196–199. doi: 10.1016/j.matlet.2016.06.041

Han, J. K., Lee, J. Y., and Choi, H. J. (2019). Rheological effect of Zn-doped ferrite nanoparticle additive with enhanced magnetism on micro-spherical carbonyl iron based magnetorheological suspension. *Colloids Surf. A Physicochem. Eng. Asp.* 571, 168–173. doi: 10.1016/j.colsurfa.2019.03.084

Han, W. J., An, J. S., and Choi, H. J. (2020). Enhanced magnetorheological characteristics of hollow magnetite nanoparticle-carbonyl iron microsphere suspension. *Smart Mater. Struct.* 29:055022. doi: 10.1088/1361-665X/ab7f43

Hong, C. H., Liu, Y. D., and Choi, H. J. (2013). Carbonyl iron suspension with halloysite additive and its magnetorheology. *Appl. Clay Sci.* 80–81, 366–371. doi: 10.1016/j.clay.2013.06.033

Iglesias, G. R., López-López, M. T., Durán, J. D. G., González-Caballero, F., and Delgado, A. V. (2012). Dynamic characterization of extremely bidisperse magnetorheological fluids. *J. Colloid Interface Sci.* 377, 153–159. doi: 10.1016/j.jcis.2012.03.077

Jang, D. S., Liu, Y. D., Kim, J. H., and Choi, H. J. (2015). Enhanced magnetorheology of soft magnetic carbonyl iron suspension with hard magnetic γ-Fe2O3 nanoparticle additive. *Colloid Polym. Sci.* 293, 641–647. doi: 10.1007/s00396-014-3475-6

Jang, I. B., Kim, H. B., Lee, J. Y., You, J. L., Choi, H. J., and Jhon, M. S. (2005). Role of organic coating on carbonyl iron suspended particles in magnetorheological fluids. *J. Appl. Phys.* 97:10Q912. doi: 10.1063/1.1853835

Kim, M. H., Choi, K., Nam, J. D., and Choi, H. J. (2017). Enhanced magnetorheological response of magnetic chromium dioxide nanoparticle added carbonyl iron suspension. *Smart Mater. Struct.* 26:095006. doi: 10.1088/1361-665X/aa7cb9

Ko, S. W., Yang, M. S., and Choi, H. J. (2009). Adsorption of polymer coated magnetite composite particles onto carbon nanotubes and their magnetorheology. *Mater. Lett.* 63, 861–863. doi: 10.1016/j.matlet.2009.01.037

Kordonskii, V. I., Demchuk, S. A., and Kuz'min, V. A. (1999). Viscoelastic properties of magnetorheological fluids. *J. Eng. Phys. Thermophys.* 72, 841–844. doi: 10.1007/BF02699403

Kwon, T. M., Jhon, M. S., and Choi, H. J. (1997). Rheological study of magnetic particle suspensions. *Mater. Chem. Phys.* 49, 225–228. doi: 10.1016/S0254-0584(97)80168-X

Li, W. H., Du, H., and Guo, N. Q. (2004). Dynamic behavior of MR suspensions at moderate flux densities. *Mater. Sci. Eng. A* 371, 9–15. doi: 10.1016/S0921-5093(02)00932-2

Li, W. H., Yao, G. Z., Chen, G., Yeo, S. H., and Yap, F. F. (2000). Testing and steady state modeling of a linear MR damper under sinusoidal loading. *Smart Mater. Struct.* 9, 95–102. doi: 10.1088/0964-1726/9/1/310

Lisjak, D., and Mertelj, A. (2018). Anisotropic magnetic nanoparticles: a review of their properties, syntheses and potential applications. *Prog. Mater. Sci.* 95, 286–328. doi: 10.1016/j.pmatsci.2018.03.003

Liu, J., Wang, X., Tang, X., Hong, R., Wang, Y., and Feng, W. (2015). Preparation and characterization of carbonyl iron/strontium hexaferrite magnetorheological fluids. *Particuology* 22, 134–144. doi: 10.1016/j.partic.2014.04.021

López-López, M. T., Gómez-Ramírez, A., Durán, J. D. G., and González-Caballero, F. (2008). Preparation and characterization of iron-based magnetorheological fluids stabilized by addition of organoclay particles. *Langmuir* 24, 7076–7084. doi: 10.1021/la703519p

Machovsky, M., Mrlik, M., Kuritka, I., Pavlinek, V., and Babayan, V. (2014). Novel synthesis of core–shell urchin-like ZnO coated carbonyl iron microparticles and their magnetorheological activity. *RSC Adv.* 4, 996–1003. doi: 10.1039/C3RA44982C

Mao, M., Hu, W., Choi, Y. T., Wereley, N., Browne, A. L., and Ulicny, J. (2014). Experimental validation of a magnetorheological energy absorber design analysis. *J. Intell. Mater. Syst. Struct.* 25, 352–363. doi: 10.1177/1045389X13494934

Maurya, C. S., and Sarkar, S. (2020). Effect of Fe3O4 nanoparticles on magnetorheological properties of flake-shaped carbonyl iron water-based suspension. *IEEE Trans. Magn.* 56, 1–8. doi: 10.1109/TMAG.2020.3031239

Moon, I. J., Kim, M. W., Choi, H. J., Kim, N., and You, C.-Y. (2016). Fabrication of dopamine grafted polyaniline/carbonyl iron core-shell typed microspheres and their magnetorheology. *Colloids Surf. A* 500, 137–145. doi: 10.1016/j.colsurfa.2016.04.037

Ngatu, G. T., and Wereley, N. M. (2007). High versus low field viscometric characterization of bidisperse mr fluids. *Int. J. Mod. Phys. B* 21, 4922–4928. doi: 10.1142/S0217979207045840

Qiao, X., Zhou, J., Binks, B. P., Gong, X., and Sun, K. (2012). Magnetorheological behavior of Pickering emulsions stabilized by surface-modified Fe3O4 nanoparticles. *Colloids Surf. A* 412, 20–28. doi: 10.1016/j.colsurfa.2012.06.026

Sedlačík, M., Pavlínek, V., Sáha, P., Švrčinová, P., Filip, P., and Stejskal, J. (2010). Rheological properties of magnetorheological suspensions based on core–shell structured polyaniline-coated carbonyl iron particles. *Smart Mater. Struct.* 19:115008. doi: 10.1088/0964-1726/19/11/115008

Susan-Resiga, D., Bica, D., and Vékás, L. (2010). Flow behaviour of extremely bidisperse magnetizable fluids. *J. Magn. Magn. Mater.* 322, 3166–3172. doi: 10.1016/j.jmmm.2010.05.055

Svåsand, E., Kristiansen, K., d,.L., Martinsen, Ø. G., Helgesen, G., Grimnes, S., et al. (2009). Behavior of carbon cone particle dispersions in electric and magnetic fields. *Colloids Surf. A* 339, 211–216. doi: 10.1016/j.colsurfa.2009.02.025

Upadhyay, R. V., Laherisheth, Z., and Shah, K. (2013). Rheological properties of soft magnetic flake shaped iron particle based magnetorheological fluid in dynamic mode. *Smart Mater. Struct.* 23:015002. doi: 10.1088/0964-1726/23/1/015002

Vasiliev, V. G., Sheremetyeva, N. A., Buzin, M. I., Turenko, D. V., Papkov, V. S., Klepikov, I. A., et al. (2016). Magnetorheological fluids based on a hyperbranched polycarbosilane matrix and iron microparticles. *Smart Mater. Struct.* 25:055016. doi: 10.1088/0964-1726/25/5/055016

Vicente, J. D., López-López, M. T., González-Caballero, F., and Durán, J. D. G. (2003). Rheological study of the stabilization of magnetizable colloidal suspensions by addition of silica nanoparticles. *J. Rheol.* 47, 1093–1109. doi: 10.1122/1.1595094

Wang, H., Li, Y., Zhang, G., and Wang, J. (2019). Effect of temperature on rheological properties of lithium-based magnetorheological grease. *Smart Mater. Struct.* 28:035002. doi: 10.1088/1361-665X/aaf32b

Wei, B., Gong, X., Jiang, W., Qin, L., and Fan, Y. (2010). Study on the properties of magnetorheological gel based on polyurethane. *J. Appl. Polym. Sci.* 118, 2765–2771. doi: 10.1002/app.32688

Wei, X., Liu, Y., Zhao, D., Mao, X., Jiang, W., and Ge, S. S. (2020). Net-shaped barium and strontium ferrites by 3D printing with enhancedmagnetic performance from milled powders. *J. Magn. Magn. Mater.* 493:165664. doi: 10.1016/j.jmmm.2019.165664

Yang, T.-H., Kwon, H.-J., Lee, S. S., An, J., Koo, J.-H., Kim, S.-Y., et al. (2010). Development of a miniature tunable stiffness display using MR fluids for haptic application. *Sens. Actuat. A Phys.* 163, 180–190. doi: 10.1016/j.sna.2010.07.004

Zhang, H., and Widom, M. (1995). Field-induced forces in colloidal particle chains. *Phys. Rev. E* 51, 2099–2103. doi: 10.1103/PhysRevE.51.2099

Zhang, X. C., Liu, X. T., Ruan, X. H., Zhao, J; and Gong, X. L. (2020). The influence of additives on the rheological and sedimentary properties of magnetorheological fluid. *Front. Mater.* 7:631069. doi: 10.3389/fmats.2020.631069

Conflict of Interest: The authors declare that the research was conducted in the absence of any commercial or financial relationships that could be construed as a potential conflict of interest.

frontiers in Materials

ORIGINAL RESEARCH
published: 20 April 2021
doi: 10.3389/fmats.2021.646579

Magneto-Induced Normal Stress of Magnetorheological Gel Under Quasi-Statically Monotonic and Periodically Cyclic Loading

*Runsong Mao, Xudan Ye, Huixing Wang, Guang Zhang and Jiong Wang**

School of Mechanical Engineering, Nanjing University of Science and Technology, Nanjing, China

Magnetorheological (MR) gel, an analog of MR fluid, is a novel kind of magnetic-responsive material. In this article, the influence of quasi-statically monotonic loading and periodically cyclic loading on the normal stress behavior of MR gel (MRG) is systemically investigated. Firstly, carbonyl iron powder (CIP) and soft polymer were adopted for the fabrication of MRG. Then, the variations of normal stress with shear strain were tested under different excited magnetic fields, shear rates, CIP contents, and shear strain amplitudes. It was found that the normal stress behavior of MRG exhibits three prominent stages: a sudden rise at the beginning, followed by a rapid decrease, and then a final steady-state value. The experiments also indicated that the excited magnetic field, compared with other influencing factors, has the most critical effect on the normal stress behavior of MRG. The corresponding mechanisms of various phenomena were methodically discussed. Furthermore, the ratio of shear stress to normal stress was proposed to better comprehend the mechanism of the evolution of internal microstructures of MRG and MR effects from a novel perspective. The results implied that the ratio has a close relation to the excited magnetic field and CIP content of MRG. The increase of normal stress is helpful for the fabrication of MRG with a high-efficiency MR effect.

Keywords: normal stress behavior, magnetorheological gel, quasi-static shear, magnetorheological effect, friction

OPEN ACCESS

Edited by:
Yancheng Li,
University of Technology Sydney, Australia

Reviewed by:
Yu Wang,
University of Science and Technology of China, China
Yingdan Liu,
Yanshan University, China
Miao Yu,
Chongqing University, China

****Correspondence:***
Jiong Wang
wjiongz@njust.edu.cn

Specialty section:
This article was submitted to Smart Materials, a section of the journal Frontiers in Materials

Received: *27 December 2020*
Accepted: *25 February 2021*
Published: *20 April 2021*

Citation:
Mao R, Ye X, Wang H, Zhang G and Wang J (2021) Magneto-Induced Normal Stress of Magnetorheological Gel Under Quasi-Statically Monotonic and Periodically Cyclic Loading. Front. Mater. 8:646579. doi: 10.3389/fmats.2021.646579

INTRODUCTION

Magnetorheological (MR) gel is a sort of intelligent material whose rheological properties could be changed expeditiously and reversibly by controlling the excited magnetic field (Xu et al., 2017; Meharthaj et al., 2019). MR gel (MRG), an analog of MR fluid and MR elastomer, is typically fabricated by dispersing soft magnetic particles into the cross-linked polymer matrix. Due to the existence of the viscoelastic polymeric matrix, MRG could overcome many defects occurred in MR fluid (Ashtiani et al., 2015) to some extent, such as sedimentation problem and sealing problem. Also, magnetic particles in MR elastomer could not move easily owing to the constraint of the rigid rubber matrix, which means that the MR effect of MR elastomer is highly weaker than that of MRG (Xu et al., 2011). Therefore, it is promising for MRG to be employed in engineering devices, such

as MR dampers (Rahman et al., 2017; Rossi et al., 2018), MR isolators (Li et al., 2013; Ahamed et al., 2018), and MR actuators (Khazoom et al., 2020).

Up to date, publications on MRG paid attention to the shear response behavior (Auernhammer, 2019; de Sousa et al., 2019; Zhang et al., 2019), such as shear yield stress, damping performance, and shear modulus. In contrast, the investigations on normal stress behavior of MRG are relatively infrequent. However, normal stress of MR material has a strong effect on the performance of some engineering devices, such as MR damper (Yazid et al., 2016) and MR finishing (Lambropoulos et al., 2010). Moreover, the normal stress behavior is also significant for understanding the mechanism of the MR effect and the evolution of particle microstructures. Gong et al. (2012) investigated the normal force behavior of MR fluid under the steady and oscillatory shear condition by employing a commercial rheometer with parallel-plate geometry. They proposed a dynamic simulation method to predict the normal force of MR fluid. Lopez-Lopez et al. (2010) conducted a series of experiments to validate the accuracy of their proposed theoretical model used to calculate the normal force of MR suspensions (Lopez-Lopez et al., 2010). The proposed model comprised the viscoelastic response of MR fluid and the influence of Maxwell stress and can help us better understand the normal force of MR fluid. See et al. observed that the normal force pushed apart the plate with the increase of the magnetic field when no deformation was applied to the MR suspension (See and Tanner, 2003). However, the normal force decreased firstly and then plateaued with the shear strain when continuous shearing was applied to MR suspension. The normal force of MRG under steady and oscillatory shear condition was firstly investigated by Ju et al. (2013). They systematically analyzed the influence of various excited factors (temperature, time history and frequency, etc.) on the normal force of MRG. The results revealed that the normal force of MRG is highly dependent on the magnetic field. Gong et al. (2012) discussed the non-linear behavior of normal stress of MR polymer gel under large amplitude oscillatory shear condition (Pang et al., 2018). They found that the alteration of normal stress was mainly influenced by two factors, Poynting effect and excited magnetic field, which are both relevant to the interior microstructures of MR polymer gel. The experimental results in the literature of Yang et al. (2017) revealed that the loss factor of MRG witnessed a reduction with the increase of CIP content. This is possibly because the molecular chain of polyurethane (PU) matrix becomes shorter and the particle chains keep thickening due to the increment of CIP content. Wang et al. (2016) used a modified split Hopkinson pressure bar (SHPB) instrument to study the strain-rate compressing behavior of a kind of new smart material, magnetically responsive shear-stiffening gel (MSTG). They found that the elastic modulus of MSTG with 45% CIP content could be as high as 126.6 MPa, nearly 791,250 times larger than that at normal state. Zhang et al. proposed a new phenomenon model for predicting the non-linear mechanical behavior of MRG, and the model is more computationally efficient than the previous models (Zhang and Wang, 2020).

As mentioned above, the current research on normal stress of MR materials is investigated mostly under the static shear and dynamic shear. However, it is worthwhile to note that many engineering devices work under the quasi-statically monotonic shear and periodically cyclic shear condition (Liu et al., 2014), such as high building and vehicle suspension system. In general, the loadings that are exerted on MR devices are divided into three kinds—static loading, dynamic loading, and quasi-static loading—which are distinguished by shear rate (Kuwano et al., 2013; Perez et al., 2016; Wang et al., 2019). The shear rate of quasi-static loading ranges from 10^{-4} to 10^{-1} s^{-1}, which works as a "bridge" between static loading and dynamic loading. The performance of MR device usually has a close correlation to the normal stress behavior of MR material in the process of quasi-static loading. On the other hand, MRG exhibits the feature of magneto-stimuli and magnetostriction due to the existence of polymeric matrix and magnetic particles. The prolongation of MRG is large in the presence of a magnetic field, resulting from the stretching and twining of soft segments in polymeric matrix and the particle-assembled chain structures. However, the microstructures of MRG, such as particle chains and soft segments, will be sheared ceaselessly under the application of large deformation. Simultaneously, the microstructures are tended resist the shearing and to recover continuously due to the quite low shear rate. This complex evolutive process of internal microstructures leads to the special normal stress behavior of MRG. However, up to now, publications on the normal stress of MRG under quasi-static loading condition are relatively rare. Thus, to better employ MRG in engineering devices, it is a necessity to close this gap, and this is also the motivation of this work.

This work intends to study the normal stress of MRG under quasi-statically monotonic loading and periodically cyclic loading condition. Firstly, MRG with different carbonyl iron powder (CIP) contents, i.e., 40%, 60%, and 70%, was fabricated. Then, the influence of the magnetic field, shear rate, and CIP content on the normal stress of MRG was systematically investigated under monotonic loading condition. Finally, influence of shear strain amplitude on the normal stress of MRG was analyzed under cyclic loading condition. The relevant microscopic mechanisms were proposed to explain the corresponding macroscopic phenomena.

EXPERIMENT

Fabrication of Magnetorheological Gel

Figure 1 shows briefly the process of fabrication of MRG sample. Polypropylene glycol [PPG-2000, M_n = 2,000, Sigma-Aldrich (Shanghai) Trading Co., Ltd., China] and toluene diisocyanate (TDI; 2,4- ≈ 80%, 2,6- ≈ 20%, Tokyo Chemical Industry Co., Ltd., Japan) are the two main reactants. They were stirred vigorously in a flask, and the reaction was conducted at 80°C. Two hours later, dipropylene glycol [SOL; Sigma-Aldrich (Shanghai) Trading Co., Ltd., China], a chain extender, was added to the flask, and the temperature was controlled at 60°C. Then, moderate stannous octoate (Sinopharm Chemical Reagent Co.,

Ltd., China) was selected as a catalyst and added to the reaction. The preparation of PU matrix was completed until the viscosity of the mixture increased considerably. Finally, the MRG samples with different CIP contents were fabricated after blending CIP with PU matrix evenly and named as MRG-40, MRG-60, and MRG-70. More details about the synthesized procedure could be seen in our previous work (Mao et al., 2020).

Testing for Normal Stress

A commercial rheometer (Type MCR 302, Anton Paar Co., Graz, Austria) with a plate–plate geometry was adopted to test the normal stress of MRG, and its schematic diagram is presented in **Figure 2**. MRG samples were placed between the upper and lower plates. The diameter of the two plates is both 20 mm, and the gap distance between them is 1 mm. In this work, the directions parallel to the magnetic field and vertical to the magnetic field are defined as the normal direction and the lateral direction, respectively. The normal stress and the lateral stress (i.e., shear stress) are simultaneously collected during the testing process. Moreover, according to Laun and Tian, the normal stress (N_d) of MRG could be calculated on the basis of the following equation (Laun et al., 2008; Jiang et al., 2011): $N_d = N_1 - N_2 = 2F_n/\pi R^2$, where N_1 is the primary normal stress, N_2 is the secondary normal stress, F_n is the measured normal force by rheometer, and R is the radius of the plate (i.e., 10 mm). The measurable range of normal force F_n is from −50 to 50 N with an accuracy of 0.03 N.

On the other hand, the quasi-static loading comprises two types of loading mode (Mao et al., 2020)—monotonic loading mode and cyclic loading mode—as shown in **Figure 3**. In the monotonic loading mode, the shear strain applied on the samples increases linearly from 0 to 100% in four different times (i.e., 200, 50, 25, and 12 s). The shear rates could be calculated as $\dot{\gamma} = \gamma/t$, and thus the shear rates are 0.005, 0.02, 0.04, and 0.083 s^{-1}, respectively. In the cyclic loading mode, the shear strain increases firstly from 0 to 100%, and then from 100 to −100%, and finally from −100 to 0%. Furthermore, all the tests were undertaken at 25°C.

RESULTS AND DISCUSSION

The influencing factors on MRG include the magnetic field, CIP content, shear rate, and shear strain. The purpose of investigating the rheological properties of MRG is to apply it into practical engineering devices, such as dynamic vibration absorber (DVA). In practice, the magnitudes of shear rate and shear strain amplitude depend on the external working conditions, and therefore, the investigation about the influence of stain rate and strain amplitude on normal stress behavior is necessary. In addition, the MRG itself is also a kind of magnetic responsive material. Thus, except for the exterior operating conditions, it is imperative to know that the magnetic field and the quantities of magnetic particles (i.e., CIP content) could influence the normal stress behavior of MRG to a certain degree.

Normal Stress Behavior of Magnetorheological Gel Under Quasi-Statically Monotonic Loading Condition

Influence of Magnetic Field on the Normal Stress Behavior

Figure 4 shows the photographs and microstructures of MRG with and without magnetic fields. MRG presents a semi-fluid-like state, and the magnetic particles disperse randomly in PU matrix when the external magnetic field is not applied. It is because the occurrence of a normal attracting effect (Guo et al., 2012) of MRG makes the plates be attracted to each other. In the presence of a magnetic field, MRG experiences a phase change from a semi-fluid-like state to a semi-solid-like state. Correspondingly, the particles form chain-like microstructures along the direction of the magnetic field, resulting in the occurrence of macroscopic peak structures (Yao et al., 2016). These peak structures will act to push apart the plate of rheometer, and this normal pushing effect will overcome the normal attracting effect. Therefore, the normal stress of MRG is measured. Also, it can be seen from **Figures 4B,C** that the larger the magnetic field strength, the more the peak structures. Therefore, one can conclude that the effect of the magnetic field will increase the attractive force between particles, resulting in the generation of normal stress. Simultaneously, the peak structures are highly dependent on the microscopic transformation of particle-chain structures (Yao et al., 2015). On the other hand, the evolution of microstructures could be significantly controlled by the external magnetic field. Thus, the normal stress behavior of MRG is hugely relevant to the excited magnetic field.

Then, a magnetic field sweep mode was applied to investigate the normal stress behavior of MRG with different CIP contents under quasi-static shear (as shown in **Figure 5**). The normal stress increases with the increase of magnetic field strength and CIP content. The experimental data in **Figure 5** are consistent with the morphology changes of MRG presented in **Figure 4**. The higher the magnetic field strength is, the stronger the magnetic attractive force between iron particles is, and the larger the normal stress is (as directly displayed in **Figures 4B,C**). Moreover, compared with MRG-40 and MRG-60, MRG-70 possesses more magnetic particles, leading to the more column-like or cluster-like particle chains under constant magnetic field strength. Therefore, MRG with a higher CIP content will achieve larger normal stress under higher magnetic field strength. Under a dynamic shear mode, the normal stress behavior of MRG could be estimated by the power model (Ju et al., 2013): $N_d = kH^2$, where k is the coefficient and H is the magnetic field strength. The fitting results are displayed as black lines in **Figure 6**, and the magnitudes of coefficient k are presented in **Table 1**. However, it can be seen from **Figure 6** that the power model could not perfectly characterize the normal stress behavior of MRG under the quasi-static shear mode. This is possibly due to the special sigmoid shapes of the N_d–H curves. The increasing speed of normal stress (i.e., the slopes of N_d–H curves) firstly appears a fast growth and then slows down after the magnetic field strength exceeds a

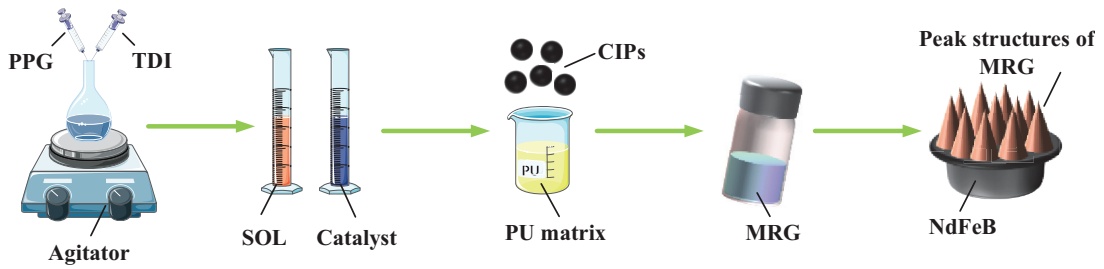

FIGURE 1 | Schematic diagram of the fabrication process for magnetorheological gel (MRG).

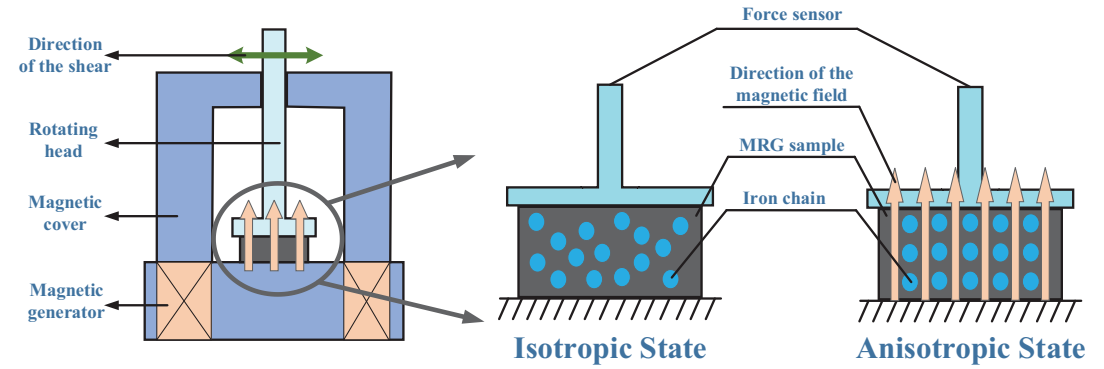

FIGURE 2 | Schematic diagram of the MCR 302 commercial rheometer.

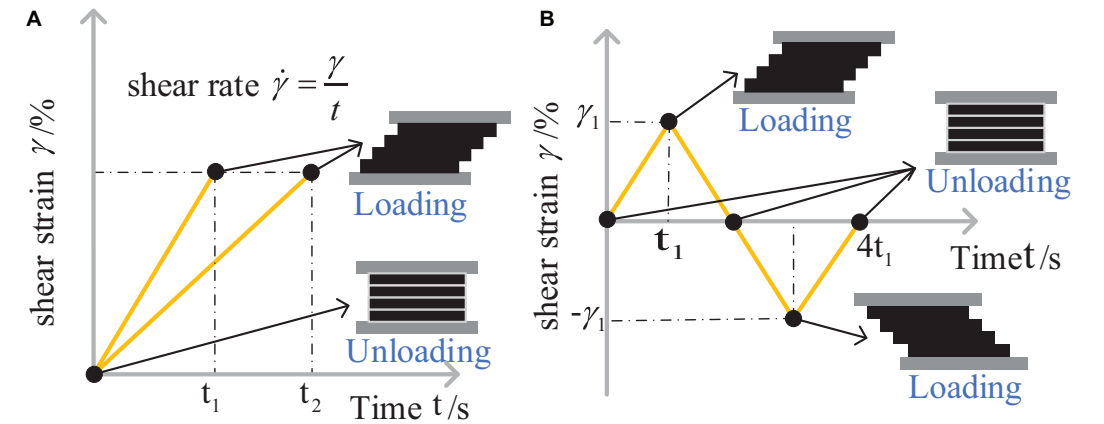

FIGURE 3 | Testing principles of quasi-static monotonic loading **(A)** and cyclic loading **(B)**.

critical value (Mao et al., 2020). Thus, a modified magnetization model (Zubieta et al., 2009) was used to describe the variation of normal stress with magnetic field strength under the quasi-static shear mode. The expression of magnetization model is $N_d = N_{H=\infty} + (N_{H=0} - N_{H=\infty})\ 2\ (e^{-\alpha H} - 0.5e^{-2\alpha H})$, where $N_{H=0}$ is the field-off normal stress, $N_{H=\infty}$ is the saturation value of normal stress, and α is saturation moment of index of normal stress (Guo et al., 2012). It can be seen from **Figure 6** that the magnetization model, compared with the power model, could fit the experimental results better because the magnetization model takes the influence of magnetic saturation into account. Thus, magnetization model is more appropriate to characterize the normal stress behavior of MRG under the quasi-static shear mode, while the power model could estimate the normal stress of MRG under a dynamic shear mode.

To further understand the mechanism of filed-dependent normal stress behavior of MRG, the normal stress of MRG-60 versus shear strain under four different magnetic fields and constant shear rates of 0.04 s^{-1} is displayed in **Figure 7**. The normal stress of MRG is nearly zero and negligible in the absence

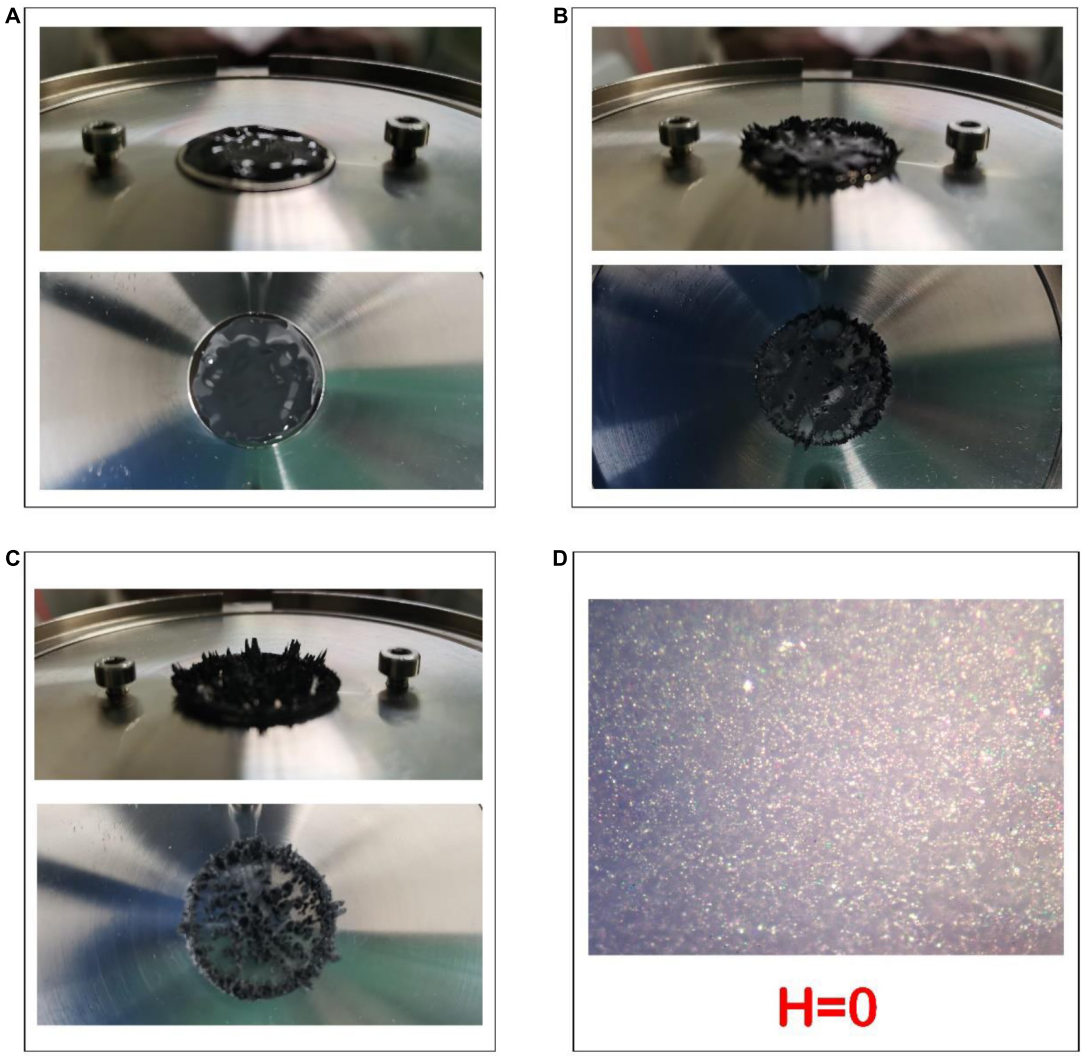

FIGURE 4 | Photographs of magnetorheological gel (MRG) with and without a magnetic field: 0 kA/m **(A)**, 293 kA/m **(B)**, and 740 kA/m **(C)**. Microstructures of MRG **(D)**. The white points represent magnetic particles.

of a magnetic field while significant in the presence of a magnetic field, corresponding to the change of morphological structures displayed in **Figures 4A–C**. When the external magnetic field is not applied, the magnetic particles disperse evenly without forming chain-like structures, and thus, no peak structures appear due to the surface tension of MRG and the gravity of magnetic particles (Yao et al., 2015). Thus, normal stress of MRG is almost constant and negligible with the increase of shear strain. This phenomenon indirectly implies that the effect of shear deformation on normal stress behavior is much weaker than that of the magnetic field. When a magnetic field is applied, normal stress of MRG firstly appears an abrupt increase (stage 1), then decreases rapidly with the increase of shear strain (stage 2), and finally reaches a plateau after the shear strain exceeds a critical value (stage 3) (Wang et al., 2019). Besides, larger normal stress will be achieved at larger magnetic field strength. Transformation of normal stress from stage 1 to stage 2 and then to stage 3 could be explained with a microstructure theory (Lopez-Lopez et al., 2010; Wang et al., 2019), as shown in **Figure 8**. The randomly dispersed magnetic particles (**Figure 8A**) will aggregate to vertical chain-like structures (**Figure 8B**) within milliseconds as soon as a magnetic field is applied, resulting in the magnetic interaction and attractive force between the magnetic particles. Thus, the normal stress of MRG appears a sudden increment firstly (stage 1), which indicates that MRG changes from a viscous flow state (**Figure 4A**) to a semi-solid state (**Figures 4B,C**). Then, the perpendicular long particle chains tilt into angles (**Figure 8C**) and break into unstable short chains with the increase of shear strain. This process leads to the rapid reduction of the normal stress of MRG (stage 2). Finally, the unstable short chains are inclined to aggregate together to form stable long chains due to the existence of the magnetic attractive force between magnetic particles. Simultaneously, the fracture of the long chains is still in process with the increase of shear strain. Therefore, a dynamic balance

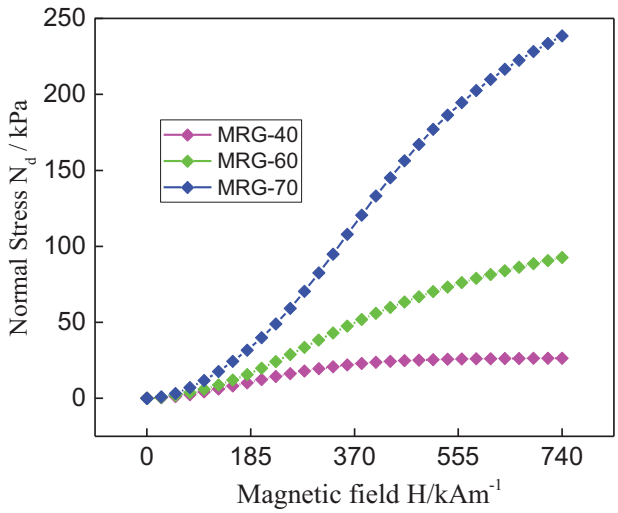

FIGURE 5 | Normal stress of magnetorheological gel (MRG) with different carbonyl iron powder (CIP) contents under magnetic field sweep (quasi-static shear with a shear rate of 0.04 s^{-1}).

will eventually occur between the fracture and reconstruction of particle chains (**Figure 8D**), which gives rise to the gradual stability of the normal stress (stage 3).

Interestingly, another notable phenomenon is that the normal stress will still decrease slightly and obscurely after getting into stage 3, which is similar with the MR fluid (Guo et al., 2012). For example, the normal stress decreases to a certain extent at 96 kA/m of magnetic field strength when the shear strain exceeds the critical value (corresponding to the diagonal line shown in **Figure 7**). However, this phenomenon will progressively disappear with the increase of the excited magnetic field. This could be interpreted with the following theory. The contribution of shear strain to the fracture of particle chains is constant no matter how large the magnetic field strength is. However, the larger the magnetic field strength, the stronger the magnetic interaction between the particles, and the greater the contribution of the magnetic field to the reconstruction of long particle chains. Thus, the effect of reconstruction on particle chains is weaker than that of fracture when the magnetic strength is relatively small, which leads to the above-mentioned phenomenon.

The MR effect, the most important rheological properties of MR materials, generally results from the magnetic interaction between the polarized magnetic particles. Since both the normal stress and shear stress are also highly relevant to the magneto-induced particle chain microstructures, an investigation on the correlation between the normal stress and shear stress is of great benefit to better understand the mechanism of the MR effect and guide the design of MR device (Jiang et al., 2011). It can be seen from **Figure 9A** that the stress behavior of MRG could be segmented into pre-yield region and post-yield region, which depends on whether the shear strain exceeds the critical value, γ_c, or not (Wang and Liao, 2011). The shear stress of MRG increases rapidly and then tends to level off with the increase of shear strain, whereas the normal stress appears on an opposite trend in the pre-yield region. Also, similar to MR fluid, MRG could be regarded as a kind of linear viscoelastic material in the pre-yield region, where the stress nearly increases (or decreases) linearly with the shear strain. Moreover, the saturations of normal stress and shear stress in the post-yield region arise from the magnetic saturations in MRG. On the other hand, since the MR effect could be simply expressed as the ratio of field-on shear stress to field-off shear stress (Chen et al., 2013) (i.e., MR effect = $\frac{\tau_{H\neq 0}}{\tau_{H=0}}$), MRG with high shear tress is of great benefit to design precise devices. Thus, it is necessary to study the factors influencing shear stress. According to the research of Li and Chen, the shear stress is mainly influenced by two factors: magnetic force and friction force. The shear stress could be predicted as follows (Li and Zhang, 2008; Chen et al., 2013): $\tau = \tau_f + \tau_m = \mu \cdot N_d + \gamma \cdot N_d$, where τ_f and τ_m represent friction-induced stress and magnetic-induced stress, respectively, and μ is the friction coefficient. From the equations, one could conclude that shear stress is strongly relevant to the normal stress, particle–particle friction coefficient, and shear strain. Thus, the ratio of shear stress to normal stress is proposed here and may be helpful for better investigating the mechanism of the magneto-responsive behavior of MRG from a new perspective. The ratio of shear stress to normal stress as a function of shear strain is displayed in **Figure 9B**. Although the ratio of shear stress to normal stress, r, is $r = \frac{\tau}{N_d} = \gamma + \mu$, the ratio under different magnetic fields does not increase linearly with the increase of shear strain. The variation of ratio with shear strain could also be divided into two regions: pre-yield and post-yield regions. The ratio appears as a rapid growth firstly (i.e., the pre-yield region) and then reaches saturation (i.e., the post-yield region) with the increase of shear strain. In the pre-yield region, unordered particle structures gradually evolve into cluster-like microstructures or complex network-like structures (Liu et al., 2013) under constant magnetic field strength, which gives rise to the increase of friction coefficient. Thus, the ratio of shear stress to normal stress grows in the pre-yield region. In addition, the ratio reaches saturation in the post-yield region for the reason that the shear stress and normal stress are both nearly constant in that region (shown in **Figure 9A**). On the other hand, larger ratio happens at smaller magnetic field strength, which is similar with the results of MR fluid (Chen et al., 2013). This is because the normal stress and shear stress increase at different levels with the increase of magnetic fields. Taking the normal stress and shear stress at 194 and 293 kA/m of magnetic field, for example, the increment of shear stress is 3.4 kPa (from 3.2 kPa under 194 kA/m to 5.6 kPa under 293 kA/m), while that of normal stress is 11.3 kPa (from 8.4 kPa under 194 kA/m to 19.7 kPa under 293 kA/m). Because normal stress was much larger than shear stress, with normal stress being the denominator ($r = \frac{\tau}{N_d}$), higher ratio happens under small magnetic fields.

It is worth noting here that the total shear stress could be divided into two parts: the magnetic-induced elastic shear stress and the friction-induced shear stress. Thus, to quantitatively analyze the contribution of friction to shear stress, the shear stress (**Figure 10A**) and storage modulus (**Figure 10B**) of MRG-60 were tested under quasi-static loading and under oscillatory loading, respectively. It can be seen from **Figure 10A** that the

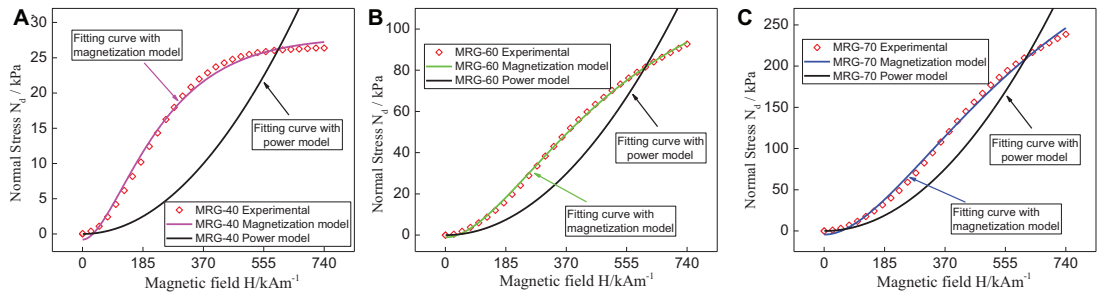

FIGURE 6 | The experimental results and fitting cures with the power model and magnetization model for MRG-40 **(A)**, MRG-60 **(B)**, and MRG-70 **(C)**.

shear stress increases rapidly at small shear strain, whereas it almost behaves independently from shear strain at high shear strain. However, **Figure 10A** cannot show the information about the specific contributions of magnetic force or friction force to shear stress. Therefore, the oscillatory experiments with low frequency were conducted, and the results are displayed in **Figure 10B**. The storage modulus, G', of viscoelastic material could represent an elastic part or magnetic force contribution because the energy stored in the material could be recovered after the shear is removed (Li and Zhang, 2008). The elastic shear stress, τ_E (i.e., magnetic force contribution), could be calculated using the equation $\tau_E = G'\gamma$, and the results are displayed in **Figure 10C**. The stress difference between the results presented in **Figures 10A,C** indirectly demonstrates the contribution of friction to the total shear stress (i.e., friction-induced shear stress, $\tau_F = \tau - \tau_E$). Taking MRG-60 at 391 kA/m of magnetic field strength for example, the total shear stress is 7,554 Pa, and the elastic shear stress is 4,672.1 Pa. Thus, the contribution of friction force to shear stress is 2,881.9 Pa (approximately 38.2% to the total shear stress). It implies that the friction contribution plays a significant role in the total shear stress. Furthermore, these discoveries may provide a great method to fabricate high-efficiency MRG from a new aspect, such as increasing the friction coefficient of magnetic particles.

Influence of Shear Rate on the Normal Stress Behavior

To investigate the influence of the shear rate on the normal stress behavior of MRG, **Figure 11** shows the normal stress of MRG-60 as a function of shear strain under four different shear rates and constant magnetic fields. In the absence of a magnetic field, the normal stress of MRG-60 is almost zero (**Figure 11A**). The reason for this has been discussed in the former section and for brevity will not be repeated here. The normal stress of MRG-60 decreases dramatically in the first place and then gradually goes into a stable state with the increase of shear strain. It can be seen from **Figure 11B** that the normal stress of MRG is higher under lower shear rate, which is opposite to the findings of Ju et al. (2013). The experiments were conducted three times, and the results did not change. Theoretically speaking, according to the previous findings in Ju et al. (2013), MRG is a kind of shear thinning material, which means that the apparent viscosity of MRG decreases with the increase of shear rate (Ju et al., 2013). Thus, the magnetic particles need to overcome the stronger restrictions to form chain-like microstructures under lower shear rate, resulting in the growth of normal stress with the increase of shear rate. However, the results shown in **Figure 11B** do not agree with that theory and its corresponding phenomenon. The results displayed in **Figure 11B** could be explained with the following hypothesis (Liu et al., 2014; Mao et al., 2020). The macroscopic normal stress behavior of MRG is primarily dependent on the evolution of particle chain microstructure. The excited magnetic field and shear strain are the two main aspects driving the transformation of the interior particle chain structure. The contribution of the magnetic field to the formation of stable long chains or dense network structures is positive, whereas shear strain tends to demolish the long chains or columnar aggregates. For a higher shear rate (i.e., 0.083 s^{-1}), the apparent viscosity is smaller, and thus the resistance to the formation of particle chain is weaker in comparison with the lower shear rate. However, smaller apparent viscosity also means weaker resistance to the shear strain. Thus, the demolishing effect of shear strain on long chains is more considerable under a higher shear rate. Besides, MRG is given less time (i.e., 12 s) to complete the shearing under a shear rate of 0.083 s^{-1}. In this case, the smaller excited magnetic field, i.e., 96 kA/m, could barely drive the transformation of the interior chain structure. Contrarily, for a lower shear rate (i.e., 0.005 s^{-1}), there is enough time (i.e., 200 s) for MRG to thoroughly complete the reconstruction of the long chains or dense network structures after being destroyed by shear deformation. Thus, larger normal stress achieves a smaller shear rate. This implies that the normal stress behavior of MRG under quasi-static loading (i.e., particularly small shear rate) is opposite to that under dynamic loading when the external magnetic field is small.

TABLE 1 | Magnitudes of the fitting parameters.

CIP content	Magnetization model			Power model
	$N_{H=0}$ (kPa)	$N_{H=\infty}$ (kPa)	α	*k*
40%	−0.80	28.02	1.06868	0.39134
60%	−1.07	126.70	0.49196	1.1683
70%	−4.36	392.46	0.39778	2.95311

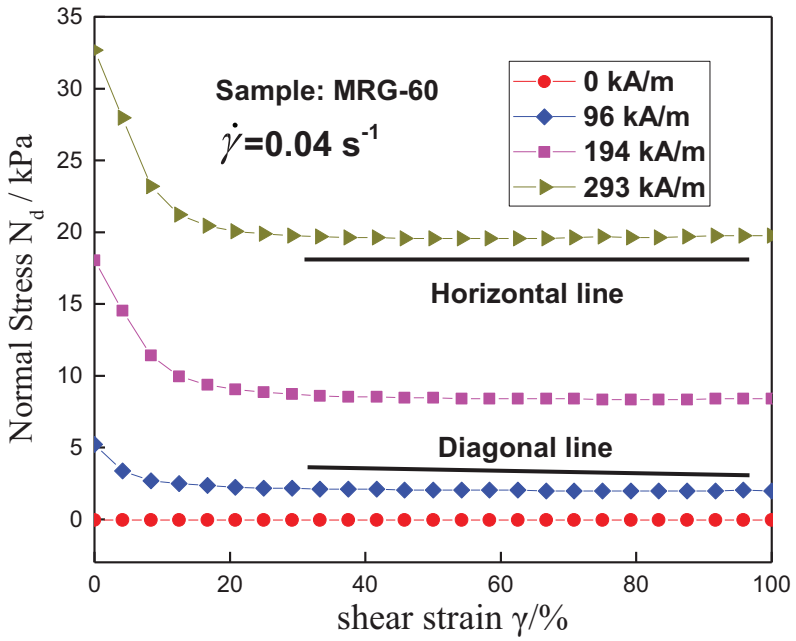

FIGURE 7 | Variation of the normal stress with shear strain for MRG-60 under four different magnetic fields and constant shear rate.

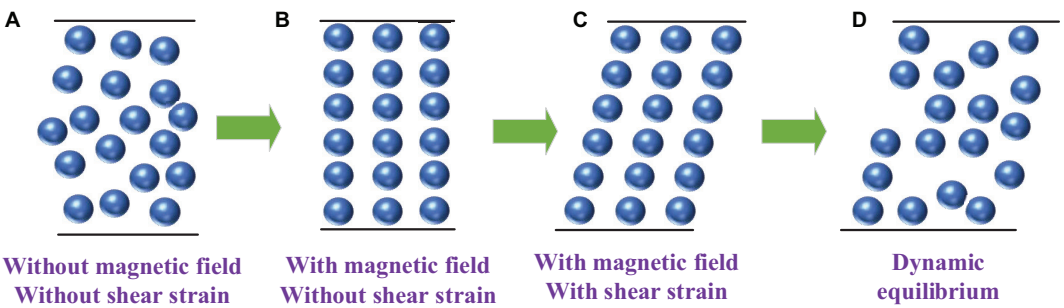

FIGURE 8 | The microstructure of magnetorheological gel (MRG): randomly dispersed particles **(A)**, magnetic field-induced perpendicular particle chains **(B)**, shear strain-induced tilted particle chains **(C)**, and dynamic equilibrium between the fracture and rebuilding of particle chains **(D)**.

Furthermore, the steady-state value of normal stress decreases with the increase of the shear rate when the magnetic field strength is small (such as 96 kA/m). That is to say, the shear rate is influential on the normal stress behavior of MRG to a certain extent. However, it is worthwhile to mention that the influence of the shear rate on the normal stress behavior gradually becomes insignificant with the growth of the excited magnetic field strength. In other words, differences between the steady-state value of normal stress still exist at 96 kA/m of magnetic field strength while it nearly disappears in 293 kA/m of magnetic field strength (as can be intuitively seen from **Figures 11B–D**). It is because the magnetic interaction between particles is powerful enough to drive the particle chains to behave stably and robustly when the excited magnetic field strength is large (e.g., 293 kA/m). Although the time for reconstruction of the broken particle chains is less at a higher shear rate, the particle–particle magnetic attractive force is strong enough to complete the rebuilding of chains due to the presence of a higher magnetic field (i.e., 293 kA/m). Also, the effect of the magnetic field on the normal stress is much more considerable than that of shear strain, as discussed in "Influence of Magnetic Field on the Normal Stress Behavior" section. Therefore, the shear rate has little effect on the normal stress of MRG in steady state under high magnetic field strength (as shown in **Figure 11D**).

Influence of Carbonyl Iron Powder Content on the Normal Stress Behavior

Figures 12A–C present the normal stress of MRG with three different CIP contents as a function of shear strain under constant magnetic fields and shear rate of 0.04 s^{-1}. The normal stress of MRG with various CIP contents is nearly negligible for the lack of an excited magnetic field. The results and reason are similar to those discussed in "Influence of Magnetic Field on the Normal Stress Behavior" and "Influence of Shear Rate on

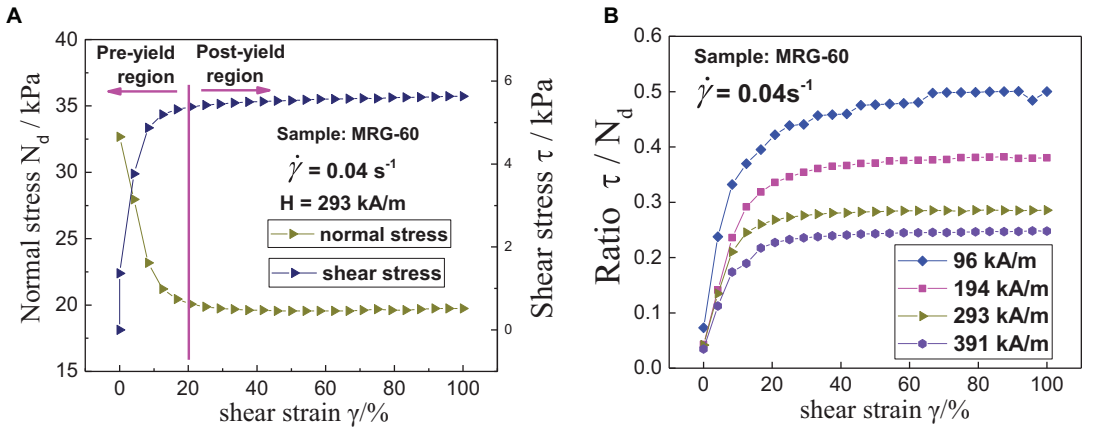

FIGURE 9 | The normal stress (N_d) and shear stress (τ) of magnetorheological gel (MRG) as a function of shear strain **(A)**; the ratio of shear stress to normal stress (τ/N_d) as a function of shear strain **(B)**.

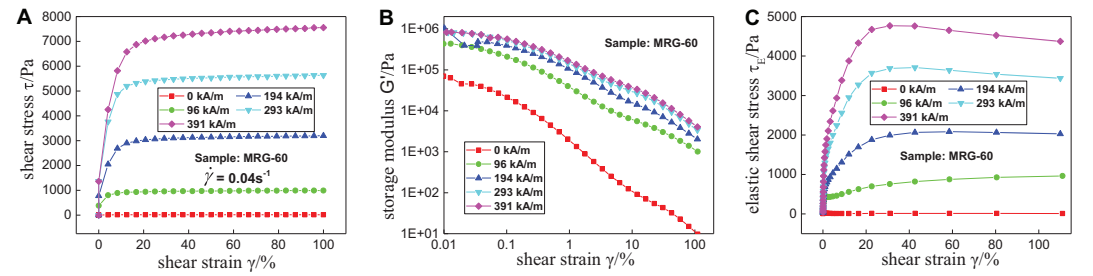

FIGURE 10 | The variation of total shear stress **(A)**, storage modulus **(B)**, and elastic shear stress **(C)** with shear strain under magnetic field sweep. The oscillatory frequency is 0.5 Hz.

the Normal Stress Behavior" sections and not displayed here for simplicity. The curves presented in **Figures 12A–C** indicate that the normal stress of MRG exhibits a rapid drop and then a plateau with the increase of shear strain, which is also similar with the changing regularity of normal stress–strain curve displayed in **Figure 7**. Moreover, a higher CIP content will contribute to larger normal stress under constant magnetic field strength. This is because the more the magnetic particles, the more the long chains, and the more the peak structures acing to push apart the rheometer plate (Yao et al., 2015). **Figures 12D–F** display the ratio of shear stress to normal stress of MRG with different CIP contents under different magnetic fields. Most notably, the ratio of MRG-60 is higher than that of MRG-40 and MRG-70 at the magnetic field strength of 293 kA/m while lower than that of MRG-70 at the magnetic field strength of 391 kA/m. Precisely speaking, the magnetic attractive force between particles is dependent on the effective magnetic field (Lemaire and Bossis, 1991) (H_{eff}) rather than the applied magnetic field (H_{app}). The effective magnetic field could be represented as $H_{eff} = H_{app} - 4\pi M$. The magnetic magnetization $M = \chi H_{eff}$, where χ is magnetic susceptibility. Thus, $H_{eff} = \frac{H_{app}}{\mu_{H_{eff}}}$, where the permeability $\mu_{H_{eff}} = 1 + 4\pi\chi_{H_{eff}}$. The permeability grows with the increase of CIP content, resulting in the decrease of magnetic force. However, a larger quantity of chains will generate due to the increase of CIP content, leading to the increase of magnetic force. Thus, there exists a competition between the CIP content and permeability. It implies that the stress behavior and ratio are highly dependent on the CIP content of MRG and the excited magnetic field (Guo et al., 2012). Actually, the research on magnetic powders also concluded similar results (Chen et al., 2013); i.e., the variation of ratio with the CIP content is irregular and unpredictable under a constant magnetic field. From the changing regularity of ratio, one can also conclude that under a constant magnetic field, the rapid increase of ratio means the interior structures of MRG evolve from isotropic state with evenly dispersed particles to anisotropic state with long particle chains or dense network microstructures. Moreover, according to the equation $r = \gamma + \mu$, the reduction of ratio represents decline of the friction between the iron particles when the magnetic field and shear strain are constant. MRG with a moderate CIP content possibly possesses a regular particle chain microstructure, while that with a large quantity of magnetic particles might form an irregular chain structure that induces the decline of friction (Chen et al., 2013). However, the contribution of friction to shear stress is considerably fundamental. Therefore, except for magnetic field and CIP content, the ratio and normal stress should both be taken into consideration when achieving a high

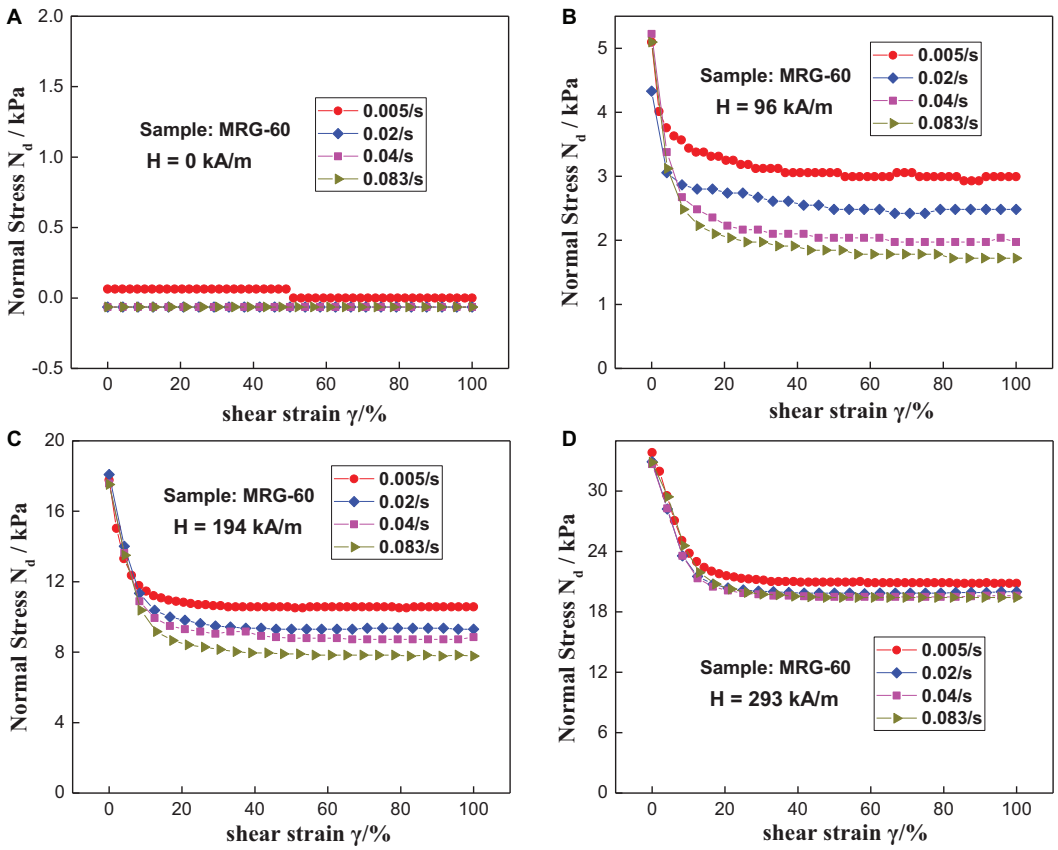

FIGURE 11 | Variation of normal stress with shear strain for MRG-60 under different shear rates and constant magnetic fields: 0 kA/m **(A)**, 96 kA/m **(B)**, 194 kA/m **(C)**, and 293 kA/m **(D)**.

MR effect or high field-on shear stress. Further investigations on the mechanism of this phenomenon are needed.

Normal Stress Behavior of Magnetorheological Gel Under Periodically Cyclic Loading Condition

Influence of Shear Strain Amplitude on the Normal Stress Behavior

In this section, MRG-60 was selected as an experimental sample to investigate the normal stress under periodically cyclic loading condition. The shear strain increases linearly from 0 to 100% (or 20%, etc.) and then decreases linearly to 0% under a constant shear rate. Subsequently, the shear strain reversely processes from 0 to −100% and then from −100 to 0%. **Figure 13A** presents the variation of normal stress with different shear strain amplitudes, and **Figures 13B–F** present the enlarged view of normal stress–strain curves under various shear strain amplitudes, i.e., 20%, 40%, 60%, 80%, and 100%. Taking normal stress–strain curve under 100% strain amplitude, for example, the black arrows represent the changing process of the magneto-induced normal stress. The normal stress appears as an abrupt increment immediately due to the application of 194 kA/m of magnetic field strength. This results from the magnetic interaction between the particles. After that, the magneto-induced normal stress decreases rapidly due to the negative contribution of tilted particle chains to normal stress. Then, the dynamic balance between the strain-induced rupture and magneto-induced rebuilding of particle chains occurs with the continuous application of shear strain, which results in the minimum value of normal stress (i.e., 8.73 kPa). When the shear strain returns to 0% after it arrives at 100%, the tilted and elongated chains start to constrict, and the gaps between the magnetic particles begin to squeeze to some extent. These effects are coupled together and contribute to the sudden rise of normal stress. Therefore, a peak of normal stress (i.e., 27.01 kPa) emerges. However, the effect of the rebuilding and fracture of particle chains on normal stress is opposite. When the effect of the fracture of particle chains is stronger than that of rebuilding, the normal stress will descend again with the continuous application of shear strain and magnetic field. Thus, the normal stress could be adjusted in a large scale from 8.73 to 27.01 kPa under cyclic loading. In addition, the changing trend of normal stress at the other side will not be discussed here due to the symmetry of normal stress–strain curve.

It can be seen from **Figures 13B–F** that the shapes enclosed by normal stress–strain curves change from

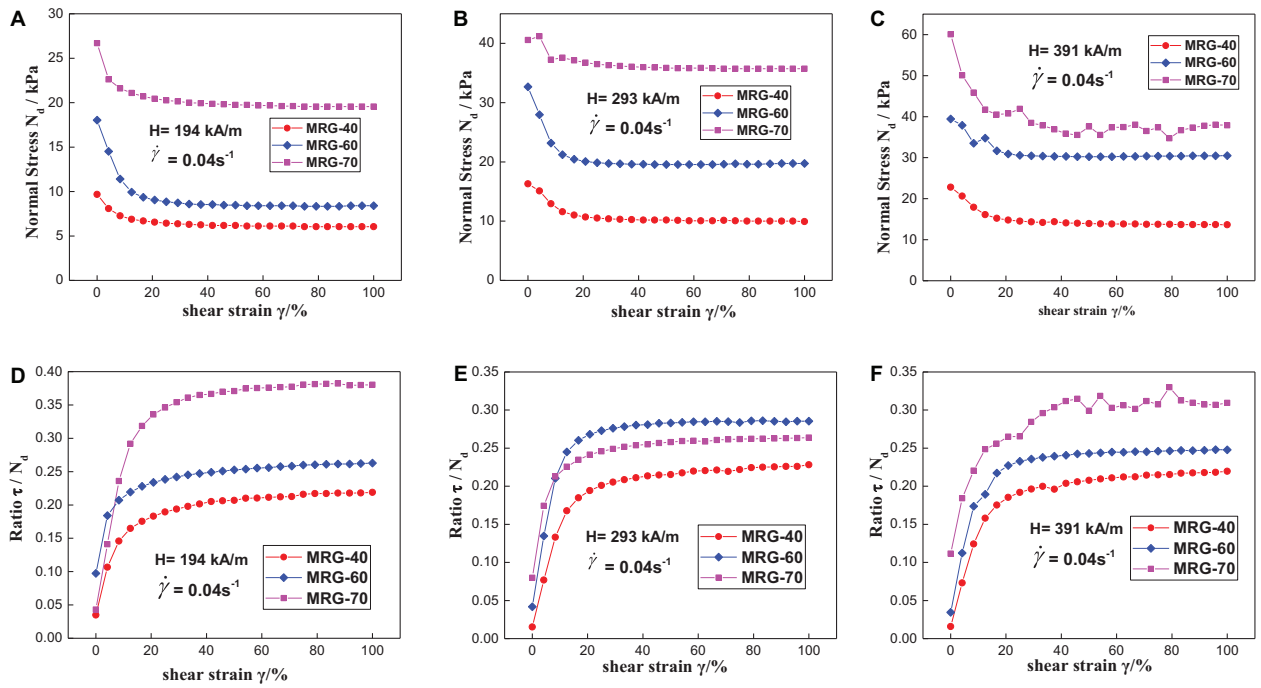

FIGURE 12 | The normal stress as a function of shear strain for magnetorheological gel (MRG) with different carbonyl iron powder (CIP) contents under different magnetic fields: 194 kA/m **(A)**, 293 kA/m **(B)**, and 391 kA/m **(C)**. The ratio of shear stress to normal stress (τ/N_d) as a function of shear strain for MRG with different CIP contents under different magnetic fields: 194 kA/m **(D)**, 293 kA/m **(E)**, and 391 kA/m **(F)**.

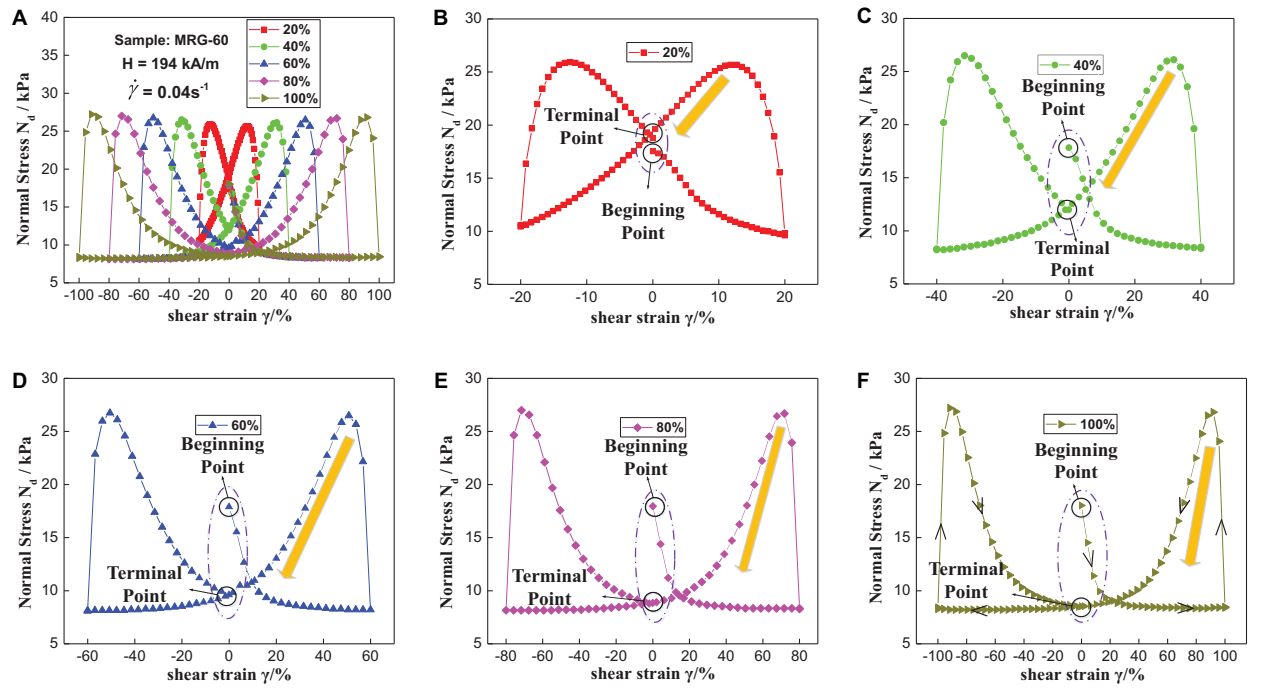

FIGURE 13 | Variation of normal stress with shear strain for MRG-60 under five different shear strain amplitudes **(A)**, i.e., 20% **(B)**, 40% **(C)**, 60% **(D)**, 80% **(E)**, and 100% **(F)**. The black arrows in **(F)** represent the changing trend of normal stress.

a "butterfly-like" shape (**Figure 13A**) to a "tooth-like" shape (**Figures 13C–F**). Moreover, the distances between the beginning point and the terminal point increase progressively with the increase of shear strain amplitudes, which can be intuitively seen from the purple dotted lines in **Figures 13B–F**. In other words, the terminal points of normal stress gradually tend to the steady-state value (i.e., minimum value) with the increase of shear strain amplitudes. For example, the terminal point is 18.79 kPa, and the steady-state value is 9.62 kPa when the shear strain amplitude is 20%. However, the terminal point of normal stress is 8.56 kPa, which is close to the steady-state value (i.e., 8.34 kPa) at the shear strain amplitude of 100%. Another interesting phenomenon is that the "slopes" of normal stress–strain curves at the unloading stage (e.g., shear strain changes from 100 to 0%) become steeper with the increase of shear strain amplitudes, which are shown as yellow arrows in **Figures 13B–F**. These phenomena indicate that normal stress of MRG changes sharply under higher shear strain amplitudes while gently under lower shear strain amplitudes. The results are significantly beneficial for the design of MR devices because the shear strain amplitude is limited by the structure of the devices.

CONCLUSION

This work focuses on the normal stress behavior of MRG under quasi-statically monotonic loading and periodically cyclic loading. The influence of magnetic field, shear rate, CIP content, and shear strain on the normal stress was systematically analyzed. The normal stress is nearly negligible due to the absence of dense particle aggregates when the excited magnetic field is not applied. In the presence of a magnetic field, the normal stress appears in three various stages—a dramatic increase, then a rapid decrease, and finally a steady-state value—corresponding to the three various microstructures (i.e., stable chains along the direction of external magnetic field firstly, then titled long chains under the application of shear and the eventual dynamic equilibrium between the fraction and rebuilding of chains, respectively). The magnetization model, compared with the power model, could better characterize the normal stress behavior of MRG under magnetic field sweeping. Moreover, the normal stress is higher at a smaller shear rate under quasi-static loading, whereas it behaves in an opposite trend under dynamic loading. It also found that the normal stress of MRG decreases with the increase of the shear rate under smaller magnetic field strength. However, the influence of the shear rate on the normal stress almost disappears under higher magnetic field strength because MRG is a highly magnetic field-dependent material. Besides, the larger the CIP content of MRG, the larger the normal stress. The normal stress of MRG-60 could be adjusted from 8.73 to 27.01 kPa at 194 kA/m of magnetic field strength under periodically cyclic loading. The shear strain amplitudes have a strong effect on the changing regularity of normal stress while a weak effect on the magnitude of normal stress. Furthermore, the ratio of shear stress to normal stress, an analog of friction coefficient, was proposed to understand the rheological effect of MRG from a novel perspective. The results demonstrate that the ratio has a great correlation with the excited magnetic field and CIP content. Larger magnetic field strength usually gives rise to the smaller ratio. To achieve a high MR effect or high field-on shear stress, the ratio and normal stress should both be taken into consideration. This is because the increase of normal stress is beneficial for the increase of friction-induced stress. However, the mechanism on how the CIP content influences the ratio still needs to be investigated.

DATA AVAILABILITY STATEMENT

The original contributions presented in the study are included in the article/supplementary material, further inquiries can be directed to the corresponding author.

AUTHOR CONTRIBUTIONS

RM: formal analysis, investigation, and writing – original draft. RM and HW: methodology. GZ: resources. JW: supervision and writing – review and editing. All authors contributed to the article and approved the submitted version.

FUNDING

This work was supported by the National Natural Science Foundation of China (Nos. 51805209, 51705467, and 51675280).

REFERENCES

Ahamed, R., Choi, S. B., and Ferdaus, M. M. (2018). A state of art on magneto-rheological materials and their potential applications. *J. Intel. Mater. Syst. Struct.* 29, 2051–2095. doi: 10.1177/1045389x18754350

Ashtiani, M., Hashemabadi, S. H., and Ghaffari, A. (2015). A review on the magnetorheological fluid preparation and stabilization. *J. Magn. Magn. Mater* 374, 716–730. doi: 10.1016/j.jmmm.2014.09.020

Auernhammer, G. K. (2019). Magnetorheological gels in two and three dimensions: understanding the interplay between single particle motion, internal deformations, and matrix properties. *Arch. Appl. Mech.* 89, 153–165. doi: 10.1007/s00419-018-1479-2

Chen, K. K., Tian, Y., Shan, L., Zhang, X. J., and Meng, Y. G. (2013). The rheological properties of magnetic field excited magnetic powders sheared between two parallel plates. *Smart Mater. Struct.* 22:115036. doi: 10.1088/0964-1726/22/11/115036

de Sousa, S. R. G., dos Santos, M. P., and Bombard, A. J. F. (2019). Magnetorheological gel based on mineral oil and polystyrene-b-poly(ethene-co-butadiene)-b-polystyrene. *Smart Mater. Struct.* 28:105016. doi: 10.1088/1361-665x/ab3600

Gong, X. L., Guo, C. Y., Xuan, S. H., Liu, T. X., Zong, L. H., and Peng, C. (2012). Oscillatory normal forces of magnetorheological fluids. *Soft. Matter.* 8, 5256–5261. doi: 10.1039/c2sm25341k

Guo, C. Y., Gong, X. L., Xuan, S. H., Zhang, Y. L., and Jiang, W. Q. (2012). An experimental investigation on the normal force behavior of magnetorheological suspensions. *Korea Aust. Rheol. J.* 24, 171–180. doi: 10.1007/s13367-012-0021-2

Jiang, J. L., Tian, Y., Ren, D. X., and Meng, Y. G. (2011). An experimental study on the normal stress of magnetorheological fluids. *Smart Mater. Struct.* 20:085012. doi: 10.1088/0964-1726/20/8/085012

Ju, B. X., Yu, M., Fu, J., Zheng, X., and Liu, S. Z. (2013). Magnetic field-dependent normal force of magnetorheological gel. *Ind. Eng. Chem. Res.* 52, 11583–11589. doi: 10.1021/ie4013419

Khazoom, C., Caillouette, P., Girard, A., and Plante, J. S. (2020). A supernumerary robotic leg powered by magnetorheological actuators to assist human locomotion. *IEEE Robot. Autom. Lett.* 5, 5143–5150. doi: 10.1109/lra.2020.3005629

Kuwano, O., Ando, R., and Hatano, T. (2013). "Granular friction in a wide range of shear rates," in *Proceedings of the Powders and Grains 2013 7th International Conference on Micromechanics of Granular Media: AIP Conference Proceedings*, Sydney, Vol. 1542, 32–37.

Lambropoulos, J. C., Miao, C., and Jacobs, S. D. (2010). Magnetic field effects on shear and normal stresses in magnetorheological finishing. *Opt. Express* 18, 19713–19723. doi: 10.1364/oe.18.019713

Laun, H. M., Gabriel, C., and Schmidt, G. (2008). Primary and secondary normal stress differences of a magnetorheological fluid (MRF) up to magnetic flux densities of 1 T. *J. Non Newton Fluid* 148, 47–56. doi: 10.1016/j.jnnfm.2007.04.019

Lemaire, E., and Bossis, G. (1991). Yield stress and wall effects in magnetic colloidal suspensions. *J. Phys. D* 24, 1473–1477. doi: 10.1088/0022-3727/24/8/037

Li, W. H., and Zhang, X. Z. (2008). The effect of friction on magnetorheological fluids. *Korea Aust. Rheol. J.* 20, 45–50.

Li, Y. C., Li, J. C., Li, W. H., and Samali, B. (2013). Development and characterization of a magnetorheological elastomer based adaptive seismic isolator. *Smart Mater. Struct.* 22:035005. doi: 10.1088/0964-1726/22/3/035005

Liu, T. X., Gong, X. L., Xu, Y. G., Pang, H. M., and Xuan, S. H. (2014). Magneto-induced large deformation and high-damping performance of a magnetorheological plastomer. *Smart Mater. Struct.* 23:105028. doi: 10.1088/0964-1726/23/10/105028

Liu, T. X., Xu, Y. G., Gong, X. L., Pang, H. M., and Xuan, S. H. (2013). Magneto-induced normal stress of magnetorheological plastomer. *AIP Adv.* 3:082122. doi: 10.1063/1.4819462

Lopez-Lopez, M. T., Kuzhir, P., Duran, J. D. G., and Bossis, G. (2010). Normal stresses in a shear flow of magnetorheological suspensions: viscoelastic versus Maxwell stresses. *J. Rheol.* 54, 1119–1136. doi: 10.1122/1.3479043

Mao, R. S., Wang, H. X., Zhang, G., Ye, X. D., and Wang, J. (2020). Magneto-induced rheological properties of magnetorheological gel under quasi-static shear with large deformation. *RSC Adv.* 10, 31691–31704. doi: 10.1039/d0ra05843b

Meharthaj, H., Sivakumar, S. M., and Arockiarajan, A. (2019). Significance of particle size on the improved performance of magnetorheological gels. *J. Magn. Magn. Mater.* 490:165483. doi: 10.1016/j.jmmm.2019.165483

Pang, H. M., Pei, L., Sun, C. L., and Gong, X. L. (2018). Normal stress in magnetorheological polymer gel under large amplitude oscillatory shear. *J. Rheol.* 62, 1409–1418. doi: 10.1122/1.5030952

Perez, J. C. L., Kwok, C. Y., O'Sullivan, C., Huang, X., and Hanley, K. J. (2016). Assessing the quasi-static conditions for shearing in granular media within the critical state soil mechanics framework. *Soils Found* 56, 152–159. doi: 10.1016/j.sandf.2016.01.013

Rahman, M., Ong, Z. C., Julai, S., Ferdaus, M. M., and Ahamed, R. (2017). A review of advances in magnetorheological dampers: their design optimization and applications. *J. Zhejiang Univ. Sci. A* 18, 991–1010. doi: 10.1631/jzus.a1600721

Rossi, A., Orsini, F., Scorza, A., Botta, F., Belfiore, N. P., and Sciuto, S. A. (2018). A review on parametric dynamic models of magnetorheological dampers and their characterization methods. *Actuators* 7:16. doi: 10.3390/act7020016

See, H., and Tanner, R. (2003). Shear rate dependence of the normal force of a magnetorheological suspension. *Rheol. ACTA* 42, 166–170. doi: 10.1007/s00397-002-0268-5

Wang, D. H., and Liao, W. H. (2011). Magnetorheological fluid dampers: a review of parametric modelling. *Smart Mater. Struct.* 20:023001. doi: 10.1088/0964-1726/20/2/023001

Wang, H. X., Zhang, G., and Wang, J. (2019). Normal force of lithium-based magnetorheological grease under quasi-static shear with large deformation. *RSC Adv.* 9, 27167–27175. doi: 10.1039/c9ra04987h

Wang, Y., Wang, S., Xu, C., Xuan, S., Jiang, W., and Gong, X. (2016). Dynamic behavior of magnetically responsive shear-stiffening gel under high strain rate. *Compos. Sci. Technol.* 127, 169–176. doi: 10.1016/j.compscitech.2016.03.009

Xu, Y. G., Gong, X. L., Xuan, S. H., Zhang, W., and Fan, Y. C. (2011). A high-performance magnetorheological material: preparation, characterization and magnetic-mechanic coupling properties. *Soft. Matter.* 7, 5246–5254. doi: 10.1039/c1sm05301a

Xu, Y. G., Liu, T. X., Liao, G. J., and Lubineau, G. (2017). Magneto-dependent stress relaxation of magnetorheological gels. *Smart Mater. Struct.* 26:115005. doi: 10.1088/1361-665x/aa89ac

Yang, P., Yu, M., Fu, J., Liu, S., Qi, S., and Zhu, M. (2017). The damping behavior of magnetorheological gel based on polyurethane matrix. *Polym. Compos.* 38, 1248–1258. doi: 10.1002/pc.23689

Yao, X. Y., Liu, C. W., Liang, H., Qin, H. F., Yu, Q. B., and Li, C. (2016). Normal force of magnetorheological fluids with foam metal under oscillatory shear modes. *J. Magn. Magn. Mater.* 403, 161–166. doi: 10.1016/j.jmmm.2015.12.014

Yao, X. Y., Yu, M., and Fu, J. (2015). Magnetic-enhanced normal force of magnetorheological fluids. *Smart Mater. Struct.* 24:035001. doi: 10.1088/0964-1726/24/3/035001

Yazid, I. I. M., Mazlan, S. A., Imaduddin, F., Zamzuri, H., Choi, S. B., and Kikuchi, T. (2016). An investigation on the mitigation of end-stop impacts in a magnetorheological damper operated by the mixed mode. *Smart Mater. Struct.* 25:125005. doi: 10.1088/0964-1726/25/12/125005

Zhang, G., Li, Y. C., Wang, H. X., and Wang, J. (2019). Rheological properties of polyurethane-based magnetorheological gels. *Front. Mater.* 6:56. doi: 10.3389/fmats.2019.00056

Zhang, G., and Wang, J. (2020). A novel phenomenological model for predicting the nonlinear hysteresis response of magnetorheological gel. *Mater. Des.* 196:109074. doi: 10.1016/j.matdes.2020.109074

Zubieta, M., Eceolaza, S., Elejabarrieta, M. J., and Bou-Ali, M. M. (2009). Magnetorheological fluids: characterization and modeling of magnetization. *Smart Mater. Struct.* 18:095019. doi: 10.1088/0964-1726/18/9/095019

Conflict of Interest: The authors declare that the research was conducted in the absence of any commercial or financial relationships that could be construed as a potential conflict of interest.

frontiers in Materials

REVIEW
published: 12 May 2021
doi: 10.3389/fmats.2021.678882

The Roles of Magnetorheological Fluid in Modern Precision Machining Field: A Review

He Lu[1,2], Dezheng Hua[1], Baiyi Wang[1], Chengli Yang[1], Anna Hnydiuk-Stefan[3], Grzegorz Królczyk[4], Xinhua Liu[1,5] and Zhixiong Li[6]**

[1] School of Mechatronic Engineering, China University of Mining and Technology, Xuzhou, China, [2] Lianyungang Normal College, Lianyungang, China, [3] Department of Power Engineering Management, Opole University of Technology, Opole, Poland, [4] Department of Manufacturing Engineering and Automation Products, Opole University of Technology, Opole, Poland, [5] Technology and Innovation Research Center of Jiang Yan EDZ, Taizhou, China, [6] School of Engineering, Ocean University of China, Qingdao, China & Yonsei Frontier Lab, Yonsei University, Seoul, South Korea

OPEN ACCESS

Edited by:
Yancheng Li,
University of Technology Sydney, Australia

Reviewed by:
U. Ubaidillah,
Sebelas Maret University, Indonesia
Xingzhe Wang,
Lanzhou University, China

***Correspondence:**
Xinhua Liu
liuxinhua@cumt.edu.cn
Zhixiong Li
zhixiong.li@yonsei.ac.kr

Specialty section:
This article was submitted to Smart Materials, a section of the journal Frontiers in Materials

Received: *10 March 2021*
Accepted: *19 April 2021*
Published: *12 May 2021*

Citation:
Lu H, Hua D, Wang B, Liu H, Yang C, Hnydiuk-Stefan A, Królczyk G, Liu X and Li Z (2021) The Roles of Magnetorheological Fluid in Modern Precision Machining Field: A Review. Front. Mater. 8:678882. doi: 10.3389/fmats.2021.678882

Owing to some of its specific advantages, magnetorheological fluid (MRF) has drawn significant attention in a broad range of modern precision machining fields. With the diversification and increase in demand, many novel structural configurations and processing methods have been applied to mechanical machining equipment. Although different applications using MRF have been proposed in the existing literature, the classification, latest approaches, and further trend are not understood clearly for the machining field. Therefore, the current applications such as machining auxiliary equipment and surface polishing equipment that used MRF are summarized from 2016 to 2020, in this article. Especially, some detailed structures of equipment are investigated, and relative limitations are analyzed based on the characteristics of MRF. Finally, in view of the current equipment, advantages and defects are briefly reported; the developing trends of modern precision machining with MRF are discussed. Therefore, in the state-of-the-art review, the significant role of MRF in the machining field is emphasized, which paves the way to innovative development and market selection.

Keywords: magnetorheological fluid, machining auxiliary equipment, magnetorheological fluid flexible fixtures, surface polishing equipment, structure configuration

INTRODUCTION

Magnetorheological fluid (MRF) with milliseconds rheological phenomenon and flexible magnetic field controllability has been widely used in the modern precision machining field (Elsaady et al., 2020; Kulandaivel and Kumar, 2020; Nugroho et al., 2020). Based on the transferable and adjustable liquid–colloid state, MRF has unique application advantages in the development of machining auxiliary equipment (Jiang X. H. et al., 2020; Saleh et al., 2020; Lv et al., 2021) and surface polishing equipment (Kumar et al., 2019; Nagdeve et al., 2019; Dubey and Sidpara, 2021; Gupta et al., 2021). Therefore, to improve

product technology and reduce cost, the research of new MRF equipment has become an important direction in the field of mechanical machining (Wang and Meng, 2001; Park et al., 2007; Bedi and Singh, 2016; Liu Z. et al., 2020).

For machining auxiliary equipment such as flexible fixture and damping mechanism, the MRF plays a key role in some research results (Wuertz et al., 2010; Ma, 2017; Jiang et al., 2021; Kumar et al., 2021; Yu et al., 2021; Zhou et al., 2021). In machining production or other technical fields, objects with an irregular surface are difficult to grasp and position by using traditional rigid fixtures, and it is easy to cause damage to the product when the surface contact stress is too large. Therefore, the flexible fixture is essential in the production of machining auxiliary equipment. MRF is a liquid flow state under normal conditions. When an external magnetic field is applied, the material appears in colloid state, whose viscosity is adjustable by an electromagnetic system. Thus, the MRF has been applied to the flexible fixture, where the security control of the product is realized by adjusting the surface hardness of the fixture in real time. Furthermore, in the machining field, such as the technologies of turning, grinding, and boring, a workpiece especially with an unstable structure may produce vibration, therefore, it is necessary that the design of damper reduces the vibration (Cheng et al., 2019; Oladapo et al., 2020; Chen et al., 2021). Because the rheological response of MRF is in milliseconds, the MRF damper has sensitive damping control ability and great application potential in machining (Rahman et al., 2017; Rafajowicz et al., 2020).

Moreover, with the requirements of surface polishing quality and the diversity of polishing materials, the application of MRF to improve the performance of polishing equipment has become a recent research hotspot (Wang Y. et al., 2016; Zhong, 2020). The MRF polishing technology uses a kind of flexible MRF film formed by the rheological properties in the magnetic field to polish the workpiece surface (Aggarwal and Singh, 2011; Jain et al., 2012; Liang et al., 2021; Nguyen et al., 2021). Compared with traditional polishing approaches, there is almost no subsurface damage in the MRF polishing technology. In addition, MRF polishing also has some other advantages, such as recycled MRF, updated abrasive in real time, few tool wear, stable removal function, and controlled hardness of MRF micro-grinding head. Thus, based on the above-mentioned advantages, MRF polishing technology plays an irreplaceable role in special structural surfaces and application requirements.

Having thus described the basic concepts and categorization, some typical machining auxiliary equipment and surface polishing equipment with MRF are investigated from 2016 to 2020. In this work, approximately 70 academic articles have been summarized from the 5 years, which report the application methods, operation modes, and structural configurations of machining equipment with MRF. Considering the above classification, the proportions of different research directions are shown in **Figure 1**. Moreover, some drawbacks of the machining equipment with MRF are also analyzed. For a better understanding of the MRF application, advantages, conclusions, and development tendency of the MRF machining equipment used in modern precision machining field are summarized.

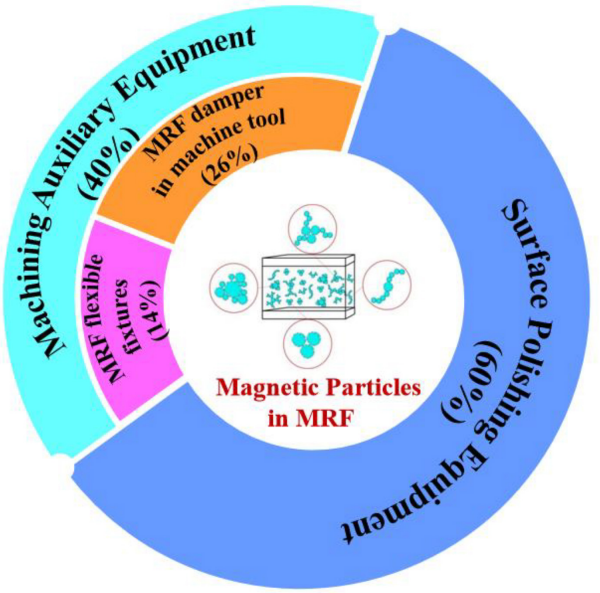

FIGURE 1 | Classification of MRF in modern precision machining according to the referred literature.

MACHINING AUXILIARY EQUIPMENT

Magnetorheological Fluid Flexible Fixtures in Machine Tool

Due to the increasingly complex shape of parts in the modern manufacturing industry, mechanical processing is also developed toward diversification and individuation. MRF flexible fixtures with the characteristic of adjustable hardness have been used for clamping brittle and complex parts, which is an important field in modern precision machining (Kong et al., 2011).

In 2016 and 2017, an MRF flexible fixture was designed to suppress vibration in the machining process for the aerospace industry (see **Figure 2**). To suppress the vibration effect during processing, natural frequency and mode shape function of the thin-walled workpiece are deduced, and a dynamic equation of the workpiece–fixture system considering the external damping factor is proposed (Ma et al., 2016). In addition, a new dynamic analytical model is proposed to determine the effect of the damping factor on the dynamic response of thin-walled workpiece in machining (Ma et al., 2017). In the device, the workpiece is placed in the MRF, whose viscosity is adjusted by the magnetic field of the coil. So, the workpiece is fixed by pushing two sliding blocks symmetrically and processed through a rotary cutter. The device reflects the advantages of the MRF flexible fixture, but there is still displacement error, which reduces the processing accuracy. In 2018, there are no outstanding results of the MRF flexible fixture. Then, an MRF flexible fixture was devised to study its performance as a support for thin-walled parts in 2019, shown in **Figure 3** (Wu, 2019; Liu H. et al., 2020). In the device, a magnetic yoke is added on one side of the electromagnetic coil to optimize the magnetic

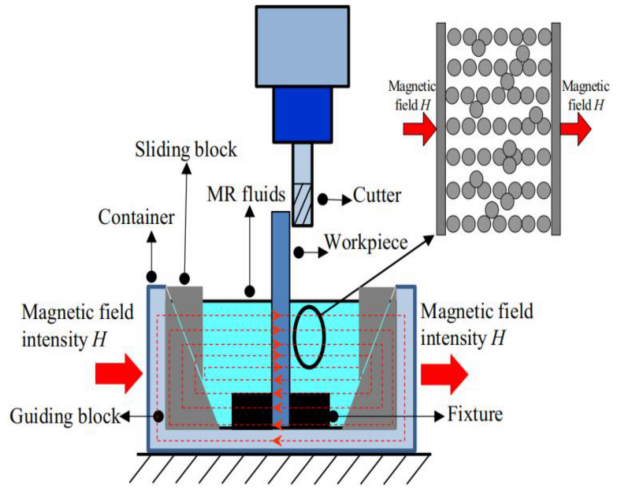

FIGURE 2 | The schematic diagram of flexible fixture system (Ma et al., 2016).

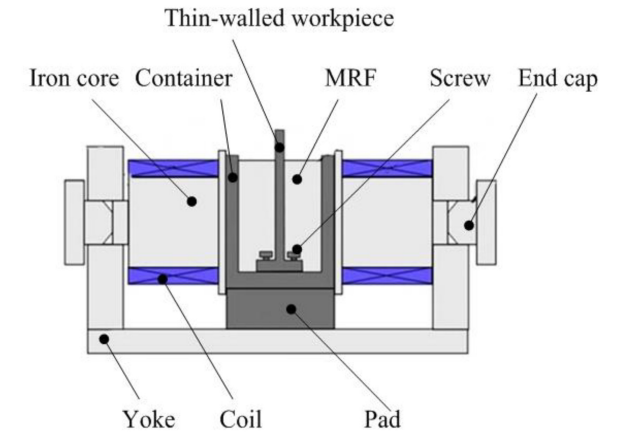

FIGURE 3 | The schematic diagram of a flexible fixture model (Liu H. et al., 2020).

circuit and improve the rheological properties of the MRF. The effectiveness of the device is verified by inhibition tests. However, the improved magnetic field reduces the working space of MRF and limits the application of workpieces with large volumes.

In 2020, a clamping method with a MRF fixture was proposed, and a theoretical model of shear stress was derived to find out the coupling relationship between magnetic field intensity, thickness, and position of a workpiece (Jiang X. et al., 2020). The method can decrease cutting force and improve the accuracy of thin-walled parts by carrying out milling experiments. Moreover, to investigate the effects of vibration on thin-walled workpiece in machining, Jiang X. H. et al. (2020) established a dynamic model based on the Rayleigh damping matrix and the equivalent force principle and proposed an auxiliary support method with MRF. In this method, based on traditional MRF fixture structure, magnetic field distribution is optimized, and the damping force of the workpiece is deduced. The optimum parameters of the MRF fixture such as the MRF volume, location, and magnetic field intensity are determined to suppress the tool vibration.

Magnetorheological Fluid Damper in Machine Tool

With the development of modern machining technology toward high precision and productivity, tool vibration not only damages the machining surface and shortens the life of the tool but also increases the load power of lathe (Jung et al., 2020; Yan et al., 2020). Tool vibration not only damages the machining surface and shortens the life of the tool but also increases the load power of lathe. Thus, various methods are used to reduce the tool vibration, and MRF dampers have been proven to be effective in suppressing vibration and improving performance (Tang et al., 2016; Girinath et al., 2018).

In 2017, to obtain high precision and surface quality, a MRF damper was developed to reduce tool vibration (Paul et al., 2017). The behavior of the tool holder with the MRF damper was investigated, where a vibration model was established to analyze the amplitudes of tool vibration and chip thickness. From their experiment, it was proved that the damping capability of the turning tool and the efficiency of turning operation could be improved considerably. Similarly, a MRF damper was designed to monitor and control the performance of cutting tool for turning operation (Kishore et al., 2018), and a second mode of vibration using finite element software was used to obtain dynamic stability of the cutting tool holder. In this device, transmissibility and half power bandwidth approaches were used to address the dynamic fluctuation of the cutting force. So, the MRF damper could better control the noise and frequency responsible for unstable machining and improve the processing technology in terms of better surface finish on workpieces. Due to the high slenderness ratio of the boring bar, boring operation is highly prone to machining instability. A special boring bar is designed with a rod mounted as an inverse cantilever (Biju and Shunmugam, 2019). As shown in **Figure 4**, vibration of the rod is adjusted by the viscosity of MRF. Experimental results show that it can reduce the amplitude of vibration, surface roughness, and roundness error. For the same purpose, a novel MRF hydrostatic guideway system was designed to control the machining vibration as shown in **Figure 5** (Liu and Hu, 2019). In addition, a computational fluid dynamics model is presented to study the performance parameters of MR hydrostatic guideway system. In this system, some working variables such as magnetic flux density, initial pressure, and load, have been analyzed, and performances such as flow rate, frictional force, and damping of the system have been optimized.

In 2020, a semi-active MRF damper was designed to suppress chatter conditions for the productions of thin-floor components. In the device, enhance multistage homotopy perturbation method and novel cutting force model were used to increase productivity with high surface quality (Puma-Araujo et al., 2020). Furthermore, an MRF damper is proposed to increase the stability of the boring process (Saleh et al., 2021). Besides that, modal analysis is conducted on the boring bar with and without the MR damper to obtain the frequency response

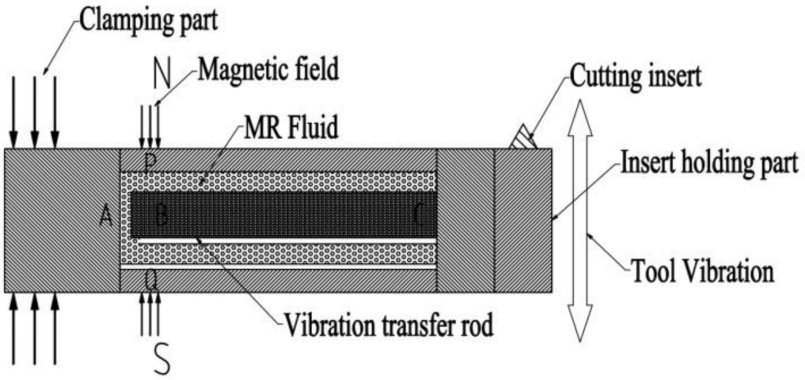

FIGURE 4 | Schematic diagram of boring bar construction (Biju and Shunmugam, 2019).

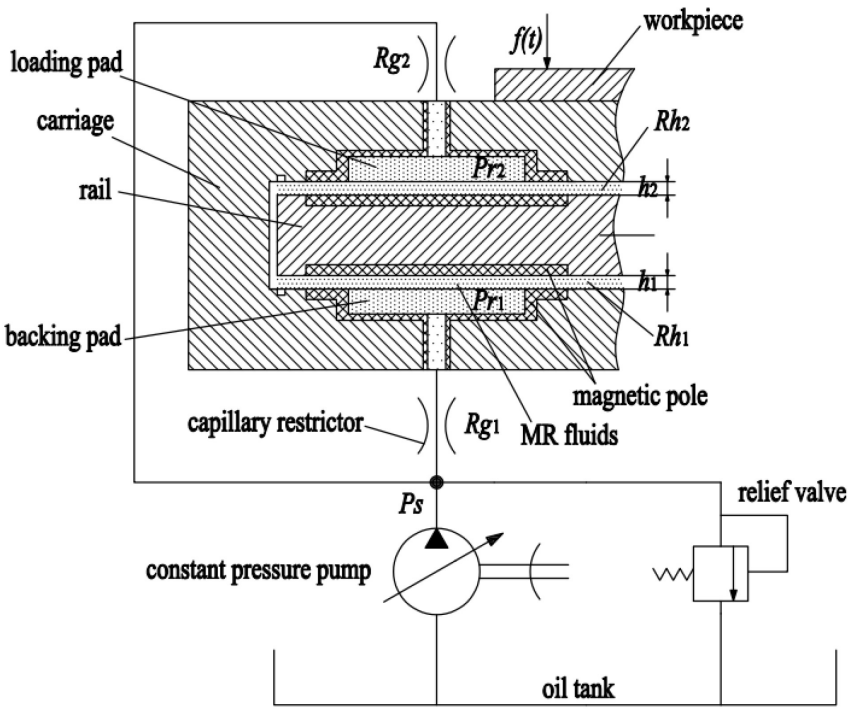

FIGURE 5 | Scheme of MRF hydrostatic guideway system (Liu and Hu, 2019).

functions. As shown in **Figure 6**, the MRF with minimal volume and electromagnetic circuit were placed on the outer part of the boring bar, which makes it easy for installation and adjustability of the bar. The damper has effectively damped the vibrations of the test materials at different modes while using two different boring bars.

Surface Polishing Equipment

Compared with the traditional polishing technology, MRF polishing with super-high precision has been applied to the plane and complex surfaces of the parts (Mutalib et al., 2019). As shown in **Figure 7**, the MRF as a polishing fluid attaches to the surface of the polishing wheel under the action of magnetic field, forming a kind of solid state of ribbon on the contact surface of the polishing wheel and workpiece. Thus, through the shear force in the process of removal of surface material, polishing machining of the workpiece is achieved. After removing the magnetic field in the processing area, MRF returns to liquid state with good fluidity and can be processed by recycling (Golini et al., 1999). The material removal effect conforms to the commonly accepted Preston equation in the field of optical machining, which is described as follows:

$$MRR = KPVt \tag{1}$$

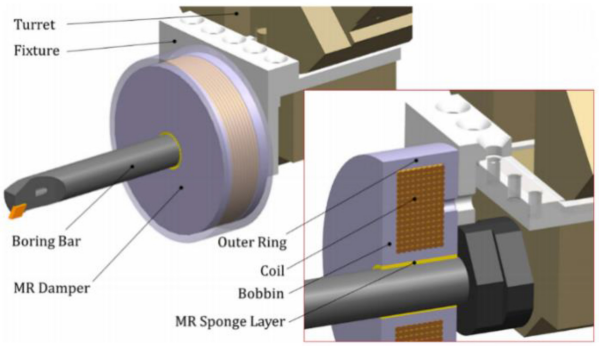

FIGURE 6 | Computer aided design (CAD) model of the boring bar MRF damper with its components (Saleh et al., 2021).

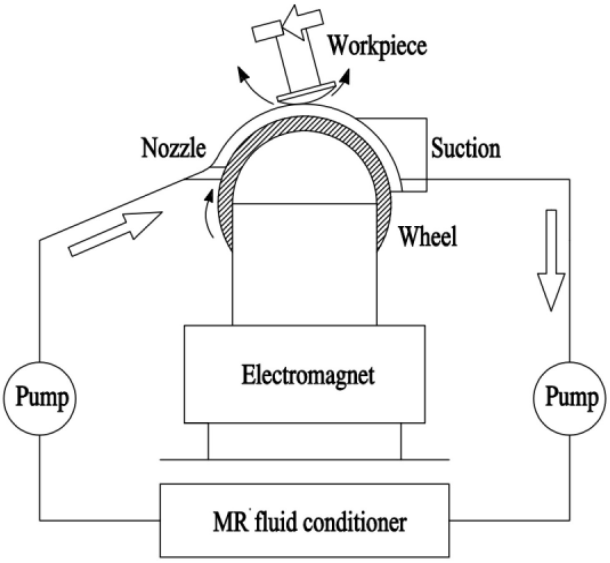

FIGURE 7 | Schematic diagram of magnetorheological polishing equipment (Golini et al., 1999).

where MRR is the amount of material removed from the workpiece surface; K is Preston coefficient, and related to MRF composition, polishing zone temperature, and workpiece material; P represents the pressure of MRF on workpieces; V is the relative speed of the polishing wheel and the workpiece surface in the polishing region; and t is the polishing time.

It can be understood from Equation (1) that in addition to the composition of MRF, the material removal effect is mainly affected by pressure, relative velocity, and polishing residence time. Therefore, to improve the polishing performance of MRF with super-high precision, the influencing parameters of MRF polishing can be optimized from the following three aspects: optimization of MRF to suit different processing materials; research on influence rule of different processing techniques on the shape of the removed material; and control system design of precision magnetorheological polishing.

In 2016, a precision MRF process using a small ball-end permanent-magnet polishing head with a diameter of 4 mm was proposed, where a peristaltic pump was applied to transport the MRF to the workpiece processing area, and MRF from the liquid tank was recycled (Chen et al., 2016). This transmission mode not only avoids the pollution of traditional gear pump but also helps to keep the composition of MRF stable. To suppress the directional surface texture on the workpiece, a dual-rotation MRF finishing (DRMRF) was developed based on the surface texture model for DRMRF and quantitative method of mathematical statistics (Wang Y. Y. et al., 2016). As shown in **Figure 8**, there are two velocities of the wheel that are perpendicular to each other for high surface quality. Similarly, MRF polishing of ultra-smooth surface based on linear air gap permanent yoke excitation is proposed for large polishing mode, shown in **Figure 9** (Wang, 2016). In the device, the particle chain in the MRF is parallel to the surface of the workpiece, which is beneficial to uniform shear force and large effective control area. Moreover, the mathematical model to assess the quantity of material removed was established, and performance parameters such as flatness and material removal rate were analyzed by the model. In addition, a magnetic field–assisted polishing technique was developed for finishing three-dimensional (3D) structured surface with MRF (Wang Y. L. et al., 2016), as shown in **Figure 10**. In the device, the MRF was specifically modified by blending carbonyl-iron (CI) particles, abrasive grains, and α-cellulose into a magnetic fluid.

In 2017, a tool that has the same curvature as a cylindrical surface was developed, which makes the MRF evenly distributed on the surface of the cylinder, and the strength of the CI particles chain is uniformly maintained over the flat tool tip surface (Singh et al., 2016). Because the tool needs to match the machined surface, this method is not suitable for machining complex curved surfaces. Then, a ball-end MR finishing was proposed for complex curved surfaces (Maan et al., 2017), and whose abrasive wear mechanism was also studied by Alam and Jha (2017). In terms of freeform surfaces, a MRF polishing tool was proposed, where a permanent magnet was used to control the rheological properties of the MRF (Barman and Das, 2017). The dimensions of the tool were optimized with finite element software for a smooth grinding process with low energy consumption. Furthermore, a solid core rotating tool with MRF was developed for finishing of hardened AISI 52100 steel (Maan and Singh, 2018). In this device, response surface methodology was used for the parametric analysis of MRF nanofinishing process, and thus surface cracks generated by the traditional finishing process are eliminated. As the surface morphology of bio-titanium alloy has a great influence on its application, Barman and Das (2018) studied the characteristics of titanium alloy polished by two types of MRFs. From the results, the surface performance obtained from the MRF containing HF and HNO_3 is better suited for the semi-permanent type of implants or implants which partake in relative motion, while MRF containing H_2O_2 is better suited for permanent implants. In addition, as the material removal rate achieved with MRF polishing is relatively low, the concepts of gap slope and virtual ribbon were used to develop a model of removal profiles in Belt-MRF, and the factors

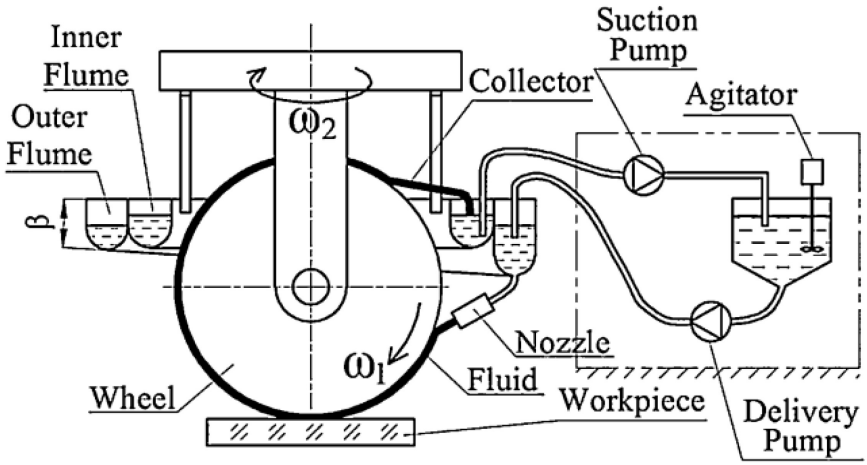

FIGURE 8 | The circulatory subsystem of DRMRF tool (Wang Y. Y. et al., 2016).

in the MRF polishing process were analyzed. From the results, the magnetic field, the composition of the CI powder, and the polishing depth have the greatest effect on material removal rate (MRR) (Wang et al., 2017; Kim et al., 2018).

In 2019, to eliminate the labor-intensive efforts and the subjective errors, a five-axis CNC ball-end MR finishing process in a fully automated manner was developed to the 3D surfaces of the workpiece (Alam et al., 2019). In this device, a customized controller was proposed, which enables the precise and sequential control of motion as well as process parameters. Furthermore, a material removal rate model of MRF finishing with dynamic magnetic fields is proposed to analyze various technological parameters such as rotational speeds of workpieces, magnetic poles, polishing disk, and machining gap (Pan et al., 2019). As shown in **Figure 11**, dynamic magnetic field is arranged in the device. In this model, the theoretical simulation results favorably agree with the experimental results. Similarly, some process parameters have been optimized using response surface methodology (Chana and Singh, 2019). By using the optimized parameters, the surface finish was reduced to 70 nm from 480 nm in 23 h, and power consumption was reduced by 25%. For finishing of small holes, an MRF finishing set-up was designed, where higher values of supply current, fluid flow rate, and finishing time with flat-pole geometry have generated optimal machining performance characteristics (Kataria and Mangal, 2019). In addition, due to the disadvantage of wheel-type MRF finishing single-point processing, multiple polishing heads with MRF are proposed, where multiple magnets are used to form a specific magnetic field and a plurality of flexible polishing heads are formed on

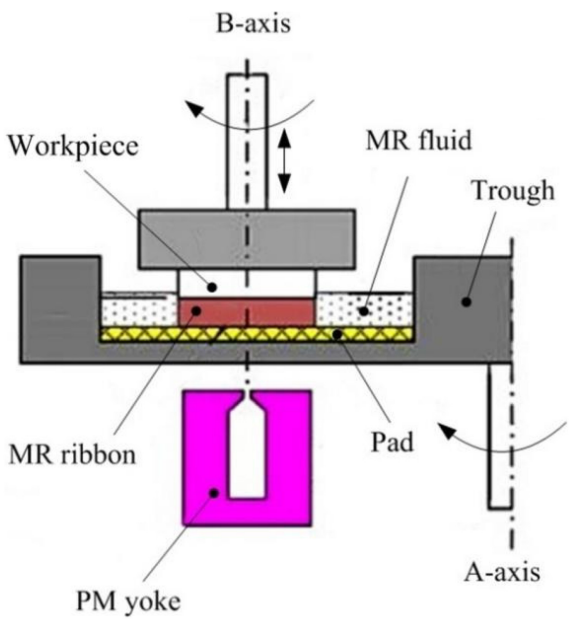

FIGURE 9 | Schematic diagram of magnetorheological plane polishing (Wang Y. et al., 2016).

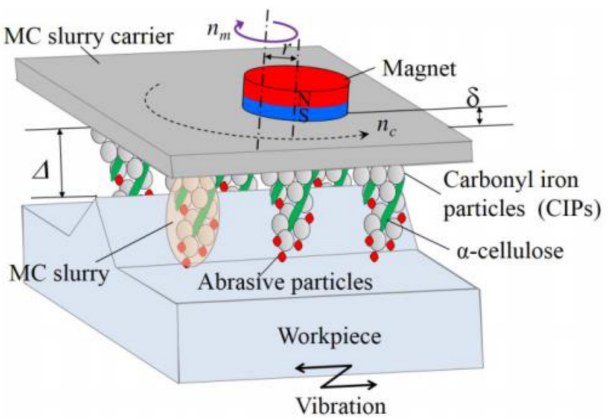

FIGURE 10 | The magnetic compound (MC) slurry polishing principle (Wang Y. L. et al., 2016).

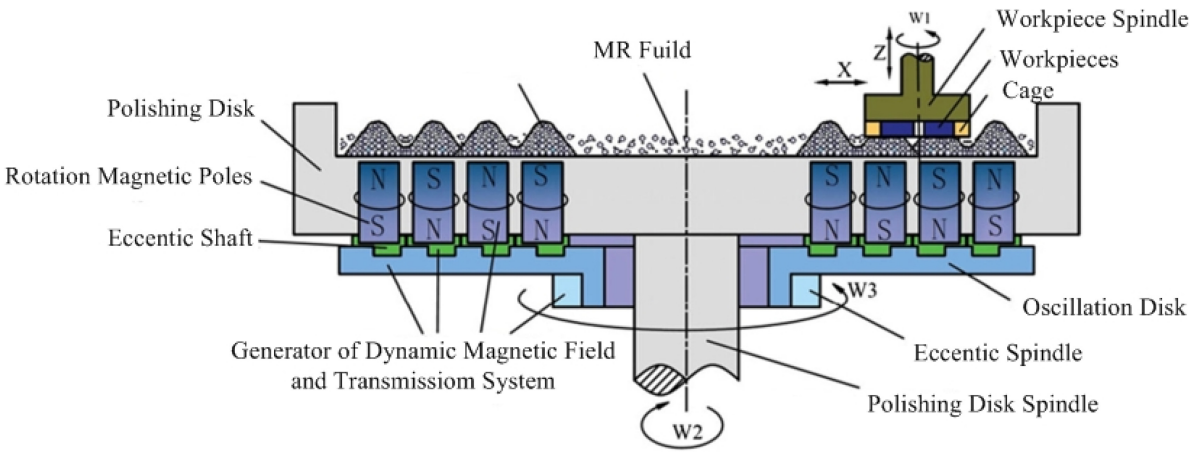

FIGURE 11 | MRF finishing with dynamic magnetic fields (Bin, 2019).

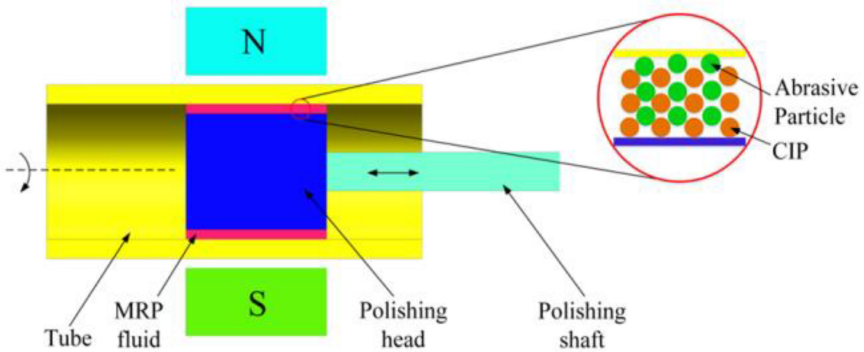

FIGURE 12 | Schematic diagram of novel polishing principle (Ghosh et al., 2021).

the surface of the heads to process the surface of the workpiece (Bin, 2019).

Recently, Yadav et al. (2020) found that the traditional and advanced gear teeth profile finishing processes without the control over the finishing forces produce different types of defects such as micro-pitting, abrasive wear, and scuffing. So, a process called MRF gear profile finishing was proposed (Yadav et al., 2020), where the parametric study for finishing of the EN24 hardened steel spur gear teeth profile was successfully demonstrated with the technology, and the functional life of gears has been significantly improved. A magnetic field–assisted finishing tool for titanium workpiece has been developed, which consists of a cylindrical permanent magnet and a magnet fixing device (Barman and Das, 2019). There are parallel and helical tool paths in the magnetic field–assisted finishing (MFAF) process, and the lowest surface roughness produced by parallel tool paths has better surface texture than helical tool paths. The reason is that the surface topography and surface texture show reduced surface roughness and scratches when the surface is finished using parallel tool paths. To enhance the surface of the tapered cylindrical workpiece, an MRF finishing process is developed with magnetic rheological polishing (Singh and Singh, 2021). In the device, some parameters such as the variation in linear velocity, helix angle, and the helical path are analyzed to perform uniform finishing on the variable surface. Moreover, a new method with MRF for polishing flat borosilicate glass surfaces has been developed (Zhang et al., 2020). For this method, a reciprocating polishing tester is designed, which uniformly supplies the MRF to produce a flat surface on the workpiece. This greatly reduces the number of peaks and pits on the surface of borosilicate glass and gives a good polishing effect. The finishing forces during the MRF polishing process are analyzed and modeled, where the final surface roughness model has been proposed to predict the polishing performance. The results show a gradual growth of surface precision with polishing time and an augment of polishing efficiency with increasing initial surface roughness (Peng et al., 2020). Moreover, a theoretical model was developed to predict the reduction in the surface asperities during the magnetorheological finishing of the external cylindrical surfaces. The percentage error is from 4.76 to 3.06%, which shows good agreement between the theoretical model and the experimental results (Singh and Singh, 2020). A novel MRF polishing process is developed to use in the internal surface of titanium alloy tubes (Song et al., 2020). In this process, rotation

TABLE 1 | The techniques and application of MRF surface polishing equipment in 2016–2020.

No.	Techniques	Application	References
1	Small ball-end permanent-magnet polishing	Small concave surfaces	Chen et al., 2016
2	Dual-rotation magnetorheological polishing	Directional surface	Wang Y. Y. et al., 2016
3	Large magnetorheological polishing	Ultra-smooth flat surface	Wang Y. et al., 2016
4	A magnetic compound (MC) slurry	Mirror surface of miniature V-grooves	Wang Y. L. et al., 2016
5	Curved tool tip surface magnetorheological polishing	External cylindrical surfaces	Singh et al., 2016
6	MR ball end with solid rotating tool core magnetorheological polishing	Nano surface	Maan et al., 2017
7	Ball-end magnetorheological finishing process	Complex 3D surfaces	Alam and Jha, 2017
8	Magnetic field–assisted finishing (MFAF) process	Freeform surfaces	Barman and Das, 2017
9	Magnetorheological solid core rotating polishing	Hardened AISI 52100 steel surfaces	Maan and Singh, 2018
10	Novel MFAF polishing	Bio-titanium workpiece surface	Barman and Das, 2018
11	Magnetorheological fluid polishing by an electromagnet with straight-pole piece	Aluminum alloy (Al6061-T5) workpiece surface	Kim et al., 2018
12	Belt magnetorheological finishing	Large-aperture optics surfaces	Wang et al., 2017
13	Automated five-axis CNC ball-end magnetorheological finishing	Nanofinishing of 3D surfaces	Alam et al., 2019
14	Cluster magnetorheological finishing with dynamic magnetic fields	Single-crystal silicon substrates	Pan et al., 2019
15	Magnetorheological solid core rotating tool	AISI H13 die steel cylindrical surface	Chana and Singh, 2019
16	Continuous flow magnetorheological fluid finishing process	Small holes of aluminum 6063 alloy-based metal matrix composite	Kataria and Mangal, 2019
17	Multiple polishing heads magnetorheological finishing	Optical components surface	Bin, 2019
18	Magnetorheological gear profile finishing process	Gear profile surface	Yadav et al., 2020
19	MFAF process	Bio-titanium alloy surface	Barman and Das, 2019
20	Magnetorheological solid core rotating polishing	Tapered cylindrical AISI grade D2 tool steel workpieces surface	Singh and Singh, 2021
21	Reciprocating MR polishing method	Borosilicate glass surface	Zhang et al., 2020
22	Novel magnetorheological polishing (MRP) process	Internal surface of titanium alloy tubes	Peng et al., 2020
23	Compound magnetic field magnetorheological (MR) polishing	Annular surface of titanium tubes	Song et al., 2020
24	Wheel-based magnetorheological finishing process	Oxygen-free high conductivity (OFHC) copper surface	Ghosh et al., 2021

motion of tube and reciprocating linear motion of polishing head are carried out simultaneously resulting in helical motion trajectory of abrasive particles on the workpiece surface, as shown in **Figure 12**. Because of the extremely lower hardness of copper, wheel-based MRF finishing process has been developed to attain Nano-level surface roughness (Ghosh et al., 2021). In the process, the main controlling parameters, such as the wheel speed, working gap, and feed rate are analyzed, where the MRF with a higher working gap, lower wheel speed, and feed rate can realize Nano-level surface roughness.

The techniques and application of MRF surface polishing equipment, developed during 2016–2020, are summarized in **Table 1**. As can be seen from the table, MRF surface polishing can be applied to the workpiece with various complex surfaces of both metal and non-metallic materials.

MRF polishing process becomes one of the most promising green and intelligent precision machining methods in the future. There is a trend toward the development of the MRF polishing process with super-high precision research from miniaturization (below millimeter) with complex shape workpiece to large scale (several meters) with ultra-smooth flat surface. To obtain precision control, MR polishing equipment is being developed to achieve intelligent control.

CONCLUSION

In this work, studies on the main applications of MRF in modern precision machining field from 2016 to 2020 are reviewed, which include machining auxiliary equipment and surface polishing equipment. Furthermore, machining auxiliary equipment is divided into MRF flexible fixture and MRF damper in the machine tool. Through the above literature, it is understood that several MRF precision machining technologies focused on the

composition of MRF, the arrangement of space magnetic field, and the structural configuration of the equipment.

Because the solid–liquid state of MRF is controlled by the external magnetic field, the MRF flexible fixture can clamp the parts with complex shape, which is convenient for processing. However, the research work on MRF flexible fixture, which is mainly used for processing small parts, is still in the laboratory stage. For larger objects such as the aviation and marine parts, the required MRF flexible fixture will be large, which is not easy to achieve in terms of technology and cost. In addition, with the increasingly complex shapes of the modern machining parts, the MRF flexible fixture has a good development prospect, but the working stability of this fixture needs to be further improved.

The application of MRF damper to suppress tool vibration is a new research field in recent years. Compared with the traditional damper, the MRF damper can better suppress the vibration of the machine tool, prolong the life of the tool, and improve the performance of the machine tool. However, the research methods are relatively simple at present, which mainly include the improvement of semi-active controller, the optimization of magnetic circuit design, and the stability of MRF performance. Due to the complex and variable vibrations in machine tool machining processes, there are few research studies on damper control algorithms. Therefore, it is urgent to improve the control effect of the machine tool and reduce adverse vibrations in the existing structural equipment.

In terms of surface polishing equipment, MRF with conversion in milliseconds forms solid state on the parts that need to be processed and turns into liquid state while taking away the debris, which ensures the accuracy of processing and improves the efficiency of processing. The MRF polishing processing has irreplaceable advantages compared with traditional polishing and has been widely used in precision and ultra-precision machining. But, the current MRF polishing equipment also needs to strengthen the magnetic rheological polishing research on the non-spherical surfaces, broaden processing adaptability, improve the machining efficiency, and reduce the processing cost.

As a new type of intelligent material, MRF has excellent performance in the field of modern precision machining. It may be further developed in the following three aspects in the future. The stability and heat dissipation of MRF are the bottlenecks, limiting its application at present, and the problem of accurate control of MRF has not been solved. With the deepening of research on MRF, the performance of MRF could be further improved. Furthermore, MRF can cooperate with various magnetic materials and magnetic structures rather than the electromagnetic field and permanent magnet, to achieve specific functions and reduce electrical energy consumption and equipment costs. Finally, the research in the field of MRF machining is still in the laboratory stage, which is mainly customized by users and has not yet achieved universality. With the in-depth study of the processing technology and system control strategy by scholars, different MRF machining equipment will be widely used.

AUTHOR CONTRIBUTIONS

HL and CY: writing original manuscript. DH: software. BW: resources. AH-S: methodology. GK: editing and review. XL: funding. ZL: supervising. All authors contributed to the article and approved the submitted version.

FUNDING

This work was supported by the National Science Foundation of China (No. 51975568), the Natural Science Foundation of Jiangsu Province (No. BK20191341), the Natural Science Foundation of the Jiangsu Higher Education Institution of China (20KJD460005), the Youth Talents Program (LSZQNXM202001), the Priority Academic Program Development of Jiangsu Higher Education Institutions (PAPD), and the Key scientific research project of Suzhou University (2017yzd14) in carrying out this research are gratefully acknowledged.

REFERENCES

Aggarwal, A., and Singh, A. K. (2011). Development of grinding wheel type magnetorheological finishing process for blind hole surfaces. *Mater. Manuf. Process.* 36, 457–478. doi: 10.1080/10426914.2020.1843666

Alam, Z., Iqbal, F., Ganesan, S., and Jha, S. (2019). Nanofinishing of 3D surfaces by automated five-axis CNC ball end magnetorheological finishing machine using customized controller. *Intern. J. Adv. Manuf. Technol.* 100, 1031–1042. doi: 10.1007/s00170-017-1518-0

Alam, Z., and Jha, S. (2017). Modeling of surface roughness in ball end magnetorheological finishing (BEMRF) process. *Wear* 374, 54–62. doi: 10.1016/j.wear.2016.11.039

Barman, A., and Das, M. (2017). Design and fabrication of a novel polishing tool for finishing freeform surfaces in magnetic field assisted finishing (MFAF) process. *Precis. Eng.* 49, 61–68. doi: 10.1016/j.precisioneng.2017.01.010

Barman, A., and Das, M. (2018). Nano-finishing of bio-titanium alloy to generate different surface morphologies by changing magnetorheological polishing fluid compositions. *Precis. Eng.* 51, 145–152. doi: 10.1016/j.precisioneng.2017.08.003

Barman, A., and Das, M. (2019). Toolpath generation and finishing of bio-titanium alloy using novel polishing tool in MFAF process. *Intern. J. Adv. Manuf. Technol.* 100, 1123–1135. doi: 10.1007/s00170-017-1050-2

Bedi, T. S., and Singh, A. K. (2016). Magnetorheological methods for nanofinishing – a review. *Partic. Sci. Technol.* 34, 412–422. doi: 10.1080/02726351.2015.1081657

Biju, C. V., and Shunmugam, M. S. (2019). Performance of magnetorheological fluid based tunable frequency boring bar in chatter control. *Measurement* 140, 407–415. doi: 10.1016/j.measurement.2019.03.073

Bin, S. M. (2019). *Device Design and Experimental Research of Magnetorheological Finishing with Multiple Polishing Heads [D]*. Guangzhou: Guangdong University of Technology.

Chana, A., and Singh, A. K. (2019). Magnetorheological nano-finishing of tube extrusion punch for improving its functional applications in press machine. *Intern. J. Adv. Manuf. Technol.* 103, 2037–2052. doi: 10.1007/s00170-019-03633-1

Chen, K., Yu, X., Wang, H., Zheng, H., Zhang, G., and Wu, R. (2021). Modeling of a Bingham model of a magnetorheological damper considering stochastic

uncertainties their geometric variables. *J. Theoret. Appl. Mechan.* 59, 53–65. doi: 10.15632/jtam-pl/128811

Chen, M. J., Liu, H. N., Su, Y. R., Yu, B., and Fang, Z. (2016). Design and fabrication of a novel magnetorheological finishing process for small concave surfaces using small ball-end permanent-magnet polishing head. *Intern. J. Adv. Manuf. Technol.* 83, 823–834. doi: 10.1007/s00170-015-7573-5

Cheng, M., Xing, J., Chen, Z., and Pan, Z. (2019). Design, Analysis and experimental investigation on the whole-spacecraft vibration isolation platform with magnetorheological dampers. *Smart Mater. Struct.* 28:075016. doi: 10.1088/1361-665X/ab0ebe

Dubey, N. K., and Sidpara, A. (2021). Numerical and experimental study of influence function in magnetorheological finishing of oxygen-free high conductivity (OFHC) copper. *Smart Mater. Struct.* 30:015034. doi: 10.1088/1361-665X/abcca5

Elsaady, W., Oyadiji, S. O., and Nasser, A. (2020). A review on multi-physics numerical modelling in different applications of magnetorheological fluids. *J. Intellig. Mater. Syst. Struct.* 31, 1855–1897. doi: 10.1177/1045389X20935632

Ghosh, G., Sidpara, A., and Bandyopadhyay, P. P. (2021). Experimental and theoretical investigation into surface roughness and residual stress in magnetorheological finishing of OFHC copper. *J. Mater. Process. Technol.* 288:116899. doi: 10.1016/j.jmatprotec.2020.116899

Girinath, B., Mathew, A., Babu, J., Thanikachalam, J., and Bose, S. S. (2018). Improvement of surface finish and reduction of tool wear during hard turning of AISI D3 using magnetorheological damper. *J. Sci. Industr. Res.* 77, 35–40.

Golini, D., Kordonski, W. I., Dumas, P., and Hogan, S. (1999). Magnetorheological finishing (MRF) in commercial precision optics manufacturing. *Proc. SPIE Intern. Soc. Optic. Eng.* 3782, 80–91. doi: 10.1117/12.369174

Gupta, M. K., Dinakar, D., Chhabra, I. M., Jha, S., and Madireddy, B. S. (2021). Experimental investigation and machine parameter optimization for nano finishing of fused silica using magnetorheological finishing process. *Optik* 226:165908. doi: 10.1016/j.ijleo.2020.165908

Jain, V. K., Sidpara, A., Sankar, M. R., and Das, M. (2012). Nano-finishing techniques: a review. *Proc. Institut. Mech. Eng. Part C J. Mech. Eng. Sci.* 226, 327–346. doi: 10.1177/0954406211426948

Jiang, M., Rui, X., Zhu, W., Yang, F., and Zhang, Y. (2021). Design and control of helicopter main reducer vibration isolation platform with magnetorheological dampers. *Intern. J. Mech. Mater. Design* 144, 1–22. doi: 10.1007/s10999-021-09529-x

Jiang, X., Zhang, Y., Lu, W., Gao, S., Liu, L., and Liu, X. (2020). Characteristics of shear stress based on magnetorheological fluid flexible fixture during milling of the thin-walled part. *Intern. J. Adv. Manufact. Technol.* 108, 2607–2619. doi: 10.1007/s00170-020-05439-y

Jiang, X. H., Zhao, G. K., and Lu, W. W. (2020). Vibration suppression of complex thin-walled workpiece based on magnetorheological fixture. *Intern. J. Adv. Manuf. Technol.* 106, 1043–1055. doi: 10.1007/s00170-019-04612-2

Jung, H., Hayasaka, T., Shamoto, E., and Xu, L. (2020). Suppression of forced vibration due to chip segmentation in ultrasonic elliptical vibration cutting of titanium alloy Ti-6Al-4V. *Precis. Eng.* 64, 98–107. doi: 10.1016/j.precisioneng.2020.03.017

Kataria, M., and Mangal, S. K. (2019). Development of continuous flow magnetorheological fluid finishing process for finishing of small holes. *J. Braz. Soc. Mech. Sci. Eng.* 41:551. doi: 10.1007/s40430-019-2027-x

Kim, B. C., Chung, J. H., Cho, M. W., Ha, S. J., and Yoon, G. S. (2018). Magnetorheological fluid polishing using an electromagnet with straight pole-piece for improving material removal rate. *J. Mech. Sci. Technol.* 32, 3345–3350. doi: 10.1007/s12206-018-0637-3

Kishore, R., Choudhury, S. K., and Orra, K. (2018). On-line control of machine tool vibration in turning operation using electro-magneto rheological damper. *J. Manuf. Process.* 31, 187–198. doi: 10.1016/j.jmapro.2017.11.015

Kong, J. X., Zheng, Y. C., and Wang, X. K. (2011). Fixture design based on magneto-rheological fluids for thin wall spherical shell precision machining. *Adv. Mater. Res.* 215, 315–319.

Kulandaivel, A., and Kumar, S. (2020). Effect of magneto rheological minimum quantity lubrication on machinability, wettability and tribological behavior in turning of Monel K500 alloy. *Machin. Sci. Technol.* 24, 810–836. doi: 10.1080/10910344.2020.1765179

Kumar, A., Alam, Z., Khan, D. A., and Jha, S. (2019). Nanofinishing of FDM-fabricated components using ball end magnetorheological finishing process. *Adv. Manuf. Process.* 34, 232–242. doi: 10.1080/10426914.2018.1512136

Kumar, T., Kumar, R., and Jain, S. C. (2021). Numerical investigation of semi-active torsional vibration control of heavy turbo-generator rotor using magnetorheological fluid dampers. *J. Vibr. Eng. Technol.* 93, 1–15. doi: 10.1007/s42417-020-00276-5

Liang, H., Yan, Q., Pan, J., Luo, B., Lu, J., and Zhang, X. (2021). Characteristics of forces in plane polishing based on the magnetorheological effect with dynamic magnetic fields formed by rotating magnetic poles. *J. Test. Eval.* 49, 255–269. doi: 10.1520/JTE20180769

Liu, C. P., and Hu, J. P. (2019). A magnetorheological hydrostatic guideway system for machining vibration control. *J. Braz. Soc. Mech. Sci. Eng.* 41, 1–12. doi: 10.1007/s40430-018-1525-6

Liu, H., Wang, J., Luo, Q., Bo, Q., Li, T., and Wang, Y. (2020). Effect of controllable magnetic field-induced MRF solidification on chatter suppression of thin-walled parts. *Intern. J. Adv. Manuf. Technol.* 109, 2881–2890. doi: 10.1007/s00170-020-05783-z

Liu, Z., Li, J., Nie, M., and Liu, Y. (2020). Modeling and simulation of workpiece surface flatness in magnetorheological plane finishing processes. *Intern. J. Adv. Manuf. Technol.* 111, 2637–2651. doi: 10.1007/s00170-020-06267-w

Lv, H., Zhang, S., Sun, Q., Chen, R., and Zhang, W. (2021). The dynamic models, control strategies and applications for magnetorheological damping systems: a systematic review. *J. Vibr. Eng. Technol.* 9, 131–147. doi: 10.1007/s42417-020-00215-4

Ma, J., Zhang, D., Wu, B., Luo, M., and Chen, B. (2016). Vibration suppression of thin-walled workpiece machining considering external damping properties based on magnetorheological fluids flexible fixture. *Chin. J. Aeronaut.* 29, 1074–1083. doi: 10.1016/j.cja.2016.04.017

Ma, J., Zhang, D., Wu, B., Luo, M., and Liu, Y. (2017). Stability improvement and vibration suppression of the thin-walled workpiece in milling process via magnetorheological fluid flexible fixture. *Intern. J. Adv. Manuf. Technol.* 88, 1231–1242. doi: 10.1007/s00170-016-8833-8

Ma, J. J. (2017). *Dynamic Model and Reconstruction Method of Magnetorheological Damping Support Fixture-Workpiece System [D]*. Xi'an: Northwestern Polytechnical University.

Maan, S., and Singh, A. K. (2018). Nano-surface finishing of hardened AISI 52100 steel using magnetorheological solid core rotating tool. *Intern. J. Adv. Manuf. Technol.* 95, 513–526. doi: 10.1007/s00170-017-1209-x

Maan, S., Singh, G., and Singh, A. K. (2017). Nano-surface-finishing of permanent mold punch using magnetorheological fluid-based finishing processes. *Mater. Manuf. Process.* 32, 1004–1010. doi: 10.1080/10426914.2016.1232823

Mutalib, N. A., Ismail, I., Soffie, S. M., and Aqida, S. N. (2019). Magnetorheological finishing on metal surface: a review. *IOP Conf. Ser. Mater. Sci. Eng.* 469:012092. doi: 10.1088/1757-899X/469/1/012092

Nagdeve, L., Jain, V. K., and Ramkumar, J. (2019). Preliminary investigations into nano-finishing of freeform surface (femoral) using inverse replica fixture. *Intern. J. Adv. Manuf. Technol.* 100, 1081–1092. doi: 10.1007/s00170-017-1459-7

Nguyen, D., Wu, J. Z., Quang, N. M., Duc, L. A., and Son, P. X. (2021). Applying fuzzy grey relationship analysis and Taguchi method in polishing surfaces of magnetic materials by using magnetorheological fluid. *Intern. J. Adv. Manuf. Technol.* 112, 1675–1689. doi: 10.1007/s00170-020-06567-1

Nugroho, K. C., Ubaidillah, P. B., Mas'udi, A., Nordin, N., Mazlan, S., and Choi, S. (2020). The effect of MnxCo(1-x) Fe_2O_4 with x =0, 0.25 and 0.5 as nanoparticles additives in magnetorheological fluid. *Smart Mater. Struct.* 29:114004. doi: 10.1088/1361-665X/abb354

Oladapo, B. I., Muhammad, M. A., Adebiyi, V. A., Oluwole, B., and Usman, H. (2020). Model hybrid magnetorheological damping prediction in machine tools. *Eng. Struct.* 213:110621. doi: 10.1016/j.engstruct.2020.110621

Pan, J. S., Guo, M. L., Yan, Q. S., Zheng, K., and Xiao, X. L. (2019). Research on material removal model and processing parameters of cluster magnetorheological finishing with dynamic magnetic fields. *Intern. J. Adv. Manuf. Technol.* 100, 2283–2297. doi: 10.1007/s00170-018-2747-6

Park, G., Bement, M. T., Hartman, D. A., Smith, R. E., and Farrar, C. R. (2007). The use of active materials for machining processes: a review. *Intern. J. Adv. Manuf. Technol.* 47, 2189–2206. doi: 10.1016/j.ijmachtools.2007.06.002

Paul, P. S., Sunil, K. S., and Varadarajan, A. S. (2017). The Effect of cutting parameters on tool vibration during magnetorheological fluid controlled turning bar. *Intern. J. Acoust. Vibr.* 22, 27–33. doi: 10.20855/ijav.2017.22.1447

Peng, Z., Song, W. L., Ye, C. L., Shi, P., and Choi, S. B. (2020). Model establishment of surface roughness and experimental investigation on magnetorheological finishing for polishing the internal surface of titanium alloy tubes. *J. Intellig. Mater. Syst. Struct.* 1, 1–12. doi: 10.1177/1045389X20930095

Puma-Araujo, S. D., Olvera-Trejo, D., Martinez-Romero, O., Urbikain, G., Elias-Zuniga, A., and Lopez de Lacalle, L. N. (2020). Semi-active magnetorheological damper device for chatter mitigation during milling of thin-floor components. *Appl. Sci. Basel* 10:5313. doi: 10.3390/app10155313

Rafajowicz, W., Wickowski, J., Moczko, P., and Rafajlowicz, E. (2020). Iterative learning from suppressing vibrations in construction machinery using magnetorheological dampers. *Autom. Construct.* 119:103326. doi: 10.1016/j.autcon.2020.103326

Rahman, M., Ong, Z. C., Julai, S., Ferdaus, M. M., and Ahamed, R. (2017). A review of advances in magnetorheological dampers: their design optimization and applications. *J. Zhejiang Univ. Sci. A* 18, 991–1010. doi: 10.1631/jzus.A1600721

Saleh, M. K. A., Nejatpour, M., Acar, H. Y., and Lazoglu, I. (2021). A new magnetorheological damper for chatter stability of boring tools. *J. Mater. Process. Technol.* 289:116931. doi: 10.1016/j.jmatprotec.2020.116931

Saleh, M. K. A., Nejatpour, M., Acar, H. Y., and Lazoglu, L. (2020). A new magnetorheological damper for chatter stability of boring tools. *J. Mater. Process. Technol.* 289:116931.

Singh, G., Singh, A. K., and Garg, P. (2016). Development of magnetorheological finishing process for external cylindrical surfaces. *Mater. Manuf. Process.* 32, 581–588. doi: 10.1080/10426914.2016.1221082

Singh, M., and Singh, A. (2020). Theoretical investigations into magnetorheological finishing of external cylindrical surfaces for improved performance. *Proc. IMechE Part C J. Mech. Eng. Sci.* 234, 4872–4892. doi: 10.1177/0954406220931550

Singh, M., and Singh, A. K. (2021). Magnetorheological finishing of variable diametric external surface of the tapered cylindrical workpieces for functionality improvement. *J. Manuf. Process.* 61, 153–172. doi: 10.1016/j.jmapro.2020.10.074

Song, W. L., Peng, Z., Li, P. F., Shi, P., and Choi, S. B. (2020). Annular surface micromachining of titanium tubes using a magnetorheological polishing technique. *Micromachines* 11:314. doi: 10.3390/mi11030314

Tang, C., Liu, D., Xiao, Q., and Wang, J. (2016). "Research on chatter suppression based on MRF in turning," in *Proceedings of the Progress in Electromagnetic Research Symposium*, Shanghai.

Wang, D. K., Hu, H. X., Li, L. X., Bai, Y., Luo, X., and Zhang, X. J. (2017). Effects of the gap slope on the distribution of removal rate in Belt-MRF. *Optics Express.* 25, 26600–26614. doi: 10.1364/OE.25.026600

Wang, J., and Meng, G. (2001). Magnetorheological fluid devices: principles, characteristics and applications in mechanical engineering. *Proc. Instit. Mech. Eng. Part L J. Mater. Design Applic.* 215, 165–174. doi: 10.1243/1464420011545012

Wang, Y. (2016). *Study on Magnetorheological Finishing Using Large Polishing Tool for Ultra-smooth Flat Surface [D]*. Changsha: Hunan University.

Wang, Y., Yin, S., and Huang, H. (2016). Polishing characteristics and mechanism in magnetorheological planarization using a permanent magnetic yoke with translational movement. *Precis. Eng. J. Intern. Soc. Precis. Eng. Nanotechnol.* 43, 93–104. doi: 10.1016/j.precisioneng.2015.06.014

Wang, Y. L., Wu, Y. B., and Mitsuyoshi, N. (2016). A novel magnetic field-assisted polishing method using magnetic compound slurry and its performance in mirror surface finishing of miniature V-grooves. *AIP Adv.* 6:056602. doi: 10.1063/1.4942952

Wang, Y. Y., Zhang, Y., and Feng, Z. J. (2016). Analyzing and improving surface texture by dual-rotation magnetorheological finishing. *Appl. Surf. Sci.* 360, 224–233. doi: 10.1016/j.apsusc.2015.11.009

Wu, J. X. (2019). *Analysis of the Influence of Magnetorheological Excitation Solidification Characteristics on Cutting Vibration Suppression of Thin-Walled Part [D]*. Dalian: Dalian University of Technology.

Wuertz, T., May, C., Holz, B., Janocha, H., Rodriguez, M. D., Collado, V., et al. (2010). "Fixturing of complex shaped Workpieces with magnetorheological fluids," in *Proceedings of the 12th International Conference on New Actuators/6th International Exhibition on Smart Actuators and Drive Systems*, Bremen.

Yadav, R. D., Singh, A. K., and Arora, K. (2020). Parametric analysis of magnetorheological finishing process for improved performance of gear profile. *J. Manuf. Process.* 57, 254–267. doi: 10.1016/j.jmapro.2020.06.024

Yan, B., Zhu, L., and Liu, C. (2020). Prediction model of peripheral milling surface geometry considering cutting force and vibration. *Intern. J. Adv. Manuf. Technol.* 110, 1429–1443. doi: 10.1007/s00170-020-05930-6

Yu, J., Dong, X., Qi, S., Wang, T., and Liang, Y. (2021). Development of a magnetorheological isolator with variable damping and variable stiffness for broadband vibration suppression. *Smart Mater. Struct.* 30:025023. doi: 10.1088/1361-665X/abd4fc

Zhang, P., Dong, Y. Z., Choi, H. J., Lee, C. H., and Gao, Y. S. (2020). Reciprocating magnetorheological polishing method for borosilicate glass surface smoothness. *J. Industr. Eng. Chem.* 84, 243–251. doi: 10.1016/j.jiec.2020.01.004

Zhong, Z. (2020). Advanced polishing, grinding and finishing processes for various manufacturing applications: a review. *Mater. Manuf. Process.* 35, 1279–1303. doi: 10.1080/10426914.2020.1772481

Zhou, P., Liu, M., Kong, W., Xu, Y., and Li, H. (2021). Modeling and evaluation of magnetorheological dampers with fluid leakage for cable vibration control. *J. Bridge Eng.* 26:04020119. doi: 10.1061/(ASCE)BE.1943-5592.0001666

Conflict of Interest: The authors declare that the research was conducted in the absence of any commercial or financial relationships that could be construed as a potential conflict of interest.

frontiers in Materials

ORIGINAL RESEARCH
published: 01 June 2021
doi: 10.3389/fmats.2021.682215

Sliding Mode Active Disturbance Rejection Control for Magnetorheological Impact Buffer System

*Bin Wang, Wanjun Wang and Zhaochun Li**

College of Mechanical and Electronic Engineering, Nanjing Forestry University, Nanjing, China

In the magnetorheological (MR) impact buffer system, the internal or external disturbance of the MR damper is one of the main factors that affect the buffer performance of the system. This study aims to suppress or eliminate the influence of the disturbance of the MR damper. The continuous terminal sliding mode control (CTSMC) strategy with a high gain has a strong antidisturbance ability. However, the high gain may cause fluctuation of the damping force of the system. Therefore, a composite control strategy of sliding mode active disturbance rejection control (ADRC) based on an extended state observer (ESO) is proposed in this study. The total disturbance of the system is estimated by the ESO in real time, and the estimated disturbance is used as a feedforward compensation to the controller to reduce the influence of disturbance on the system. The gain of the CTSMC law of the closed-loop system can be reduced. In addition, the Lyapunov stability criterion is used to ensure the stability of the proposed controller. In order to verify the performance of the proposed CTSMC controller on response speed, overshoot, and hysteresis suppression ability, the window function, square wave function, and multistep function are given as the inputs of the control system. To verify the performance of the proposed sliding mode ADRC for the MR impact buffer system, the mechanical model and the control model are established and simulated using MATLAB/Simulink. The simulation results show that the CTSMC controller has the fastest response time and no overshoot and can suppress the hysteresis nonlinearity of the MR device compared with the open-loop control, PID control, and fractional order PID control. The MR impact buffer system with the sliding mode ADRC obtained the minimum peak value of 4350N within the permitted buffer displacement range compared with the other three traditional control methods. That means the proposed control method in this study has the advantage on buffer performance for the MR impact buffer system.

Keywords: MR fluid damper, disturbance, continuous terminal sliding mode, active disturbance rejection control, shock buffer system

OPEN ACCESS

Edited by:
Yancheng Li,
University of Technology Sydney, Australia

Reviewed by:
Huixing Wang,
Nanjing University of Science and Technology, China
Honghui Zhang,
Chongqing University, China

****Correspondence:***
Zhaochun Li
lzc.hn@163.com

Specialty section:
This article was submitted to Smart Materials, a section of the journal Frontiers in Materials

Received: *18 March 2021*
Accepted: *11 May 2021*
Published: *01 June 2021*

Citation:
Wang B, Wang W and Li Z (2021) Sliding Mode Active Disturbance Rejection Control for Magnetorheological Impact Buffer System. Front. Mater. 8:682215. doi: 10.3389/fmats.2021.682215

INTRODUCTION

With magnetorheological (MR) fluid as the working medium, MR dampers, a kind of semiactive control device with a new structure, have a simple mechanical structure, fast response speed at the millisecond level, low power consumption, damping force that can be continuously adjusted forward and backward in a wide range, etc. These excellent characteristics make them have broad application prospects in the fields of impact resistance and high-speed vibration reduction and have been initially applied in the fields of aerospace, vehicles, buildings, bridges, and civil engineering (Carlson, 2002; Liu et al., 2005; Wereley et al., 2011; Hughes et al., 2017; Guo et al., 2019; Tudon-Martinez et al., 2019; Du et al., 2020; Yoon et al., 2020). Currently, MR dampers are mainly used in low-speed, low-frequency random load scenarios. In recent years, the application of MR dampers in high-speed impact bumper systems has aroused great interest among researchers, for example, in the landing process of aircraft, the recoil process of weapons, and vehicle operation on bumpy roads (Ouyang et al., 2016; Shou et al., 2018; Bai et al., 2019; Yuan et al., 2019).

MR dampers, a low-cost small-size smart device that generates a big damping force, have been applied in the field of high-speed vibration damping, such as semiactive suspension systems of vehicles, aircraft landing cushion systems, and wave impact processes of speedboats. The MR intelligent suspension system plays an important role in improving vehicle damping, and the selection of suitable controllers can reduce the road-transmitted shocks, thus attracting the widespread attention of domestic and foreign researchers. M. Ahmadian of Virginia Tech University proposed that one of the key issues for the successful application of MR dampers in shock buffer control systems is what control strategy is used to make up for the lack of dampers (Ahmadian and Poynor, 2001). Choi and Wereley (2003, 2005, 2015) studied the response of MR damper suspension systems in military vehicles and automotive seats under impact load and developed a set of nonlinear semiactive control systems. Bai et al. (2012) designed a bidirectional controllable MR damper to improve the performance of impact and vibration by using the sky-hook control algorithm. Rahmat et al. (2019) designed a fast practical control (FPC) algorithm with less computational strength. The control performance of the system was compared by using the control algorithms of sky-hook and FPC under different levels of impact energy. The results show that compared with the sky-hook control, the FPC controller improves the impact response, acceleration response, and force response by about 17.73%, which can better reduce the impact energy. Dong et al. (2010) adopted the sky-hook control algorithm, hybrid controller, LQG controller, sliding mode controller, and fuzzy controller and compared the performance of vehicle vibration reduction using these five control algorithms under different road conditions. Sliding mode control has a significant damping effect. During the landing of helicopters, the pilots or passengers often suffer waist injuries due to the huge impact force. Therefore, researchers applied MR dampers as energy absorbers in aircraft damping systems and devoted considerable effort to control strategies in this system. Choi and Wereley (2003, 2015) successively proposed a sliding mode controller with good robustness for parameter variations and external disturbances and an optimal Bingham number control strategy, and they verified the effectiveness of the control strategies by experiment. Dong et al. from Chongqing University developed a new type of variable stiffness damper based on the MR damper and established the control model. The damping performance of the MR damper was evaluated by drop test. The experimental results show that an MR damper can effectively reduce the impact load of spring–mass (Dong et al., 2011). The above research progress shows that MR dampers are sufficiently feasible and advanced in the field of high-speed vibration damping. In addition, the large amount of effort put into this field has led to a good understanding of the control method of MR dampers under high-speed vibration damping.

However, the impact buffer system is usually subject to instantaneous large shock loads, with a short acting time and strong uncertainty, which makes the shock-resistant system more severe than the high-speed vibration damping system. As an important factor in the controlled damping force of the impact bumper systems, the control strategy of MR dampers has been discussed extensively. But there is little research about the control strategy of MR dampers due to the highly nonlinear, time-varying, and uncertain nature of the system parameters of MR dampers in impact loading applications. Browne et al. of General Motors carried out a series of 1.0–10 m/s velocity and magnetic field strength impact tests on MR fluids by using a free-flight falling tower device. The results showed that the damping force, displacement, and energy absorption of MR dampers are dependent on the strength of the applied magnetic field and can be adjusted by varying the strength of the applied magnetic field (Browne et al., 2009). The inherent hysteresis nonlinearity of the MR dampers makes it difficult to obtain the desired magnetic field strength. To compensate for the MR damper hysteresis, Li and Gong et al. designed an MR damper embedded in a Hall sensor and a hysteresis compensation system by using PID controllers to adjust the magnetic flux density. Experiments and simulations show that the measured flux density can track the set signal well and verify the effectiveness of the hysteresis compensation control algorithm in the MR impact buffer system (Li et al., 2019). M. Ahmadian et al. obtained different impact energies by releasing the drop hammers from different heights from the falling tower, producing an impact load with a maximum velocity of 6.604 m/s acting on the MR dampers, and experimentally controlling the recoil motion in the antirecoil device of large- and medium-caliber firearms. The results showed that the MR damper can effectively reduce the recoil force and improve the firing accuracy and the stability of the system (Goncalves et al., 2006; Ahmadian and Norris, 2008). Professor Wang Jiong from Nanjing University of Science and Technology studied the control algorithms of an MR damper under impact load. The delay fuzzy adaptive control, delay fuzzy PID control strategy, optimal buffer control strategy, and fuzzy control strategy have been proposed successively. The four control methods were verified by experiments and have a better buffer effect to improve the cushioning property of the

MR damper recoil system compared with the passive control (Li and Wang, 2012). The above studies show that the effectiveness of MR dampers under impact buffer conditions has been verified experimentally, and valuable control methods were provided. However, there are some shortcomings in the control effect, such as the "platform effect," where the output damping force–buffer displacement does not reach the optimum due to the initial peak value. One of the reasons for the unsatisfactory control effect may be that the MR damper is subject to various external and internal disturbances under the impact load. Domestic and foreign scholars mainly research the influence of temperature on the MR damper. Under the impact load, the MR damper experiences a great temperature change due to electromagnetic coil resistance heating and energy dissipation, while the temperature can affect the rheological properties of MR fluids significantly (McKee et al., 2011). The experimental results of Breese et al. with regard to MR dampers of different sizes showed that the peak damping force is significantly lower with the increase in temperature and pointed out that this was caused by the decrease in fluid viscosity (Gordaninejad and Breese, 1999). D.C. Batterbee's research showed that the force/velocity and force/displacement characteristics of the MR damper are significantly affected by the temperature variation. The research also pointed out that the increased temperature increases the effective fluid stiffness and reduces the yield stress and post-yield viscosity characteristics (Batterbee and Sims, 2009). Xia Fan et al. from Nanjing University of Science and Technology studied the effect of temperature on the damping performance of the MR damper. The shear test of the MRF-132DG MR fluid of the LORD company was carried out with or without a magnetic field. The experiment showed that the viscosity and yield stress of the MR fluid changed more obviously under the influence of temperature and the influence degree of temperature decreases with the increase in magnetic field strength. In addition, the mechanical properties of the MR damper were tested using a W + B mechanical property testing machine, and the results show that the viscous damping force of the damper is greatly affected by temperature (Xia et al., 2020). These studies show that the fluid viscosity and damping force of the MR damper decrease with the increase in temperature, affecting the stability of the controller. Therefore, the effect of temperature on the dynamic performance of the MR damper cannot be ignored. However, in the impact buffer system, not only temperature disturbance exists in the MR damper but also some other disturbances, for example, the parameters of the mechanical model of the damper will change due to uncertain disturbances such as settlement and oil leakage (Wang, 2018), the intrinsic hysteresis nonlinearity of the MR damper, the unmodeled dynamics of the system, and unknown disturbances in the external environment under the impact load, all of which may lead to unsatisfactory control results. Therefore, the ADRC strategy is one of the possible solutions to solve the unsatisfactory control effect of MR damping in the impact bumper system.

ADRC and sliding mode control are two good control methods to deal with system uncertainty and external disturbances. With its low dependence on the system model, ADRC can act on various internal uncertainties and external disturbances and has strong robustness, including extended state observer, feedback controller, and disturbance compensation (Han, 1998). The extended state observer estimates the unmeasurable state and the total disturbances of the system through the input–output information and compensates them in the process of controller design so as to achieve the antidisturbance effect. Sliding mode control is a kind of nonlinear control algorithm. The sliding mode surface can be designed and is independent of object parameters and disturbance, which makes sliding mode control have the advantages of fast response, insensitivity to system parameter change and disturbance, no need for system online identification, and simple implementation. Because of these advantages, both domestic and international scholars have carried out deep research on the use of sliding mode ADRC to suppress disturbances in control systems, and it is gradually applied in practical projects, such as motor and power system control (Zheng et al., 2015), robot control (Tan et al., 2010), aircraft control (Wang et al., 2010), and satellite attitude control (Meng et al., 2010). As the tilt-rotor aircraft system is susceptible to internal and external disturbances, Zheng et al. applied the ADRC sliding mode composite controller to the attitude control of tilt-rotor aircraft and designed a new sliding mode observer that can accurately estimate all kinds of disturbances, and the dependence of the controller on the model was reduced. The simulation results show that the composite controller is effective in attitude tracking and disturbance rejection of tilt-rotor aircraft (Pan et al., 2017). In the context of severely uncertain system parameters and completely unknown external disturbances, Awais Shah and Huang et al. designed a nonlinear adaptive sliding mode controller for height and attitude tracking, which is suitable for all four-rotor UAV systems, and the effectiveness and robustness of the control method were verified by simulation and experiment (Huang et al., 2020). Wang et al. (2020) adopted the fuzzy sliding mode ADRC method to reduce the influence of dynamic uncertainty, hydrodynamic force, and unknown disturbance on the trajectory tracking performance of underwater robots. Compared with the traditional PID and fuzzy logic control, the simulation results show that the proposed control method has lower power consumption and better performance. Problems such as system parameter changes and uncertain disturbances have led to the low control accuracy of the permanent magnet synchronous motor servo system. To address this problem, Alonge. F. of the University of Palermo proposed an ADRC based on the sliding mode. On the one hand, the ADRC method was used to deal with internal and external disturbances. On the other hand, the sliding mode controller was used to compensate the uncertainty in the estimation error and control gain. Simulations and experiments were performed to verify the antidisturbance and robustness of the controller (Alonge et al., 2017). Lai et al. (2011), in order to suppress the effect of the hysteresis characteristics on piezoelectric ceramic actuators, designed a segmented boundary layer sliding mode variable control rate to compensate for the hysteresis nonlinearity that the Preisach inverse model cannot completely offset, the uncertainty of model parameters, and disturbances. The experimental results show that the control method can ensure

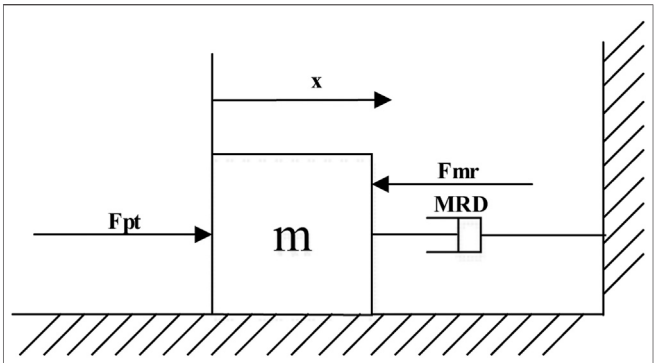

FIGURE 1 | Simplified mechanical model of magnetorheological (MR) impact buffer system.

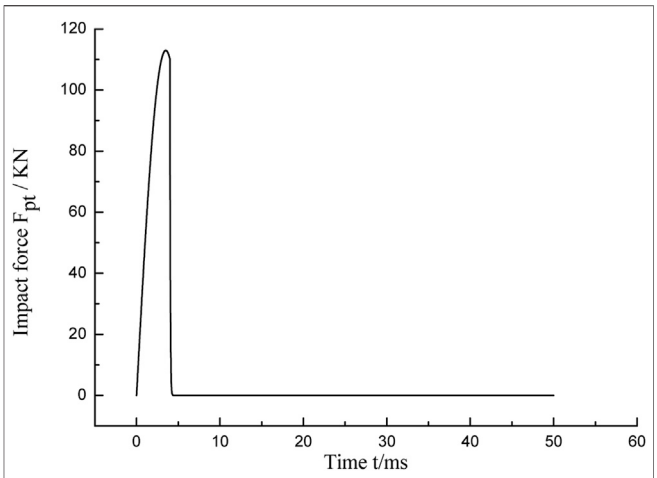

FIGURE 2 | Simulated impact signal.

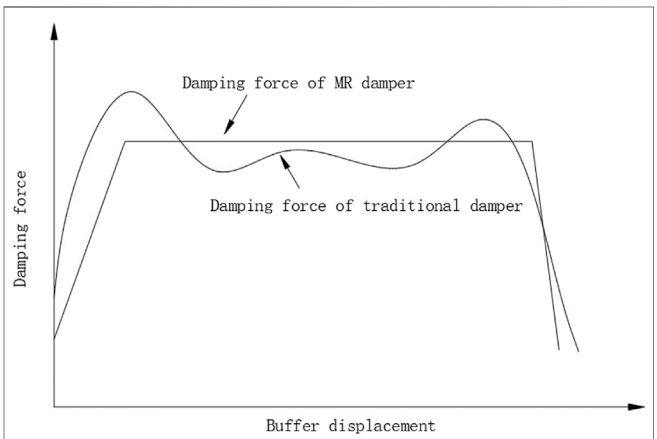

FIGURE 3 | Curve of control target.

the positioning accuracy of the nanometer positioning platform. The ADRC based on the sliding mode combines the ADRC and sliding mode controller to learn from each other. The above research has verified that the sliding mode ADRC can overcome the uncertainty of the system and has strong robustness to disturbance, parameter perturbation, and unmodeled dynamics.

This study mainly discusses the influence of disturbance on the MR shock buffer system and proposes an ADRC based on the sliding mode. First, the disturbance signals of temperature and hysteresis are analyzed and established, and the CTSMC is proposed. Then, for the high gain of the CTSMC control law, the steady-state damping force of the impact buffer system will fluctuate, and the sliding mode ADRC strategy is proposed. By introducing an extended state observer (ESO), the internal or external disturbances of the system were regarded as "total disturbances," which are estimated online as extended states, and the influence of disturbances on the system is compensated by the feedback control law; the CTSMC control method can ensure that the system converges to the equilibrium point in a finite time. At the same time, the Lyapunov stability criterion is used to ensure the stability of the proposed controller. Finally, two systems are established in MATLAB/Simulink: one is to verify the response time, overshoot, and the ability of hysteresis suppression of CTSMC, and the other is to verify the buffering performance of the MR shock buffer system using the sliding mode ADRC, which uses the Bingham mechanical model to calculate the damping force of the damper. To verify the advantages of the proposed controllers, an open-loop controller, a PID controller, and a fractional PID controller are established and simulated for comparison. The simulation results verify the disturbance suppression ability of the proposed controller, and a better buffer effect was achieved overall.

CONTROL STRATEGY

Control Objectives

The mechanical model of the MR impact buffer system is simplified as shown in **Figure 1**. The system includes an MR damper and a mass. When the mass is subjected to an impact force F_{pt}, the MR damper outputs the damping force F_{mr} and the buffer displacement of the mass is expressed as x. According to Newton's second law, the motion (**Eq. 1**) of the system can be described as follows:

$$F_{pt} - F_{mr} = m\ddot{x}, \tag{1}$$

where F_{pt} is the impact force, x is the buffer displacement of the mass, m is the mass of the object subjected, and F_{mr} is the output damping force of the MR damper, which is composed of two parts: controllable Coulomb damping force $F_\tau = c_2\tau_y sgn[u(t)]$ and uncontrollable viscous damping force $F_\eta = c_1\dot{x}$. c_1 and c_2 are the coefficients related to the size of the MR damper, where $c_1 = \frac{3\pi\eta_T L(D^2-d^2)^2}{4Dh^3}$ and $c_2 = \frac{3L\pi(D^2-d^2)}{4h}$. The MR damper used in this study is the same as that used in the article by Li et al. (2019), where $c_2 = 0.01546N/pa$. Without considering the disturbance caused by temperature, let η=0.19, then c_1=921.8 $N\ s/m$.

The impact buffer system is characterized by large impact force and extremely short action time. The impact force is adopted in the simulation as shown in **Figure 2**. As shown in

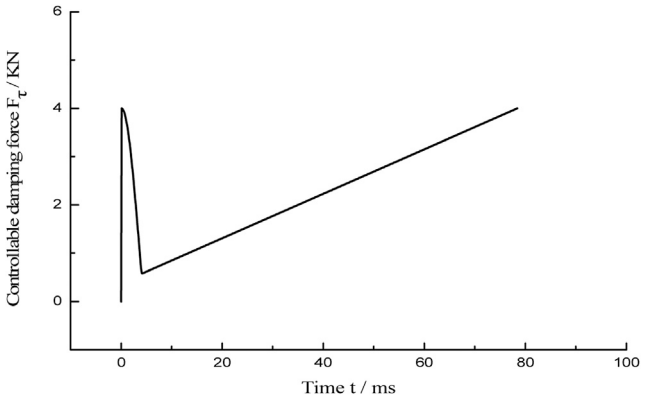

FIGURE 4 | Ideal curve of controllable damping force F_{τ_i}.

Eq. 2, only when the output damping force F_{mr} of the MR damper is equal to a constant, a good buffer effect can be obtained. To be specific, according to the law of conservation of energy, the area enclosed by the buffer displacement and the output damping force of the damper is constant, as shown in **Figure 3**. It can be seen from this figure that only when the output damping force curve is constant, can the peak of the damping force be minimized within the limited displacement. Therefore, only when the relationship of the damping force and the buffer displacement shows a "platform effect," the MR impact buffer system is the most stable and can obtain the best buffer effect (Li et al., 2019).

$$F_{mr\_i} = F_\tau + F_\eta = F_\tau + c_1\dot{x} = \text{constant}, \tag{2}$$

where F_{mr_i} is the ideal damping force.

Assuming that the ideal output damping force of the MR damper is equal to 4,000 N regardless of the influence of temperature on the damping force, the ideal controllable Coulomb damping force of the MR damper F_{τ_i} can be obtained by combining **Eqs. 1, 2**, as shown in **Figure 4**. According to the Bingham mechanical model, the controllable damping force F_τ is a nonlinear single-valued function of magnetic flux density B. Therefore, the input of the control system can be converted from ideal Coulomb force to ideal magnetic flux density, as shown in the following equation:

$$B_r = f\left(\frac{F_\tau}{c_2}\right). \tag{3}$$

However, the dynamic viscosity and the damping force of the MR fluid decrease with the increase in temperature (Wilson et al., 2013). Therefore, the effect of temperature on the damping force must be considered when the MR damper is applied. LORD company's research (Blanchard, 2003) showed that the viscosity of the MR fluid is in a power exponent relation with the change in temperature; approximately, the viscosity–temperature characteristic of mineral hydraulic oil meets the viscosity–temperature relation, namely,

$$\eta_T = \eta_{T_0} e^{-\lambda(T-T_0)}. \tag{4}$$

In this study, the MR fluid used in the damper was produced by Ningbo Shangong Intelligent Safety Technology Co., Ltd. Its model is SG-MRF2035. According to the experimental data of dynamic viscosity and temperature in the manual, the relationship between temperature and dynamic viscosity of the MR fluid can be fitted in MATLAB, the fitting result is shown in **Figure 5** and the corresponding equation is as follows:

$$\eta_T = 0.9357e^{-0.0088(T-4.47)}. \tag{5}$$

Under the influence of temperature, the damping coefficient c_1 of the damper changes with the dynamic viscosity η_T of the MR fluid, which leads to the change in the viscous damping force F_η eventually. The change in the damping force caused by temperature is regarded as a disturbance in this study. By referring to the theoretical model of temperature increase (Gordaninejad and Breese, 1999; **Figure 6**), three sets of

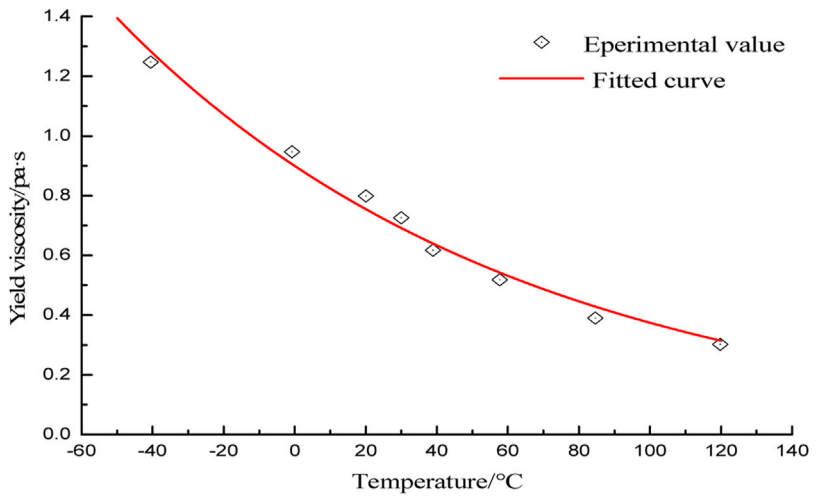

FIGURE 5 | Characteristic curve of MR fluid ($\eta \sim T$).

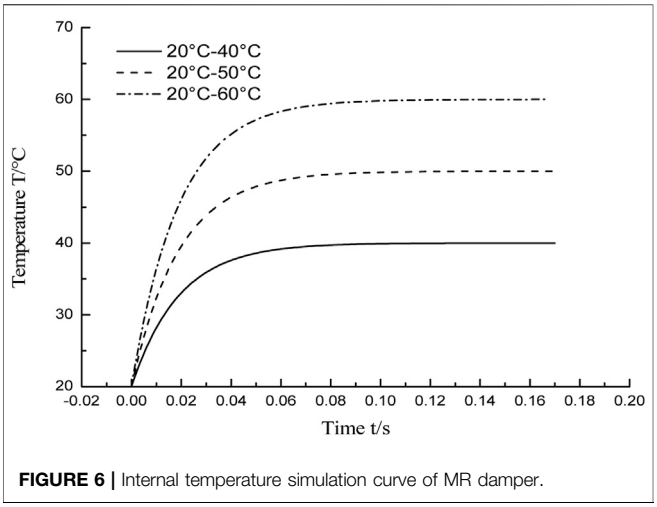

FIGURE 6 | Internal temperature simulation curve of MR damper.

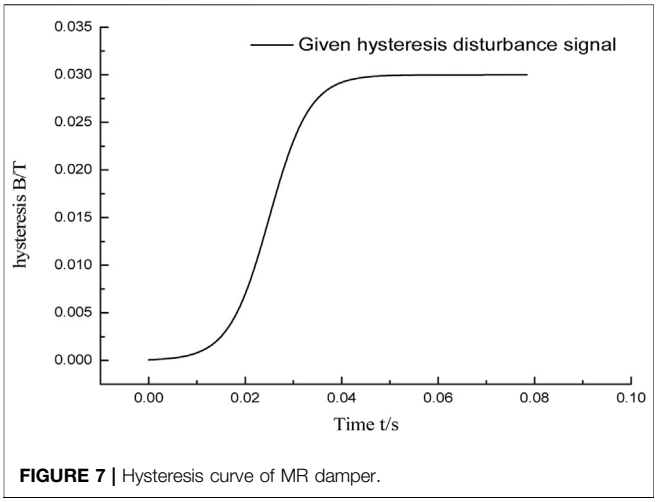

FIGURE 7 | Hysteresis curve of MR damper.

different temperature disturbance curves are designed, which are 20–40, 20–50, and 20–60°C.

It is well known that the ferromagnetic particles in the MR damper cause the hysteresis nonlinearity of the damper, which is manifested as the hysteresis nonlinearity between $F_{mr} \sim I$ (Li et al., 2019), which limits the application of the MR damper to a great extent, so hysteresis is treated as a disturbance in this study. The experimental results of the article (Li et al., 2019) show that the maximum hysteresis of the MR damper used in this article is 0.03 T. So the hysteresis disturbance signal of the MR impact buffer system is established, as shown in **Figure 7**.

Design of Magnetic Flux Density Controller Based on CTSMC

According to the MR coil electromagnetic circuit, the theoretical model for the response features of magnetic flux density was established (Li et al., 2018):

$$\dot{\mathrm{B}} = -\frac{1}{T_1}B + \frac{K_1}{T_1}U_c, \tag{6}$$

where T_1 is the response time constant and K_1 is the system gain.

Considering the internal uncertainty and external disturbance of the system, the system can be rewritten as follows:

$$\dot{\mathrm{B}} = bU_c + f(\mathrm{B}, \mathrm{d}, t), \tag{7}$$

where $\mathrm{b} = \frac{K_1}{T_1}$, $f(\mathrm{B}, \mathrm{d}, t)$ is considered to be the total disturbances, and $\mathrm{d}(\mathrm{t})$ is the external disturbances. The total disturbances include the external and internal disturbances of the MR damper, such as hysteresis, temperature, and unmodeled dynamics.

Let B_r denote the magnetic flux density reference signal. Then the magnetic flux density tracking error is defined as follows:

$$\mathrm{e} = B_r - B. \tag{8}$$

When the derivative of e is substituted into **Eq. 7**, the differential equation of the flux density tracking error can be obtained as follows:

$$\dot{e} = \dot{B}_r - bU_c - f(\mathrm{B}, \mathrm{d}, t). \tag{9}$$

The terminal sliding surface is designed as

$$\mathrm{s} = \mathrm{ce} + \dot{e}. \tag{10}$$

The CTSMC law is designed as (Wang et al., 2016)

$$U_c = b^{-}\left(u_{eq} + u_v\right), \tag{11}$$

$$u_{eq} = ce + \dot{B}_r, \tag{12}$$

$$u_v = k\int_0^t sgn(s)d\tau, \tag{13}$$

where $c > 0$, $\mathrm{k} > 0$, and *sgn* is the symbolic function. We ignore the disturbance and uncertainty of the system and set $\dot{s} = 0$ to obtain the equivalent control u_{eq}. Through analyzing $\dot{s}$, substituting $\mathrm{u} = u_{eq} + u_v$ to $s\dot{s}$, and making $s\dot{s} \le -\eta|s|$ hold, the switching robust term u_v of the control law can be obtained.

Hypothesis 1: Suppose the derivative of $f(\mathrm{B}, \mathrm{d}, t)$ is bounded, and there is a constant $k_d > 0$, such that

$$\left|\dot{f}(\mathrm{B}, \mathrm{d}, t)\right| \le k_d, \quad t \ge 0. \tag{14}$$

Theorem 1: Suppose the system satisfies Hypothesis 1. Under the control law (**Eqs. 11–13**), when the gain meets $k > k_d$, the magnetic flux density error of the system converges to zero in a finite time.

Proof: According to **Eq. 9**, the terminal sliding surface (10) can be rewritten as follows:

$$\begin{aligned} \mathrm{s} &= \mathrm{ce} + \dot{e} \\ &= \mathrm{ce} + \dot{B}_r - bU_c - f(\mathrm{B}, \mathrm{d}, t), \end{aligned} \tag{15}$$

Substituting **Eqs 11–13** into **Eq. 15** yields

$$\mathrm{s} = -u_v - f(\mathrm{B}, \mathrm{d}, t). \tag{16}$$

Taking the Lyapunov equation as $\mathrm{V} = \frac{1}{2}s^2$ and the derivative of the sliding surface (16) along the flux density tracking error system (9) yields

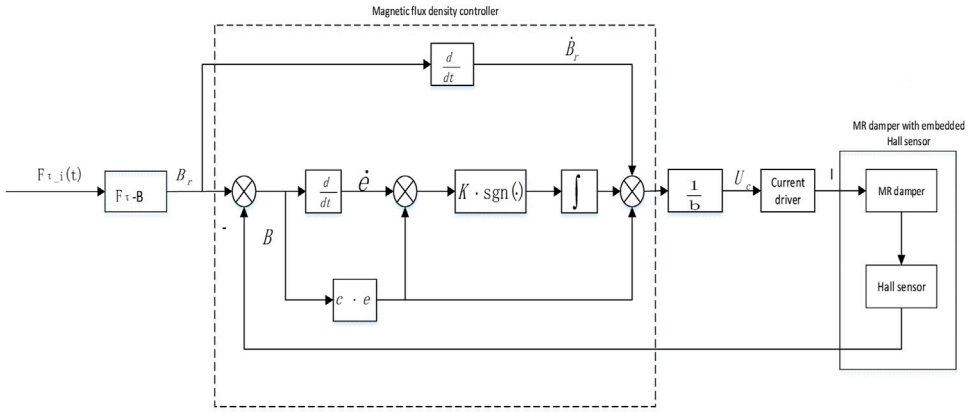

FIGURE 8 | Control schematic diagram of MR impact buffer control system based on the CTSMC.

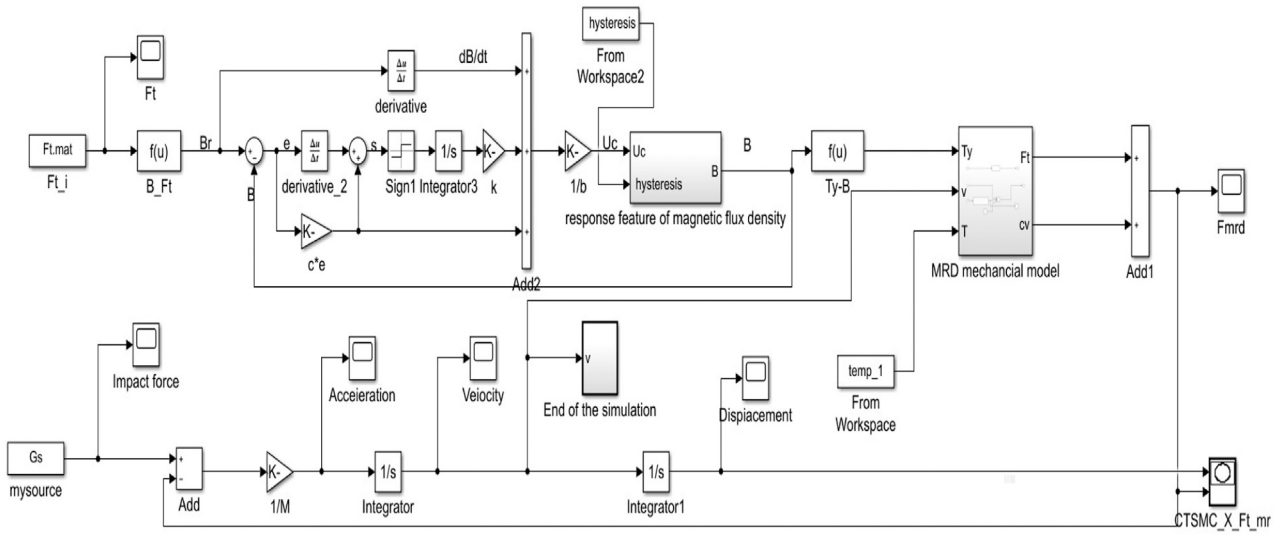

FIGURE 9 | Simulation block diagram of MR impact buffer control system containing disturbance based on the CTSMC.

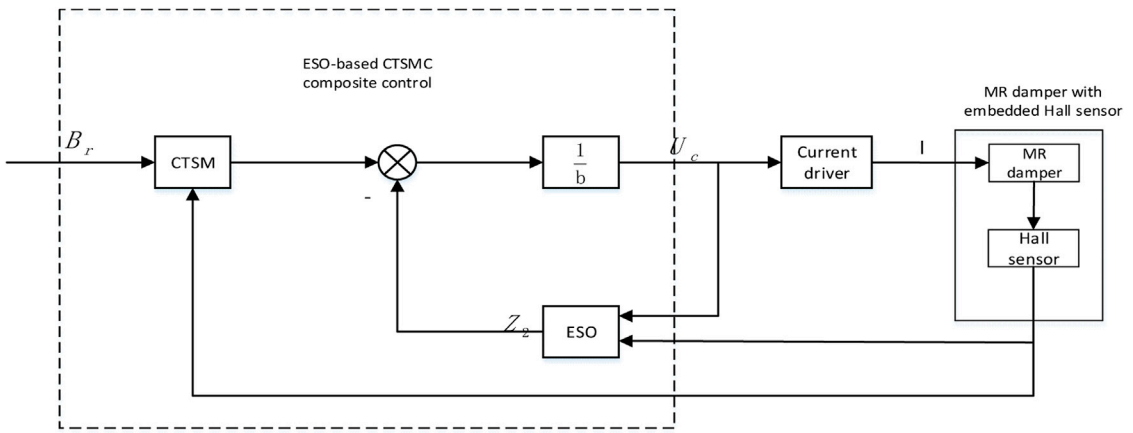

FIGURE 10 | Control schematic diagram of the sliding ADRC (CTSMC + ESO).

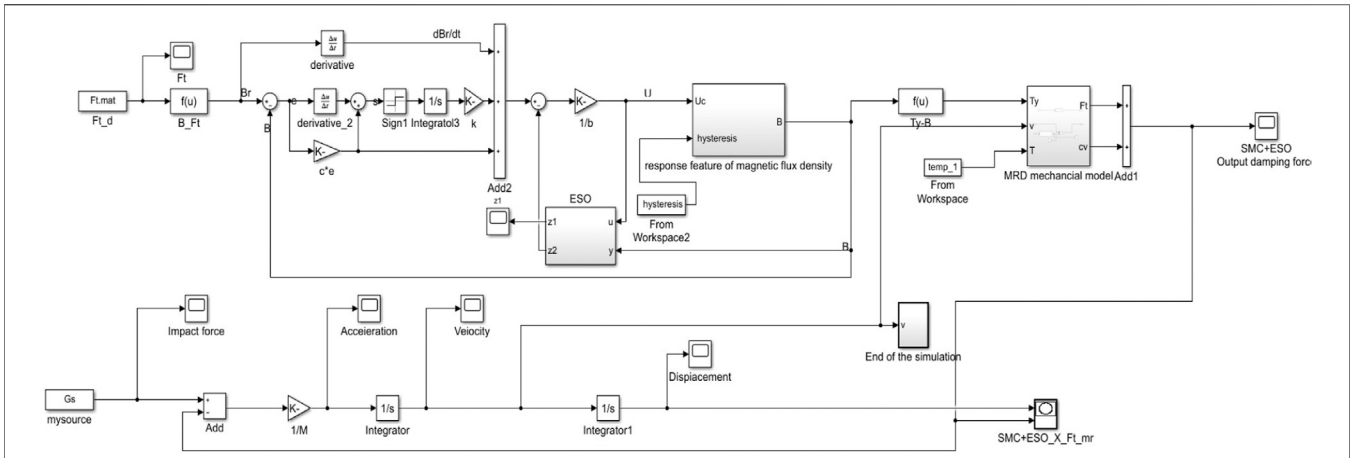

FIGURE 11 | Simulation block diagram of MR impact buffer sliding mode ADRC system with disturbances.

$$\dot{s} = -\dot{u}_v - \dot{f}(\mathrm{B}, \mathrm{d}, t). \tag{17}$$

Hence,

$$\begin{aligned} s\dot{s} &= -k|s| - \dot{f}(\mathrm{B}, \mathrm{d}, t)s, \\ \dot{V} = s\dot{s} &= -k|s| - \dot{f}(\mathrm{B}, \mathrm{d}, t)s \\ &\le -\mathrm{k}|s| + \left|\dot{f}(\mathrm{B}, \mathrm{d}, t)\right||s| \\ &= -\left[\mathrm{k} - \left|\dot{f}(\mathrm{B}, \mathrm{d}, t)\right|\right]|s| \\ &\le -[\mathrm{k} - k_d]|s| \\ &= -\sqrt{2}(k - k_d)V^{\frac{1}{2}}. \end{aligned} \tag{18, 19}$$

It can be proved from the above inequality that if $k > k_d$, the magnetic flux density error will reach the terminal sliding surface in finite time t_r. The total time from $s(0) \neq 0$ to $\mathrm{e}(t_s) = 0$ can be calculated as follows:

$$t_s = t_r \le \frac{\sqrt{2}\, V^{\frac{1}{2}}(0)}{(\mathrm{k} - \mathrm{kd})}, \tag{20}$$

where t_r is the time from $s(0) \neq 0$ to $s(t_r) = 0$. Therefore, the magnetic flux density error will converge to zero in a finite time. The theorem is proved.

From **Eqs. 11–13**, it can be seen that the control term U_c is continuous, although **Eq. 13** includes the high-frequency conversion term $sgn(s)$. Therefore, the CTSMC law eliminates the chattering caused by the switching term.

According to the above design process, the control system based on CTSMC is obtained, as shown in **Figure 8**. The magnetic flux density sliding mode controller is in the dashed box, the input of the sliding mode controller is the error e between the ideal magnetic flux density and the actual magnetic flux density, and the output is the control voltage U_c of the MR damper. The system adjusts the magnetic flux density B by voltage U_c to track the ideal magnetic flux density. In addition, the MR impact buffer control system based on CTSMC was built in MATLAB/Simulink, as shown in **Figure 9**. The system includes the sliding mode magnetic flux density controller, the simulated impact force, the theoretical model for the response features of magnetic induction intensity, and the Bingham mechanical model. At the beginning of the simulation, let $T = 20℃$, from **Eq. 5**, $\eta_T = 0.82$, then $c_1 = 3978.3\mathrm{N} \cdot \mathrm{s/m}$. The corresponding damping force can be calculated by substituting the Bingham mechanical model. More specifically, as shown in **Figure 6**, the temperature changes with time, and the value of η_T at this temperature can be calculated according to **Eq. 5**, and then, the corresponding damping force can be calculated. The disturbance hysteresis curve, shown in **Figure 7**, is added with the magnetic induction generated by the theoretical model of the magnetic induction response characteristics to obtain the inherent hysteresis characteristics of the MR fluid damper.

DESIGN OF THE SLIDING MODE ADRC CONTROLLER

Design of the ESO

The ESO can estimate the original system state and disturbance together; in addition, the ESO regards internal and external disturbances as the new state of the system. The biggest advantage of the ESO is that it does not rely on the generated disturbance model, nor does it use the functional relationship of the controlled object. The controller can eliminate the system disturbance signal estimated by the ESO, so as to achieve the purpose of auto disturbance rejection (Han, 1998).

$f(\mathrm{B}, \mathrm{d}, t)$ is considered as a new extended state of the system. Let $x_1 = \mathrm{B}$ and $x_2 = f(\mathrm{B}, \mathrm{d}, t)$, then system (7) can be written as the following equation of state:

$$\begin{cases} \dot{x}_1 = x_2 + bU_c \\ \dot{x}_2 = c(t) \end{cases}, \tag{21}$$

where $\mathrm{c}(\mathrm{t}) = \dot{f}(\mathrm{B}, \mathrm{d}, \mathrm{t})$.

The second-order linear ESO design of system (21) is as follows:

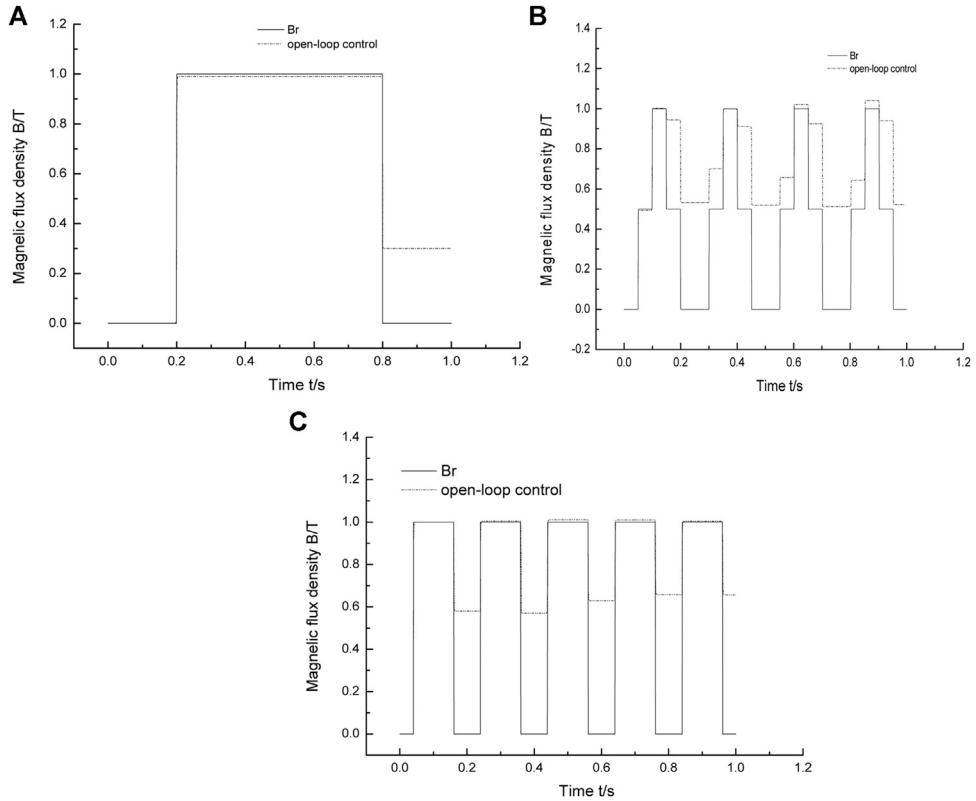

FIGURE 12 | Open-loop control response of different high-frequency and low-frequency input signals that uses the J–A model. **(A)** Window function response using open-loop control. **(B)** Multistep response using open-loop control. **(C)** Step response using open-loop control.

$$\begin{cases} \dot{z}_1 = z_2 - 2w_0(z_1 - x_1) + bU_c \\ \dot{z}_2 = -w_0^2(z_1 - x_1) \end{cases}, \tag{22}$$

where b is the gain of the control, $-w_0$ is the double pole expected by the ESO, and $w_0 > 0$. z_1 and z_2 are estimates of the states x_1 and x_2, respectively. State z_1 converges to B asymptotically and state z_2 converges to total disturbance $f(\mathrm{B}, \mathrm{d}, t)$. The convergence rate can be adjusted by the parameter w_0. Based on the disturbance estimate of the ESO, a feedforward compensator is designed to suppress the system disturbances.

Control Law Design of the Sliding Mode ADRC

The CTSMC control law not only enables the closed-loop system to have strong antidisturbance ability but also can eliminate buffeting. However, in the case of strong disturbance, the CTSMC control law needs a higher gain to eliminate disturbance. The sliding mode ADRC control method can greatly reduce the CTSMC law gain while compensating the total disturbances of the observation system in real time.

The control law of the sliding mode ADRC is shown in **Eqs. 23–25**:

$$U_c = b^{-}\left(u_{eq} + u_v - z_2\right), \tag{23}$$

$$u_{eq} = ce + \dot{B}_r, \tag{24}$$

$$u_v = k\int_0^t sgn(s)d\tau, \tag{25}$$

where $c > 0$, $k > 0$, and sgn is the symbolic function.

Hypothesis 2: Suppose the derivative of e_d is bounded, and there is a constant $k_{ed} > 0$, such that

$$\left|\dot{e}_d(\mathrm{t})\right| \le k_{ed}, \quad t \ge 0,$$

where $e_d(\mathrm{t}) = \mathrm{f}(\mathrm{B}, \mathrm{d}, \mathrm{t}) - z_2$ is the error of the estimate of the disturbance and $\mathrm{f}(\mathrm{B}, \mathrm{d}, \mathrm{t})$ is the disturbance of system (7).

Theorem 2: Suppose system (7) satisfies Hypothesis 2. In the control law (**Eqs. 23–25**), the magnetic flux density error of the system will converge to zero in a finite time if the gain satisfies $\mathrm{k} \ge k_{ed}$.

Proof: According to **Eq. 9**, the terminal sliding mode surface (10) can be rewritten as

$$\begin{aligned} \mathrm{s} &= \mathrm{ce} + \dot{e} \\ &= \mathrm{ce} + \dot{B}_r - bU_c - \mathrm{f}(\mathrm{B}, \mathrm{d}, \mathrm{t}). \end{aligned} \tag{26}$$

Substituting the control law (**Eqs. 23–25**) into **Eq. 25** yields

$$\mathrm{s} = -u_v - e_d(\mathrm{t}). \tag{27}$$

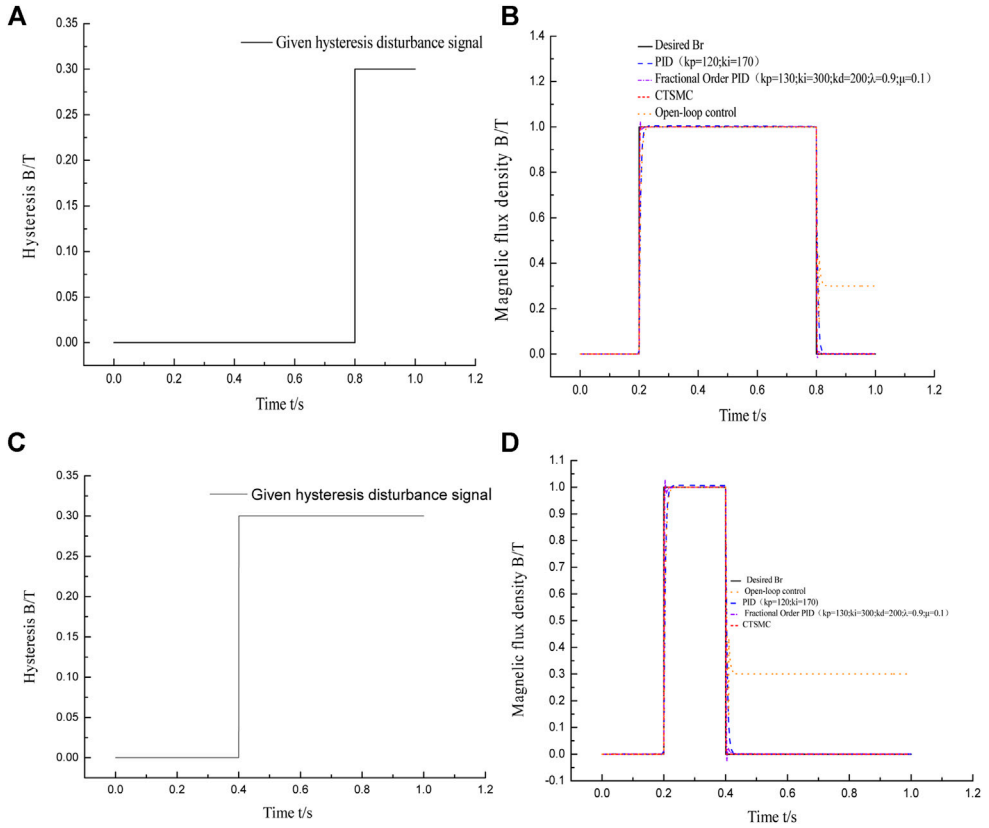

FIGURE 13 | Four control responses of different low-frequency input signals. **(A)** Hysteresis curve. **(B)** Response of four control multistep functions. **(C)** Hysteresis curve. **(D)** Response of four control window functions.

Taking the Lyapunov equation as $V = \frac{1}{2}s^2$ and the derivative of the sliding surface (27) along the flux density tracking error system (9) yields

$$\begin{aligned} \dot{s} &= -\dot{u_v} - \dot{e_d}(t) \\ &= k \cdot \mathrm{sgn}(s) - \dot{e_d}(t), \end{aligned} \tag{28}$$

Hence,

$$s\dot{s} = -k|s| - \dot{e_d}(t)s. \tag{29}$$

According to Hypothesis 2, the above equation can be rewritten as follows:

$$\begin{aligned} \dot{V} = s\dot{s} &= -k|s| - \dot{e_d}(t)s \\ &\le -k|s| + \left|\dot{e_d}(t)\right||s| \\ &= -\left[k - \left|\dot{e_d}(t)\right|\right]|s| \\ &\le -[k - k_{ed}]|s| \\ &= -\sqrt{2}(k - k_{ed})V^{\frac{1}{2}}. \end{aligned} \tag{30}$$

The above inequality can prove that if $k > k_{ed}$, the magnetic flux density error will reach the terminal sliding surface in a finite time and hold there. The calculation of total time t_r from $s(0) \neq 0$ to $e(ts) = 0$ can be referred to the CTSMC control strategy, and the proof is completed.

The block diagram of the sliding mode ADRC system is shown in **Figure 10**. The input of the controller is the error e of the ideal magnetic flux density and the actual magnetic flux density, and the output is the control voltage U_c of the MR damper. Moreover, the input of the ESO is the control voltage U_c and the actual magnetic flux density B of the MR damper, and the outputs are the estimations of the disturbance $f(B, d, t)$ and the estimated magnetic flux density value of the MR damper. Furthermore, the estimated disturbance is used as the feedforward compensation to the sliding mode controller to reduce the disturbance effect on the MR damper, and the gain of the CTSMC law can be adjusted. As shown in **Figure 11**, an MR impact buffer control system based on the sliding mode ADRC law was built in MATLAB/Simulink. It is different from the CTSMC control law in that this system has one more ESO. The treatment of temperature disturbance and hysteresis disturbance is the same as in the CTSMC control system.

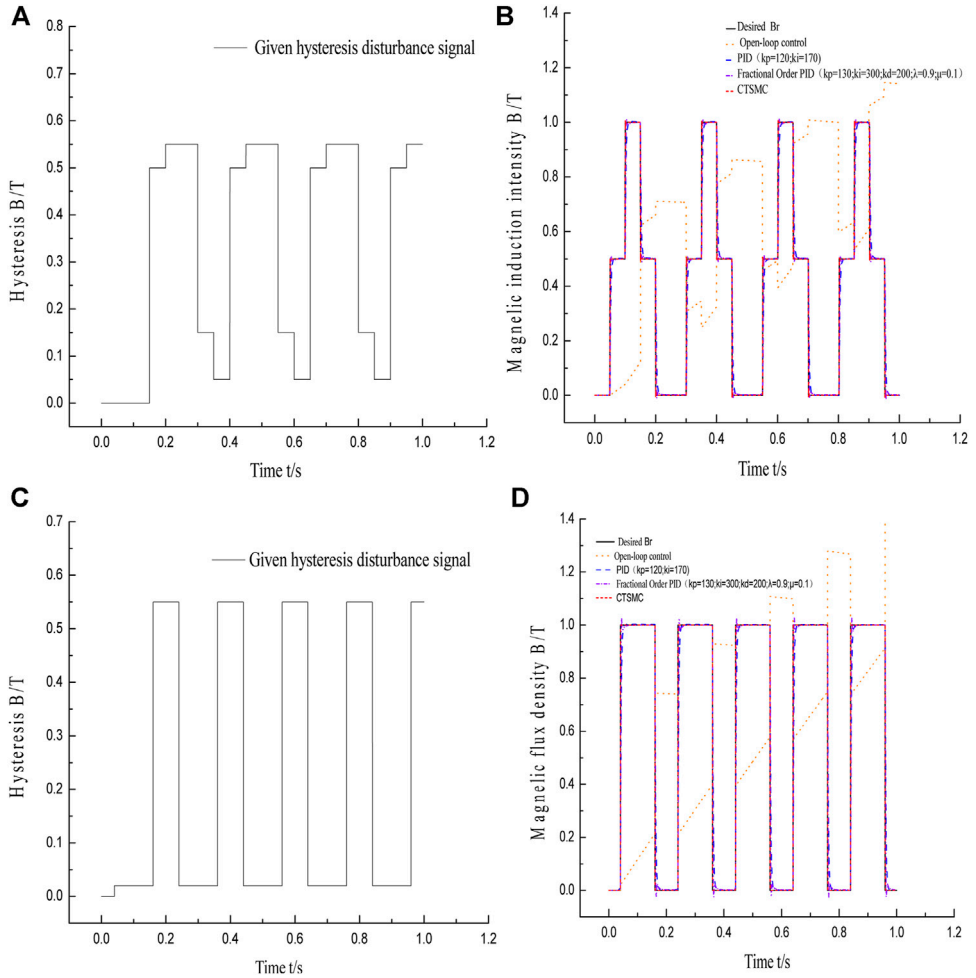

FIGURE 14 | Four control responses of different high-frequency input signals. **(A)** Hysteresis curve. **(B)** Response of four controlmultistep functions. **(C)** Hysteresiscurve. **(D)** Response of four control window functions.

RESULTS AND DISCUSSION

Verification of Hysteresis Suppression

The ideal magnetic flux density input signal includes low-frequency signals and high-frequency signals. Among them, the low-frequency signal is a window function and the high-frequency signal includes a high-frequency window function and a multistep function. The maximum amplitude of each analog input signal is set to 1T. Open loop, PID, fractional PID, and CTSMC strategies are adopted to suppress the hysteresis nonlinearity of the MR damper. The simulation results are shown in **Figure 13** and **Figure 14**. In **Figure 14**, A and C are hysteresis disturbance curves, which are drawn based on the open-loop simulation result that uses the Jiles–Atherton (J–A) model to describe the hysteresis characteristics of the MR damper (Li et al., 2019), as shown in **Figure 12**. It can be seen from **Figure 12A** that the hysteresis characteristic of the MR damper in the positive stroke can be ignored, but there is a 30% hysteresis of the reverse stroke in 0.8~1 s. Therefore, in the simulation in this article, 30% hysteresis is added to the system in 0.8~1 s of the reverse stroke to form the hysteresis disturbance curve of the window function. As above, the hysteresis curves of the system with the input signals of the high-frequency multistep function and high-frequency window function can be obtained.

According to B and D in **Figure 13**, after the signal begins to drop in the open-loop control system, the magnetic flux density output by the MR damper cannot track the ideal magnetic flux density. There is a certain amount of hysteresis; at the same time, there is about 20% oscillation at the signal drop point, which seriously affects the control accuracy of the system. In the PID and fractional PID control systems, the changes of the input signal can be tracked by the output signal of the magnetic flux density, but compared with CTSMC, the PID control system has a response time of 0.03 s and 0.7% remaining magnetic, fractional PID control system has 2% overshoot. Compared with the other three control methods, CTSMC has a response time that can almost be neglected and no overshoot in the dynamic process, so that the output can quickly track the input, which shows that

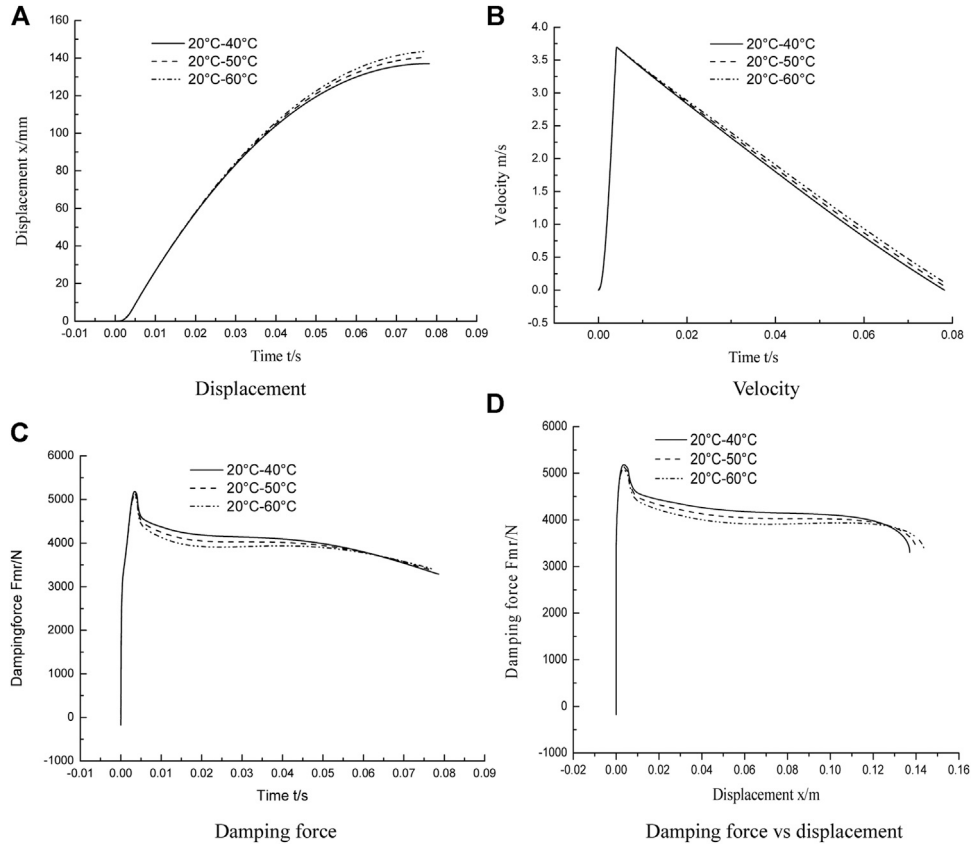

FIGURE 15 | Simulation results of MR impact buffer system under CTSMC control strategy. **(A)** Displacement. **(B)** Velocity. **(C)** Damping force. **(D)** Damping force vs. displacement.

compared with the other three control methods, CTSMC has the most obvious suppression effect on hysteresis. The impact loading duration of the MR impact buffer system is very short, always less than 0.1 s. To verify whether the hysteresis suppression control method can work normally in the impact buffer system, two high-frequency input signals were used for simulation. As shown in **Figure 14A and C**, the origin of the hysteresis curve at high frequency is the same as that at low frequency. The simulation results are shown in **Figure 14B and D**. Under the condition of high-frequency input signals, the suppression effect of the hysteresis of the four control strategies is not much different from that under low-frequency input signals, which shows that the disturbance suppression control method put forward in this article is suitable for the impact buffer system with a short working cycle and is beneficial for improving the disturbance suppression ability in the MR impact buffer system.

Verification of Temperature Suppression

When using an MR damper, the influence of temperature must be considered. As shown in **Figure 6**, three groups of different temperature disturbance curves are designed, which are 20°C–40°C, 20°C–50°C, and 20°C–60°C. In the case of three groups of different temperature disturbances, the simulation results of the impact buffer system using the CTSMC controller and the CTSMC + ESO controller are shown in **Figure 15** and **Figure 16**. It can be seen from **Figure 15** and **Figure 16D** that the buffering effect of the system is close to the "platform effect" and consistent with the control objective, except for the peak damping force at the beginning. Moreover, the peak damping force output by the MR damper does not change with temperature changes, which indicates that the CTSMC control system and the CTSMC + ESO control system are not sensitive to temperature changes and can effectively suppress the temperature disturbance in the MR shock buffer system.

Simulation Results of the MR Impact Buffer Disturbance Rejection Control System

Under the circumstance of hysteresis disturbance and temperature (20–50°C) disturbance, the simulation results of the MR impact buffer system under the controller of open loop, PID, fractional PID, CTSMC, and the sliding mode ADRC are shown in **Figure 17** and **Table 1**. The standard for evaluating the performance of the MR impact buffer system is that the curve of the output damping force and buffer displacement shows a "platform effect." In the action stage of the impact force, since the impact force is far greater than the

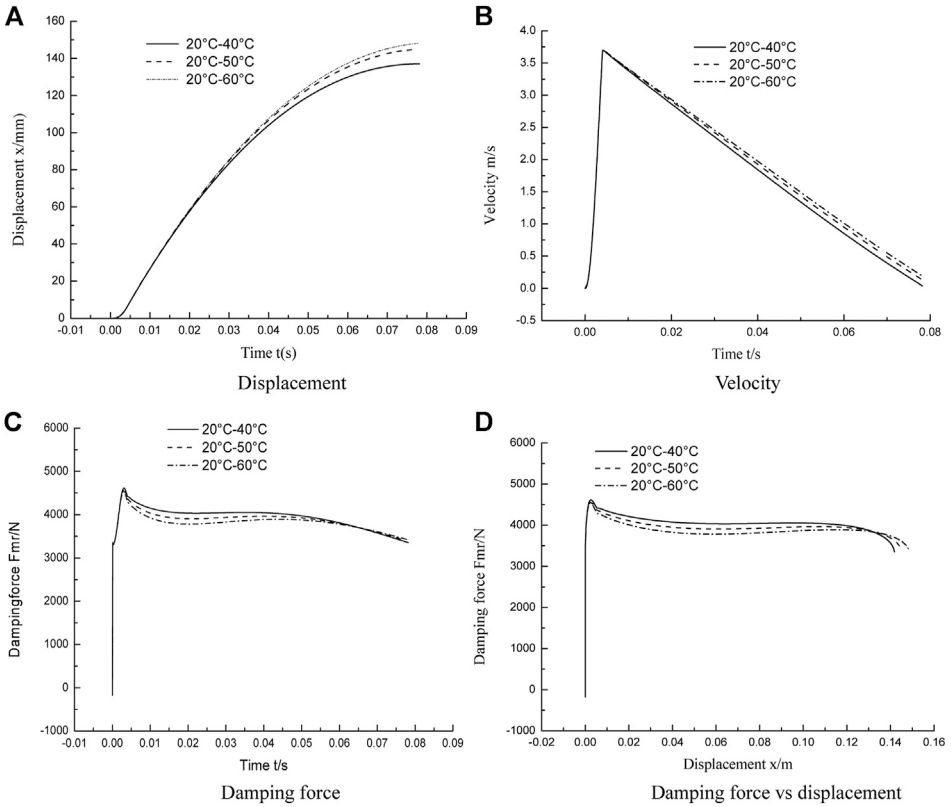

FIGURE 16 | Simulation results of MR impact buffer system under CTSMC + ESO control strategy. **(A)** Displacement. **(B)** Velocity. **(C)** Damping force. **(D)** Damping force vs. displacement.

resistance, the energy of the impact load determines the peak value of the speed. As shown in **Figure 17B**, the speed reaches the peak quickly before 0.005 s, and the peak speed is about 3.7 m/s and then quickly drops to 0. This indicates that the peak speed has nothing to do with the control algorithm and is determined by the energy of the impact load and the structural size of the damper. From the perspective of the output damping force–displacement curve in **Figure 17D**, it can be seen that the buffering effect under open-loop control is far from the ideal buffering effect during the entire buffering process, and the damping force cannot be maintained as a constant. The damping force–displacement curves under the PID and fractional PID control strategies show that the peak damping force is much larger than the ideal value of 4000 N, and the control effect is close to constant except for the initial part of the buffering process. CTSMC and the sliding mode ADRC method have a better buffering effect, of which the latter is the most satisfactory one. Compared with the other four control algorithms, the sliding mode ADRC algorithm has the smallest initial damping force peak, the "platform effect" between damping force and buffer displacement is more obvious, and the control process is close to a constant. Meanwhile, the buffer displacement of the entire damper system increases significantly, while the output damping force becomes smaller, which is completely consistent with the set control target.

To facilitate the analysis and comparison of the effects of the five control methods, Table 1 is made. In addition to open-loop control, the displacement of the other control methods is about 148 mm, but the peak value of the output damping force of the sliding mode ADRC algorithm is much smaller than that of the other control algorithms, 1944 N smaller than the maximum output damping force, and the peak damping force is effectively weakened. In addition, compared with CTSMC, the gain of the sliding mode ADRC is 9,000 smaller, which can reduce the pressure of the controller and improve the control accuracy. The simulation results show that disturbance is one of the important reasons for the unsatisfactory buffering effect and further show that the two control strategies proposed in this study have a certain degree of suppression on disturbance during the impact stage. In brief, in the presence of disturbances, compared with other control strategies, the sliding mode ADRC obtains the overall optimal buffering effect, which is consistent with the set control target, and suppresses the influence of temperature and hysteresis disturbances on the shock buffer system and reduces the high gain of the CTSMC law simultaneously.

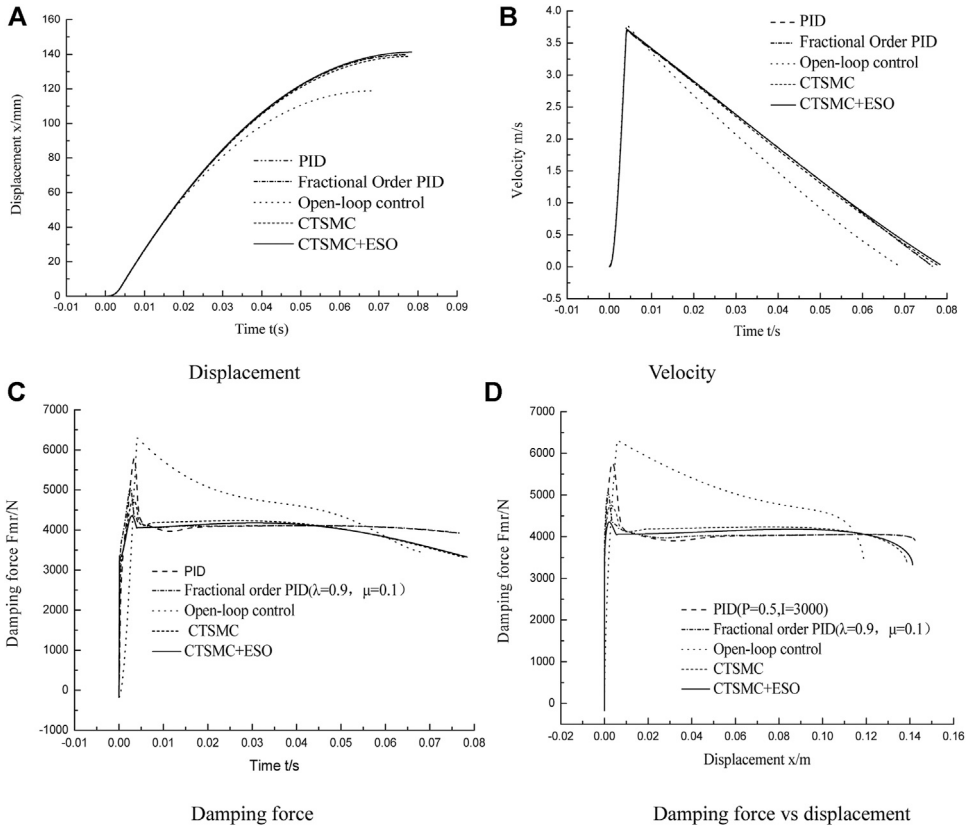

FIGURE 17 | Simulation results of MR impact buffer system under five control strategies. **(A)** Displacement. **(B)** Velocity. **(C)** Damping force. **(D)** Damping force vs. displacement.

TABLE 1 | Comparison of maximum displacement and peak damping force of five control methods.

Control method	Gain (K)	Maximum displacement (mm)	Peak damping force (N)
Open loop	–	112	6,294
PID	–	148	5,769
$PI^{\lambda}D^{\mu}$	–	148	5,066
CTSMC	11,000	147	4,759
CTSMC + ESO	2000	148	4,350

CONCLUSION

In this article, the disturbance suppression control method of the MR impact buffer system is studied. First, in order to suppress the influence of disturbance on the MR impact buffer system, the temperature disturbance and hysteresis disturbance of the system are analyzed. Meanwhile, the related disturbance signals are described, and the CTSMC law is proposed. Then, considering that the high gain of the CTSMC control law will cause the steady-state damping force fluctuation of the MR impact buffer system, a sliding mode ADRC is proposed. The Lyapunov stability criterion can ensure the stability of the CTSMC strategy, and the feedforward compensation term based on the ESO disturbance estimation is designed to compensate for the system's total disturbance to reduce the gain of the CTSMC law and disturbance suppression. Finally, two simulation experiments are carried out in MATLAB/Simulink. One of them uses window function, square wave function, and multistep function as ideal input signals to verify the response time, overshoot, and suppression of hysteresis nonlinearity of the CTSMC method. The second is to establish a simulation model of the MR shock buffer system in MATLAB/Simulink to verify the antidisturbance ability and buffer performance of the system by using the CTSMC method and the sliding mode ADRC method. In order to highlight the advantages of the proposed controllers, an open-loop controller, a PID controller, and a fractional order PID controller are used as a comparison. Numerical simulations show that the CTSMC controller has fast response speed,

no overshoot, and effectiveness in restraining the hysteresis of the MR damper. In addition, the simulation results of the MR shock buffer system show that the peak value of the output damping force is the smallest, about 4350 N, when the sliding mode ADRC strategy is adopted in the presence of hysteresis and temperature disturbance; however, the output damping force of the system with the other four control methods is much larger than the ideal value of 4000 N. Furthermore, the gain of the CTSMC can be reduced from 11,000 to 2000 while ensuring better buffer performance. This means that the sliding mode ADRC method proposed in this study is suitable for the MR shock buffer system and can improve the buffer performance of the system under impact load.

DATA AVAILABILITY STATEMENT

The raw data supporting the conclusions of this article will be made available by the authors, without undue reservation.

AUTHOR CONTRIBUTIONS

ZL proposed a sliding mode active disturbance rejection control method and analyzed the experimental data. BW carried out formula derivation and simulation on sliding mode active disturbance rejection control of magnetorheological damper. WW did some work for revising the manuscript and participated in the experiments of this paper.

FUNDING

This work is supported by the National Natural Science Foundation of China (NSFC); grant funded by the Chinese Government (No. 51305207), Youth Science and Technology Innovation Fund of Nanjing Forestry University (grant no. CX2019007) and Natural Science Foundation of Jiangsu Provincial College (Grand No. 17KJB413002).

REFERENCE

Ahmadian, M., and Norris, J. A. (2008). Experimental analysis of magnetorheological dampers when subjected to impact and shock loading. *Communications in Nonlinear Science and Numerical Simulation* 13, 1978–1985. doi:10.1016/j.cnsns.2007.03.028

Ahmadian, M., and Poynor, J. C. (2001). An Evaluation of Magneto Rheological Dampers for Controlling Gun Recoil Dynamics. *Shock and Vibration* 8, 147–155. doi:10.1155/2001/674830

Alonge, F., Cirrincione, M., D'Ippolito, F., Pucci, M., and Sferlazza, A. (2017). Robust Active Disturbance Rejection Control of Induction Motor Systems Based on Additional Sliding-Mode Component. *IEEE Trans. Ind. Electron.* 64, 5608–5621. doi:10.1109/TIE.2017.2677298

Bai, X.-X., Shen, S., Wereley, N. M., and Wang, D.-H. (2019). Controllability of magnetorheological shock absorber: I. Insights, modeling and simulation. *Smart Mater. Struct.* 28, 015022. doi:10.1088/1361-665X/aaf072

Bai, X.-X., Wereley, N. M., Hu, W., and Wang, D.-H. (2012). Mechanics and Behavior of Active Materials; Integrated System Design and Implementation; Bio-Inspired Materials and Systems; Energy Harvesting *(Stone Mountain*, Volume 2. Georgia, USA: American Society of Mechanical Engineers), 485–495. doi:10.1115/SMASIS2012-8250A Bidirectional-Controllable Magnetorheological Energy Absorber for Shock and Vibration Isolation Systems

Batterbee, D., and Sims, N. D. (2009). Temperature Sensitive Controller Performance of MR Dampers. *Journal of Intelligent Material Systems and Structures* 20, 297–309. doi:10.1177/1045389X08093824

Blanchard, E. D. (2003). *On the Control Aspect of Semiactive Suspensions for Automobile Applications*.

Browne, A. L., Mccleary, J. D., Namuduri, C. S., and Webb, S. R. (2009). Impact Performance of Magnetorheological Fluids. *Journal of Intelligent Material Systems and Structures* 20, 723–728. doi:10.1177/1045389X08096358

Carlson, J. D. (2002). WHAT MAKES A GOOD MR FLUID?. *Journal of Intelligent Material Systems and Structures* 13, 431–435. doi:10.1106/104538902028221

Choi, Y.-T., and Wereley, N. M. (2005). Mitigation of biodynamic response to vibratory and blast-induced shock loads using magnetorheological seat suspensions. *Proceedings of the Institution of Mechanical Engineers, Part D: Journal of Automobile Engineering* 219, 741–753. doi:10.1243/095440705x28330

Choi, Y.-T., and Wereley, N. M. (2003). Vibration Control of a Landing Gear System Featuring Electrorheological/Magnetorheological Fluids. *Journal of Aircraft* 40, 432–439. doi:10.2514/2.3138

Choi, Y.-T., and Wereley, N. M. (2015). Drop-Induced Shock Mitigation Using Adaptive Magnetorheological Energy Absorbers Incorporating a Time Lag. *J. Vib. Acoust.* 137, 011010. doi:10.1115/1.4028747

Dong, X.-m., Yu, M., Liao, C.-r., and Chen, W.-m. (2010). Comparative research on semi-active control strategies for magneto-rheological suspension. *Nonlinear Dyn* 59, 433–453. doi:10.1007/s11071-009-9550-8

Dong, X., Yu, M., and Zhu, L. (2011). *Electro-Rheological Fluids and Magneto-Rheological Suspensions*. Philadelphia, USA: WORLD SCIENTIFIC), 186–192. doi:10.1142/9789814340236_0026. RESEARCH ON MAGNETORHEOLOGICAL ELASTOMER ABSORBER AND ITS IMPACT TEST

Du, X., Yu, M., Fu, J., and Huang, C. (2020). Experimental study on shock control of a vehicle semi-active suspension with magneto-rheological damper. *Smart Mater. Struct.* 29, 074002. doi:10.1088/1361-665X/ab859e

Goncalves, F. D., Ahmadian, M., and Carlson, J. D. (2006). Investigating the magnetorheological effect at high flow velocities. *Smart Mater. Struct.* 15, 75–85. doi:10.1088/0964-1726/15/1/036

Gordaninejad, F., and Breese, D. G. (1999). Heating of magnetorheological fluid dampers. *Journal of Intelligent Material Systems and Structures* 10, 634–645. doi:10.1106/55d1-xaxp-yfh6-b2fb

Guo, Y.-Q., Xie, W.-H., and Jing, X. (2019). Study on Structures Incorporated With MR Damping Material Based on PSO Algorithm. *Front. Mater.* 6, 37. doi:10.3389/fmats.2019.00037

Han, J. (1998). Active disturbance rejection controller and application. *CONTROL Decis* 13, 3–5.

Huang, T., Huang, D., Wang, Z., Dai, X., and Shah, A. (2020). Generic Adaptive Sliding Mode Control for a Quadrotor UAV System Subject to Severe Parametric Uncertainties and Fully Unknown External Disturbance. *Int. J. Control Autom. Syst.* 19, 698–711. doi:10.1007/s12555-019-0853-3

Hughes, J. E., Kim, Y., El-Korchi, T., and Cyganski, D. (2017). Radar-based impact load prediction for damage mitigation of infrastructure. *Journal of Vibration and Control* 23, 1908–1924. doi:10.1177/1077546315603856

Lai, Z., LIU, X., GENG, J., and LI, L. (2011). Sliding mode control of hysteresis of piezoceramic actuator based on inverse Preisach compensation. *Opt. Precis. Eng.* 19, 1281–1290. doi:10.3788/OPE.20111906.1281

Li, Z. C., and Wang, J. (2012). A gun recoil system employing a magnetorheological fluid damper. *Smart Mater. Struct.* 21, 105003. doi:10.1088/0964-1726/21/10/105003

Li, Z., Gong, Y., Li, S., and Wang, W. (2019). Magnetic Hysteresis Compensation Control of a Magnetorheological Damper. *Front. Mater.* 6, 299. doi:10.3389/fmats.2019.00299

Li, Z., GU, Q., ZHOU, B., and WANG, J. (2018). Modeling and tests for response features of MR damper as a shock isolation device. *J. Vib. SHOCK* 37, 163–168+187.

Liu, Y., Gordaninejad, F., Evrensel, C. A., Wang, X., and Hitchcock, G. (2005). Comparative Study on Vibration Control of a Scaled Bridge Using Fail-Safe Magneto-Rheological Fluid Dampers. *J. Struct. Eng.* 131, 743–751. doi:10.1061/(ASCE)0733-944510.1061/(asce)0733-9445(2005)131:5(743)20051315743

McKee, M., Wang, X., and Gordaninejad, F. (2011). *ASME 2011 Conference on Smart Materials, Adaptive Structures and Intelligent Systems*, Volume 1. Arizona, USA: ScottsdaleASMEDC), 603–612. doi:10.1115/SMASIS2011-5127Behavior of a Compressible Magnetorheological Fluid Damper at High Temperatures

Meng, Z., Ren, W., and You, Z. (2010). Distributed finite-time attitude containment control for multiple rigid bodies. *Automatica* 46, 2092–2099. doi:10.1016/j.automatica.2010.09.005

Ouyang, Q., Zheng, J., Li, Z., Hu, M., and Wang, J. (2016). Controllability analysis and testing of a novel magnetorheological absorber for field gun recoil mitigation. *Smart Mater. Struct.* 25, 115041. doi:10.1088/0964-1726/25/11/115041

Pan, Z., Wang, W., Song, S., and Lu, K. (2016). Nonlinear Attitude Control of Tiltrotor Aircraft Based on Active Disturbance Rejection Sliding Mode Method. in Nanjing, PEOPLES R CHINA, 1351–1356.

Rahmat, M. S., Hudha, K., Kadir, Z. A., Nuri, N. R. M., Amer, N. H., and Abdullah, S. (2019). Comparison of Control Strategy on Magneto-Rheological Fluid Damper Performance for Impact Reduction. *IOP Conf. Ser.: Mater. Sci. Eng.* 530, 012032. doi:10.1088/1757-899X/530/1/012032

Shou, M., Liao, C., Zhang, H., Li, Z., and Xie, L. (2018). Modeling and testing of magnetorheological energy absorbers considering inertia effect with non-averaged acceleration under impact conditions. *Smart Mater. Struct.* 27, 115028. doi:10.1088/1361-665X/aae6a0

Tan, C. P., Yu, X., and Man, Z. (2010). Terminal sliding mode observers for a class of nonlinear systems. *Automatica* 46, 1401–1404. doi:10.1016/j.automatica.2010.05.010

Tudon-Martinez, J. C., Hernandez-Alcantara, D., Amezquita-Brooks, L., Morales-Menendez, R., Lozoya-Santos, J. d. J., and Aquines, O. (2019). Magneto-rheological dampers-model influence on the semi-active suspension performance. *Smart Mater. Struct.* 28, 105030. doi:10.1088/1361-665X/ab39f2

Wang, H., Li, S., Lan, Q., Zhao, Z., and Zhou, X. (2016). Continuous terminal sliding mode control with extended state observer for PMSM speed regulation system. *Trans. Inst. Meas. Control* 10.

Wang, H., Li, X., Liu, X., Karkoub, M., and Zhou, L. (2020). Fuzzy Sliding Mode Active Disturbance Rejection Control of an Autonomous Underwater Vehicle-Manipulator System. *J. Ocean Univ. China* 19, 1081–1093. doi:10.1007/s11802-020-4250-6

Wang, J., Zhu, C., Yang, Z., and Huang, L. (In Press). *Control Algorithm Study of Magneto-rheological Damper under Impact Load*.

Wang, X. (2018). Observer Based Force Estimation of Magnetorheological Damper Subjective to Unertainties and Faults. *Comput. Simul.* 35.

Wang, X., Liu, J., and Cai, K.-Y. (2010). Tracking control for VTOL aircraft with disabled IMUs. *International Journal of Systems Science* 41, 1231–1239. doi:10.1080/00207720903244048

Wereley, N. M., Choi, Y.-T., and Singh, H. J. (2011). Adaptive Energy Absorbers for Drop-induced Shock Mitigation. *Journal of Intelligent Material Systems and Structures* 22, 515–519. doi:10.1177/1045389X10393767

Wilson, N. L., Wereley, N. M., Hu, W., and Hiemenz, G. J. (2013). Analysis of a magnetorheological damper incorporating temperature dependence. *Ijvd* 63, 137. doi:10.1504/IJVD.2013.056102

Xia, F., Zhu, W., and Wei, M. (2020). Analysis of Influence of Temperature on Performance of Magnetorheological Fluid Dampers. *Noise Vib. Control* 40, 253–258.

Yoon, J.-Y., Kang, B.-H., Kim, J.-H., and Choi, S.-B. (2020). New control logic based on mechanical energy conservation for aircraft landing gear system with magnetorheological dampers. *Smart Mater. Struct.* 29, 084003. doi:10.1088/1361-665X/ab9e11

Yuan, X., Tian, T., Ling, H., Qiu, T., and He, H. (2019). A Review on Structural Development of Magnetorheological Fluid Damper. *Shock and Vibration* 2019, 1–33. doi:10.1155/2019/14989622019

Zheng, H., Chen, Q., and Tang, X. (2015). *IEEE 10th Conference on Industrial Electronics and Applications (ICIEA)*. Auckland, New Zealand: IEEE), 1588–1592. doi:10.1109/ICIEA.2015.7334362Composite chattering-free sliding mode control of chaotic permanent magnet synchronous motors*2015*

Conflict of Interest: The authors declare that the research was conducted in the absence of any commercial or financial relationships that could be construed as a potential conflict of interest.

frontiers in Materials

ORIGINAL RESEARCH
published: 04 June 2021
doi: 10.3389/fmats.2021.659780

Magneto-Sensitive Rubber in a Vehicle Application Context – Exploring the Potential

Bochao Wang[1], Tao Hu[1], Longjiang Shen[2], Jun Li[3], Zhenbang Xu[4], Leif Kari[5] and Xinglong Gong[1]**

[1] Chinese Academy of Sciences (CAS) Key Laboratory of Mechanical Behavior and Design of Materials, Chinese Academy of Sciences (CAS) Center for Excellence in Complex System Mechanics, Department of Modern Mechanics, University of Science and Technology of China, Hefei, China, [2] Hunan Bogie Engineering Research Center, Zhuzhou, China, [3] Anhui Weiwei Rubber Parts Group Co. Ltd., Tongcheng, China, [4] CAS Key Laboratory of On-orbit Manufacturing and Integration for Space Optics System, Changchun Institute of Optics, Fine Mechanics and Physics, Chinese Academy of Sciences, Changchun, China, [5] KTH Royal Institute of Technology, Department of Engineering Mechanics, The Marcus Wallenberg Laboratory for Sound and Vibration Research (MWL), Stockholm, Sweden

OPEN ACCESS

Edited by:
Jinglei Yang,
Hong Kong University of Science and Technology, Hong Kong

Reviewed by:
Yancheng Li,
University of Technology Sydney, Australia
Xingzhe Wang,
Lanzhou University, China
Tongqing Lu,
Xi'an Jiaotong University, China
Xianzhou Zhang,
Independent Researcher, Tomago, NSW, Australia

***Correspondence:**
Leif Kari
leifkari@kth.se
Xinglong Gong
gongxl@ustc.edu.cn

Specialty section:
This article was submitted to Smart Materials, a section of the journal Frontiers in Materials

Received: *28 January 2021*
Accepted: *20 April 2021*
Published: *04 June 2021*

Citation:
Wang B, Hu T, Shen L, Li J, Xu Z, Kari L and Gong X (2021) Magneto-Sensitive Rubber in a Vehicle Application Context – Exploring the Potential. Front. Mater. 8:659780. doi: 10.3389/fmats.2021.659780

The application of magneto-sensitive (MS) rubber in a vehicle vibration control area is likely to be expected. This conclusion is based on the following two reasons: the maturity of fabrication of MS rubber which meets the application requirement and the feasibility of the constitutive model of MS rubber that accurately reflects its mechanical performance. Compared with the traditional rubber, small ferromagnetic particles are embedded in the elastomer of MS rubber, leading to a change of mechanical properties when an external magnetic field is applied. Therefore, devices with MS rubber, can be viewed as a semi-active actuator. In this study, MS rubber with a relative high increase in the magneto-induced modulus is fabricated and characterized. Furthermore, a one-dimensional constitutive model to depict the magnetic field-, frequency-, and strain amplitude-dependent dynamic modulus of MS rubber is applied. Finally, simulations of a MS rubber semi-active suspension under a bump and a random ground excitation with different control strategies on a quarter vehicle model are conducted to illustrate the feasibility of the MS rubber in the vehicle vibration control application context.

Keywords: magneto-sensitive rubber, vehicle vibration control, constitutive model, magnetic-dependent dynamic modulus, frequency-dependent dynamic modulus, strain amplitude-dependent dynamic modulus, MS rubber semi-active suspension

1. INTRODUCTION

The performance of vehicle suspensions is closely related to the automotive noise, vibration, and harshness (NVH) issue (Heißing and Ersoy, 2011). In order to improve the ride comfort and the road holding ability and to reduce suspension deflection, three types of suspensions, namely, passive, active, and semi-active, are utilized. The passive suspension has the advantage of cost-effectiveness and design simplicity. However, its stiffness cannot be adjusted according to the external loadings. Therefore, the performance of the passive suspension is limited. Regarding the active suspension, it can exert control force independently without relying on the structural response, which makes it effective to reduce vibration. Nevertheless, its high cost, design complexity, and the lack of stability when the power input is cut off under extreme conditions

prohibit its practical application (Martins et al., 1999). The recent progress in smart material development makes the semi-active vehicle suspension to have a superior suspension measure. In particular, desired vibration-reduction performance is more likely to be achieved by semi-active suspensions, compared to the results using passive suspensions. Furthermore, less energy is consumed by semi-active suspensions when compared with active ones. In the past few years, magneto rheological (MR) fluid (MRF) (Zhang et al., 2004; Biglarbegian et al., 2008; Wilson and Abdullah, 2010; Phu and Choi, 2019; Du et al., 2020) was widely used in the semi-active control area due to its rapid response, temperature insensitivity of the mechanical property, and its high MR effect. However, it is worth noting that although the motion of the suspension can hinder the settlement of ferromagnetic particles in MRF, the increased zero-field viscosity due to the wear of ferromagnetic particles after a long-term operation will reduce the vibration control effect of MRF suspensions (Hu et al., 2012). For magneto-sensitive (MS) rubber, ferromagnetic particles are fixed in the elastomer matrix, thus avoiding the problem of ferromagnetic particle wear and material leakage (Bastola et al., 2019). Therefore, semi-active suspensions based on MS rubber provide a feasible and practical solution to the vibration control problem for vehicles.

The research of MS rubber can be divided into three categories, including fabrication optimization to improve the mechanical property, constitutive modeling of MS rubber, and exploring of possible applications of MS rubber. Davis (1999) analyzed that the optimum particle volume fraction for MS rubber to achieve the highest magnetic modulus is 27%. This conclusion was verified experimentally by Lokander and Stenberg (2003) and Zhou (2003). Subsequently, the influence of the matrix type (Shen et al., 2004), coupling agent (Chen et al., 2007a), pre-structuring (Li et al., 2008), and the surface modification (Jiang et al., 2008) of particles on the MR effect and damping property of MS rubber were investigated. Tong et al. (2018) fabricated a kind of MS rubber with an improved field-induced storage modulus by mixing flow-like particles into the elastomer matrix. It can be foreseen that it will be possible to fabricate MS rubber with a good mechanical performance and a high relative MR effect to meet the engineering application needs, due to the rapid development of MS rubber, including the optimization of their manufacturing process.

In order to predict the mechanical performance of MS rubber, constitutive models with strain and magnetic field strength as inputs and stress as output are needed. Initially, Jolly et al. (1996) developed a magnetic dipole model to simulate the shear modulus increase of MS rubber under a magnetic field. The dipole model was further extended by taking the viscoelastic behavior of MS rubber (Chen et al., 2007b), the interaction of multi-chains (Zhu et al., 2006), and the distribution (Zhang et al., 2010) of chain angles into account. In parallel, constitutive models based on the rheological theory were developed to depict the magnetic field-related non-linear viscoelastic behavior of MS rubber (Li et al., 2010; Chen and Jerrams, 2011). Wang et al. (2018) developed a constitutive modeling-electromagnetic analysis combining method to describe the mechanical behavior of MS rubber. By using the methods mentioned, the mechanical behavior of MS rubber under a small deformation can be predicted accurately. In order to predict the mechanical performance of MS rubber under a large deformation, Dorfmann and Ogden (2003) as well as Kankanala and Triantafyllidis (2004) derived the fundamental balance principles of magneto-elastic materials based on the continuum mechanical theory. Subsequently, the continuum mechanical-based model was further expanded to include the viscoelasticity (Saxena et al., 2014), anisotropy (Bustamante, 2010; Danas et al., 2012), and the strain amplitude-dependent non-linear behavior of MS rubber (Wang and Kari, 2020). Based on the work of Kankanala and Triantafyllidis (2004) and Zhao et al. (2019) developed a model for hard-magnetic particle-based MS rubber. However, for the application of MS rubber in the field of semi-active vibration control, normally, the required force and structural responses are known values where the magnetic field required to achieve the control force needs to be calculated. Accordingly, an inverse model with stress and strain as inputs and the magnetic field strength as output is needed. Current research (Jung et al., 2011; Yang et al., 2016; Wang and Kari, 2019) showed that a better vibration reduction effect can be achieved by MS rubber-based devices, as compared to the traditional passive ones, by controlling the stiffness of MS rubber-based devices discontinuously through switching the magnetic field between zero and saturation state (on-off control). Compared with the on-off control strategy, the development of the inverse model makes the continuous adjustment of the stiffness of the MS rubber-based device a reality. Therefore, it can be foreseen that a semi-active control strategy based on the inverse model of MS rubber can achieve an even better vibration control effect than the previously mentioned on-off control strategy.

To explore the application of MS rubber, Liao et al. (2013) and Sun et al. (2018) designed MS rubber vibration absorbers with the function of tracking external excitation frequency and verified the vibration control effect experimentally. Wang et al. (2017) designed a conical shaped MS rubber-tuned mass damper with an improved stiffness changing ability. Blom and Kari (2012) designed an MS rubber bushing and demonstrated that an optimal isolation effect can be obtained by changing the magnetic field under different frequencies. Subsequently, Alberdi-Muniain et al. (2012, 2013) verified the previous conclusion experimentally. Wang and Kari (2019) simulated the vibration control effect of a MS rubber isolator under a random loading case by using a fuzzy logical control algorithm. Jin et al. (2020) explored the possible application of MS rubber in high-speed railway vehicles. Fu et al. (2019) investigated the design method of an adaptive fuzzy controller for a MS rubber vibration isolator under time-varying sinusoidal excitation. In the field of automobile suspension, Du et al. (2011) deduced the design method of the control gain of the MS rubber semi-active seat suspension H-infinity controller under the conditions of stiffness saturation and parameter uncertainty. Liu et al. (2020) used an adaptive neutral network control design method to simulate the control effect of the MS rubber-based seat isolator under a bump and a random road excitation. However, the magnetic field-dependent non-linear viscoelastic behavior of MS rubber has not been fully taken into account. Meanwhile, Liu et al. (2020)

applied a polynomial expansion fitting method to determine the relationship between the shear modulus of the MS rubber isolator and the magnetic field strength. However, the method is only suitable for some specific working conditions which is difficult to extend directly to practical application situations.

In this study, a silicone rubber-based MS rubber with a relatively high MR effect is fabricated and characterized on a commercial rheometer. Subsequently, a constitutive model which depicts the magnetic field-dependent non-linear viscoelastic behavior of MS rubber is applied to depict the mechanical performance of MS rubber. Furthermore, an inverse model based on the constitutive model of MS rubber with stress and strain as input and the magnetic field strength as output is proposed. On the basis of the constitutive and inverse model, the H-infinity control strategy is used to simulate the vibration control effect of the MS rubber-based vehicle suspension under a bump and a random road excitation.

The research in this study includes material fabrication, characterization, forward and inverse modeling, and simulation analysis, covering a broad application range for MS rubber in vibration control area. The research performed in this article is meaningful for advancing the application of MS rubber in the vehicle suspension area. Furthermore, the forward constitutive model and the inverse model proposed can also be used in other semi-active control scenarios.

2. CHARACTERIZATION AND CONSTITUTIVE MODELING OF MS RUBBER

2.1. Material Fabrication and Characterization

The MS rubber sample in this study was fabricated by mixing silicon rubber (type multi-purpose silicone sealant, Selleys Pty Ltd., Australia), silicon fluid (XIAMETER PMX-200, Dow Corning GmbH, United States), and carbonyl iron particles (CIPs, type CN, BASF, Germany diameter 7 μm on average) with a mass fraction ratio of 2:1:7 at room temperature. After mixing for 5 min, the mixture was placed in a vacuum chamber with a pressure of 0.06 MPa for 10 min to remove air bubbles. Subsequently, the mixture was put into a mold under a magnetic field strength of 1 T for 30 min. After the CIPs were chained, the mixture was left for 48 h at room temperature for post-curing. The images of the MS rubber sample under the scanning electron microscope (Gemini 500, Carl Zeiss, Jena, Germany) at different magnification rates are in **Figure 1**, where arrows represent the chain direction of the iron particles. It can be seen that most iron particles are distributed along the chain direction in the matrix and that there is no large-scale clustering of the iron particles.

After MS rubber was fabricated, the sample with a diameter of 20 mm and a thickness of 2.12 mm were put into a commercial rheometer (Physica MCR 301, Anton Paar Co., Austria) to test the dynamic performance of MS rubber. The test was performed at room temperature $22 \pm 1\,^{\circ}$C. Throughout the test, the external magnetic field was parallel to the iron particle chain direction, while the twist direction of the commercial rheometer was perpendicular to the chain direction. During the measurement, three kinds of conditions were altered: strain amplitude (1, 2, and 5%), magnetic field strength (0, 0.17, 0.34, 0.51, 0.68, and 0.83 T), and frequency (1, 2, 5, 10, 20, 30, 40, 50, 60, 70, and 80 Hz). All combinations of the above three types of conditions were measured, recorded, and averaged over 20 periods. In order to avoid the influence of the Mullins effect (Mullins, 1969), a repeated shear strain where the strain amplitude is slightly larger than the maximum test shear strain was applied before the measurements started. The repeated preloading was terminated when the test results of two consecutive cycles are the same.

Test results for the magnitude and loss factor of the shear modulus vs. frequency with different strain amplitudes and magnetic field strengths are shown in the dot symbols in **Figures 2–4**. Similar to the measurement result by Blom and Kari (2005), the measured shear modulus of MS rubber shows a magnetic field, frequency, and strain amplitude dependence. Specifically, a higher frequency, a stronger magnetic field strength, and a lower strain amplitude led to an increased shear modulus magnitude, while the loss factor almost keeps constant under different frequencies, magnetic field strengths, and strain amplitudes. Furthermore, it can be found that the increasing rate of the shear modulus magnitude, with respect to the increasing magnetic field strength, slows down gradually until a magnetic saturation is reached for the material. Although the shear modulus magnitude of MS rubber seems to increase after 0.83 T, the upper limit of the magnetic field strength in the test was nevertheless set to be 0.83 T due to the sharp rise of the test object temperature that is generated by even stronger magnetic fields.

2.2. Constitutive Modeling

An elastic spring with a parameter μ_e , a viscoelastic element with parameters a and b, and a frictional element with parameters τ_{fmax} and $\gamma_{1/2}$ in parallel are used to depict the dynamic mechanical behavior of MS rubber. Initially, a fractional derivative viscoelastic element is utilized to depict the frequency-dependent shear modulus of MS rubber and to simplify the parameter identification. The relation between the viscoelastic stress τ_{ve} and strain γ for the fractional derivative element in frequency domain is

$$\hat{\tau}_{ve} = b(j\omega)^a \hat{\gamma}, \tag{1}$$

where $\widehat{(\cdot)}$ represents the Fourier transform, j is the imaginary unit, and ω is the angular frequency. From Equation (1), it can be observed that the modulus magnitude $b\omega^a$ increases with increasing frequency and the loss factor $\tan(a\pi/2)$ is a constant value for the fractional derivative element. For more details regarding the fractional derivative model, please refer to Lubich (1986), Lion and Kardelky (2004), and Kari (2017, 2020).

In order to simulate the strain amplitude dependence of the shear modulus of MS rubber, a smooth frictional stress model is used (Berg, 1998). The relation between the friction stress (τ_f) and

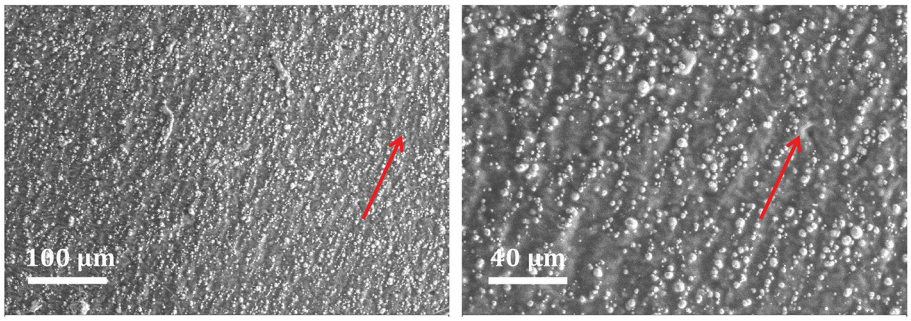

FIGURE 1 | Scanning electron microscope image of MS rubber sample.

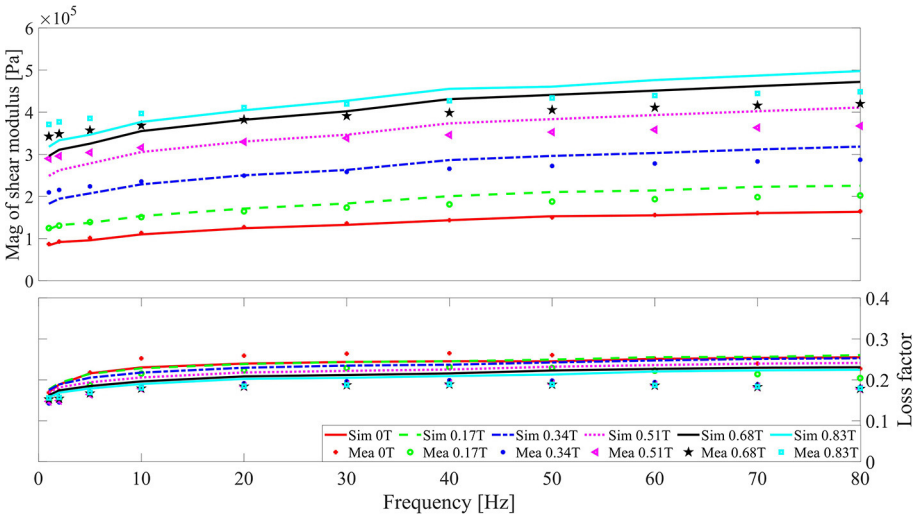

FIGURE 2 | Shear modulus magnitude and loss factor of MS rubber vs. frequency with 1% strain. Lines and symbols are the simulation and experiment results, respectively.

strain γ is

$$\tau_{\mathrm{f}} = \tau_{\mathrm{fs}} + \frac{(\gamma - \gamma_{\mathrm{s}})\left[\tau_{\mathrm{fmax}} - \mathrm{sign}\,(\dot{\gamma})\,\tau_{\mathrm{fs}}\right]}{\gamma_{1/2}\left[1 - \mathrm{sign}\,(\dot{\gamma})\,\frac{\tau_{\mathrm{fs}}}{\tau_{\mathrm{fmax}}}\right] + \mathrm{sign}\,(\dot{\gamma})\,[\gamma - \gamma_{\mathrm{s}}]}, \tag{2}$$

where τ_{fmax} and $\gamma_{1/2}$ are model parameters, representing the maximum friction stress and the strain where one half of τ_{fmax} is reached and $\dot{\gamma}$ represents the strain rate. Initially, $\tau_{\mathrm{fs}} = 0$ and $\gamma_{\mathrm{s}} = 0$. When the loading direction is changed, τ_{fmax} and $\gamma_{1/2}$ are updated (if $\dot{\gamma} = 0$, $\tau_{\mathrm{fs}} = \tau_{\mathrm{f}}|_{\dot{\gamma}=0}$ and $\gamma_{\mathrm{s}} = \gamma|_{\dot{\gamma}=0}$). For more details regarding the smooth frictional stress model, the reader is referred to Berg (1998). By Equations (1) and (2), the total dynamic modulus G^* in frequency domain is

$$G^* = \mu_e + b(\mathrm{j}\omega)^a + \frac{\hat{\tau}_{\mathrm{f}}}{\hat{\gamma}}. \tag{3}$$

After establishing the basic frame of the constitutive model, a non-linear least square fit method is implemented to obtain the basic material parameters by using the measurement results at zero magnetic field. The function lsqnonlin in MATLAB® (MATLAB Release 2015b, The MathWorks, Inc., Natick, Massachusetts, United States) is utilized for parameter identification. In the process of parameter identification, the objective function is set as

$$\mathrm{Obj} = \sum_{i=1}^{n} \left|G^*_{\mathrm{mea}}(i) - G^*_{\mathrm{sim}}(i)\right|^2, \tag{4}$$

where $G^*_{\mathrm{mea}}(i)$ and $G^*_{\mathrm{sim}}(i)$ are the measured and simulated shear modulus of MS rubber, respectively. The symbol i represents the number of loading cases ranging from 1 to 33 since there are 3 kinds of strain amplitude and 11 kinds of frequency during the test under zero magnetic field. The identified material parameters are $\mu_{\mathrm{e}}^0 = 3.4587 \times 10^4\,\mathrm{N\,m^{-2}}$, $a = 0.2071$, $b = 3.4587 \times 10^4\,\mathrm{N\,s^a\,m^{-2}}$, $\tau_{\mathrm{fmax}}^0 = 3.2583 \times 10^2\,\mathrm{N\,m^{-2}}$, and $\gamma_{1/2}^0 = 2.6820 \times 10^{-2}$, where symbols with a superscript zero represent the material parameters at zero magnetic field.

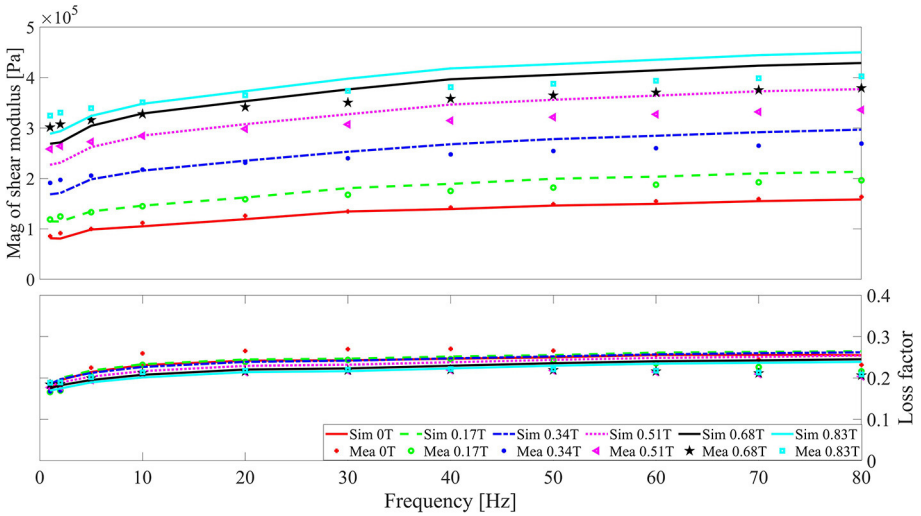

FIGURE 3 | Shear modulus magnitude and loss factor of MS rubber vs. frequency with 2% strain. Lines and symbols are the simulation and experiment results, respectively.

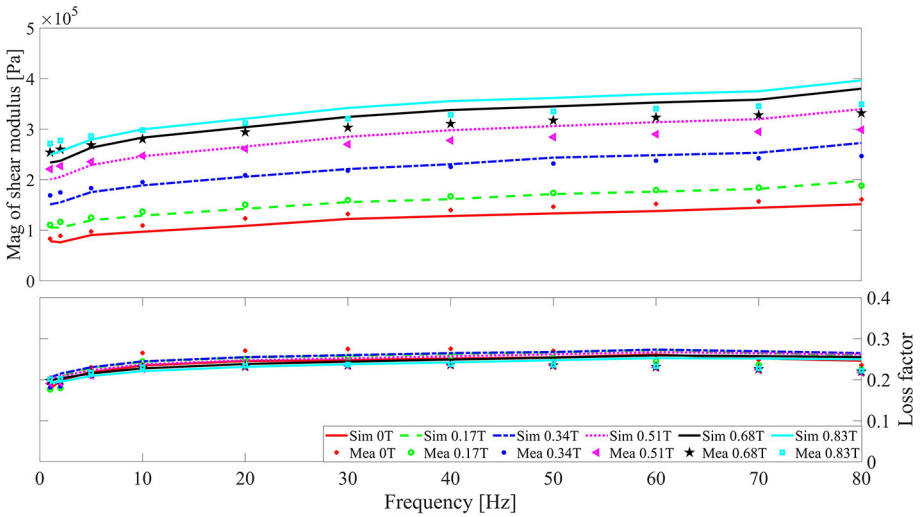

FIGURE 4 | Shear modulus magnitude and loss factor of MS rubber vs. frequency with 5% strain. Lines and symbols are the simulation and experiment results, respectively.

Compared with the generalized Maxwell model, less material parameters are needed for the fractional derivative element to depict the viscoelastic behavior of rubber materials (Haupt and Lion, 2002). Thus, the material parameters are easier to identify for the fractional derivative element. The solution of the viscoelastic stress of the fractional derivative model at the current time step $\tau_{\mathrm{ve}}\left(n\Delta t\right)$ in time domain is

$$\tau_{\mathrm{ve}}\left(n\Delta t\right) = b\sum_{j=1}^{n} c_j(\alpha)^{n-j}\gamma\left[\left(n-j\right)\Delta t\right], \tag{5}$$

where $c_1(\alpha) = 1$, $c_j(\alpha) = \left(j-1-\alpha\right)c_{j-1}(\alpha)/j$ and Δt is the time interval for the numerical implementation. As a comparison, the solution of the viscoelastic stress of the Maxwell element at the current time step (Simo and Hughes, 2006) is

$$\begin{aligned}\tau_{\mathrm{ve}}\left(n\Delta t\right) &= G\exp\left(-\frac{\Delta t}{\eta}\right)\tau_{\mathrm{ve}}\left[\left(n-1\right)\Delta t\right]\\ &+ G\exp\left(-\frac{\Delta t}{2\eta}\right)\left\{\gamma\left(n\Delta t\right)-\gamma\left[\left(n-1\right)\Delta t\right]\right\},\end{aligned} \tag{6}$$

where G and η are the modulus and the relaxation time of the Maxwell model, respectively. The equivalence of Equation (6) in frequency domain (Serra-Aguila et al., 2019) is

$$\hat{\tau}_{\mathrm{ve}} = G\frac{i\omega\eta}{1+i\omega\eta}\hat{\gamma}. \tag{7}$$

By comparing Equations (5) and (6), it can be seen that in order to obtain the viscoelastic stress at the current time step, only stress and strain data at the previous time step are needed for the Maxwell model. However, data of all strain history are needed to obtain the current viscoelastic stress for the fractional derivative element. Therefore, for numerical implementation concern, the Maxwell model is more effective than the fractional derivative element as the time step increases. Taking into account the need for the subsequent time domain simulation, three Maxwell models in parallel are used to substitute the previous fractional derivative model. The identified parameters τ^0_{fmax} and $\gamma^0_{1/2}$ are fixed for the second round of parameter identification. The new material parameters identified are $\mu^0_e = 6.7583 \times 10^4\,\text{N m}^{-2}$, $G_1 = 1.8256 \times 10^4\,\text{N m}^{-2}$, $G_2 = 3.1283 \times 10^4\,\text{N m}^{-2}$, $G_3 = 6.2925 \times 10^4\,\text{N m}^{-2}$, $\eta_1 = 1.8256 \times 10^{-1}$ s, $\eta_2 = 1.5884 \times 10^{-2}$ s, and $\eta_3 = 2.3592 \times 10^{-3}$ s with a relative error between the measurement and simulation result of 2.769%. The comparison between the measurement and simulation results are in **Figure 5**.

After modeling the frequency and the strain amplitude dependence, the magnetic field dependence of the shear modulus of MS rubber depicted by a hyperbolic tangent function is included in the constitutive model. According to Berg (1998), the area of the hysteresis loop for the smooth frictional stress model increases with increasing τ_{fmax} and decreasing $\gamma_{1/2}$. Following the path of Blom and Kari (2011), the magnetic field dependence is included in τ_{fmax} and $\gamma_{1/2}$ by

$$\tau_{\text{fmax}} = \left[1 + \delta_1 \tanh^2\left(\frac{B}{B_s}\right)\right]\tau^0_{\text{fmax}} \tag{8}$$

and

$$\gamma_{1/2} = \left[1 + \delta_2 \tanh^2\left(\frac{B}{B_s}\right)\right]\gamma^0_{1/2}, \tag{9}$$

where B_s is a material parameter used to reflect the magnetic saturation behavior of MS rubber and δ_1 and δ_2 are parameters to reflect the magnetic enhancement of MS rubber. To guarantee that the loss factor is a relatively constant value with respect to the magnetic field strength, the hyperbolic tangent function is included into the elastic part as well

$$\mu_e = \left[1 + \delta_3 \tanh^2\left(\frac{B}{B_s}\right)\right]\mu^0_e, \tag{10}$$

where the meaning of δ_3 is similar to δ_1 and δ_2. The third round of parameter identification was conducted and the magnetic-related parameters are $B_s = 0.4263$ T, $\delta_1 = 16.2172$, $\delta_2 = 0.6538$, and $\delta_3 = 2.0776$, with a relative error of 8.707 %. The comparison between the simulation and measurement results are in **Figures 2–4**. It can be found that the magnetic field-, frequency-, and the strain amplitude-dependent modulus of MS rubber can be well depicted by the model developed. Since three Maxwell elements without magnetic dependency are utilized to simulate the frequency dependency of MS rubber, there is a certain degree of deviation between the simulation and measure results at high frequency and high magnetic field. Due to the wide distribution of the relaxation time of polymer material in the time domain and the possible particle-elastomer interaction within MS rubber, more Maxwell elements with magnetic dependency are favorable to further improve the fitting accuracy between the simulation and experimental results.

3. INVERSE MODEL AND DESIGN OF STATIC OUTPUT H-INFINITY CONTROLLER

3.1. Bisection Method-Based Inverse Model of MS Rubber

As a semi-active actuator, the desired control force cannot be applied by MS rubber suspension directly. The implementation of the control force depends on the interaction between the structure response and the controlled magnetic field. Therefore, it is of great importance to obtain the required magnetic field by the desired control force and the structure response. However, for the constitutive models developed in section 2.2, there is no corresponding direct inverse model with an explicit form. In order to obtain the magnetic field, methods using polynomial fitting of the constitutive models (Choi et al., 2001; Meng et al., 2018) and using an adaptive neuro-fuzzy inference system (Wang et al., 2011; Zong et al., 2012; Yang et al., 2019) are often used. The magnetic field applied to the MS rubber device in practical applications has a lower limit (zero magnetic field strength) and an upper limit (saturated magnetic field strength). Therefore, a bisection-based method can be used to obtain the required magnetic field strength.

The the constitutive model developed in section 2.2 can be expressed as

$$\tau = f(\gamma, \dot{\gamma}, B). \tag{11}$$

The difference between the target stress and the actual stress is expressed by a function

$$g(B) = \tau_{\text{needed}} - f(\gamma, \dot{\gamma}, B). \tag{12}$$

Then, the bisection-based algorithm can be applied to obtain the required magnetic field. Firstly, the strain response γ, the strain rate $\dot{\gamma}$, stress needed τ_{needed}, and the tolerance ε are known. The upper limit of the magnetic field B_{upper} is set to be 0.83 T and the lower limit of the magnetic field B_{lower} is set to be 0 T. Next, if

$$g\left(B_{\text{upper}}\right) \cdot g\left(B_{\text{lower}}\right) > 0, \tag{13}$$

then B_{required} is selected as the value of $f\left(\gamma, \dot{\gamma}, B_{\text{upper}}\right)$ and $f\left(\gamma, \dot{\gamma}, B_{\text{lower}}\right)$ that is closest to τ_{needed}. Else, the tolerance of the magnetic field B_{tol} is set to be

$$B_{\text{tol}} = B_{\text{upper}} - B_{\text{lower}}. \tag{14}$$

If $|B_{\text{tol}}|$ is larger than the tolerance ε, then

$$B_{\text{upper}} = 0.5\left(B_{\text{upper}} + B_{\text{lower}}\right). \tag{15}$$

After updating the magnetic field upper limit, if

$$g\left(B_{\text{upper}}\right) \cdot g\left(B_{\text{lower}}\right) < 0, \tag{16}$$

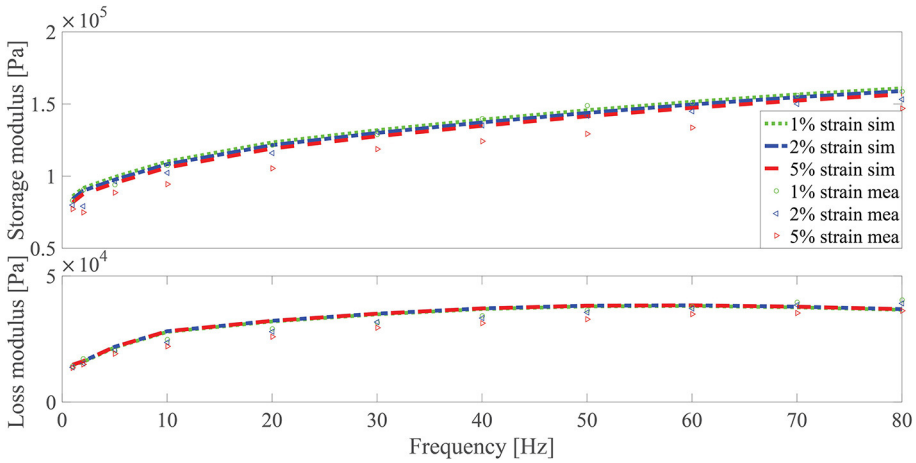

FIGURE 5 | Shear modulus magnitude and loss factor of MS rubber vs. frequency under zero magnetic field. Lines and symbols are the simulation and experiment results, respectively. Three kinds of strain (1, 2, and 5%) are considered.

then

$$B_{\text{lower}} = 0.5\left(B_{\text{upper}} + B_{\text{lower}}\right); \tag{17}$$

else,

$$B_{\text{upper}} = 0.5\left(B_{\text{upper}} + B_{\text{lower}}\right). \tag{18}$$

After the upper and the lower limit of the magnetic field is updated again, the value of B_{required} is compared with ε. If the convergence criteria is not met, new rounds of iterations from Equations (15) to (18) are applied until the convergence criteria is met. Finally, for the case when the condition in Equation (13) is met, B_{applied} is selected as the value of $f\left(\gamma, \dot{\gamma}, B_{\text{upper}}\right)$ and $f\left(\gamma, \dot{\gamma}, B_{\text{lower}}\right)$ that is closest to τ_{needed}; otherwise, $B_{\text{applied}} = B_{\text{upper}}$.

In order to verify the bisection-based inverse model, a Gaussian white noise-based strain signal, ranging from 0 to 25 Hz, with an RMS value of 0.03 m and a time duration of 2 s, and a Gaussian white noise-based magnetic field signal, ranging from 0 to 100 Hz, with magnitudes vary from 0 to 1.5 T, are applied. By the constitutive model developed in section 2.2, the total stress (target stress) corresponding to the strain and magnetic field can be obtained. Subsequently, by the bisection-based inverse model, the predicted magnetic field and the corresponding predicted stress can be obtained. The comparison of the target and predicted values (magnetic field and stress) by the constitutive model and the inverse model is given in **Figure 6**. The overlapping between the target and predicted magnetic field/stress in **Figure 6** demonstrates the effectiveness of the bisection-based inverse model. The values of the target magnetic field, which is larger than 0.83 T cannot, be tracked by the inverse model, since the upper limit of the magnetic field strength is set to be 0.83 T.

3.2. Vehicle Suspension Model and Formulation of H-Infinity Controller

A quarter-car suspension model consists of a one-fourth car body, suspension components (spring plus MS rubber-based semi-active actuator), a wheel, and a tire are investigated in this study. For more details of the quarter-car suspension model, please see **Figure 7**. Symbols z_s, z_t, and z_g represent the car body, wheel, and the ground displacement, respectively. The symbol u represents the control force that can be adjusted by the MS rubber suspension through changing the magnetic field. The model parameters for the quarter-car suspension model are $m_s = 504.5\,\text{kg}$, $m_t = 62\,\text{kg}$, $k_s = 10{,}100\,\text{N m}^{-1}$, $c_s = 200\,\text{N s}\cdot\text{m}^{-1}$, and $k_t = 252{,}000\,\text{N m}^{-1}$.

In order to increase the driving performance, it is required that the transfer function from the road disturbance to the vertical acceleration of the car body ($\ddot{z}_s$), the tire deflection ($z_t - z_g$), and the suspension deflection ($z_s - z_t$) should be small enough. Therefore, the controlled output is defined as $z = [\,\ddot{z}_s \;\; z_s - z_t \;\; z_t - z_g\,]^T$. The measured output is defined as $y = [\,z_t - z_g \;\; \dot{z}_s\,]^T$ due to the fact that the suspension deflection ($z_t - z_g$) and the car-body velocity ($\dot{z}_s$) can be directly measured in practice. The dynamic equilibrium equation for the quarter-car system in state space form is

$$\begin{cases} \dot{x} = Ax + B_1 u + B_2 w \\ z = Ex + Fu \\ y = Cx \end{cases}, \tag{19}$$

where

$$A = \begin{bmatrix} 0 & 0 & 1 & -1 \\ 0 & 0 & 0 & 1 \\ -\frac{k_s}{m_s} & 0 & -\frac{c_s}{m_s} & \frac{c_s}{m_s} \\ \frac{k_s}{m_u} & -\frac{k_t}{m_u} & \frac{c_s}{m_u} & -\frac{c_s}{m_u} \end{bmatrix}, \tag{20}$$

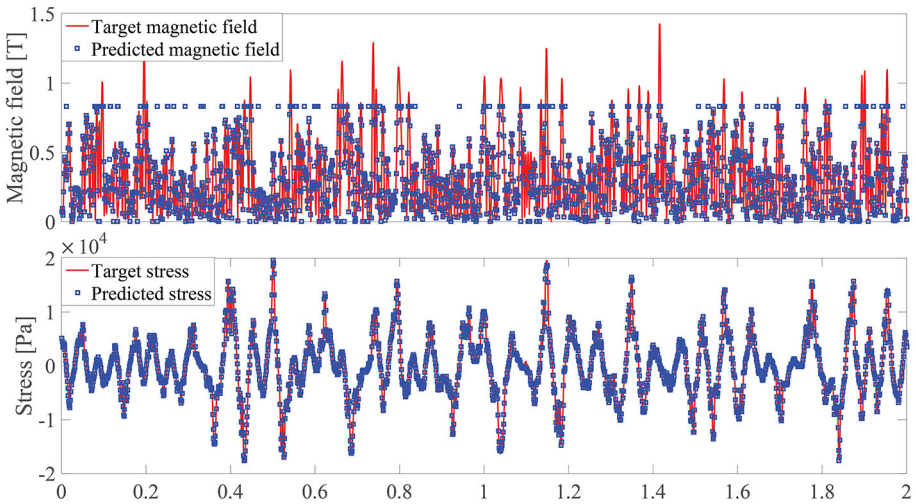

FIGURE 6 | Magnetic field strength and stress vs. time. Line and square are the target and predicted values by the constitutive model and the inverse model, respectively.

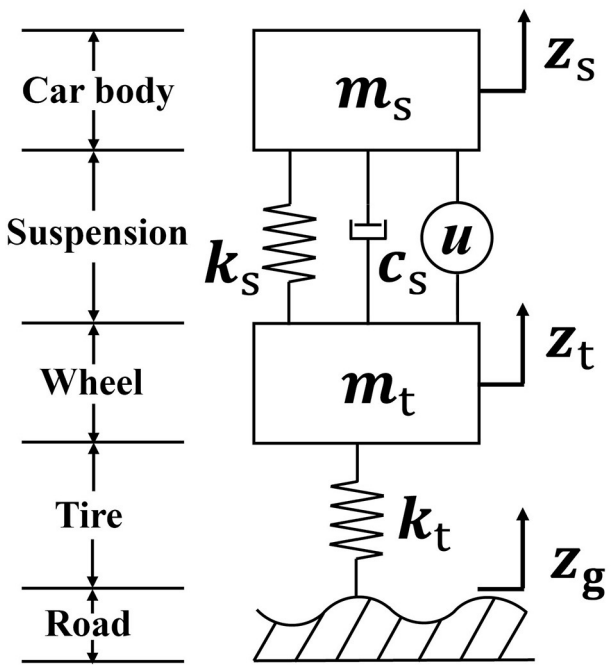

FIGURE 7 | Schematic configuration of a quarter-car system with a MS rubber semi-active suspension.

$$B_1 = \begin{bmatrix} 0 \\ 0 \\ \frac{-1}{m_s} \\ \frac{1}{m_u} \end{bmatrix}, \tag{21}$$

$$B_2 = \begin{bmatrix} 0 \\ -1 \\ 0 \\ 0 \end{bmatrix}, \tag{22}$$

$$C = \begin{bmatrix} 1 & 0 & 0 & 0 \\ 0 & 0 & 1 & 0 \end{bmatrix}, \tag{23}$$

$$E = \begin{bmatrix} -\frac{k_s}{m_s} & 0 & -\frac{c_s}{m_s} & \frac{c_s}{m_s} \\ \alpha & 0 & 0 & 0 \\ 0 & \beta & 0 & 0 \end{bmatrix}, \tag{24}$$

$$F = \begin{bmatrix} -\frac{1}{m_s} \\ 0 \\ 0 \end{bmatrix}, \tag{25}$$

$$x = \begin{bmatrix} z_s - z_t \\ z_t - z_g \\ \dot{z}_s \\ \dot{z}_t \end{bmatrix} \tag{26}$$

and

$$w = \dot{z}_g. \tag{27}$$

The parameters α and β in matrix E are weighting factors for the suspension and tire deflection, respectively. By tuning the weight factors, the trade-off among the car-body acceleration, suspension deflection, and the tire deflection can be controlled. The relation between the controlled force u and the measured output y is

$$u = Ky, \tag{28}$$

where $K = [\, k_1 \;\; k_2 \,]$ is the static output feedback control gain to be designed. To reduce the object transfer functions, robust control algorithms, such as LQR (Zhang et al., 2008; Zhang and Zhuan, 2020), H-2 (Li et al., 2003; Shukla et al., 2016), and H-infinity (Xie et al., 2004; Alma et al., 2011; Khot et al., 2017) controller, are often utilized. Compared with other controllers, the H-infinity norm measure the energy-to-energy gain between

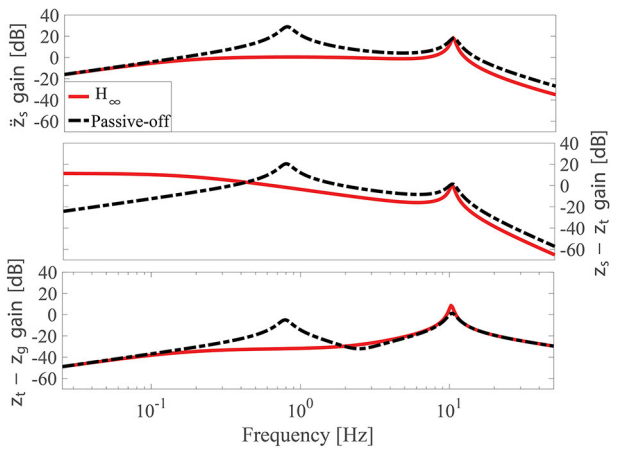

FIGURE 8 | Transfer functions of the car acceleration ($\ddot{z}_s$), suspension deflection ($z_s - z_t$), and tire deflection ($z_t - z_g$) where the gain magnitude is plotted in decibels with unit [dB].

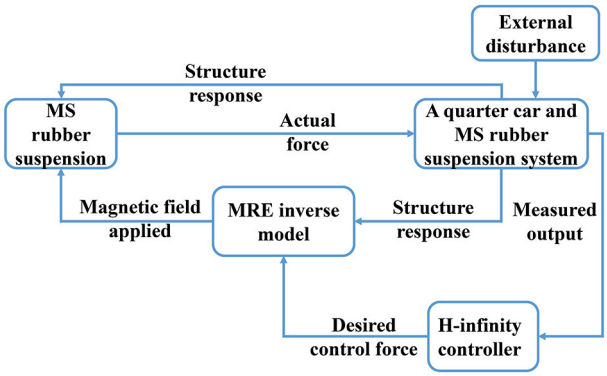

FIGURE 9 | Close-loop flowchart of the whole quarter-car MS rubber suspension system.

the external disturbance and the target outputs directly, which can be viewed as the worst-case gain in frequency domain. In this study, the H-infinity index is used for the controller design. According to Du et al. (2003), the system in Equation (19) is asymptotically stable with a disturbance attenuation $\gamma > 0$ if and only if there exist matrices $G = G^T > 0$ and K such that

$$\begin{bmatrix} \mathrm{sym}\left[G\left(A + B_1 K C\right)\right] & * & * \\ \left(GB_2\right)^{\mathrm{T}} & -\gamma^2 I & * \\ \left(E + FKC\right)^{\mathrm{T}} & 0 & -I \end{bmatrix} < 0, \tag{29}$$

where sym(·) represents symmetric term, (∗) denotes the symmetry matrix block, superscript T denotes matrix transpose, and I is the unit matrix. Normally, the bi-linear matrix inequality problem in Equation (29) cannot be solved directly. According to Ebihara et al. (2015), a coordinate-descent algorithm can be used to transfer the bi-linear matrix inequality problem in Equation (29) to several iterative linear matrix inequality problems, which can be solved in MATLAB LMI package directly. The dimensionless weighting factor α and β in Equation (24) are set to be 4 and 10, respectively. After applying the coordinate-descent algorithm-based iterative method, the H-infinity norm and the static output feedback control gain are obtained with $\gamma = 8.441$ and $K = [\,8.9459\,\mathrm{N\,m^{-1}}\ \ 2.9522\,\mathrm{N\,s\cdot m^{-1}}\,] \times 10^3$. The corresponding transfer functions from the road disturbance to the car acceleration ($\ddot{z}_s$), suspension deflection ($z_s - z_t$), and the tire deflection ($z_t - z_g$) are in **Figure 8**. Compared with the open loop case, after applying H-infinity control algorithm, the peak gain for the car acceleration, suspension deflection, and the tire deflection are all reduced.

4. SIMULATION RESULTS

4.1. Design of MS Rubber Suspension and Numerical Implementation Method

The whole flowchart corresponding to the semi-active control of the MS rubber-based vehicle suspension system is given in **Figure 9**. After the external disturbance excitation is applied, the measured outputs y in Equation (19) is transmitted to the H-infinity controller as the input for the controller. Subsequently, a desired control force output is calculated by the H-infinity controller. However, the desired control force cannot be exerted directly. Therefore, the MS rubber inverse model in section 2.2 is utilized to determine the magnetic field corresponding to the desired control force. Finally, the actual force by the MS rubber suspension is applied to the quarter car system and new measured outputs are detected. In order to verify the vibration control performance of the MS rubber semi-active suspension, simulations under a bump and a random ground excitation are conducted. Before the simulation, the dimension of the MS rubber-based suspension is designed. To reduce the static deformation of the MS rubber suspension caused by the preloading of the car body mass, a linear spring with a stiffness of 2,100 $\mathrm{N\,m^{-1}}$ is installed in parallel with the MS rubber-based suspension. Sun et al. (2018) applied a multi-layer strategy for the MS rubber suspension in order to improve the deformation ability of the whole suspension, meanwhile ensuring the strain of each layer of MS rubber is small. Considering the simplest case, a multi-layer sandwich typed structure made of steel plate and MS rubber working in a shear mode are utilized. The total layer number of MS rubber is 10. For each layer MS rubber, the thickness is 0.04 m and the area is $A = (0.10\,\mathrm{m})^2$. Therefore, the approximate initial stiffness of the suspension by using the shear modulus of MS rubber at 5% strain amplitude under 1 Hz is

$$\begin{aligned} k_s &\approx \left(2\frac{0.10^2 \times 8 \times 10^4}{5 \times 0.04} + 2100\right)\mathrm{N\,m^{-1}} \\ &= 10100\,\mathrm{N\,m^{-1}}. \end{aligned} \tag{30}$$

To illustrate the effectiveness of the control strategy, MS rubber suspension with the maximum stiffness (passive-on), MS rubber suspension with the minimum stiffness (passive-off), sky-hook on-off control strategy, and the active control strategy are simulated as well. The corresponding magnetic field control strategy for the sky-hook on-off control strategy is

$$B_{\text{control}} = \begin{cases} 0.83\,\text{T} & \dot{z}_\text{s}\left(z_\text{s} - z_\text{t}\right) > 0 \\ 0\,\text{T} & \dot{z}_\text{s}\left(z_\text{s} - z_\text{t}\right) \le 0 \end{cases}. \tag{31}$$

In order to fully consider the magnetic field-, frequency-, and the strain amplitude-dependent dynamic behavior of MS rubber and obtain the structure response, the Newmark-beta method (Géradin and Rixen, 2014) based on implicit time integration is applied. The dynamic equilibrium equation of the whole system can be written as

$$\begin{cases} M\ddot{q} + Kq + C\dot{q} + F(q,\dot{q}) = G(t) \\ q_0,\ \dot{q}_0 \quad \text{given} \end{cases}, \tag{32}$$

where

$$M = \begin{bmatrix} m_\text{s} & m_\text{s} \\ m_\text{t} & 0 \end{bmatrix}, \tag{33}$$

$$q = \begin{bmatrix} z_\text{t} \\ z_\text{s} - z_\text{t} \end{bmatrix}, \tag{34}$$

$$K = \begin{bmatrix} 0 & k_\text{s} \\ k_\text{t} & -k_\text{s} \end{bmatrix}, \tag{35}$$

$$C = \begin{bmatrix} 0 & c_\text{s} \\ 0 & -c_\text{s} \end{bmatrix}, \tag{36}$$

$$F\left(q,\dot{q}\right) = A\begin{bmatrix} f(\gamma,\dot{\gamma},B) \\ f(\gamma,\dot{\gamma},B) \end{bmatrix} \tag{37}$$

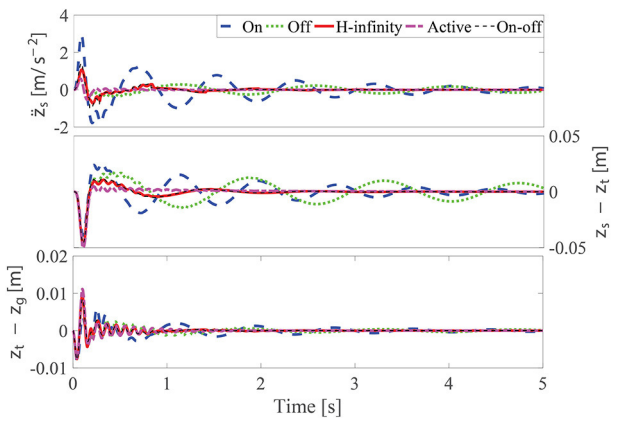

FIGURE 10 | Comparison of the target responses at different control strategies under a bump excitation.

and

$$G(t) = \begin{bmatrix} 0 \\ k_\text{t} z_\text{g} \end{bmatrix}. \tag{38}$$

First, an initial acceleration $\ddot{q}_\text{trial}$ is obtained by the known response at the previous time step, $q_{\text{n}-1}$,

$$\begin{aligned} \ddot{q}_\text{trial} &= M^{-1}G_\text{n} \\ &- M^{-1}\left[Kq_{\text{n}-1} + C\dot{q}_{\text{n}-1} + F\left(q_{\text{n}-1},\dot{q}_{\text{n}-1}\right)\right] \end{aligned} \tag{39}$$

where symbols with subscript $\text{n}-1$ and n represent the response at the previous and the current time step, respectively. Subsequently, the predicted displacement q, velocity $\dot{q}$, and acceleration $\ddot{q}$ at the current time step are obtained by the average acceleration method

$$q = q_{\text{n}-1} + \Delta t\dot{q}_{\text{n}-1} + \frac{\Delta t^2}{4}\ddot{q}_\text{trial}, \tag{40}$$

$$\dot{q} = \dot{q}_{\text{n}-1} + \frac{\Delta t}{2}\ddot{q}_\text{trial} \tag{41}$$

and

$$\ddot{q} = \begin{bmatrix} 0 & 0 \end{bmatrix}^\text{T}. \tag{42}$$

Following these, the residual force R is obtained

$$R = M\ddot{q} + Kq + C\dot{q} + F\left(q,\dot{q}\right) - G(t). \tag{43}$$

A threshold for the residual force $\kappa = 1 \times 10^{-3}\,\text{N}$ is set as the criteria for convergence. If R is larger than κ, a correction is applied by

$$q = q + \Delta q, \tag{44}$$

$$\dot{q} = \dot{q} + \frac{2}{\Delta t}\Delta q, \tag{45}$$

and

$$\ddot{q} = \ddot{q} + \frac{4}{\Delta t^2}\Delta q, \tag{46}$$

TABLE 1 | RMS values of the target responses at different control strategies under a bump excitation.

Control strategies	Car-body acceleration [m s^{-2}]	Suspension deflection [m]	Tire deflection [m]
Passive-on	5.9816×10^{-1}	8.9908×10^{-3}	1.3001×10^{-3}
Passive-off	1.9965×10^{-1}	9.6832×10^{-3}	1.1542×10^{-3}
H-infinity	1.5413×10^{-1}	5.5579×10^{-3}	1.0462×10^{-3}
Active	7.3811×10^{-2}	5.4319×10^{-3}	1.1910×10^{-3}
Sky-hook on-off	1.9108×10^{-1}	5.5873×10^{-3}	9.8991×10^{-4}

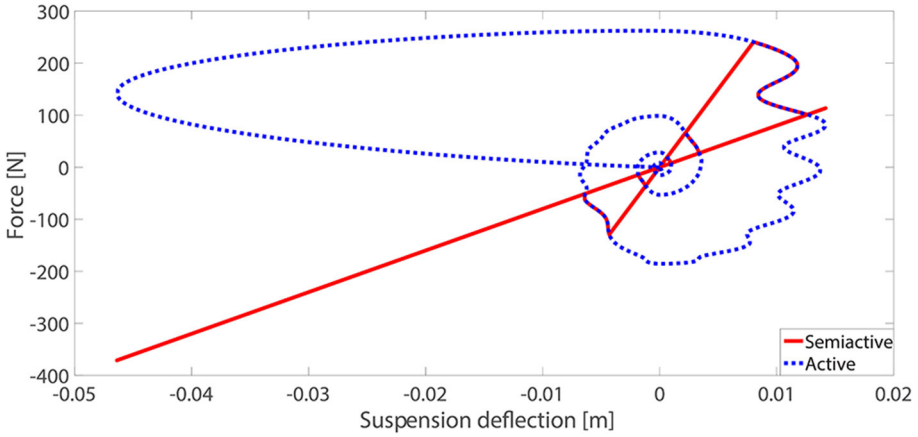

FIGURE 11 | Comparison of the desired control force (red line) and the actual applied force (blue dotted line) vs. the MS rubber suspension deflection.

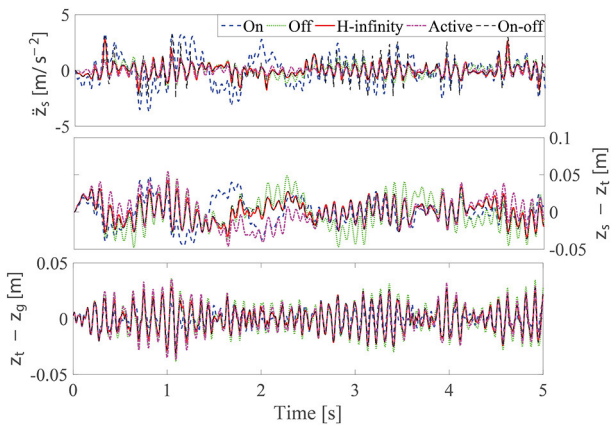

FIGURE 12 | Comparison of the target responses at different control strategies under the random excitation.

where $\Delta q = -R/S$, with S as the Jacobian matrix for the system

$$S = M\frac{4}{\Delta t^2} + C\frac{2}{\Delta t} + K + \frac{\partial F(q,\dot{q})}{\partial q}. \tag{47}$$

After q is updated, the new residual force R is compared with the threshold κ. If the converge criteria is not satisfied, new rounds of iterations are applied until the convergence criteria is met. Finally, the structure response at the current time step can be obtained. Regarding $\partial F/\partial q$, a finite difference numerical method can be applied to obtain its value (An et al., 2011).

4.2. Comparison on Bump Response

According to Sun et al. (2020), a road bump shock can be represented by

$$z_g = \begin{cases} 0.5H\left[1-\cos\left(\frac{2\pi v}{L}t\right)\right] 0 \le t \le \frac{L}{v} \\ 0 \end{cases}, \tag{48}$$

where $H = 0.04\,\text{m}$, $L = 5\,\text{m}$, and $v = 25\,\text{m s}^{-1}$ are the bump height, bump length, and the passing car velocity, respectively. After applying the numerical simulation analysis by the numerical methods in sections 2.2, 3.1, and 4.1 , the comparison of the passive-on, passive-off, H-infinity semi-active, sky-hook on-off, and the active control strategies of the car-body acceleration, suspension deflection, and the tire deflection is given in **Figure 10**. Compared with passive-on and passive-off cases, a better vibration control effect can be achieved by the H-infinity semi-active, sky-hook on-off, and the active control strategies. The root mean square (RMS) values for the target responses ($\ddot{z}_s$, $z_s - z_t$, and $z_t - z_g$) under different control strategies for the bump excitation are in **Table 1**. It can be found that the vibration control effect is the best for the active control case, followed by the H-infinity semi-active control and the sky-hook on-off control strategies. In **Figure 11**, the desired control force for the active control strategy and the actual applied force by the MS rubber semi-active suspension vs. suspension deflection are compared. The first and third quadrants in the figure correspond to the positive stiffness area, while the second and forth quadrants correspond to the negative stiffness area. Due to the positive shear modulus and the limited MR effect of MS rubber, the advantage of the active control strategy cannot be fully utilized by the MS rubber suspension. This conclusion can be verified by the partially overlapping between the desired control force-deflection curve and the actual applied force-deflection curve.

4.3. Comparison on a Random Response

After conducting the simulation under the bump response, a new round of simulation analysis under a random response is conducted. According to Sun et al. (2020), the road roughness can be treated as a random process with a given displacement power spectral density under frequency domain $G_q(f)$ by

$$G_q(f) = G_q(n_0)\, v\left(\frac{n_0}{f}\right)^2, \tag{49}$$

where $G_q(n_0)$ is the road roughness coefficient, $n_0 = 0.1\,\text{m}^{-1}$ and v is the car velocity. In the simulation, C road roughness is applied, where $G_q(n_0) = 64 \times 10^{-6}\,\text{m}^3$. The car velocity is set to be $v = 60\,\text{km h}^{-1}$. The corresponding road vibration signal

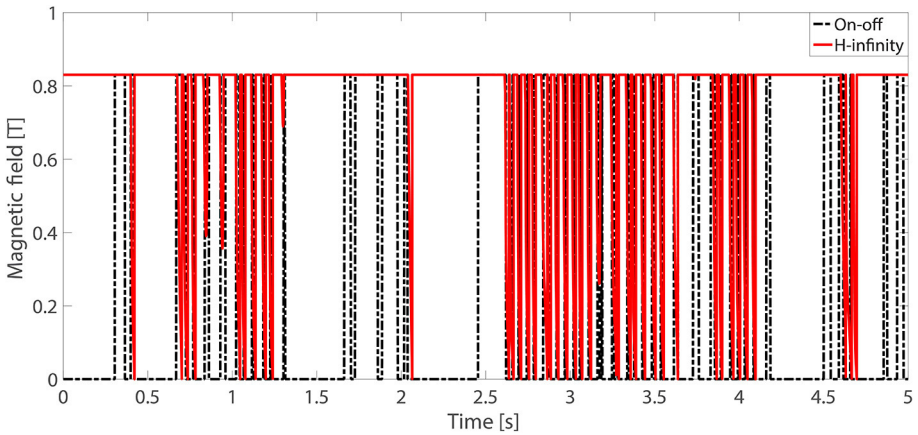

FIGURE 13 | Comparison of the magnetic field under the sky-hook on-off control strategy and the H-infinity semi-active control strategy.

TABLE 2 | RMS values of the target responses at different control strategies under a random excitation.

Control strategies	Car-body acceleration [m s^{-2}]	Suspension deflection [m]	Tire deflection [m]
Passive-on	5.1623×10^{-1}	5.9717×10^{-3}	3.9646×10^{-3}
Passive-off	3.1670×10^{-1}	1.3337×10^{-2}	7.2957×10^{-3}
H-infinity	2.9139×10^{-1}	7.3164×10^{-3}	5.9427×10^{-3}
Active	1.9974×10^{-2}	8.7158×10^{-3}	6.2132×10^{-3}
Sky-hook on-off	3.5575×10^{-2}	7.3842×10^{-3}	6.0066×10^{-3}

generated by a fast Fourier transformation method (Beaulieu and Tan, 1997) with a sampling frequency of 1,000 Hz and a time length of 5 s is applied to the quarter car system. The comparison of the passive on, passive off, H-infinity semi-active, sky-hook on-off, and the active control strategies of the car-body acceleration, suspension deflection, and the tire deflection is given in **Figure 12**. The magnetic field vs. time under the H-infinity semi-active strategy and the sky-hook on-off control strategy is given in **Figure 13**. The result of the RMS values of the targeted responses are in **Table 2**. It can be found that compared with passive off and passive on cases, a better vibration reduction effect can be achieved by the H-infinity semi-active control strategy in controlling the car-body acceleration and the suspension deflection. Strangely, according to **Table 2**, the RMS value of the suspension and the tire deflection under the passive-on control strategy is the smallest. This can be attributed to the increase of the overall stiffness of the quarter-car system after implementing the maximum stiffness of the MS rubber suspension. Therefore, the deflection response under external excitation is smaller under the passive on case compared to other cases. However, the reduction of the car-body acceleration cannot be achieved directly by simply increasing the overall stiffness of the quarter-car system. This conclusion can be verified by the comparison of the car-body acceleration results under different control strategies where the acceleration under the passive on case is the largest. Furthermore, it can be found that there exists a flutter phenomena in the car body acceleration for the sky-hook on-off control strategy compared with the H-infinity control strategy. Due to the continuous adjusting of the magnetic field, the vibration control effect of the H-infinity semi-active control strategy is superior as compared to the sky-hook on-off control strategy.

5. CONCLUSION

The fabrication, characterization, and the modeling of the mechanical performance of MS rubber along with the application of MS rubber in vehicle semi-active suspension are studied in this research. The matching between the simulated and measured shear modulus of MS rubber demonstrates that the applied constitutive model can depict the magnetic field-, frequency-, and strain amplitude-dependent shear modulus of MS rubber with accuracy. In order the desired control force can be implemented by the MS rubber semi-active device, an inverse model is developed to obtain the magnetic field corresponding to the desired control force. The matching between the target stress and the predicted stress generated by the calculated magnetic field through the inverse model indicates that the inverse model developed can track the desired control force with high accuracy. Furthermore, in order to explore the possible application of MS rubber in vehicle vibration control, a MS rubber semi-active suspension with the H-infinity control strategy applied to a quarter car model under a bump and a random ground excitation is studied. The results reveal that compared with the passive and the sky-hook on-off control cases, a better vibration reduction effect can be achieved by the MS rubber semi-active suspension with the H-infinity control strategy. However, in order to implement MS rubber in the vehicle vibration control area and achieve a good vibration reduction effect, issues such as further increase the MR effect of MS rubber, modeling the mechanical behavior of MS rubber with considering preload effect and the design optimization of the

magnetic field generation circuit should be investigated. Besides, an increased vibration reduction effect is expected while adding an adjustable damping component to the current MS rubber-based suspension since the former adapts its damping while the latter adapts its stiffness. Furthermore, as the deflection of the suspension increases, the MR effect of MS rubber will weaken. Although the constitutive model can reflect the strain dependence of the MS rubber modulus, in practical applications, it is necessary to optimize the design of the MS rubber suspension to ensure that the MR effect of MS rubber can be utilized to the ultimate extent and achieve a good vibration control effect.

DATA AVAILABILITY STATEMENT

The original contributions presented in the study are included in the article/supplementary material, further inquiries can be directed to the corresponding author/s.

AUTHOR CONTRIBUTIONS

BW developed the theoretical formalism and performed the numerical simulations. TH helped to carry out the fabrication and characterization of MS rubber. XG and LK supervised the project and provided revisions to the scientific content of the manuscript. LS, JL, and ZX provided funding. All authors contributed to manuscript revision, read, and approved the submitted version.

FUNDING

Financial supports from the National Natural Science Foundation of China with Grant No. 11972343 and the National Key R&D Program of China with Grant No. 2018YFB1201703, the Anhui Key R&D program of China are gratefully acknowledged. The open access publication fee support by KTH Royal Institute of Technology is gratefully acknowledged.

REFERENCES

Alberdi-Muniain, A., Gil-Negrete, N., and Kari, L. (2012). Direct energy flow measurement in magneto-sensitive vibration isolator systems. *J. Sound Vib.* 331, 1994–2006. doi: 10.1016/j.jsv.2012.01.015

Alberdi-Muniain, A., Gil-Negrete, N., and Kari, L. (2013). Indirect energy flow measurement in magneto-sensitive vibration isolator systems. *Appl. Acoust.* 74, 575–584. doi: 10.1016/j.apacoust.2012.09.011

Alma, M., Martinez, J. J., Landau, I. D., and Buche, G. (2011). Design and tuning of reduced order h-infinity feedforward compensators for active vibration control. *IEEE Trans. Control Syst. Technol.* 20, 554–561. doi: 10.1109/TCST.2011.2119485

An, H., Wen, J., and Feng, T. (2011). On difference approximation of a matrix-vector product in the Jacobian-free Newton–Krylov method. *J. Comput. Appl. Math.* 236, 1399–1409. doi: 10.1016/j.cam.2011.09.003

Bastola, A., Ang, E., Paudel, M., and Li, L. (2019). Soft hybrid magnetorheological elastomer: gap bridging between MR fluid and MR elastomer. *Colloids Surf. A Physicochem. Eng. Asp.* 583:123975. doi: 10.1016/j.colsurfa.2019.123975

Beaulieu, N., and Tan, C. (1997). "An FFT method for generating bandlimited gaussian noise variates," in *GLOBECOM 97. IEEE Global Telecommunications Conference. Conference Record*, Vol. 2 (IEEE), 684–688.

Berg, M. (1998). A non-linear rubber spring model for rail vehicle dynamics analysis. *Veh. Syst. Dyn.* 30, 197–212. doi: 10.1080/00423119808969447

Biglarbegian, M., Melek, W., and Golnaraghi, F. (2008). A novel neuro-fuzzy controller to enhance the performance of vehicle semi-active suspension systems. *Veh. Syst. Dyn.* 46, 691–711. doi: 10.1080/00423110701585420

Blom, P., and Kari, L. (2005). Amplitude and frequency dependence of magneto-sensitive rubber in a wide frequency range. *Polym. Test.* 24, 656–662. doi: 10.1016/j.polymertesting.2005.04.001

Blom, P., and Kari, L. (2011). A nonlinear constitutive audio frequency magneto-sensitive rubber model including amplitude, frequency and magnetic field dependence. *J. Sound Vib.* 330, 947–954. doi: 10.1016/j.jsv.2010.09.010

Blom, P., and Kari, L. (2012). The frequency, amplitude and magnetic field dependent torsional stiffness of a magneto-sensitive rubber bushing. *Int. J. Mech. Sci.* 60, 54–58. doi: 10.1016/j.ijmecsci.2012.04.006

Bustamante, R. (2010). Transversely isotropic nonlinear magneto-active elastomers. *Acta Mech.* 210, 183–214. doi: 10.1007/s00707-009-0193-0

Chen, L., Gong, X., Jiang, W., Yao, J., Deng, H., and Li, W. (2007a). Investigation on magnetorheological elastomers based on natural rubber. *J. Mater. Sci.* 42, 5483–5489. doi: 10.1007/s10853-006-0975-x

Chen, L., Gong, X., and Li, W. (2007b). Microstructures and viscoelastic properties of anisotropic magnetorheological elastomers. *Smart Mater. Struct.* 16:2645. doi: 10.1088/0964-1726/16/6/069

Chen, L., and Jerrams, S. (2011). A rheological model of the dynamic behavior of magnetorheological elastomers. *J. Appl. Phys.* 110:013513. doi: 10.1063/1.3603052

Choi, S., Lee, S., and Park, Y. (2001). A hysteresis model for the field-dependent damping force of a magnetorheological damper. *J. Sound Vib.* 245, 375–383. doi: 10.1006/jsvi.2000.3539

Danas, K., Kankanala, S., and Triantafyllidis, N. (2012). Experiments and modeling of iron-particle-filled magnetorheological elastomers. *J. Mech. Phys. Solids* 60, 120–138. doi: 10.1016/j.jmps.2011.09.006

Davis, L. (1999). Model of magnetorheological elastomers. *J. Appl. Phys.* 85, 3348–3351. doi: 10.1063/1.369682

Dorfmann, A., and Ogden, R. (2003). Magnetoelastic modelling of elastomers. *Eur. J. Mech. A Solids* 22, 497–507. doi: 10.1016/S0997-7538(03)00067-6

Du, H., Lam, J., and Sze, K. Y. (2003). Non-fragile output feedback h-infinity vehicle suspension control using genetic algorithm. *Eng. Appl. Artif. Intell.* 16, 667–680. doi: 10.1016/j.engappai.2003.09.008

Du, H., Li, W., and Zhang, N. (2011). Semi-active variable stiffness vibration control of vehicle seat suspension using an MR elastomer isolator. *Smart Mater. Struct.* 20:105003. doi: 10.1088/0964-1726/20/10/105003

Du, X., Yu, M., Fu, J., and Huang, C. (2020). Experimental study on shock control of a vehicle semi-active suspension with magneto-rheological damper. *Smart Mater. Struct.* 29:074002. doi: 10.1088/1361-665X/ab859e

Ebihara, Y., Peaucelle, D., and Arzelier, D. (2015). *S-Variable Approach to LMI-Based Robust Control*. New York, NY: Springer.

Fu, J., Bai, J., Lai, J., Li, P., Yu, M., and Lam, H.-K. (2019). Adaptive fuzzy control of a magnetorheological elastomer vibration isolation system with time-varying sinusoidal excitations. *J. Vib. Control* 456, 386–406. doi: 10.1016/j.jsv.2019.05.046

Géradin, M., and Rixen, D. J. (2014). *Mechanical Vibrations: Theory and Application to Structural Dynamics*. Chichester: John Wiley & Sons.

Haupt, P., and Lion, A. (2002). On finite linear viscoelasticity of incompressible isotropic materials. *Acta Mech.* 159, 87–124. doi: 10.1007/BF01171450

Heißing, B., and Ersoy, M. (2011). "Ride comfort and NVH," in *Chassis Handbook*, eds, B. Heißing and M. Ersoy. (Wiesbaden: Springer), 421–448.

Hu, Z., Yan, H., Qiu, H., Zhang, P., and Liu, Q. (2012). Friction and wear of magnetorheological fluid under magnetic field. *Wear* 278, 48–52. doi: 10.1016/j.wear.2012.01.006

Jiang, W., Yao, J., Gong, X., and Chen, L. (2008). Enhancement in magnetorheological effect of magnetorheological elastomers by surface modification of iron particles. *Chin. J. Chem. Phys.* 21:87. doi: 10.1088/1674-0068/21/01/87-92

Jin, T., Liu, Z., Sun, S., Ren, Z., Deng, L., Yang, B., et al. (2020). Development and evaluation of a versatile semi-active suspension system for high-speed railway vehicles. *Mech. Syst. Signal Process.* 135:106338. doi: 10.1016/j.ymssp.2019.106338

Jolly, M. R., Carlson, J. D., and Munoz, B. C. (1996). A model of the behaviour of magnetorheological materials. *Smart Mater. Struct.* 5:607. doi: 10.1088/0964-1726/5/5/009

Jung, H.-J., Eem, S.-H., Jang, D.-D., and Koo, J.-H. (2011). Seismic performance analysis of a smart base-isolation system considering dynamics of MR elastomers. *J. Intell. Mater. Syst. Struct.* 22, 1439–1450. doi: 10.1177/1045389X11414224

Kankanala, S., and Triantafyllidis, N. (2004). On finitely strained magnetorheological elastomers. *J. Mech. Phys. Solids* 52, 2869–2908. doi: 10.1016/j.jmps.2004.04.007

Kari, L. (2017). Dynamic stiffness of chemically and physically ageing rubber vibration isolators in the audible frequency range. *Contin. Mech. Thermodyn.* 29, 1027–1046. doi: 10.1007/s00161-017-0569-7

Kari, L. (2020). Are single polymer network hydrogels with chemical and physical cross-links a promising dynamic vibration absorber material? A simulation model inquiry. *Materials* 13:5127. doi: 10.3390/ma13225127

Khot, S., Yelve, N. P., Kumar, P., Purohit, G. A., and Singh, D. (2017). "Implementation of H-infinity controller in experimental active vibration control of a cantilever beam," in *2017 International Conference on Nascent Technologies in Engineering (ICNTE)* (Mumbai: IEEE), 1–5.

Li, H. J., James Hu, S.-L., and Jakubiak, C. (2003). H2 active vibration control for offshore platform subjected to wave loading. *J. Sound Vib.* 263, 709–724. doi: 10.1016/S0022-460X(02)01095-7

Li, J., Gong, X., Xu, Z., and Jiang, W. (2008). The effect of pre-structure process on magnetorheological elastomer performance. *Int. J. Mater. Res.* 99, 1358–1364. doi: 10.3139/146.101775

Li, W., Zhou, Y., and Tian, T. (2010). Viscoelastic properties of MR elastomers under harmonic loading. *Rheol. Acta* 49, 733–740. doi: 10.1007/s00397-010-0446-9

Liao, G., Gong, X., and Xuan, S. (2013). Phase based stiffness tuning algorithm for a magnetorheological elastomer dynamic vibration absorber. *Smart Mater. Struct.* 23:015016. doi: 10.1088/0964-1726/23/1/015016

Lion, A., and Kardelky, C. (2004). The Payne effect in finite viscoelasticity: constitutive modelling based on fractional derivatives and intrinsic time scales. *Int. J. Plast.* 20, 1313–1345. doi: 10.1016/j.ijplas.2003.07.001

Liu, C., Hemmatian, M., Sedaghati, R., and Wen, G. (2020). Development and control of magnetorheological elastomer-based semi-active seat suspension isolator using adaptive neural network. *Front. Mater.* 7:171. doi: 10.3389/fmats.2020.00171

Lokander, M., and Stenberg, B. (2003). Performance of isotropic magnetorheological rubber materials. *Polym. Test.* 22, 245–251. doi: 10.1016/S0142-9418(02)00043-0

Lubich, C. (1986). Discretized fractional calculus. *SIAM J. Numer. Anal.* 17, 704–719.

Martins, I., Esteves, M., Da Silva, F. P., and Verdelho, P. (1999). "Electromagnetic hybrid active-passive vehicle suspension system," in *1999 IEEE 49th Vehicular Technology Conference (Cat. No. 99CH36363)*, Vol. 3 (Houston, TX: IEEE), 2273–2277.

Meng, X., Wang, Z., Liu, B., and Wang, S. (2018). Third-order polynomial model for analyzing stickup state laminated structure in flexible electronics. *Acta Mech. Sin.* 34, 48–61. doi: 10.1007/s10409-017-0670-y

Mullins, L. (1969). Softening of rubber by deformation. *Rubber Chem. Technol.* 42, 339–362.

Phu, D. X., and Choi, S.-B. (2019). Magnetorheological fluid based devices reported in 2013–2018: mini-review and comment on structural configurations. *Front. Mater.* 6:19. doi: 10.3389/fmats.2019.00019

Saxena, P., Hossain, M., and Steinmann, P. (2014). Nonlinear magneto-viscoelasticity of transversally isotropic magneto-active polymers. *Proc. Math. Phys. Eng. Sci.* 470:20140082. doi: 10.1098/rspa.2014.0082

Serra-Aguila, A., Puigoriol-Forcada, J., Reyes, G., and Menacho, J. (2019). Viscoelastic models revisited: characteristics and interconversion formulas for generalized Kelvin–Voigt and Maxwell models. *Acta Mech. Sin.* 35, 1191–1209. doi: 10.1007/s10409-019-00895-6

Shen, Y., Golnaraghi, M. F., and Heppler, G. R. (2004). Experimental research and modeling of magnetorheological elastomers. *J. Intell. Mater. Syst. Struct.* 15, 27–35. doi: 10.1177/1045389X04039264

Shukla, P., Ghodki, D., Manjarekar, N. S., and Singru, P. M. (2016). A study of H infinity and H2 synthesis for active vibration control. *IFAC PapersOnLine* 49, 623–628. doi: 10.1016/j.ifacol.2016.03.125

Simo, J. C., and Hughes, T. J. (2006). *Computational Inelasticity*, Vol. 7. New York, NY: Springer Science & Business Media.

Sun, S., Yang, J., Du, H., Zhang, S., Yan, T., Nakano, M., et al. (2018). Development of magnetorheological elastomers-based tuned mass damper for building protection from seismic events. *J. Intell. Mater. Syst. Struct.* 29, 1777–1789. doi: 10.1177/1045389X17754265

Sun, W., Gao, H., and Shi, P. (2020). *Advanced Control for Vehicle Active Suspension Systems*. Cham: Springer.

Tong, Y., Dong, X., and Qi, M. (2018). Improved tunable range of the field-induced storage modulus by using flower-like particles as the active phase of magnetorheological elastomers. *Soft Matter* 14, 3504–3509. doi: 10.1039/C8SM00359A

Wang, B., and Kari, L. (2019). Modeling and vibration control of a smart vibration isolation system based on magneto-sensitive rubber. *Smart Mater. Struct.* 28:065026. doi: 10.1088/1361-665X/ab1ab4

Wang, B., and Kari, L. (2020). A visco-elastic-plastic constitutive model of isotropic magneto-sensitive rubber with amplitude, frequency and magnetic dependency. *Int. J. Plast.* 132:102756. doi: 10.1016/j.ijplas.2020.102756

Wang, J., Li, S., Cui, J., and Man, L. (2011). "Parameter inversion of constitutive model of soil using neural networks," in *Advances in Computer Science, Intelligent System and Environment* (Berlin: Springer), 417–420.

Wang, Q., Dong, X., Li, L., and Ou, J. (2017). Study on an improved variable stiffness tuned mass damper based on conical magnetorheological elastomer isolators. *Smart Mater. Struct.* 26:105028. doi: 10.1088/1361-665X/aa81e8

Wang, Q., Dong, X., Li, L., and Ou, J. (2018). Mechanical modeling for magnetorheological elastomer isolators based on constitutive equations and electromagnetic analysis. *Smart Mater. Struct.* 27:065017. doi: 10.1088/1361-665X/aabdb5

Wilson, C. M. D., and Abdullah, M. M. (2010). Structural vibration reduction using self-tuning fuzzy control of magnetorheological dampers. *Bull. Earthq. Eng.* 8, 1037–1054. doi: 10.1007/s10518-010-9177-7

Xie, S. L., Zhang, X. N., Zhang, J. H., and Yu, L. (2004). H(infinity) robust vibration control of a thin plate covered with a controllable constrained damping layer. *J. Vib. Control* 10, 115–133. doi: 10.1177/1077546304032994

Yang, J., Sun, S., Tian, T., Li, W., Du, H., Alici, G., et al. (2016). Development of a novel multi-layer MRE isolator for suppression of building vibrations under seismic events. *Mech. Syst. Signal Process.* 70, 811–820. doi: 10.1016/j.ymssp.2015.08.022

Yang, Z., Fu, J., Bai, J., Liao, G., and Yu, M. (2019). "An inverse model of magnetorheological elastomer isolator with neural network," in *2019 Chinese Control And Decision Conference (CCDC)* (Nanchang: IEEE), 1664–1667.

Zhang, J., He, L., Wang, E., and Gao, R. (2008). "A LQR controller design for active vibration control of flexible structures," in *2008 IEEE Pacific-Asia Workshop on Computational Intelligence and Industrial Application*, Vol. 1 (Washington, DC: IEEE), 127–132.

Zhang, L., and Zhuan, X. (2020). Vibration control method of an electromagnetic isolation system based on LQR and coevolutionary NGA. *Shock Vib.* 2020:6384160. doi: 10.1155/2020/6384160

Zhang, W., Gong, X., and Chen, L. (2010). A Gaussian distribution model of anisotropic magnetorheological elastomers. *J. Magn. Magn. Mater.* 322, 3797–3801. doi: 10.1016/j.jmmm.2010.08.004

Zhang, X., Gong, X., Zhang, P., and Wang, Q. (2004). Study on the mechanism of the squeeze-strengthen effect in magnetorheological fluids. *J. Appl. Phys.* 96, 2359–2364. doi: 10.1063/1.1773379

Zhao, R., Kim, Y., Chester, S. A., Sharma, P., and Zhao, X. (2019). Mechanics of hard-magnetic soft materials. *J. Mech. Phys. Solids* 124, 244–263. doi: 10.1016/j.jmps.2018.10.008

Zhou, G. (2003). Shear properties of a magnetorheological elastomer. *Smart Mater. Struct.* 12:139. doi: 10.1088/0964-1726/12/1/316

Zhu, Y., Gong, X., Dang, H., Zhang, X., and Zhang, P. (2006). Numerical analysis on magnetic-induced shear modulus of magnetorheological elastomers based on multi-chain model. *Chin. J. Chem. Phys.* 19, 126–130. doi: 10.1360/cjcp2006.19(2).126.5

Zong, L., Gong, X., Guo, C., and Xuan, S. (2012). Inverse neuro-fuzzy MR damper model and its application in vibration control of vehicle suspension system. *Veh. Syst. Dyn.* 50, 1025–1041. doi: 10.1080/00423114.2011.645489

Conflict of Interest: JL was employed by the company Anhui Weiwei Rubber Parts Group Co. Ltd.

The remaining authors declare that the research was conducted in the absence of any commercial or financial relationships that could be construed as a potential conflict of interest.

frontiers in Materials

ORIGINAL RESEARCH
published: 09 June 2021
doi: 10.3389/fmats.2021.665814

Nonlinear Magneto-Electro-Mechanical Response of Physical Cross-Linked Magneto-Electric Polymer Gel

Xiwen Fan[1], Yu Wang[1], Bochao Wang[1], Longjiang Shen[2], Jun Li[3], Zhenbang Xu[4], Sheng Wang[1] and Xinglong Gong[1]**

[1]CAS Key Laboratory of Mechanical Behavior and Design of Materials, CAS Center for Excellence in Complex System Mechanics, Department of Modern Mechanics, University of Science and Technology of China, Hefei, China, [2]Hunan Bogie Engineering Research Center, Zhuzhou, China, [3]Anhui Weiwei Rubber Parts Group Co. Ltd., Tongcheng, China, [4]CAS Key Laboratory of On-orbit Manufacturing and Integration for Space Optics System, Fine Mechanics and Physics, Changchun Institute of Optics, Chinese Academy of Sciences, Changchun, China

OPEN ACCESS

Edited by:
Xun Yu,
New York Institute of Technology, United States

Reviewed by:
Wenling Zhang,
Nanjing University of Science and Technology, China
Soheil Razavi,
Technical and vocational university of Tabriz, Iran

***Correspondence:**
Xinglong Gong
gongxl@ustc.edu.cn
Yu Wang
wyu@ustc.edu.cn

Specialty section:
This article was submitted to Smart Materials, a section of the journal Frontiers in Materials

Received: 09 February 2021
Accepted: 03 May 2021
Published: 09 June 2021

Citation:
Fan X, Wang Y, Wang B, Shen L, Li J, Xu Z, Wang S and Gong X (2021) Nonlinear Magneto-Electro-Mechanical Response of Physical Cross-Linked Magneto-Electric Polymer Gel. Front. Mater. 8:665814. doi: 10.3389/fmats.2021.665814

This work reports on a novel magnetorheological polymer gel with carbon nanotubes and carbonyl iron particles mixed into the physical cross-linked polymer gel matrix. The resulting composites show unusual nonlinear magneto-electro-mechanical responses. Because of the low matrix viscosity, effective conductive paths formed by the CNTs were mobile and high-performance sensing characteristics were observed. In particular, due to the transient and mutable physical cross-linked bonds in the polymer gel, the electromechanical behavior acted in a rate-dependent manner. External stimulus at a high rate significantly enhanced the electrical resistance response during mechanical deformation. Meanwhile, the rheological properties were regulated by the external magnetic field when magnetic particles were added. This dual enhancement mechanism further contributes to the active control of electromechanical performance. These polymer composites could be adopted as electromechanical sensitive sensors to measure impact and vibration under different frequencies. There is great potential for this magnetorheological polymer gel in the application of intelligent vibration controls.

Keywords: piezo-resistivity, carbon nanotubes, soft sensor, shear stiffening, magnetorheological gel

INTRODUCTION

Magnetorheological (MR) gel is a kind of magneto-controllable soft gel that acts by dispersing the magnetic particles into a low cross-linking density gel matrix (Wang et al., 2014; Zhang et al., 2019). Under external magnetic fields, magnetic particles could overcome the constraint of the matrix and form a chain-like structure. In contrast to MR fluid, the MR gel is more stable and can offer more favorable and convenient conditions for engineering applications. Therefore, with its excellent performance in magnetorheology, the MR gel is expected to be used as a new alternative material for intelligent devices, such as magneto-dampers, energy absorbers, and vibration isolations (Lin et al., 2018; O'Driscoll et al., 2018; Petare and Jain, 2018).

To further improve the mechanical properties, shearing stiffening gel (SSG) has been adopted as the polymer matrix of the MRG (Gurgen and Yildiz, 2020; Hapipi et al., 2020; Zheng et al., 2020). SSG is a kind of soft and viscous boron-siloxane polymer gel with dynamic boron-oxygen (B-O)

weak cross-linking bonds, of which the storage modulus, elastic modulus, and viscosity would significantly increase under the external high rate excitation (Xu et al., 2020). Owing to the non-covalent, physical cross-link characteristic of the B-O bonds, SSG can exhibit a typical strain-rate dependence by transforming the gel, rubber, and glassy states under different external loading rates. Moreover, due to the reversibility of the B-O bond, SSG has the capacity for restoration and self-healing even under high speed loading (Wang et al., 2016; Wang et al., 2018). The magnetic additives render the SSG with special magnetically responsive behaviors. The storage modulus of magneto-sensitive SSG will increase under the external magnetic field stimulation (Xu et al., 2018; Liu et al., 2020). The dual hardening mechanism of the mechanics and magnetic field provides a new method for engineering equipment such as vibration isolators and energy absorbers.

Because of the additives of conductive magnetic fillers, the electrical properties of MR materials also change under an external magnetic field (Xu et al., 2013; Puente-Cordova et al., 2018). Magnetic CIPs can be easily moved from isotropic status to anisotropic status by the stimulus of the magnetic field. The CIPs are aligned along the direction of the magnetic field, which forms effective conductive paths (ECPs). The transient time of the alignment progress was studied via the change of storage modulus (An et al., 2012). Meanwhile, owing to the microstructure variations induced by ECPs, the electrical conductivity properties of the magneto-sensitive SSG show synchronous behaviors with the mechanical behaviors when the external magnetic field is varied (Wang et al., 2015; Cvek et al., 2020; Yun et al., 2020). The alignment of the CIPs can be monitored by conductivity. However, even if the anisotropic chain-like structure of CIPs is formed, the resistance of the magneto-sensitive SSG is still very high due to the obstacle of the polymer gel matrix, which hinders the potential application in the field of magnetic sensing sensors for intelligent devices (Xu et al., 2013). To improve the conductivity of MR composite, (Mietta et al., 2012) modified the CIPs with silver and obtained the anisotropic effects in magnetic properties and piezoelectric. (Pang et al., 2015) blended carbon black into an MR plastomer and studied the relationship between electrical conductivity vs. magnetic flux density. (Yun et al., 2019) mixed liquid metal into MRE and obtained a self-sensing material with anisotropic and unconventional piezo-conductivity. These studies reveal that anisotropic electricity is highly dependent on the alignment of CIP clusters. Past research was generally conducted under quasi-static and cyclic loading with low frequency. However, the application of engineering materials under high frequency is also often encountered. More work should be done to study the conductive sensitivity and the magneto-sensitivity of SSG under dynamic stimulus.

In this study, a novel magneto-electric polymer composite was fabricated by introducing the CNTs and CIPs into SSG. Rheological experiments, which studied the magneto-rheological properties and shear stiffening characteristic of e-SSG. The compressive tests showed the enhancement of the magnetic field on self-sensing capacity and durability. A drop weight machine was adopted to test its electrical responses under low-velocity impact. It was found that with the application of the magnetic field, enhancement of mechanical behaviors, electrical sensitivity, and stability were shown by this material. In summary, due to its excellent dual response mechanism of strain and magnetic field, this material has the potential for intelligent vibration control.

EXPERIMENT MATERIALS

Boric acid and benzoyl peroxide (BPO) were purchased from Sinopharn Chemical Reagent Co. Ltd., Shanghai, China. Hydroxyl silicone oil was purchased from Jining Huakai Resin Co. Ltd. Multi-walled CNTs with 3–5 nm in diameter and 8–13 μm in length were purchased from Conductive Materials of Luelida Co. Ltd., Xinxiang City, Henan Province, China. Carbonyl iron particles were purchased from BASF Germany. All the reagents were analytically pure and were adopted without additional purification.

The fabrication progress is illustrated in **Figure 1**. First, the boric acid and hydroxyl silicone oil were mixed with the mass ratio of 1:15 and heated in the oven at 180°C for 2 h. During the heating progress, CNTs and BPO were added into the matrix in turn and the mass fractions were 1 and 0.4%. 5 μL caprylic acid was added to every 100 g composite and mixed uniformly. Here, caprylic acid was cross-linking agent and plasticizer in the polymer matrix, which helped improve the roughness and the shear stiffening behaviors. After one hour of heating, the SSG matrix was obtained. The CIPs were mixed into the matrix homogeneously through a rubber mill (Taihu Rubber Machinery Factory, China, Model XK-160). According to our previous work (Fan et al., 2019), the electrical conductivity and sensing capacity of the composite achieved their highest values when the mass fraction of CIPs was 50%. Subsequently, the composite was vacuumed to remove air bubbles for 2 h and the conductive self-sensing composite, e-SSG, was obtained. The composite was molded into a cylinder shape with a 5 mm radius and 10 mm height. Finally, copper electrodes with 0.01 mm in thickness and 5 mm in radius were stuck to the specimen.

Characterization

The rheological behaviors of SSG were tested by a commercial rheometer (Physical MCR 302, Anton Paar Co., Austria). Plane to plane with 19 mm in diameter rheological test system was adopted and the height of specimen was set as 1 mm. Compressive tests were conducted by a universal testing machine (MTS criterion 43, MTS System Co., America). The dynamic mechanical behaviors of the specimen were tested by a drop tower testing machine (Mode ZCJ1302-A, MTS Industrial Systems, China). The drop hammer weighed 500 g and the impact head was a round surface with 25 mm diameter. A piezo-electrical acceleration sensor was used to record the velocity change of the drop hammer. The data acquisition system was composed of a charge amplifier (Mode YE5853, Jiangsu Sinocera Piezotronics, INC., China) and an oscilloscope (Mode DPO 2012B, Tektronix INC., United States). A programmable power supply (ITECH

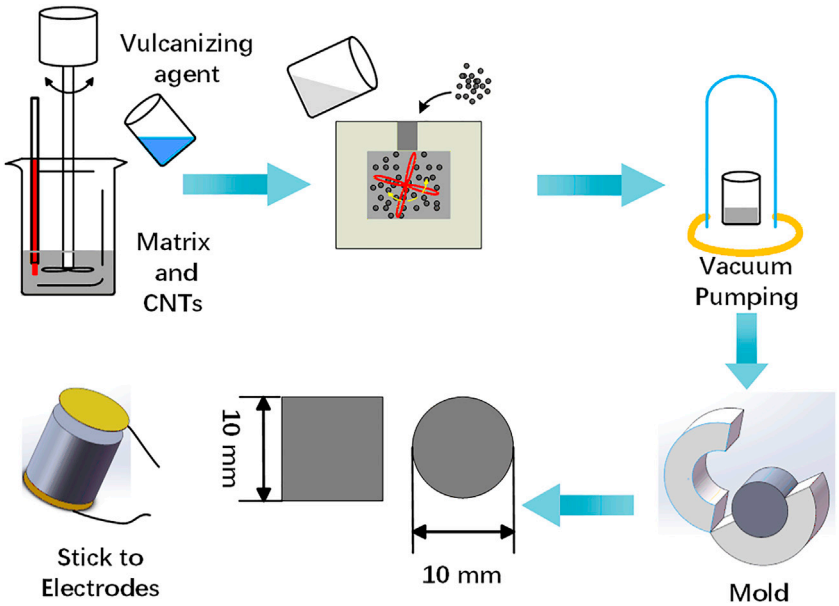

FIGURE 1 | Schematic of the material progress.

Electronic C. Ltd., China) was used to excite the magnetic field. All tests were conducted at room temperature.

Rheology Characterization of e-SSG

The rheology behaviors were tested under oscillatory shear mode. The shear amplitude was set to be 0.1%. As shown in **Figure 2A**, the storage modulus of the SSG increased from 45 Pa to 0.53 MPa when the shear frequency increased from 0.1 to 100 Hz. At 20 Hz, the loss modulus achieved its peak value, 0.30 MPa. The damping factor, which is defined as the ratio of the loss modulus to the storage modulus, can usually be adopted to illustrate the state of the composite materials. According to the work of (Boland et al., 2016) and (Sun et al., 2019), when the damping factor is larger than 1, the viscous components play a dominant role in material deformation. Herein, with the external frequency increasing from 0.1 to 100 Hz, the damping factor decreased from 74.46 to 0.31, indicating the polymer composite translated from a viscous state (or plastic state) to a rubbery state. Inherited from the SSG matrix, the e-SSG also showed typical rate-dependent behaviors. Compared to SSG, the primary and peak modulus of e-SSG were much higher. Simultaneously, the damping factor was smaller. With test frequencies increasing from 0.1 to 100 Hz, the storage modulus increased from 0.26 to 1.15 MPa. The loss modulus increased from 0.11 to 0.33 MPa at 2 Hz. Then, the loss modulus decreased down to 0.05 MPa when the shear frequency reached 100 Hz.

The strain-dependent and magnetorheological behaviors of the e-SSG were tested as well **Figure 2C**. When the shear strain reached 0.18, a drastic decrease was observed in the storage modulus of SSG and e-SSG, which indicated failure to emerge in composites. The influence of the magnetic field was remarkable. Increasing strain led to the decrease of storage, known as the Payne effect. However, no failure happened to the e-SSG when the magnetic field was applied. To investigate the MR effect, a shear strain with an amplitude of 0.1% and frequency of 1 Hz was applied. When the magnetic flux density increased from 0 to 1.2 T, the storage modulus of e-SSG increased from 0.49 to 1.39 MPa **Figure 2D**. The loss modulus increased from 0.28 to 0.57 MPa when the magnetic flux density increased to 0.44 T and finally decreased to 0.37 MPa with 1.2 T. Furthermore, the shear stiffening behaviors under magnetic field were also investigated. The green lines in **Figures 2A,B** illustrated the shear stiffening behavior of e-SSG under 0.8 T. The storage modulus increased from 1.1 to 2.3 MPa when the shear frequency increased from 0.1 to 100 Hz. Higher storage modulus and lower damping factors helped the composite materials hold shapes and recover from external stress loading.

The creep and recovery behaviors of the e-SSG were shown in **Figures 2E,F**. The creep compliance was dependent on the external stress, which showed a typical nonlinear material characteristic. Generally, the creep strain, γ_t, consisted of instantaneous strain, γ_e, delayed elastic strain, γ_d, and residual strain, γ_r. The function could be expressed as follows (Xu et al., 2012).

$$\gamma_t = \gamma_e + \gamma_d + \gamma_r = J(t)\,\tau_0 \tag{1}$$

where τ_0 indicates the cnstant stress. The constant stresses were set at 50, 500 and 5,000 Pa. **Figure 2E** shows the creep behaviors with different magnetic fields. When the shear stress was 50 Pa, γ_e was negligible and the composite showed plastic characteristics. With the shear stress increasing to 5 kPa, γ_e increased to 0.19 and the instantaneous creep compliance changed to 1.75×10^{-5} Pa^{-1}. With the presence of a magnetic field, the creep compliance was further diminished and the recovery behaviors were more remarkable. The instantaneous creep compliance of e-SSG under the magnetic flux density of 0.8 T was 6.83×10^{-6} and

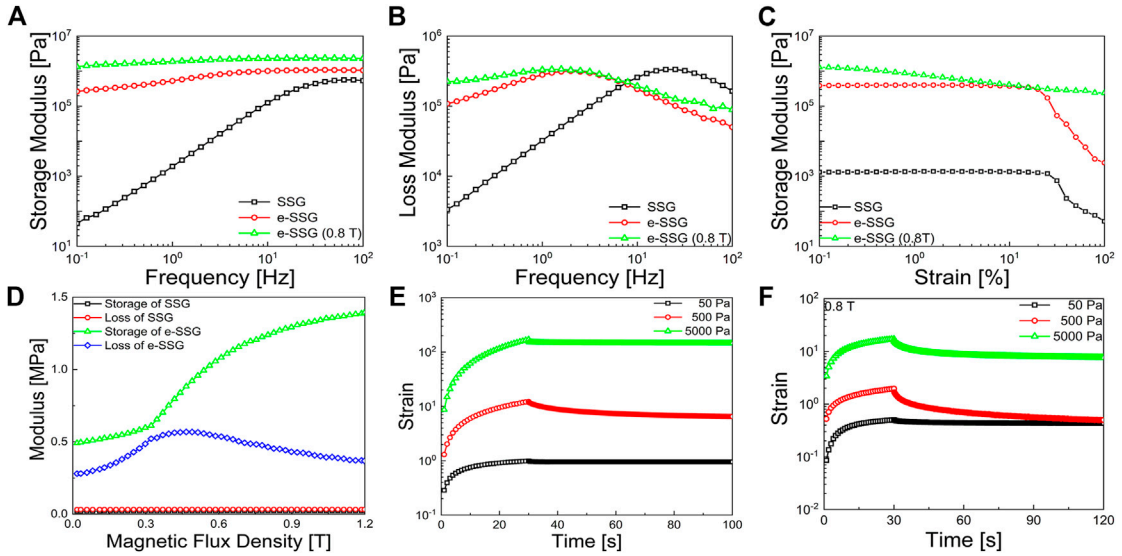

FIGURE 2 | The rheology behaviors of the SSG. **(A,B)** The shear stiffening behaviors of SSG and e-SSG. **(C)** The storage modulus under different shear strain. **(D)** The magnetorheological effect of SSG and e-SSG. The creep and recovery behaviors of the e-SSG under different shear stress and with the absence **(E)** and presence **(F)** of the magnetic field.

$4.68 \times 10^{-6}\,\mathrm{Pa}^{-1}$ when the shear stress was 0.5 and 5 kPa, respectively. The viscous flow component became smaller with the increase of shear stress and magnetic flux density. This dual hardening mechanism provided a favorable condition to absorb external stimuli and hold linear mechanical properties.

Piezo-Resistive Response Under Quasi-Static Loading

The piezo-resistive response under quasi-static state was investigated via MTS. The initial electrical conductivity of e-SSG was 25 Ω·m. The measurement method is illustrated in **Figures 3A,B**. The test rate was set at 0.010, 0.015, and 0.020 s^{-1}. The compress stress was recorded at the same time. In series circuits with constant electromotive force, the voltages of different components were proportional to resistance. The electrical resistance was calculated by the following function:

$$R_x = \frac{E - U}{U} R \tag{2}$$

where the E, U, and R represented the electromotive force of the constant voltage source, the voltage of the constant resistance, and the resistor.

Electrical conductivity showed a negative relationship to the compressive strain. With the increase of compressive speed, the sensitivity of the electrical conductivity was also improved. Here, gauge factor was defined as,

$$GF = \frac{\Delta\rho}{\rho_0} \Big/ \Delta\varepsilon \tag{3}$$

when it came to 10 s, the changes of $\frac{\Delta\rho}{\rho_0}$ achieved peak values and came to be 0.088, 0.162, and 0.233 with a compressive strain rate of 0.010, 0.015, and 0.020 s^{-1}, respectively, **Figure 3D** shows the relationship between the compressive strain and resistivity. The resistivity increased with compressive strain. The final resistivity was lower than the initial value. According to Zhang (Zhang et al., 2000), a possible reason for this phenomenon could be attributed to the time dependence characteristic of the electrical threshold. The GFs were 0.88, 1.08, and 1.065. With the enhancement of the magnetic field, the sensitivity was improved and the time effect was negligible. The electrical response held nearly linearly **Figure 3G** and GFs increased to 1.01, 1.89, and 2.19. The presence of a magnetic field increased the linear response and helped to hold the stable electrical properties. To provide an insight into the influence of the magnetic field, the stress-strain curves are shown in **Figures 3E,H**.

Typical rate-dependent behaviors could be observed in **Figures 3C,H**. With the increase of compressive speed, the compress modulus and yield stress increased rapidly. When the compressive strain came to 0.54% with the compressive rate of 0.010 s^{-1}, the compressive stress started to decrease. Plastic flow deformation came to dominate. When the compressive rate was 0.020 s^{-1}, the yield strain increased to 0.64%. The stress-strain hysteresis areas are shown in **Figure 3H**. With the presence of a magnetic field, the elasticity of the e-SSG was highly improved. The compressive modulus could be calculated at 0.22, 0.23, and 0.24 MPa, corresponding to the compressive rates of 0.010, 0.015, and 0.020 s^{-1}. The magnetic field improved the strain sensitivity of e-SSG. Furthermore, we should attach more importance to the fact that the magnetic field improved mechanical behaviors. The linear elastic scope of the e-SSG was greatly extended. The unloading progress was also linear. The dynamic response was then investigated to ensure the role of the magnetic field.

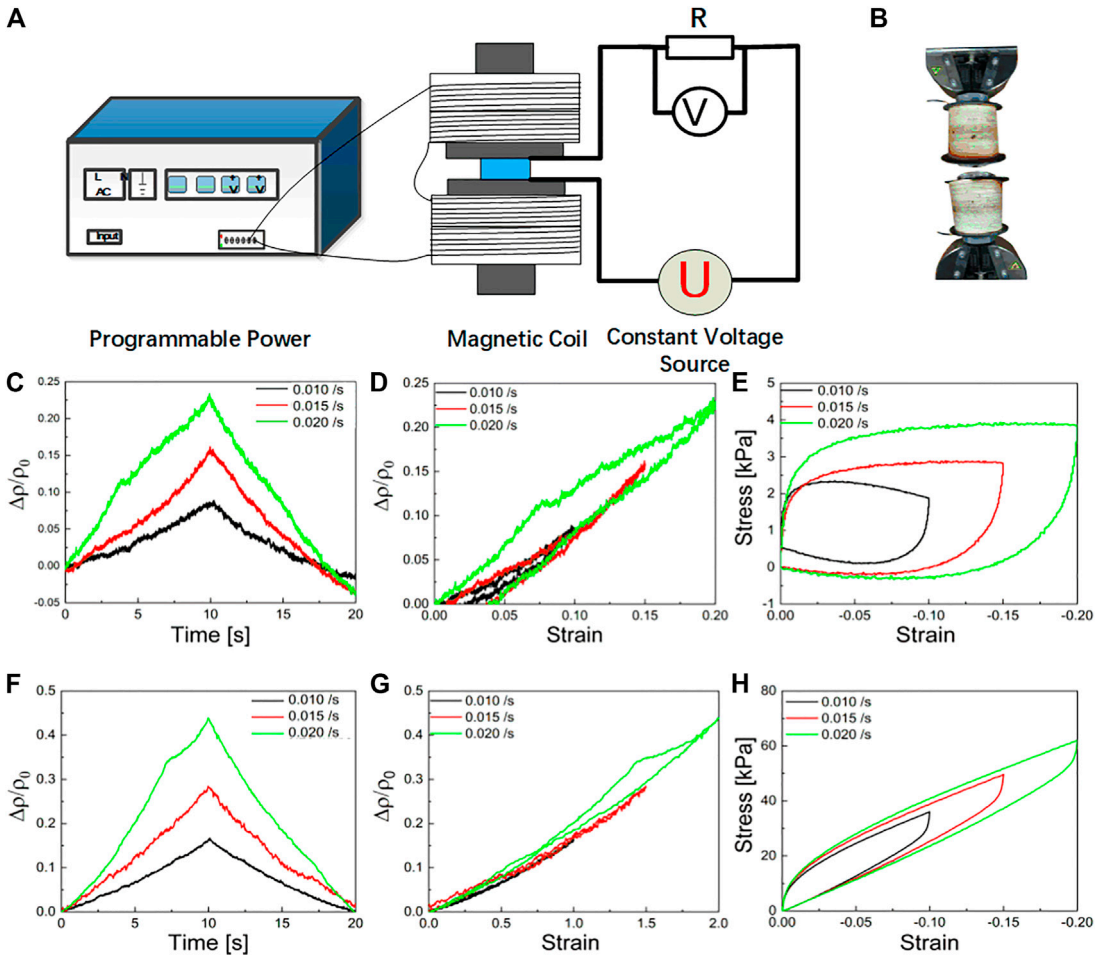

FIGURE 3 | (A) Schematic of the test equipment and the measuring method. **(B)** The testing equipment. **(C–E)** The electrical resistivity behaviors vs. time and compressive strain, the stress-strain without magnetic field. **(F–H)** illustrated the behaviors under a magnetic flux density of 0.3 T.

Piezo-Resistive Response Under Low-Velocity Impact

The dynamic mechanical and electrical responses were investigated via a drop weight machine. The acceleration data and voltage were recorded by one oscilloscope to ensure the synchronization of mechanical and electrical responses. Regarding the impact duration within several microseconds, the data sampling rate was set at 50 MHz. A constant voltage source was adopted to excite the coils to generate a magnetic field. To achieve a uniform magnetic field, the specimen was fixed upon an aluminum cylinder and placed at the center of an iron hollow cylinder as seen in the schematic in **Figure 4**. When the exciting current was 3A, the magnetic flux density reached 0.3 T.

Figures 5A–C showed the dynamic responses of the e-SSG to drop weight without a magnetic field**. Figures 5D–F** illustrates the results with the magnetic field. With the increase of drop height, the impact duration was shortened, which indicated hardening progress corresponding to the higher impact energy (**Figure 5A**). The force-displacement curves are shown in **Figure 5B**. With an increase in drop height, the stiffness was improved. Herein, the peak stiffness of the composites was illustrated by the secant slope. With the drop height increasing from 0.2 to 0.7 m, the peak stiffness shifted from 0.56×10^6 to 0.94×10^6 N/m. When the compressive progress was finished, e-SSG became soft. The electrical behaviors recorded this progress in **Figure 5C**. During the compressive progress, the electrical resistance of e-SSG increased rapidly and then stayed nearly constant. The peak values of $\Delta R/R_0$ depended on the drop height. With higher drop height, the $\Delta R/R_0$ achieved higher values. However, the rise progress was not linear and could be divided into three stages, which were the fast rise stage, the slow rise stage, and the secondary fast rise stage. The values and duration of the three stages are shown in **Table 1**. With the increase of drop height, the slow rise stage was gradually eliminated and the response of electrical resistance came to be linear.

The enhancement of the magnetic field was remarkable. Compared to the results with the absence of a magnetic field,

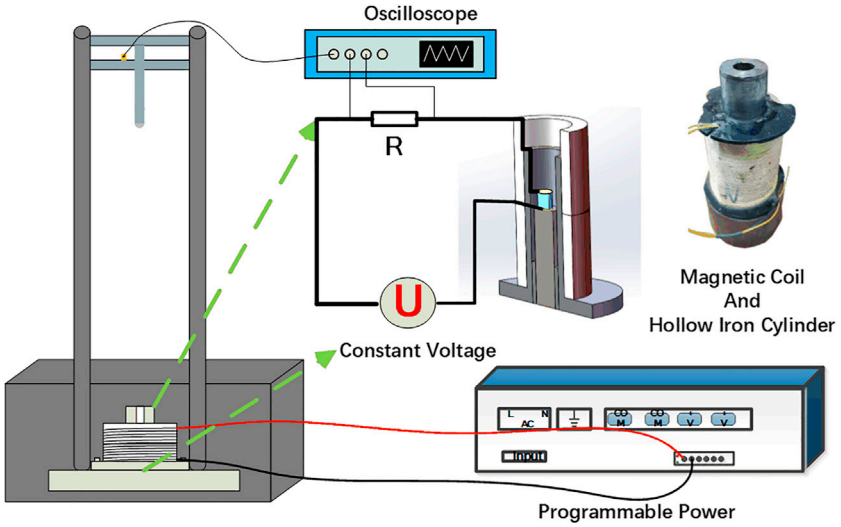

FIGURE 4 | Schematic of the test equipment and measuring method.

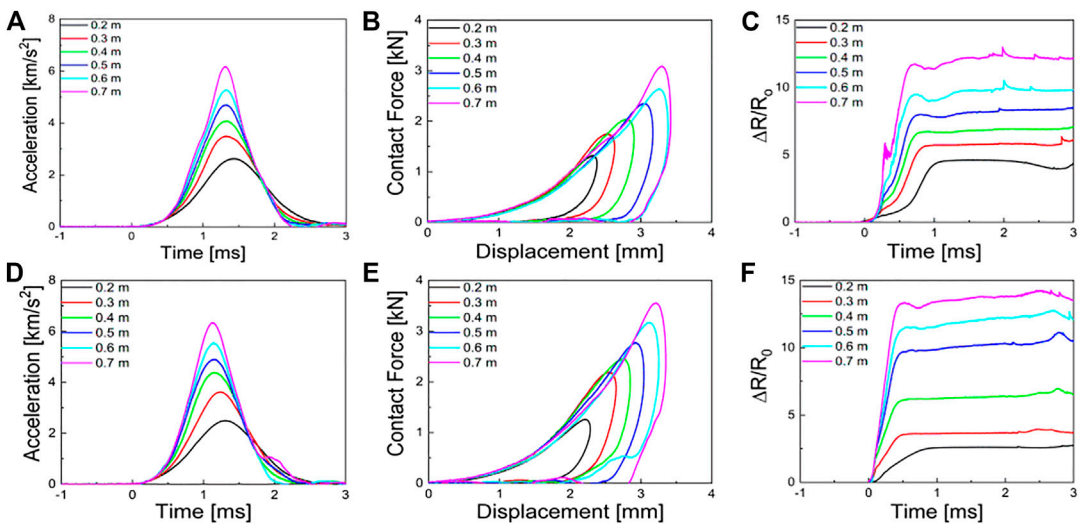

FIGURE 5 | (A) The acceleration data vs. time, **(B)** the contact force vs. displacement curves, **(C)** the changes of electrical resistance under different drop heights without magnetic field. **(D–F)** illustrated response behaviors with the magnetic flux density of 0.3 T.

TABLE 1 | The stage value and duration time of the results in **Figure 5C**.

Drop	Stage 1		Stage 2		Stage 3	
Height (m)	$\frac{\Delta R}{R_0}$	Duration (ms)	$\frac{\Delta R}{R_0}$	Duration (ms)	$\frac{\Delta R}{R_0}$	Duration (ms)
0.2	0.50	0.2	1.24	0.61	4.60	0.59
0.3	1.00	0.25	1.34	0.43	5.70	0.60
0.4	1.53	0.27	2.34	0.40	6.73	0.63
0.5	2.00	0.29	3.10	0.38	7.98	0.66
0.6	3.04	0.31	3.51	0.36	9.49	0.76
0.7	5.12	0.31	5.01	0.36	11.71	0.94

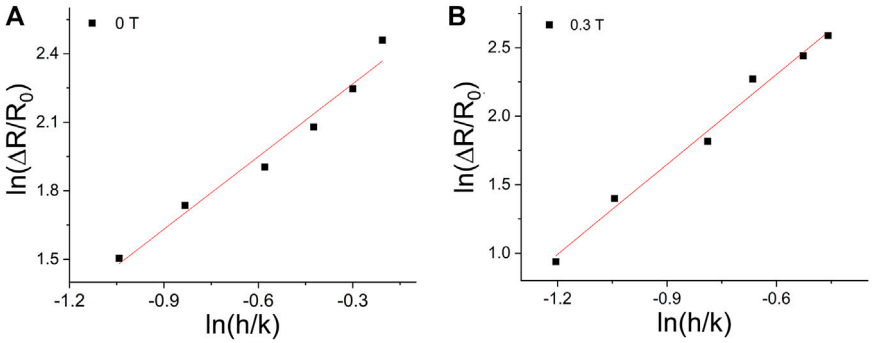

FIGURE 6 | The peak values of $\Delta R/R_0$ with different drop height in the absence **(A)** and presence **(B)** of the magnetic field. The lines showed fitting results.

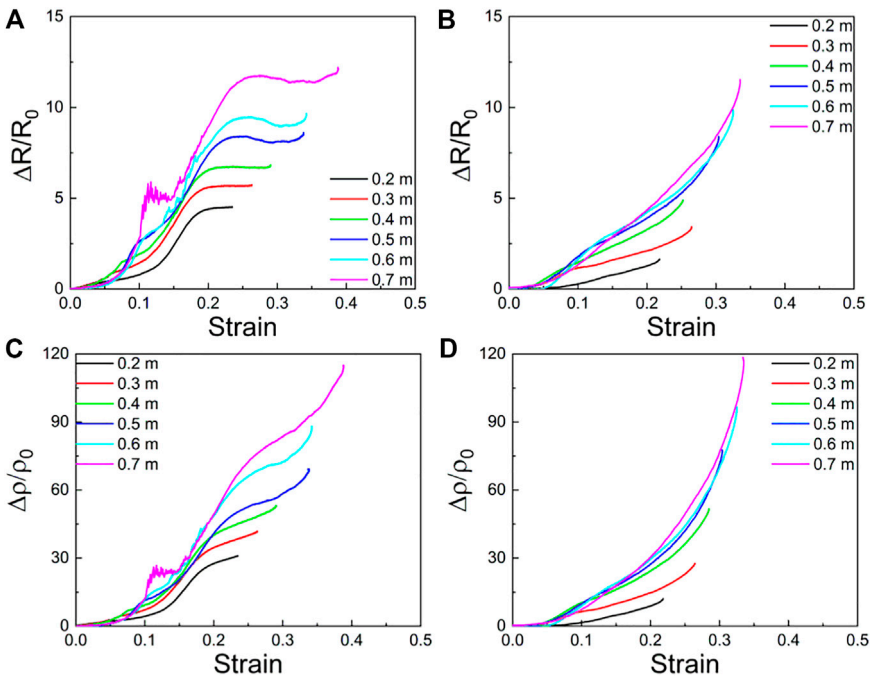

FIGURE 7 | Response of **(A)** resistance and **(C)** resistivity to compressive strain. **(B,D)** illustrated the results with a magnetic flux density of 0.3 T.

the impact duration was further shortened under the same drop weight (**Figure 5D**). The peak values of the $\Delta R/R_0$ of different drop heights also increased. When the drop height ranged from 0.2 to 0.7 m, the $\Delta R/R_0$ were 2.52, 4.05, 6.16, 9.69, 11.47, and 13.31. As seen from the results of MTS, the magnetic field enhanced the linear elastic scope of the e-SSG and the electrical resistance showed continuous rise progress.

According to the theory of Boland et al. (Boland et al., 2016),

$$\frac{\Delta R}{R_0} = \frac{n_\varepsilon}{W}\left(\frac{2E_{mgh}}{\varepsilon_c^2 E y_0}\right)^m = a\left(\frac{h}{k}\right)^m \quad (4)$$

where n_ε, W and y_0 were the electrical constants and the geometric parameters. ε_c was the yield strain. k was the stiffness of the specimen, E was Young's modulus, $k = \frac{ES}{h}$. In **Figure 6**, the relation between $\frac{\Delta R}{R_0}$ and $\frac{h}{k}$ was plotted. With the absence of a magnetic field, $m_0 = 1.06$ and $a_0 = 13.28$. With the presence of a magnetic field, $m_1 = 2.19$ and $a_1 = 4.81$. The parameter "a" in **Eq. 4** was negatively corrected with the yield strain of the e-SSG. Its changes indicated the improvement of the stiffness of composites. With the presence of a magnetic field, the CIP clusters aligned in a specific direction. The anisotropy microstructure helped improve the electrical sensitivity of e-SSG.

To obtain detailed information on the electrical response, the relationship between resistance and resistivity vs. compressive strain is shown in **Figure 7**. The three stages could be observed in **Figure 7A**. With the increase of drop height, the sensitivity of e-SSG to strain was improved. When the compressive strain was

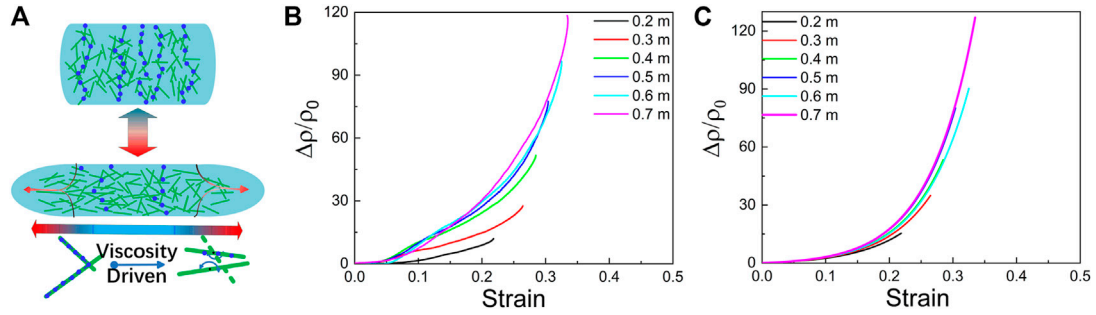

FIGURE 8 | (A) The illustration of the negative behaviors of the piezo-resistance. **(B)** The experiment results and **(C)** the fitting results of **Eq. 6**.

larger than a critical point, the resistance kept stable. However, the resistivity kept increasing. The increase of resistivity and the deformation of the compression came to balance and the resistance of e-SSG kept nearly constant (**Figures 7A,C**). The response of e-SSG under the magnetic field showed continuous upward progress (**Figure 7B,D**). The magnetic field improved the elastic behaviors and kept the electrical response continuous.

To illustrate the rate-dependent behaviors, a phenomenological function was adopted. According to the tunneling effect theory (Wang and Cheng, 2014), the conductivity of the composite depends on the effective conductive paths (ECPs). The aggregation and alignment of the conductive fillers are the key factors that determine the numbers of ECPs. The initial state of the composite was homogeneous and isotropic. During the compressive progress, the lateral extension led by the Poisson effect made the CNTs move from their initial position and rotate to a specific direction (**Figure 8A**). The rearrangement of the CNTs destroyed the original ECPs. Since the restriction of the matrix to the CNTs depended on the mechanical properties of SSG (Zimmerman et al., 2009; de Vicente et al., 2011; Bastola et al., 2020), it was assumed that the sensitivity of the e-SSG was related to the strain rate of external stimulus and the elastic modulus of the specimen. Based on the theory of Boland (Boland et al., 2016), the resistivity of composites depended on the total number of ECPs per volume,

$$\rho = \rho_0 \left\{ [1 + (\varepsilon)^m]^{-1} + \frac{\varepsilon}{\varepsilon_t} \right\}^n \tag{5}$$

where the first term in **Eq. 5** represented the strain term and the second represented the time dependence. Parameter "n" was a constant related to the microstructure of ECPs. Since the impact duration was short, the time dependence was ignored. Considering that the electrical sensitivity showed remarkable dependence on the strain rate, strain rate, $\dot{\varepsilon}$, was adopted to describe the resistivity behaviors. k was the stiffness of the specimen. With the drop height varied from 0.2 to 0.7 m, k was 0.67×10^6, 0.80×10^6, 0.88×10^6, 0.92×10^6, 1.00×10^6, and 1.01×10^6 N/m. Then, the function could be given:

$$\frac{\rho}{\rho_0} = [1 + (\varepsilon)^m]^{\frac{n\dot{\varepsilon}}{k}} \tag{6}$$

TABLE 2 | The fitting results of Prony function.

(T)	–	0.2 m	0.3 m	0.4 m	0.5 m
0	A1	2.07	2.40	2.92	3.14
	τ_1 (s)	3.00	2.90	2.82	2.39
0.3	A1	2.27	3.30	3.98	5.50
	τ_1 (s)	2.98	2.87	2.60 s	2.02

The curves in **Figures 8B,C** plot the experiment data and fitting results of function 6. The relationship between electrical resistivity and strain could be expressed as:

$$\frac{\rho}{\rho_0} = [1 + (\varepsilon)^{1.06}]^{6.5\times10^4\frac{\dot{\varepsilon}}{k}} \tag{7}$$

This phenomenological model illustrated the relationship between strain, strain rate, and the equivalent stiffness of the specimen. The shear stiffening behaviors weakened the effect of impact. This expression could be adopted in engineering applications to monitor external stimulus.

The recovery behaviors of the electrical properties under different drop heights and the strength of the external magnetic field were investigated (**Figure 9**). The impact response was finished in several microseconds, but the recovery progress lasted for seconds. With higher drop heights, the electrical conductivity recovers sooner. To characterize the recovery behaviors, the Prony series with one order was adopted (Belyaeva et al., 2016; Wen et al., 2018).

$$\frac{\Delta R}{R_0}(t) = A_0 - \sum A_n e^{-\frac{t}{\tau_n}} \tag{8}$$

The fitting results are shown in **Table 2.** Herein, symbols A_1 and τ_1 represent the amplitude and the characteristic time of the decay time, respectively. With an increase of the drop height, the decay amplitude increased from 2.07 to 3.14, and the characteristic time decreased from 3.00 to 2.39 s. The magnetic field further enlarged the amplitude and shortened the characteristic time. The recovery progress was related to the viscoelasticity behaviors of e-SSG. Generally, the relaxation behaviors of the polymer composite depended on the ratio of viscosity to elasticity. High drop height led to the shear stiffening behaviors and the elastic recovery

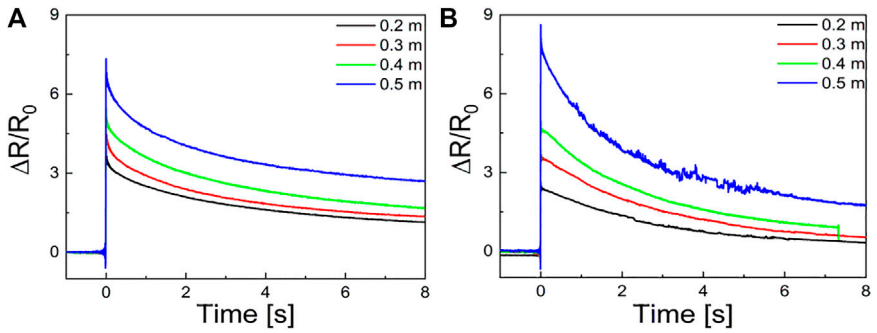

FIGURE 9 | The recovery behaviors of the electrical properties under drop weight impact with the strength of the external magnetic field are zero **(A)** and the strength of the external magnetic field is 0.3 T **(B)**.

became more remarkable. Meanwhile, the magnetic field improved the elastic modulus and enhanced the recovery progress.

To demonstrate the durability of the e-SSG, a cyclic drop test was conducted (**Figure 10**). The drop heights varied from 0.2 to 0.5 m. The magnetic flux density was 0.3 T. With the increase of test number, the response accumulated. Regarding the initial resistance of every impact, $\Delta R/R_0$ kept stable. After the impact, the conductivity of the composite could recover to its initial state.

CONCLUSION

In summary, we developed a novel soft sensor with high sensitivity to strain under quasi-static and low-velocity impact. Inherited from the SSG matrix, this soft sensor could harden itself to burden external stimuli. Magnetic-dependent characteristics further improved the stiffness of the smart material. Quasi-static tests and drop weight experiments were conducted to investigate the electrical and mechanical behaviors. The relationship between resistivity and strain rate was revealed.

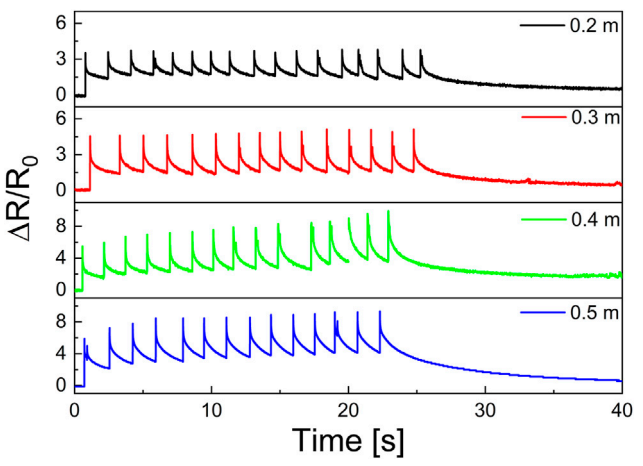

FIGURE 10 | The electrical resistance response to cyclic drop weight test with the drop heights of 0.2, 0.3, 0.4, and 0.5 m.

Based on these results, this study came to the below conclusions.

(1) The mechanical and electrical behaviors of e-SSG depend on the strain rate and the magnetic field. A higher strain rate led to an increase in yield stress and enhanced the recovery progress of the e-SSG.Due to the magneto-rheological effect, the electrical response of e-SSG to strain was higher and linear under a uniform magnetic field.
(2) The response of the e-SSG to dynamic loading with large amplitude was nonlinear. Magnetic field improved the sensitivity and stability. The shear stiffening behaviors and magneto-rheology behaviors could improve the recovery capacity.
(3) e-SSG could be utilized to monitor the quasi-static deformation and low-velocity impact. Within an appropriate range, the e-SSG could hold stable mechanical and electrical properties and respond regularly to external stimuli.

DATA AVAILABILITY STATEMENT

The raw data supporting the conclusions of this article will be made available by the authors, without undue reservation.

AUTHOR CONTRIBUTIONS

XF conducted all the experiments and wrote the draft of the article. YW, BW, LS, JL, ZX, SW, and XG revised and discussed the article.

FUNDING

The authors acknowledge financial supports from the National Natural Science Foundation of China (Grant No. 11972337, 11772320, 11972343), the National Key R&D Program of China (Grant No. 2018YFB1201703) and the Strategic Priority Research Program of the Chinese Academy of Sciences (Grant No. XDB2204002) are gratefully acknowledged.

REFERENCES

An, H.-N., Sun, B., Picken, S. J., and Mendes, E. (2012). Long Time Response of Soft Magnetorheological Gels. *J. Phys. Chem. B* 116, 4702–4711. doi:10.1021/jp301482a

Bastola, A. K., Paudel, M., Li, L., and Li, W. (2020). Recent Progress of Magnetorheological Elastomers: a Review. *Smart Mater. Struct.* 29, 123002. doi:10.1088/1361-665X/abbc77

Belyaeva, I. A., Kramarenko, E. Y., Stepanov, G. V., Sorokin, V. V., Stadler, D., and Shamonin, M. (2016). Transient Magnetorheological Response of Magnetoactive Elastomers to Step and Pyramid Excitations. *Soft Matter* 12, 2901–2913. doi:10.1039/c5sm02690c

Boland, C. S., Khan, U., Ryan, G., Barwich, S., Charifou, R., Harvey, A., et al. (2016). Sensitive Electromechanical Sensors Using Viscoelastic Graphene-Polymer Nanocomposites. *Science* 354, 1257–1260. doi:10.1126/science.aag2879

Cvek, M., Kutalkova, E., Moucka, R., Urbanek, P., and Sedlacik, M. (2020). Lightweight, Transparent Piezoresistive Sensors Conceptualized as Anisotropic Magnetorheological Elastomers: A Durability Study. *Int. J. Mech. Sci.* 183, 105816. doi:10.1016/j.ijmecsci.2020.105816

De Vicente, J., Klingenberg, D. J., and Hidalgo-Alvarez, R. (2011). Magnetorheological Fluids: a Review. *Soft Matter* 7, 3701. doi:10.1039/c0sm01221a

Fan, X., Wang, S., Zhang, S., Wang, Y., and Gong, X. (2019). Magnetically Sensitive Nanocomposites Based on the Conductive Shear-Stiffening Gel. *J. Mater. Sci.* 54, 6971–6981. doi:10.1007/s10853-019-03360-8

Gürgen, S., and Yıldız, T. (2020). Stab Resistance of Smart Polymer Coated Textiles Reinforced with Particle Additives. *Compos. Structures* 235, 111812. doi:10.1016/j.compstruct.2019.111812

Hapipi, N. M., Mazlan, S. A., Ubaidillah, U., Abdul Aziz, S. A., Ahmad Khairi, M. H., Nordin, N. A., et al. (2020). Solvent Dependence of the Rheological Properties in Hydrogel Magnetorheological Plastomer. *Ijms* 21, 1793. doi:10.3390/ijms21051793

Lin, X.-G., Guo, F., Du, C.-B., and Yu, G.-J. (2018). The Mechanical Properties of a Novel STMR Damper Based on Magnetorheological Silly Putty. *Adv. Mater. Sci. Eng.* 2018, 1–15. doi:10.1155/2018/2681461

Liu, B., Du, C., Yu, G., and Fu, Y. (2020). Shear Thickening Effect of a Multifunctional Magnetorheological Gel: the Influence of Cross-Linked Bonds and Solid Particles. *Smart Mater. Struct.* 29, 015004. doi:10.1088/1361-665X/ab5243

Mietta, J. L., Ruiz, M. M., Antonel, P. S., Perez, O. E., Butera, A., Jorge, G., et al. (2012). Anisotropic Magnetoresistance and Piezoresistivity in Structured Fe3O4-Silver Particles in PDMS Elastomers at Room Temperature. *Langmuir* 28, 6985–6996. doi:10.1021/la204823k

O'driscoll, D. P., Vega-Mayoral, V., Harley, I., Boland, C. S., and Coleman, J. N. (2018). Optimising Composite Viscosity Leads to High Sensitivity Electromechancial Sensors. *2d Mater.* 5 (3). doi:10.1088/2053-1583/aacba6

Pang, H., Xuan, S., Liu, T., and Gong, X. (2015). Magnetic Field Dependent Electro-Conductivity of the Graphite Doped Magnetorheological Plastomers. *Soft Matter* 11, 6893–6902. doi:10.1039/c5sm00984g

Petare, A. C., and Jain, N. K. (2018). Improving spur Gear Microgeometry and Surface Finish by AFF Process. *Mater. Manufacturing Process.* 33, 923–934. doi:10.1080/10426914.2017.1376074

Puente-Córdova, J., Reyes-Melo, M., Palacios-Pineda, L., Martínez-Perales, I., Martínez-Romero, O., and Elías-Zúñiga, A. (2018). Fabrication and Characterization of Isotropic and Anisotropic Magnetorheological Elastomers, Based on Silicone Rubber and Carbonyl Iron Microparticles. *Polymers* 10, 1343. doi:10.3390/polym10121343

Sun, C., Jia, H., Lei, K., Zhu, D., Gao, Y., Zheng, Z., et al. (2019). Self-healing Hydrogels with Stimuli Responsiveness Based on Acylhydrazone Bonds. *Polymer* 160, 246–253. doi:10.1016/j.polymer.2018.11.051

Wang, L., and Cheng, L. (2014). Piezoresistive Effect of a Carbon Nanotube Silicone-Matrix Composite. *Carbon* 71, 319–331. doi:10.1016/j.carbon.2014.01.058

Wang, S., Jiang, W., Jiang, W., Ye, F., Mao, Y., Xuan, S., et al. (2014). Multifunctional Polymer Composite with Excellent Shear Stiffening Performance and Magnetorheological Effect. *J. Mater. Chem. C* 2, 7133–7140. doi:10.1039/c4tc00903g

Wang, S., Xuan, S., Jiang, W., Jiang, W., Yan, L., Mao, Y., et al. (2015). Rate-dependent and Self-Healing Conductive Shear Stiffening Nanocomposite: a Novel Safe-Guarding Material with Force Sensitivity. *J. Mater. Chem. A.* 3, 19790–19799. doi:10.1039/c5ta06169e

Wang, Y., Ding, L., Zhao, C., Wang, S., Xuan, S., Jiang, H., et al. (2018). A Novel Magnetorheological Shear-Stiffening Elastomer with Self-Healing Ability. *Composites Sci. Tech.* 168, 303–311. doi:10.1016/j.compscitech.2018.10.019

Wang, Y., Wang, S., Xu, C., Xuan, S., Jiang, W., and Gong, X. (2016). Dynamic Behavior of Magnetically Responsive Shear-Stiffening Gel under High Strain Rate. *Composites Sci. Tech.* 127, 169–176. doi:10.1016/j.compscitech.2016.03.009

Wen, Q., Wang, Y., Feng, J., and Gong, X. (2018). Transient Response of Magnetorheological Elastomers to Step Magnetic Field. *Appl. Phys. Lett.* 113, 081902. doi:10.1063/1.5048368

Xu, J., Wang, P., Pang, H., Wang, Y., Wu, J., Xuan, S., et al. (2018). The Dynamic Mechanical Properties of Magnetorheological Plastomers under High Strain Rate. *Composites Sci. Tech.* 159, 50–58. doi:10.1016/j.compscitech.2018.02.030

Xu, Y., Gong, X., Liu, T., and Xuan, S. (2013). Magneto-induced Microstructure Characterization of Magnetorheological Plastomers Using Impedance Spectroscopy. *Soft Matter* 9, 7701. doi:10.1039/c3sm51072g

Xu, Y., Gong, X., Xuan, S., Li, X., Qin, L., and Jiang, W. (2012). Creep and Recovery Behaviors of Magnetorheological Plastomer and its Magnetic-dependent Properties. *Soft Matter* 8, 8483. doi:10.1039/c2sm25998b

Xu, Y., Lubineau, G., Liao, G., He, Q., and Xing, T. (2020). Rate-dependent Viscoelasticity of an Impact-Hardening Polymer under Oscillatory Shear. *Mater. Res. Express* 7, 075701. doi:10.1088/2053-1591/ab9fbc

Yun, G., Tang, S.-Y., Sun, S., Yuan, D., Zhao, Q., Deng, L., et al. (2019). Liquid Metal-Filled Magnetorheological Elastomer with Positive Piezoconductivity. *Nat. Commun.* 10, 1300. doi:10.1038/s41467-019-09325-4

Yun, G., Tang, S.-Y., Zhao, Q., Zhang, Y., Lu, H., Yuan, D., et al. (2020). Liquid Metal Composites with Anisotropic and Unconventional Piezoconductivity. *Matter* 3, 824–841. doi:10.1016/j.matt.2020.05.022

Zhang, G., Li, Y., Wang, H., and Wang, J. (2019). Rheological Properties of Polyurethane-Based Magnetorheological Gels. *Front. Mater.* 6, 56. doi:10.3389/fmats.2019.00056

Zhang, X.-W., Pan, Y., Zheng, Q., and Yi, X.-S. (2000). Time Dependence of Piezoresistance for the Conductor-Filled Polymer Composites. *J. Polym. Sci. B Polym. Phys.* 38, 2739–2749. doi:10.1002/1099-0488(20001101)38:21<2739::Aid-Polb40>3.0.Co;2-O

Zheng, J., He, X., Li, Y., Zhao, B., Ye, F., Gao, C., et al. (2020). Viscoelastic and Magnetically Aligned Flaky Fe-Based Magnetorheological Elastomer Film for Wide-Bandwidth Electromagnetic Wave Absorption. *Ind. Eng. Chem. Res.* 59, 3425–3437. doi:10.1021/acs.iecr.9b06143

Zimmerman, D. T., Bell, R. C., Filer, J. A., Karli, J. O., and Wereley, N. M. (2009). Elastic Percolation Transition in Nanowire-Based Magnetorheological Fluids. *Appl. Phys. Lett.* 95, 014102. doi:10.1063/1.3167815

Conflict of Interest: Author JL was employed by the company Anhui Weiwei Rubber Parts Group Co.Ltd.

The remaining authors declare that the research was conducted in the absence of any commercial or financial relationships that could be construed as a potential conflict of interest.

Advantages of publishing in Frontiers

OPEN ACCESS
Articles are free to read for greatest visibility and readership

FAST PUBLICATION
Around 90 days from submission to decision

HIGH QUALITY PEER-REVIEW
Rigorous, collaborative, and constructive peer-review

TRANSPARENT PEER-REVIEW
Editors and reviewers acknowledged by name on published articles

Frontiers
Avenue du Tribunal-Fédéral 34
1005 Lausanne | Switzerland

Visit us: www.frontiersin.org
Contact us: frontiersin.org/about/contact

REPRODUCIBILITY OF RESEARCH
Support open data and methods to enhance research reproducibility

DIGITAL PUBLISHING
Articles designed for optimal readership across devices

FOLLOW US
@frontiersin

IMPACT METRICS
Advanced article metrics track visibility across digital media

EXTENSIVE PROMOTION
Marketing and promotion of impactful research

LOOP RESEARCH NETWORK
Our network increases your article's readership